UNIVERSITY OF SOUTHAMPTON

FACULTY OF NATURAL AND ENVIRONMENTAL SCIENCES
School of Ocean and Earth Sciences

Detection and attribution of climate change in satellite records of ocean productivity

---

by

Gayatri Dudeja

Thesis for the degree of Doctor of Philosophy

December, 2014

UNIVERSITY OF SOUTHAMPTON

ABSTRACT

FACULTY OF NATURAL AND ENVIRONMENTAL SCIENCES
School of Ocean and Earth Sciences

Doctor of Philosophy

DETECTION AND ATTRIBUTION OF CLIMATE CHANGE IN SATELLITE RECORDS OF OCEAN PRODUCTIVITY

By Gayatri Dudeja

Phytoplankton make up approximately half of the global biosphere production. Climate change is predicted to affect phytoplankton productivity. Detecting the climate change signal in satellite records of productivity would imply that ocean primary production has been affected by anthropogenic influences. Long-term trends in chlorophyll (chl) concentration in the ocean have been observed by several studies. However, the effect of internal variability in chl was not taken into account in these observed trends. This thesis aims to perform a formal detection and attribution analysis on observed chl concentration using the optimal fingerprint (OF) method. The methodology has been applied to detect and attribute greenhouse gas induced climate change in sea-surface temperature records, ocean heat content, atmospheric air temperature etc., but this is the first attempt to apply it to ocean productivity records.

The OF method was applied to monthly observations of chl data (1999-2005) from NASA's Ocean Biogeochemical Model (NOBM) which assimilates satellite-derived chl. Control run and forced simulations from four Earth System Models were used to derive the internal variability of chl and response of chl to climate forcings (anthropogenic and natural), respectively. Three metrics were defined to describe the climate change signal in chl - spatial linear trend of chl; linear trend of zonal average; and time series of the size of the oligotrophic gyres. The OF technique of detection and attribution was implemented on the observational datasets for each of the three metrics. The amplitude of the responses provide an indication of whether a climate forcing signal is present in the observations.

Out of the three metrics, the study demonstrated that the second metric (linear trend of zonal average in chl) is the best, and the third metric (size of the oligotrophic gyres) is the worst, 'direction' to look for a climate change signal in chl. Thus, metrics should be defined such that they capture the relevant change in chl and at the same time do not contain too much small scale variability which leads to noise. It was also illustrated that climate models do not necessarily simulate the internal variability of chl well, or the response of chl to climate forcings, indicating the need to improve the performance of climate models.

A greenhouse gas signal was detected in observations in some regions of the ocean indicating that chl concentration is likely being affected by climate change. The canonical model of chl response to global warming, i.e. decrease in chl in lower latitudes and increase in chl in higher latitudes, was not consistently observed in all the regions of the ocean. This signifies that changing climate is affecting chl in a way which is not yet completely understood and in future the effects of climate change on chl may be surprisingly different from our current conceptual model.

Table of Contents

List of Figures

List of Tables

List of Equations

Declaration of Authorship

I, Gayatri Dudeja declare that this thesis titled, “Detection and Attribution of Climate Change in Satellite Records of Ocean Productivity” and the work presented in it are my own.

I confirm that:

- This work was done wholly or mainly while in candidature for a research degree at this University.
- Where any part of this thesis has previously been submitted for a degree or any other qualification at this University or any other institution, this has been clearly stated.
- Where I have consulted the published work of others, this is always clearly attributed.
- Where I have quoted from the work of others, the source is always given. With the exception of such quotations, this thesis is entirely my own work.
- I have acknowledged all main sources of help.
- Where the thesis is based on work done by myself jointly with others, I have made clear exactly what was done by others and what I have contributed myself.

Signed: .....

Date:.....

Acknowledgements

Firstly, I would like to sincerely thank my supervisors Stephanie Henson, Peter Challenor and Claudie Beaulieu for giving me this opportunity, for guiding and supporting me over the last three years, for encouraging and motivating me, and for always being there to help when I needed it. I am very grateful to Stephanie for always listening to me patiently and guiding me throughout the PhD.

I would like to thank Oliver Andrews for helping me understand some aspects of the optimal fingerprint method and I am grateful to Fancis Zweirs for his helpful suggestions and comments on some of the results.

Thanks to my officemates, Andrew, Anna and Victoria for listening to me, helping me when I needed it, providing some lovely snacks occasionally and for the refreshing tea breaks. I would like to thank my friend and colleague Jason for all the help and advice. Thanks to Katsia and Richard for their support and encouragement.

Many thanks to my friends Katsia, Anna, Sandra, Archana, Pallavi, Priyanka, Supriya, Fernanda, Jane and Thao for their support, encouragement, for making this journey of three years fun and for always being there during hard times.

Special thanks to my father and mother for always believing in me. Thanks to my brother and his wife, my nephew Tanish, my two nieces and my whole family for their support, for motivating and encouraging me when my spirits were down, for always loving me and filling my heart with love.

Last but not the least, thanks to my beloved friend and husband Vineet for his support, patience, encouragement, advice and love.

Abbreviations

AM2.0	Atmospheric Model, version 2
AOGCM	Atmosphere Ocean General Circulation Model
AUV	Autonomous Underwater Vehicles
AVHRR	Advanced Very High Resolution Radiometer
BATS	Bermuda Atlantic Time Series
CalCOFI	Cooperative Oceanic Fisheries Investigations
CanESM2	Canadian Earth System Model 2
CCCma	Carbon-Climate Modelling and Analysis
CCI	Climate Change Initiative
CFC	Chlorofluorocarbons
CGCM	Coupled Global Climate Model
chl	Chlorophyll
CI	Confidence Interval
CMIP	Coupled Model Intercomparison Project
CMOC	Canadian Model of Ocean Carbon
CTEM	Canadian Terrestrial Ecosystem Model
D&A	Detection and Attribution
Diat-HadOCC	Diat-Hadley Centre Ocean Carbon Cycle
DIC	Dissolved Inorganic Carbon
DMS	Dimethyl Sulphide
DOM	Dissolved Organic Matter
EBM	Energy Balance Model
ENSO	El Niño Southern Oscillation
EOF	Empirical Orthogonal Function
ESA	European Space Agency
ESG	Earth System Grid

ESM	Earth System Model
GAM	Generalized Additive Model
GHG	Greenhouse gases
GCM	General Circulation Model
GES DISC	Goddard Earth Sciences Data and Information Services Center
GFDL	Geophysical Fluid Dynamics Laboratory
GMAO	Global Modeling and Assimilation Office
GOLD	Generalized Ocean Layer Dynamics
HadGEM2	Hadley Centre Global Environment Model
HFC	Hydrofluorocarbons
HOT	Hawaii Ocean Time-Series
HPLC	High Performance Liquid Chromatography
INCA	INteraction with Chemistry and Aerosol
IO	Indian Ocean
LIM	Louvain-la-Neuve
LM3.0	Land Model, version 3
LMDZ	Laboratoire de Me´te´orologie Dynamique
NCOM	National Centre for Atmospheric Research Community Ocean Model
NPZD	Nutrient, Phytoplankton, Zooplankton and Detritus
MEOF	Multivariate Empirical Orthogonal Function
MetUM	Met Office Unified Model
MOM4	Modular Ocean Model version 4.1
NA	North Atlantic
NAG	North Atlantic Gyre
NAO	North Atlantic Oscillation
NEMO	Nucleus for European Modelling of the Ocean
netCDF	Network Common Data Form

NOAA	National Oceanic and Atmospheric Administration
NOBM	NASA Ocean Biogeochemical Model
NP	North Pacific
NPG	North Pacific Gyre
OASIM	Ocean Atmosphere Spectral Irradiance Model
OF	Optimal Fingerprint
OGCM	Ocean General Circulation Model
OLS	Ordinary Least Squares
ORCHIDEE	ORganizing Carbon and Hydrology In Dynamic EcosystEms
PAR	Photosynthetically active radiation
PC	Principal Component
PCA	Principal Component Analysis
PDO	Pacific Decadal Oscillation
PISCES	Pelagic Interaction Scheme for Carbon and Ecosystem Studies
PFC	Perfluorocarbons
POM	Particulate Organic Matter
PP	Primary Production
ppm	Parts per million
R	Reduced
RCP	Representative Concentration Pathways
REPROBUS	Reactive Processes Ruling the Ozone Budget in the Stratosphere
RMS	Root Mean Square
SA	South Atlantic
SAG	South Atlantic Gyre
SeaWiFS	Sea-viewing Wide Field-of-view Sensor
SIS	Sea Ice Simulator
SLP	Sea-level pressure

SP	South Pacific
SPG	South Pacific Gyre
SST	Sea Surface Temperature
TOPAZ2	Tracers of Ocean Phytoplankton with Allometric Zooplankton, version 2.0
W	Whole
WGCM	Working Group on Coupled Modelling
WMO	World Meteorological Organization

GRADUATE SCHOOL OF THE NATIONAL OCEANOGRAPHY CENTRE, SOUTHAMPTON

This PhD thesis by

Gayatri Dudeja

has been produced under supervision of the following persons:

Supervisors:

Dr. Stephanie Henson
Peter Challenor
Dr. Claudie Beaulieu

Chair of the Advisory Panel:

Dr. Kevin Oliver

1. Introduction

Single-celled algae and other plant-like organisms known as 'phytoplankton' are the primary producers in the food chain of the ocean. More than two-thirds of the Earth's surface is covered by Oceans and phytoplankton make up approximately half of the global biosphere production (Field et al., 1998). Phytoplankton become food for tiny creatures called zooplankton. Zooplankton are food for large animals like small fish and jellyfish which in turn are food for larger animals like squids, sharks, marine mammals, birds and people. More than 2.6 billion people rely on fish for 20% of their average annual per capita protein intake (FAO, 2007). Every year approximately 80 Mt of marine fish is consumed as food or to produce fishmeal and oils for aquaculture and agriculture (FAO, 2010). Hence, phytoplankton being the primary elements of the food chain, affect the abundance and diversity of marine organisms throughout the food-chain and play a major role in marine ecosystem functioning and fishery yields. Ocean warming due to climate change will affect the distribution of phytoplankton in the ocean and thereby change the productivity and diversity of species higher up in the food chain.

Phytoplankton contain a pigment called 'chlorophyll' which initiates photosynthesis in the ocean i.e. it absorbs atmospheric carbon dioxide and nutrients in the water in the presence of sunlight to produce carbohydrates and releases oxygen. Phytoplankton play a crucial role in the global carbon cycle. Phytoplankton biomass in the ocean is approximately 1-2% of the global plant carbon. In spite of the low biomass, phytoplankton fix approximately 40% of the global atmospheric carbon dioxide per annum (Falkowski and Woodhead, 1992, Berger et al., 1989). Some of this carbon is transferred from the surface layers of the ocean to the deep ocean when phytoplankton die and the detritus sinks. Some carbon is transferred to different layers of the ocean by other animals higher in the food chain which feed on phytoplankton and themselves reproduce, generate waste and die. Some of the sinking material gets buried at the sea floor potentially for millennia while some gets remineralised back to the surface ocean and

atmosphere. This component of the cycle of carbon from atmosphere to the deep ocean is known as the biological pump. Climate change warms the ocean and hence stratification increases. In low latitudes of the ocean, increased stratification will decrease mixing and reduces the supply of nutrients to the surface ocean. This decreases the phytoplankton productivity in the ocean and the amount of atmospheric carbon fixed by phytoplankton will decrease. This will further promote climate change as carbon dioxide is a greenhouse gas and it increases the atmospheric temperature by increasing the radiative forcing of Earth.

As phytoplankton are so vital to ecosystem and climate, it is necessary to study their location and distribution in the water and how climate change is affecting them. Phytoplankton concentration can be measured by taking water samples from the ocean. Another way to determine phytoplankton concentration is by studying the ocean color. Chlorophyll (chl) and other pigments in the water change the way it reflects and absorbs sunlight. For example chl absorbs wavelengths in red and blue regions of the visible spectrum, but not in green. Hence, as phytoplankton increases in the ocean, the color of the ocean appears green. This property of the water constituents to absorb certain wavelengths and reflect others is used in remote sensing to derive the concentration of these constituents (McClain et al., 2000). Satellites measure the light reflected by the surface ocean, known as the water leaving radiance. This quantity is converted to chl concentrations by empirical ocean color algorithms (Gordon et al., 1988). Hence, chl concentrations are a way to map and locate the amount of phytoplankton in the ocean. Chl concentration in the ocean varies from location to location, seasonally, annually and also on decadal time scales. Thus, there is a natural cycle of variability of chlorophyll. Any change observed in chl over a certain time period is a combination of natural variability and change caused by external factors such as climate change due to anthropogenic activities. In order to detect the climate change signal in chlorophyll, a distinction needs to be made between variability of chlorophyll which occurs naturally and which occurs due to anthropogenic activities.

The focus of this thesis is firstly, to determine change in chl concentration in the ocean above its natural cycle and secondly, to determine if the observed change is due to anthropogenic activities. The results will help in fully understanding the impacts of climate change on phytoplankton by detecting and attributing potential chl changes to global warming.

1.1. Aims and Objectives

The main aim of the thesis is to detect a climate change signal in chlorophyll concentration of the ocean. Once the signal is detected, it is then attributed to climate forcings and the contribution of the forcings towards the observed change is determined. This is achieved by using an optimal fingerprint method of detection and attribution. The key objectives of the study are -

- To define and compute various suitable climate change signals for detecting and attributing anthropogenic climate change in chlorophyll concentration in the ocean.
- To implement the optimal fingerprint method of detection and attribution using a spatial pattern of linear trend in chlorophyll.
- To detect and attribute a climate change signal for the linear trend of the zonal average of chlorophyll in all the regions of the ocean.
- To implement the optimal fingerprint method using size of the subtropical gyres as the climate change signal.

It is assumed here that changes in chl due to climate change will be linear and therefore, linear trend of chl is chosen in this study. However, climate change may cause non-linear changes in chl concentration. In that case, climate change will not be detected in the signals chosen in this study.

1.2. Climate Change

Climate is defined as the average pattern of weather in a certain region over long periods of time (approximately 30 years), as defined by the World

Meteorological Organization (WMO) (Strahler, 1960). For example, weather in a particular place may be cold today, but climate of that place is hot most of the time. Climate varies with latitude, with distance from the sea, proximity of mountains and other geographical factors. Climate over a given period of time may deviate from the long-term statistics of climate over that corresponding calendar period. For example, springtime at a certain place coming earlier than it did 30 years ago is an indication of climate variability. Statistically significant variations occurring over long periods of time, typically decades or longer are termed as climate change (IPCC, 2007b, SYR). In order to understand climate change, we first need to know what climate is and what factors cause it to change.

The climate system is an interacting system consisting of various components such as the atmosphere, the ocean, ice and snow cover, the land and the various physical, chemical and biological processes that take place in and among these components. Interaction among these components causes the climate, as reflected in variables such as temperature, wind, clouds and precipitation, to vary. Figure 1-1 shows a schematic of the climate system. Components of the system (shown in bold) are atmosphere, hydrosphere, cryosphere and biosphere. Interaction processes of the system (represented by thin arrows) are atmosphere-ice interaction, heat exchange, wind stress and so on. Any change in the components or the interaction processes, caused naturally or by anthropogenic activities results in variations in some aspects of the climate system (shown by bold arrows). For example, changes in solar inputs, changes in atmosphere composition and circulation, changes in the ocean circulation, sea level and so on.

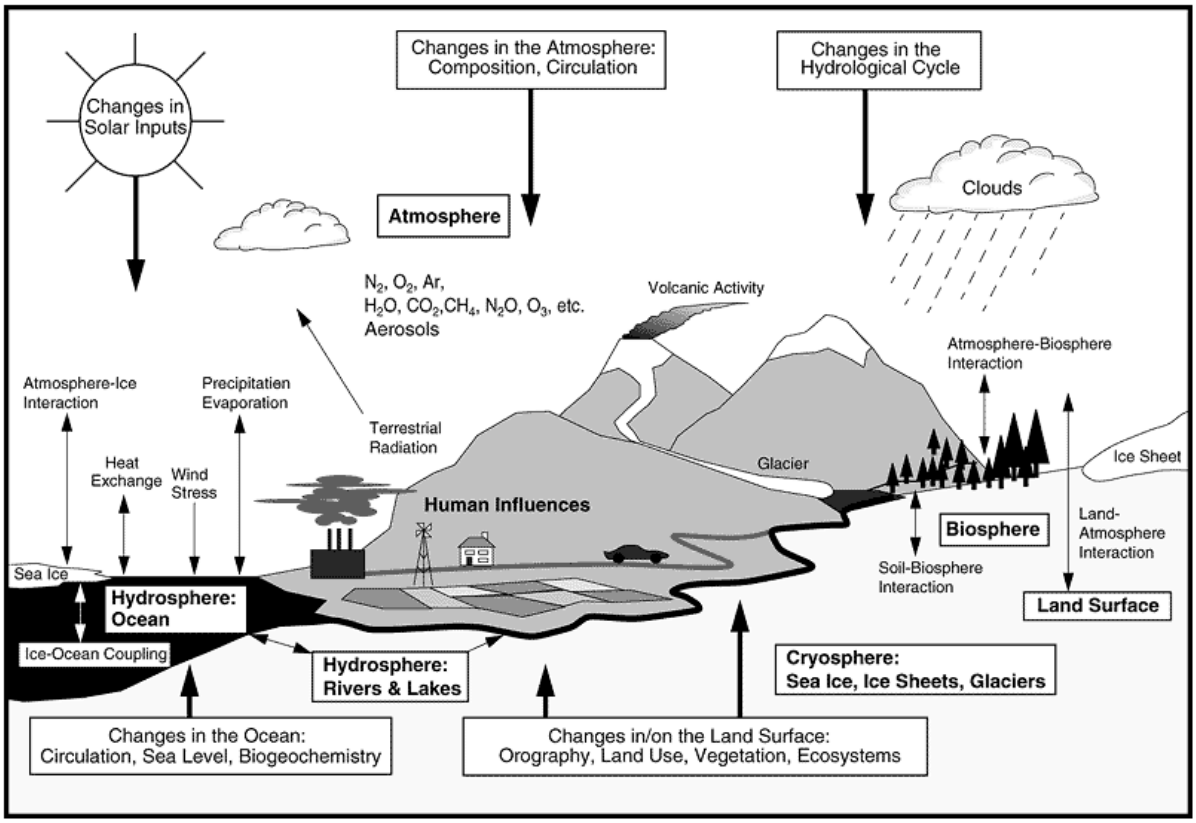

Figure 1-1. Schematic view of components of the global climate system (bold), their processes and interactions (thin arrows) and some aspects that may change (bold arrows) (IPCC, C. C. 2007 : Chapter 1).

Several factors shape the climate, known as forcings. These can be internal or external forcings. Internal forcing mechanisms act within the climate system itself, whereas external forcing mechanisms act from outside the climate system. Forcings can also be radiative or non-radiative.

The Sun is the ultimate source of energy that drives the climate system. The radiative balance i.e. the balance between the incoming solar radiation and outgoing infrared radiation controls the Earth's surface temperature. Disturbance in this radiative balance, caused naturally or by anthropogenic activities, results in pushing the climate system away from its normal state. For example, an increase in the incoming solar input will cause an increase in the Earth's temperature. A climate forcing may affect the radiative balance in a positive or negative way. If the forcing affects the balance positively then it leads to warming of the climate system, and vice-versa. An estimate of the value of different forcings in 2005 relative to the start of the industrial era

(about 1750) is shown in Figure 1-2. From the Figure it can be seen that human activities have a large positive effect, solar irradiance has a small positive effect and aerosols have a negative effect on the radiative balance.

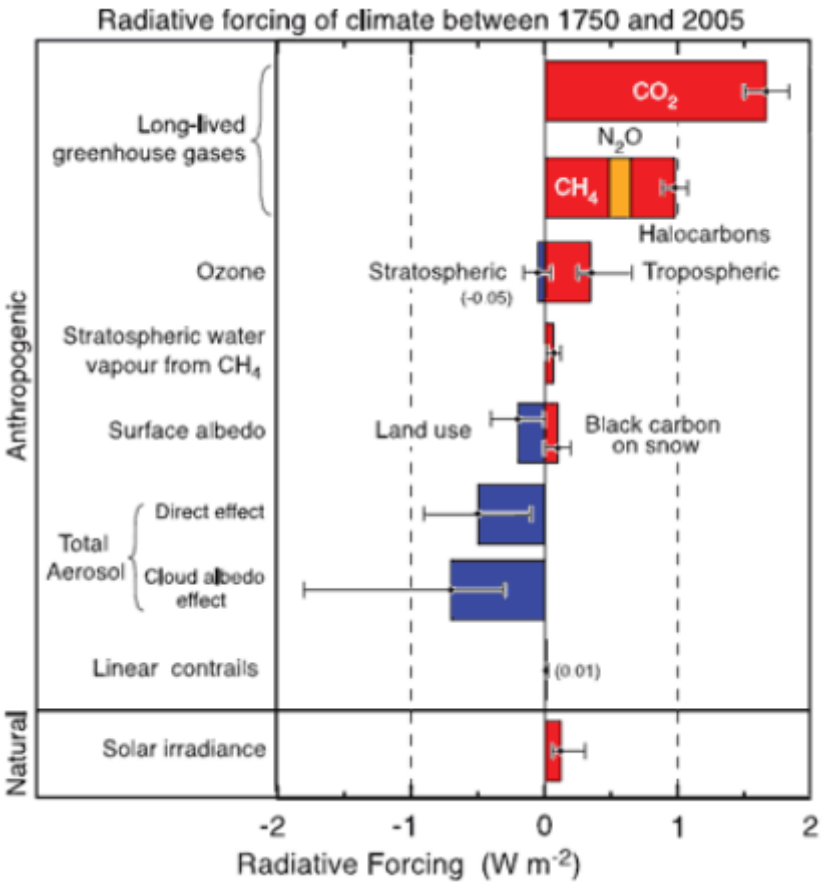

Figure 1-2. Summary of the principal components of radiative forcing of climate change. The values represent the forcings in 2005 relative to the start of the industrial era (about 1750) (IPCC, 2007b, SYR).

Forcing mechanisms that do not directly affect the radiative balance of the Earth are known as non-radiative forcings. These forcings affect the climate system by changing the Earth's surface geometry. Examples of these forcing mechanisms are the tectonic process of mountain building and tectonic movement of land masses. These occur on the time scale of 10^7 to 10^9 years, and so are outside the scope of this thesis.

1.2.1 External forcing

The term "solar cycle" refers to the amount of radiation emitted by the sun. In recent decades, satellites have allowed measurement of solar irradiance fluctuations. Before satellites, measurement of solar activity was made by proxy variables. Hence, confidence in the solar radiation on century time scales is low (Harrison et al., 1999). Recent reconstructions have estimated that solar irradiance has increased gradually since the industrial era (Figure 1-2). This is in addition to periodic fluctuations in solar radiation with the main one being the 11-year sun spot cycle.

Other external forcings relating to galactic or orbital variations occur on much longer timescales than anthropogenic climate change (~10^3 – 10^4 years) and so are ignored here.

1.2.2 Internal forcing

Interaction processes among the components of the climate system occur over a large spatial and temporal span. These processes may vary naturally and cause variations in the climate system. Examples of internal forcing mechanisms are volcanic activity, changes in ocean currents and anthropogenic activities.

Volcanic eruptions inject large amounts of aerosols into the stratosphere, increasing the Earth's albedo (reflectivity) and cooling the climate. The aerosols spread laterally before they start to decay. These eruptions create a short-lived (2-3 years) negative forcing. There can be very low aerosols between volcanic eruptions. The stratosphere is currently free of large quantities of volcanic aerosol, since the last major eruption was in 1991 (Mt. Pinatubo) (IPCC, 2007b, SYR).

Another internal forcing mechanism is ocean currents. Oceans store and distribute large amounts of heat energy around the planet via global ocean currents and hence they play an important role in the regulation of the climate system. For example, the Gulf stream, which is a warm current

flowing from the Caribbean and Florida towards Northwestern Europe, causes the temperature in these regions to be relatively mild compared to regions at the same latitude in Canada and Northwestern US. The ocean currents system, also known as the global thermohaline circulation system, is driven by winds, tides, Earth's rotation, solar energy and water density differences. The currents originate in North Atlantic Ocean where cold, dense water sinks to the deep ocean. These waters flow towards the tropics where they warm and upwell to the surface. The warm and less dense waters of the tropics flow towards the higher latitudes to replace the cold sinking water. These waters transfer the heat to the atmosphere and become cold and dense and thus sink to the deep ocean and renew the circulation system. Melting of polar ice due to global warming will reduce the salinity and density of the polar waters. This less dense water, sits on the surface of oceans and prevents sinking. Thus, melting would affect the thermohaline circulation system and distribution of heat around the globe i.e. higher latitudes will become more cold as there would be no warm surface waters brought to the poles and the lower latitudes will become more warm as there would be no upwelling of cold waters. Cooler sea-surface temperatures in high latitudes will reduce evaporation which reduces salinity of the waters, thus further reducing the sinking and slowing the thermohaline circulation..

Anthropogenic forcing refers to human activities rather than natural factors. Since the beginning of the industrial era the impact of human activities on the climate system has extended to a much larger scale. Human activities include increases in greenhouse gases associated with combustion of fossil fuels, sulphate aerosols produced as an industrial by-product, land-use change due to urbanization, forestry and agricultural practices. These all affect the physical and biological properties of the Earth’s surface that changes the radiative forcing and hence results in climate change.

The Earth's radiative balance is the balance between the incoming solar radiation and outgoing infrared radiation (Shine et al., 1990). If all the incoming energy from the sun were to be reflected from the Earth's surface in the form of outgoing infrared radiation, then the average surface temperature

of the Earth would be -18°C, which is 32°C colder than it would be if some of the incoming radiation is absorbed by Earth's atmosphere. Several gases present in the Earth's atmosphere, known as the greenhouse gases (GHGs), absorb some of the outgoing infrared radiation before it escapes to outer space, which makes the Earth's atmosphere warmer. Without this effect life would not be possible on Earth. Greenhouse gases that are naturally present in the atmosphere are water vapour, carbon dioxide, methane, nitrous oxide and ozone. Human activities such as burning of fossil fuel and clearing of forests enhance the concentration of most of the GHGs in the atmosphere. This leads to an increased greenhouse gas effect, causing more heat energy to be trapped in the atmosphere which results in global warming. Figure 1-3 shows concentrations of GHGs in the atmosphere for the last 2000 years. An increase in the concentrations is observed since 1750, which is due to human activities in the industrial era. Some anthropogenic activities such as air conditioning and refrigeration emit greenhouse gases such as chlorofluorocarbons (CFCs), hydrofluorocarbons (HFCs) and perfluorocarbons (PFCs). These GHGs do not occur naturally in the atmosphere but are the result of anthropogenic activities.

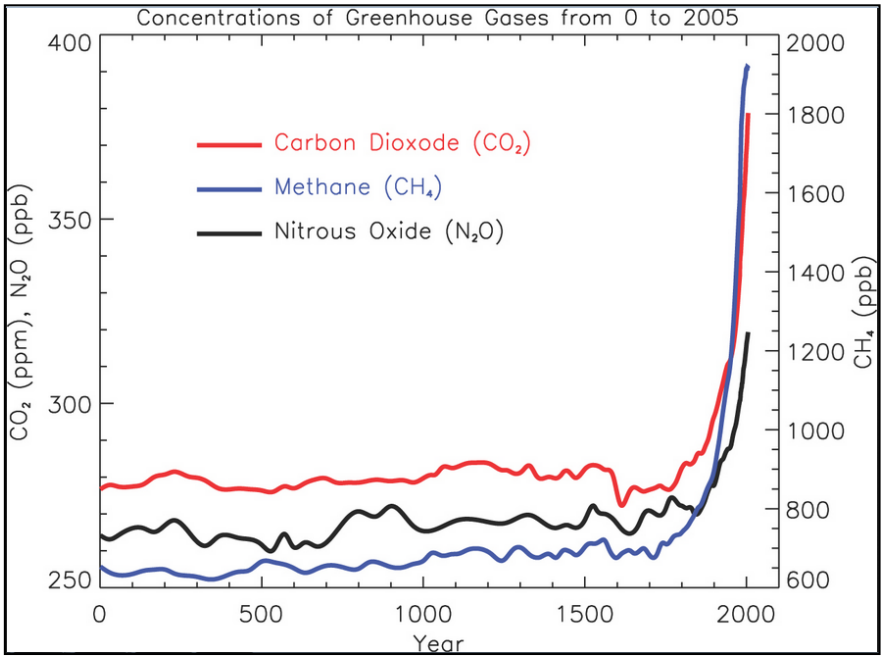

Figure 1-3. Atmospheric concentrations of important long-lived greenhouse gases over the last 2000 years. Concentration units are parts per million (ppm) or parts per billion (ppb) (IPCC, 2007a).

Another human activity that causes climate change is emission of aerosols into the atmosphere by industrial pollution. The effect of an increasing amount of aerosols on radiative forcing is complex and is a source of uncertainty in interpretation of climate change. Some aerosols affect the radiative balance in a positive way, while others affect the radiative balance in a negative way. Overall the effect of increasing aerosols is negative, i.e. it results in radiative cooling. .

Human activities such as deforestation, urbanization and changes in agriculture result in changing the physical and biological properties of the land surface which in turn cause change in the climate system. These changes generally result in more radiation being reflected from the Earth's surface and hence affect the radiative balance negatively.

Increase in the concentration of greenhouse gases is a dominant cause of climate change i.e. GHGs contribution towards increasing the radiative forcing is much more than the contribution by other factors such as aerosols and solar irradiance. This means that any change observed in the climate system apart from the natural variability, would be mainly due to greenhouse gases. Therefore, climate change detection studies distinguish between natural variability and greenhouse gas variability as the contribution towards climate change by other variabilities is very less and hence difficult to detect. In this thesis too, detection of climate change in chlorophyll is made by distinguishing between natural variability of chl and variability due to greenhouse gases.

The Climate system is in a state of dynamic balance as the components of the climate system are coupled to one another. This balance is disturbed by change in any component of the climate system. To restore equilibrium requires a cascade of effects in all the coupled components of the system. When this cascading effect in any of the coupled components of the system influences the initial cause of change, it is known as a feedback mechanism on the climate system. The effect of the response of the components on the initial cause may vary from one component to another i.e. the effect might be amplified (positive feedback) or it might be reduced (negative feedback)

(Cess and Potter, 1988). For example, increased concentration of GHGs in the atmosphere causes global warming by increasing the radiative forcing. As the Earth's surface temperature rises, some of the ice at high latitudes begins to melt. This exposes either bare ground or ocean, both of which have lower reflectivity than ice. Reduced reflectivity of incoming solar radiation increases the radiative forcing. This further heats up the Earth resulting in more ice melt and exposure of less reflective terrain. Thus a cycle of cause and effect is established, where each effect acts as the cause for the next step. This cycle is known as the ice-albedo feedback (Cubasch and Cess, 1990) and is a positive feedback. Similarly, there are many other feedback mechanisms in the climate system which influence the climate in response to some initial radiative forcing.

1.3 Ocean Primary Production

As discussed previously, marine primary production (PP) makes up approximately half of the global biosphere production (Field et al., 1998). Marine PP affects the abundance and diversity of marine organisms and drives marine ecosystem functioning and fishery yields (Iverson, 1990, Chavez et al., 2003, Ware and Thomson, 2005, Cheung et al., 2009, Cheung et al., 2010). It is also a major sink of carbon dioxide from the atmosphere and plays an important role in the global carbon cycle. Primary production is defined as the rate of grams of carbon fixed per unit volume per unit time. In other words it is the rate at which phytoplankton fix carbon by the process of photosynthesis. Photosynthesis is initiated by a pigment in phytoplankton named 'chlorophyll'. Thus, PP is dependent on the amount of phytoplankton present in the water. Total weight of all the phytoplankton in a given volume of water, also known as phytoplankton biomass, is expressed as mass of carbon per unit volume. Biomass can be estimated by measuring the amount of chlorophyll pigment present in the water and then applying a conversion factor to that value to obtain mass of carbon. Thus, PP can be estimated from chlorophyll concentration if estimates of other parameters such as photosynthetically active radiation (PAR), mixed layer depth and incident solar radiation are available. This is mainly helpful when estimating primary

production by remote sensing. It can be concluded that chlorophyll concentration allows an estimation of PP, as it describes the first order changes in the phytoplankton biomass and also reflects the photoacclimation state of phytoplankton (Ryther and Yentsch, 1957). Phytoplankton biomass can be derived from chlorophyll concentration but it does not give us any knowledge about the community structure of phytoplankton. Chlorophyll concentration in the ocean is mainly regulated by solar energy and nutrients. Physical processes such as winds, wind stress, ocean circulation, mixing, upwelling, mesoscale eddies etc. affect the nutrient supply to the euphotic zone of the ocean. These processes occur on seasonal, inter-annual and decadal time scales and hence, they alter the chlorophyll concentration in the ocean on local, regional and global scale.

It has been predicted that with the increase in temperature of ocean surface waters, chl concentration in tropical and mid latitudes will decrease, whereas it will increase in higher latitudes (Doney, 2006) (Figure 1-4). Tropical and mid-latitudes are nutrient limited regions of the ocean i.e. chl concentration in these regions is limited by the amount of nutrients in the water. An Increase in surface water temperatures would increase stratification that causes reduction in mixing which in turn decreases the supply of nutrients to the upper ocean and hence results in a decrease in chl. Productivity in high latitude regions of the ocean are light limited. Water column in these regions is less stratified compared to the tropical regions. Reduced stratification in the high latitude regions leads to a deep mixed layer depth in winter which results in reduced availability of light to phytoplankton. Increase in surface water temperatures increases stratification, which reduces mixing and leads to a shallower mixed layer depth. This increases the light available to phytoplankton which results in an increase in chl concentration in the water. This conceptual model of change in chl is based on changes in stratification however, changes in other factors such as position and strength of winds due to climate change (Swart and Fyfe, 2012) may also cause changes in the supply of nutrients to phytoplankton by altering the mixing and in turn resulting in change in chl concentration.

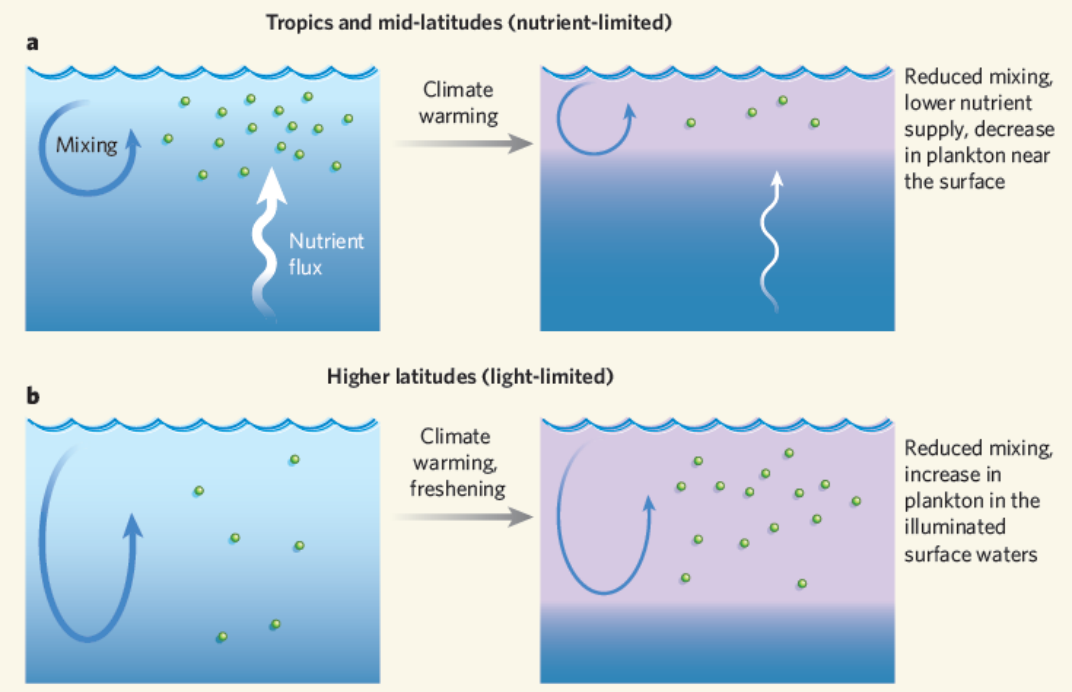

Figure 1-4. Increased surface temperature increases stratification that has varied effects on chlorophyll concentration in different regions of the global ocean (Doney, 2006).

As discussed in section 1.2, various natural and anthropogenic processes affect the climate system. To proceed with detection and attribution of climate change signal in chlorophyll, distinction between natural and anthropogenic variability in chlorophyll concentration needs to be made. In order to make this distinction, it is first necessary to understand the naturally occurring variability in chlorophyll.

1.3.1 Seasonal variability

Seasonal variability describes the increase and decrease of chlorophyll with respect to the seasons. Although it is relatively short time-scale variability in chlorophyll, it forms the basis of understanding as to how chlorophyll varies. A latitudinal shift in the timing of the spring bloom has been observed, i.e. it starts in winter in subtropical waters and in spring in sub polar waters (Follows and Dutkiewicz, 2002). Subtropical waters (20-40^{o} North or South) have approximately twice the chlorophyll concentration (chl) in winter than in summer. These waters have high levels of solar irradiance,

but are nutrient limited. Winter mixing entrains nutrients into the euphotic zone, which leads to phytoplankton growth and therefore high chlorophyll (Yoder et al., 1993, Yoder, 2003, Riley, 1947). Sub-polar waters typically have two peaks in chlorophyll concentration, one in spring and the other in fall. This region is abundant in nutrients but is light limited; therefore during winter, deep mixing ensures that phytoplankton biomass does not increase. As spring approaches and the mixed layer shoals above the critical depth, a phytoplankton bloom can start and chlorophyll increases (Sverdrup, 1953, Behrenfeld, 2010). Some of the important drivers of phytoplankton blooms are solar irradiance, nutrient supply, grazing wind speed (Kahru et al., 2010), stratification (Behrenfeld et al., 2006) and sea surface temperature (SST) (Martinez et al., 2009, Boyce et al., 2010). Variability in these parameters causes variability in timing and magnitude of phytoplankton bloom. For example, melting of sea-ice in polar regions forms a layer of less dense water on the surface of the ocean. This increases the stratification in the water column and its effect have been observed to affect the timing of the spring bloom (Platt et al., 2010). Platt et al. (2010) observed satellite chlorophyll for northwest Atlantic and found that spring bloom occurred on average 33 days earlier at 61.5^{o}N than at 59.5^{o}N. This is in contradiction to the norm where spring blooms occur later further north due to later occurrence of spring warming. Change in the timing and magnitude of the phytoplankton seasonal cycle affects the higher trophic level because phytoplankton form the base of the marine food web. This is based on the Cushing match-mismatch hypothesis (Cushing, 1975). It states that if there is mismatch in the timing of availability of food and critical life stages of higher trophic levels then the survival rate of higher trophic levels is reduced. For example, Kristiansen et al. (2011) studied the cod larvae development on George's Bank, north-western Atlantic. It was observed that there is an overlap in the coexistence of phytoplankton and cod larvae for warmer years which have earlier bloom onset and longer growing season. This results in higher survival rates of cod larvae as their food is available in abundance for longer time periods. If due to change in certain parameters such as SST, wind speed etc, phytoplankton bloom occurs earlier (or later) than normal in George's Bank, then food availability to cod larvae may decrease (or increase).

1.3.2 Inter-annual variability

Chlorophyll concentration in the ocean varies inter-annually due to changes in local physical forcings such as strengthening of the thermocline or deepening of the mixed layer depth. These changes in the physical forcings can be due to certain climate patterns occurring in a region such as the El Niño Southern Oscillation (ENSO) and North Atlantic Oscillation (NAO) or it may be due to mesoscale activities, changes in circulation patterns or may be due to warming of the surface temperature due to climate change.

The El Niño Southern Oscillation (ENSO) is a climate pattern consisting of two parts. The first part is the El Niño occurring in the tropical Pacific and the second part is the Southern Oscillation which describes the atmospheric changes associated with ENSO (Trenberth, 2001). On average ENSO occurs every five years and lasts for nine months to two years. During the cold phase of the ENSO known as the La Niña, the equatorial Pacific is characterized by a shallow thermocline and surface mixed layer depth and strong trade winds, which results in upwelling of cold-nutrient rich water to the surface and hence increased chl concentration. During the warm phase of ENSO known as the El Niño, trade winds weaken resulting in reduced upwelling and nutrient poor waters and hence, chl concentration decreases (Chavez et al., 1999, McClain et al., 2002, Wilson and Adamec, 2001).

The North Atlantic Oscillation (NAO) is a dominant contributor to winter climate variability over the Atlantic basin and is mainly driven by atmospheric circulation variability. It is defined as the difference in atmospheric pressure at sea level between Icelandic (low) and the Azores (high). This pressure difference controls the climate in the Atlantic basin and also influences the direction of storms. During the positive phase of the NAO i.e. when the pressure difference between Icelandic and Azores is large, the westerlies are stronger and the storms are directed towards northern Europe. This causes warm winters and cool summers in northern Europe whereas southern Europe has warm and dry weather. The Northwest Atlantic experiences cold and dry weather and the US east coast has mild and wet

winters (Hurrell, 1995). During the negative phase of the NAO i.e. when the pressure difference between Icelandic and Azores is not large, the storm direction shifts southward and brings rainfall to Southern Europe and North Africa. Northern Europe and the US east coast experience very cold winters. Storms cause deeper mixing in the subpolar region during positive phases of NAO. This leads to delayed spring bloom as it takes longer for the mixed layer to shoal above the critical depth. This bloom is weaker in magnitude as the solar irradiance availability time window decreases due to delayed bloom, which shortens the growing season for phytoplankton (Barton et al., 2003, Henson et al., 2006, Henson et al., 2009a, Henson et al., 2009b). During the negative phase of NAO, deeper mixing in subtropical latitudes increases the supply of nutrients to the surface ocean which increases phytoplankton growth (Follows and Dutkiewicz, 2002).

Variability in the timing and magnitude of phytoplankton blooms is also caused by meteorological conditions such as wind speed and net heat flux. For example, in eastern North Pacific, 1-3 months of interannual variation was observed by (Henson and Thomas, 2007). The variation in phytoplankton bloom start date coincided with the coastal upwelling caused by winds of the California current system.

1.3.3 Oligotrophic gyre Variability

Oligotrophic gyres are large systems of rotating ocean currents driven by winds. Earth's rotation deflects these currents in clockwise pattern in northern hemisphere and in anticlockwise pattern in southern hemisphere. Westerly winds on northern side and easterly winds on the southern side create a high pressure zone at the center and also cause downwelling at the center of the gyres due to which the supply of nutrients to the euphotic zone is low in these regions. Also, gyres are generally formed in open ocean areas therefore there is no supply of nutrients by river run off. Low supply of nutrients in the gyres causes low biomass and productivity. Oligotrophic gyres are generally defined in satellite-based studies as the regions where surface chlorophyll is below 0.07 mg m^{-3} (McClain et al., 2004). They are

located at subtropical latitudes and occupy approximately 40% of the Earth's surface. Due to their large size, gyres still contribute more than 30% of the total marine primary production (Longhurst, 1995), even though the biological activity within the gyres is low (Hayward, 1987b, Karl et al., 1996). Thus, gyres are an important part of the ecosystem and play an important role in the global marine carbon fixation. Variation in the size of these gyres has been observed in various studies. For example, Polovina et al. (2008) observed monthly mean area of surface chlorophyll in oligotrophic gyres by using satellite ocean color data from SeaWiFS (1998 to 2006) (Figure 1-5). In the South Atlantic, South Pacific, North Pacific and North Atlantic, the area of low surface chl waters have expanded at average annual rates of 0.8, 1.4, 2.2 and 4.3% per year respectively. Increase in the size of the gyres indicates an increase in low chlorophyll regions of the ocean. This lowers the overall phytoplankton productivity in the ocean which reduces the amount of carbon fixed from the atmosphere. Thus, increase in the size of the gyres will affect the global carbon cycle which will have cascading effects on the climate system. The increase observed in the size of gyres is may be caused by natural forcings such as solar and orbital forcing or it may be due to the effect of ocean surface warming as an effect of climate change by anthropogenic activities.

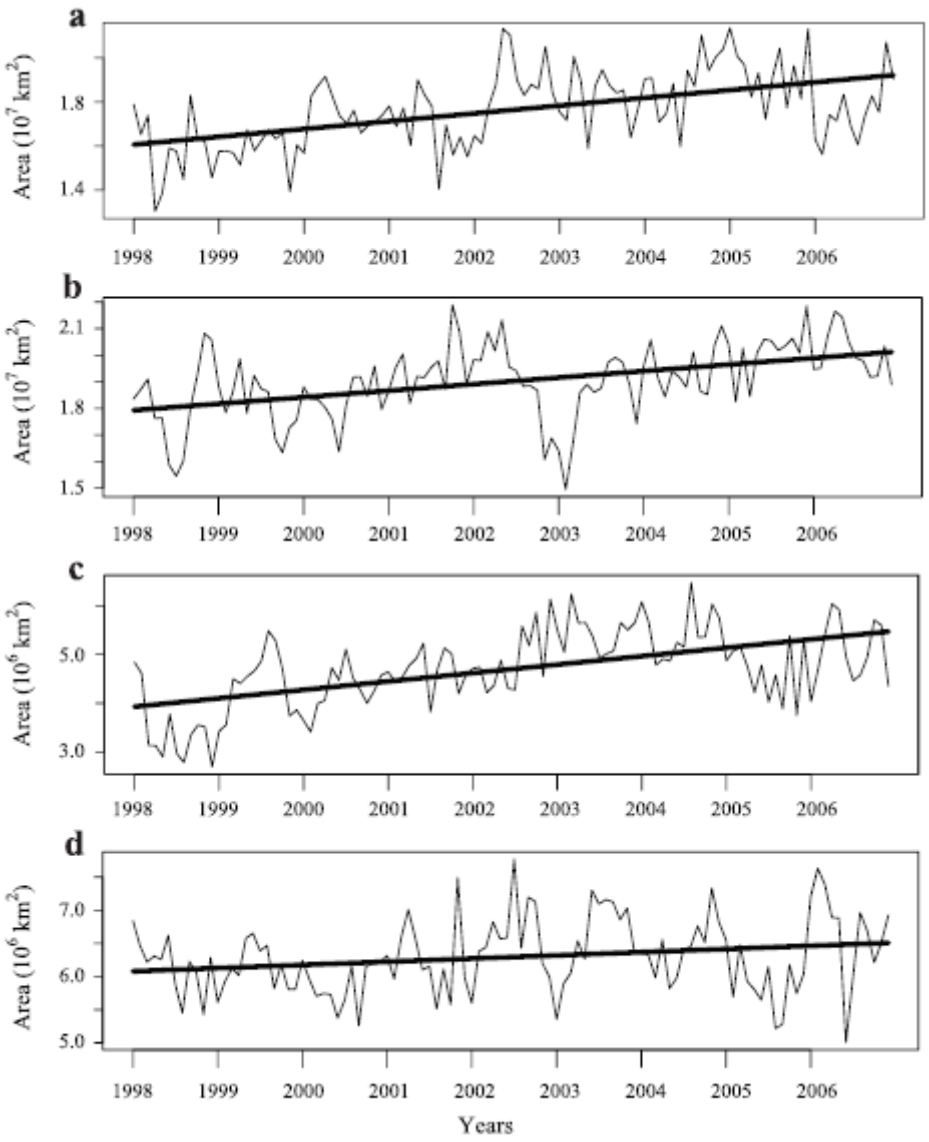

Figure 1-5. Time series of the monthly mean area of surface chl in subtropical gyres. (a) the North Pacific, (b) the South Pacific, (c) the North Atlantic, and (d) the South Atlantic (Polovina et al., 2008).

1.3.4 Decadal Variability

Chlorophyll has been observed to vary on decadal time scales. These variations may be caused due to certain climate phenomenon such as Pacific Decadal Oscillation (PDO) or it may be due to natural forcings or due to global warming.

PDO is described as a long-lived ENSO. The two main differences between the two are : firstly, the time-period of oscillations i.e. PDO persists

for 20-30 years while ENSO persists for 6-18 months and secondly, the strongest PDO signal is located in the North Western Pacific as opposed to El Niño whose strongest signal is located in equatorial regions of the Pacific (Mantua and Hare, 2002). Warm phase of the PDO is characterized by an area of warmer SST in eastern equatorial Pacific and a horseshoe pattern of cooler SST connecting the north, west and south Pacific. Lower SST in the North Pacific are accompanied by low sea-level pressure (SLP) and intensified westerlies in the storm track. Increase in winds coming from the west towards the coast, suppress upwelling in the northwest and west coast of North America. This causes decrease in the supply of nutrients and hence PP decreases. On the other hand, cold phase of the PDO is characterized by an area of colder SST in eastern equatorial Pacific and a horseshoe pattern of warmer SST connecting the north, west and south Pacific. Higher SST in the North Pacific are accompanied by high sea-level pressure (SLP) and weakened westerlies in the storm track. Weakening of the westerlies, strengthens the north wind along the coast. This enhances the upwelling along the north west coast of North America and cold nutrient rich waters are brought to the surface ocean and therefore, PP increases. The effect of PDO on chl variability was investigated by (Martinez et al., 2009). Martinez et al. (2009) observed that on decadal time scales, chl variability follows PDO as shown in Figure 1-6. These spatial patterns were derived by doing Multivariate Empirical Orthogonal Function analyses (MEOFs), on the combined dataset of ten years from Coastal Zone Color Scanner (CZCS) and Sea-viewing Wide Field-of-view Sensor (SeaWiFS). In the Pacific, the time series of the first principal component shifts from positive to negative from 1979-1983 to 1998-2002, in correspondence with the shift in PDO from negative to positive phase. The same pattern is observed in Indian Ocean chl variability and PDO because of the connectivity of Pacific Ocean and Indian Ocean.

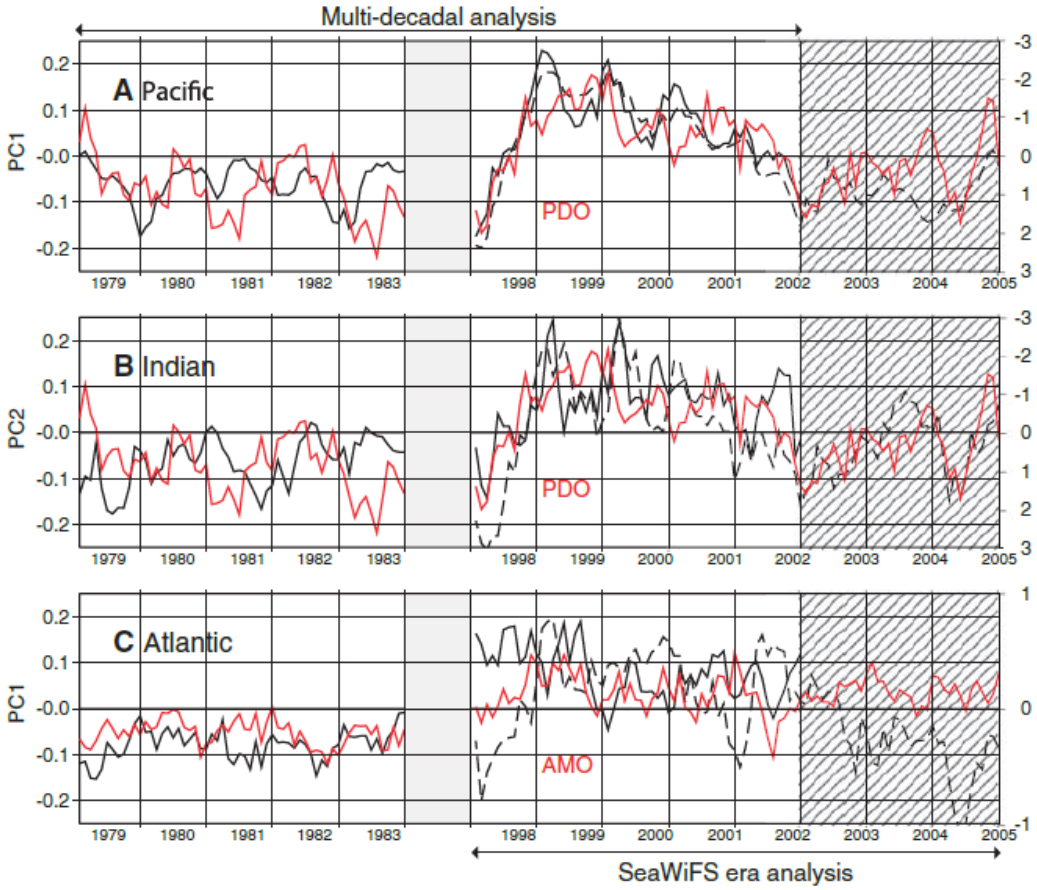

Figure 1-6. Chl-sst common time variability corresponding to MOEF patterns for the Pacific, Indian and Arctic oceans (black thick curve and scale on the left axes). PDO and Atlantic Multi-decadal Oscillation (AMO) are superimposed (red curves and scales on the right axes) from (Martinez et al., 2009).

Studies have been made to observe long-term variability in chl by observing the trends in in-situ measurements made at Bermuda Atlantic Time Series (BATS) station, Hawaii Ocean Time-Series (HOT) station (Saba et al., 2010a) and Cooperative Oceanic Fisheries Investigations (CalCOFI) (Kahru et al., 2009). The results from these studies indicate an increased biomass over the last 20-50 years. Contradictory results were obtained by Boyce et al. (2010). He blended in-situ chlorophyll data i.e. shipboard measurements of chl made since early 1900's and ocean transparency measurements made since 1899 to establish long time-series records (1899-2008) of chl in order to detect long-term trends (Figure 1-7). It was observed that the global rate of decline of chl is approximately 1% of the global median per year and that inter-annual to decadal fluctuations in chl strongly correlates with basin-

scale climate indices, such as Pacific Decadal Oscillation and North Atlantic Oscillation.

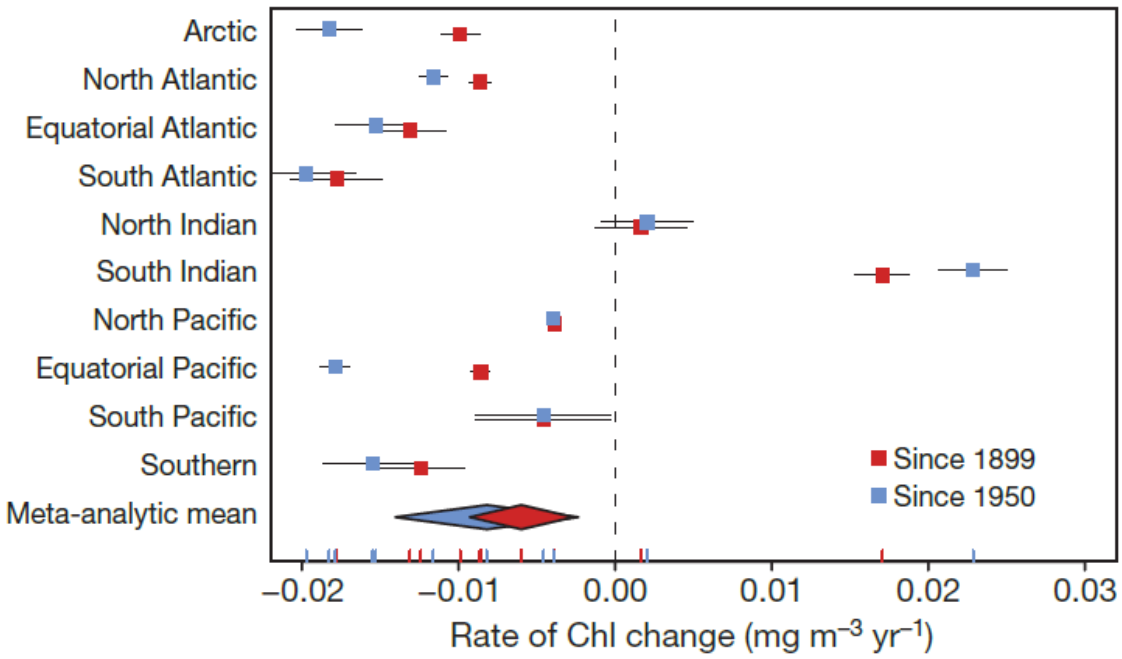

Figure 1-7. Regional and global trends in chl over 1899 - 2008. Mean of the instantaneous rates of chl were estimated for each region, with 95% confidence limits. Diamonds indicate the global mean of the instantaneous rate of chl. Trends were estimated using all available data (red symbols) and data since 1950 only (blue symbols).

Due to the lack of long-term chl data from a single ocean colour sensor, efforts have been made to blend the data from different sensors, particularly the CZCS which operated from 1979-1983 and SeaWiFS operating from 1998-2010 (Signorini and McClain, 2012, Irwin and Oliver, 2009). In some cases these datasets have also been blended with in situ chlorophyll estimates (Gregg and Conkright, 2002). It is difficult to blend datasets from different ocean colour sensors as sensors differ in the instruments used for measurements, calibration techniques used, the spatial and temporal scales of the sensors and also the time period of operation. These dissimilarities between sensors make it difficult to produce algorithms that are compatible for both the sensors. However, an attempt made by Gregg and Conkright (2002) to observe long term changes in chl concentrations by

blending the data from CZCS and SeaWiFS, showed that global mean average chl decreased by 1% from the CZCS to SeaWiFS era.

Thus, it is observed that chlorophyll varies spatially and temporally. Response of chlorophyll to climate oscillators indicates a strong natural variability in chl. This makes it difficult to distinguish between natural variability and anthropogenic variability in chl. Therefore, a formal detection and attribution study is required in order to make this distinction statistically.

1.4 Impacts of climate change

The surface temperature of Earth has increased as a result of increased radiative forcing (also known as the global warming). According to the temperature analysis conducted by scientists at National Oceanic and Atmospheric Administration (NOAA), the average global temperature on Earth has increased by about 0.85^{o}C from 1880 to 2012. The increase in temperature will result in a number of impacts on the climate system such as increase in evaporation, melting of snow and ice, increase in sea-level and increased precipitation. Figure 1-8 shows the consequences of the increase in temperature of the Earth, various cascading effects and the feedback cycles. Some of the indirect effects of global warming are an increase in extreme events such as floods, drought and wildfires, biodiversity loss and threat to human health.

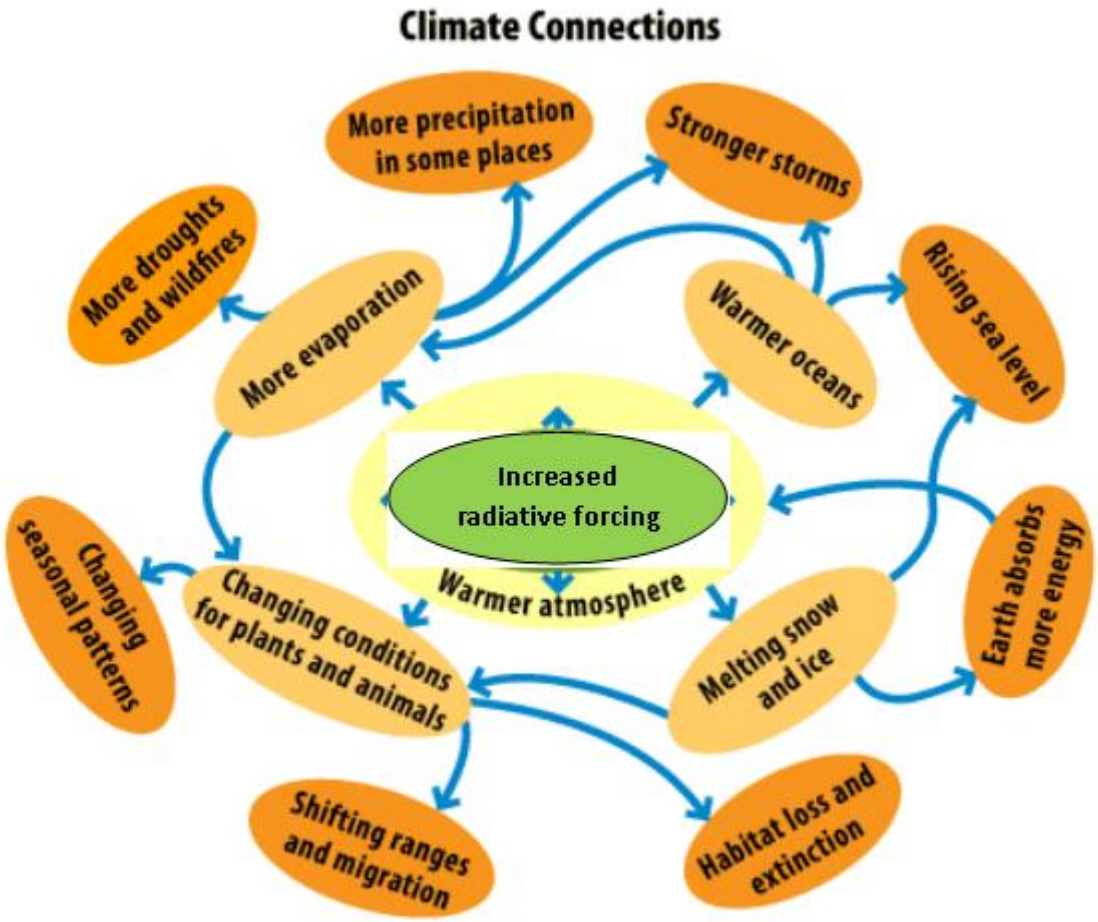

Figure 1-8. Impacts of temperature increase to the climate system (http://www.epa.gov/climatestudents/basics/concepts.html).

Rising atmospheric temperatures cause the sea-surface temperatures also to rise (Barnett et al., 2001, Levitus et al., 2001). Changes in SST varies regionally as shown in Figure 1-9. The Figure shows how average SST changed globally between 1901 and 2012. An increase in SST is observed in most of the global ocean except in a few areas where temperatures have decreased, for example in the North Atlantic Ocean.

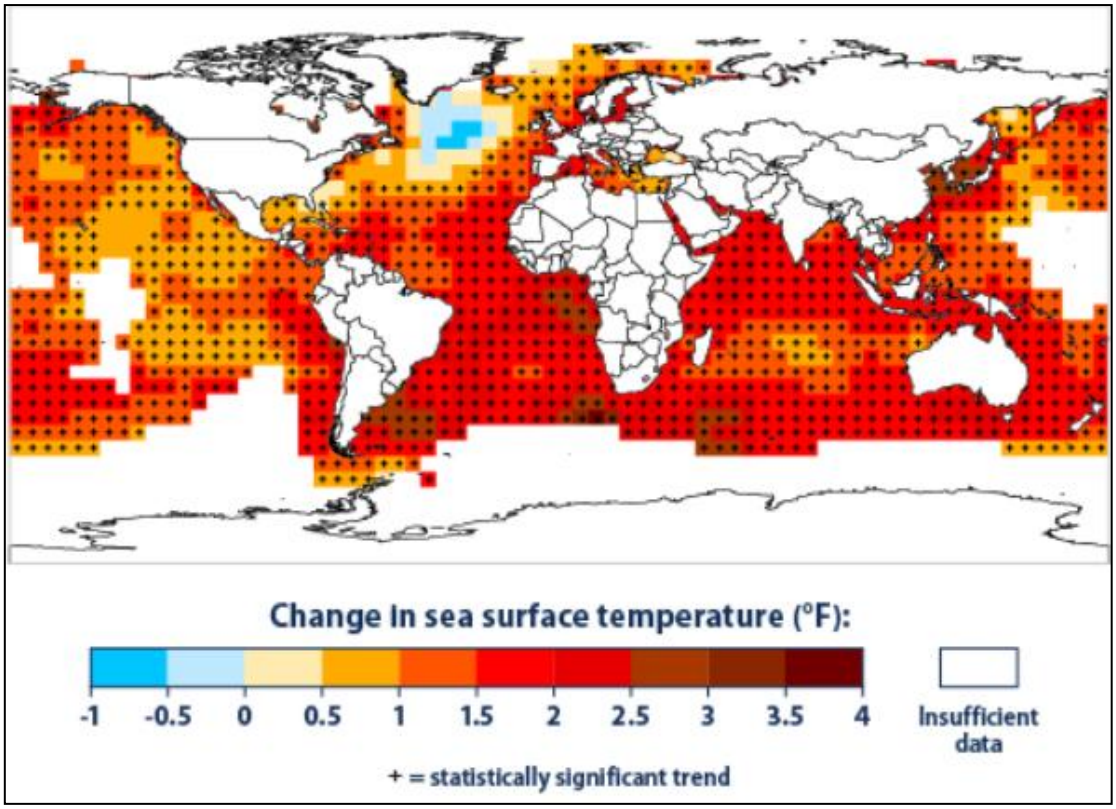

Figure 1-9. Change in Sea Surface Temperature, 1901-2012 (IPCC, 2013). The Figure is based on in-situ measurements and satellite measurements. The "+" symbol shows statistically significant trends.

Rising temperature of the surface ocean has several effects on phytoplankton. Phytoplankton contain chlorophyll which initiates photosynthesis i.e. in the presence of sunlight chl produces energy by absorbing atmospheric carbon dioxide and nutrients in the water. Thus, light and nutrients are two main ingredients for photosynthesis. Change in the availability of these two ingredients affects the concentration of chl in the water. An increase in surface water temperature due to climate change will increase stratification in the ocean which decreases the mixed layer depth and also decreases the entrainment of nutrients from deep waters to surface waters (Doney, 2006). This change in the mixing and availability of nutrients will affect the seasonal cycle of chl concentration. For example, it might affect the timing of the start, peak or end of phytoplankton bloom (Platt et al., 2010, Henson et al., 2006); it might alter the highest chl concentration obtained during the bloom i.e. the amplitude at the peak (Barton et al., 2003, Henson et al., 2009a, Henson et al., 2009b).

Increasing surface temperature, will also affect the species distribution in the ocean as different phytoplankton species have different optimum temperature range at which they prosper. Species having higher optimum growth temperature will thrive in higher SSTs and the growth rate of their community will also increase (Eppley, 1972). Spatial distribution of species have also been observed to change. For example, Hays et al. (2005) observed that dinoflagellate ceratium trichoceros which was usually found south of UK before 1970 is now found off the coast of Scotland. This indicates that warm water species have a tendency to shift poleward with rising SST (Hegseth and Sundfjord, 2008).

Climate change may strengthen or weaken the effect of the climate oscillations by altering the atmospheric and oceanic variables such as sea-level pressure, surface wind vector, sea surface temperature, surface air temperature, and total cloudiness fraction. As it has been described in the sections on interannual and decadal variability, climate oscillations such as ENSO, NAO and PDO affect the phytoplankton in the ocean. Therefore, any change in these climate oscillations will affect phytoplankton concentration in the ocean.

Ocean circulation influences the concentration of chl in the water by influencing the supply of nutrients to the surface ocean. Areas of the ocean where ocean currents cause upwelling, cold nutrient-rich water entrains from deep layers to the surface ocean. Increased nutrients in the sunlit layers of the ocean enhances the process of photosynthesis and hence, phytoplankton biomass increases, which is quantified by measuring the concentration of chl in the water. For example, wind-driven gyre circulation causes downwelling in the gyres which decreases the supply of nutrients and results in low chl concentration in the gyres (McClain, 2009, Siegel et al., 2013). Upwelling caused by eastern boundary current systems such as the California current off the west coast of North America and the Benguela current of the west coast of South Africa increases the supply of nutrients in these regions and hence the chl concentration increases (Thomas et al., 2001). Small-scale events such as the mesoscale eddies also affect the chl concentration by changing

the supply of nutrients in the surface ocean by mechanisms such as vertical and horizontal advection, trapping of water and upwelling and downwelling (Gaube et al., 2013, Capone and Hutchins, 2013). Ocean currents are mainly driven by winds, Earth's rotation and water density differences. Increased atmospheric temperature due to increased radiative forcing, changes the atmospheric pressure which in turn affects the direction and intensity of winds in the climate system. Changes in the direction and intensity of winds would alter ocean circulation which will affect the chl concentration in the ocean. Water density is dependent on temperature and salinity of the oceans. Oceans are getting warmer due to increased radiative forcings. Global warming is also causing polar ice caps to melt, which decreases the salinity of the oceans. Thus, both temperature and salinity of the oceans are changing due to climate change, resulting in changes in ocean circulation which in turn affects the chl concentration in the ocean.

1.5 Detection and Attribution

Detection of climate change is the method of identifying a change in the climate system in a defined statistical sense. Identifying a change does not specify cause of the change. Attribution is the process of estimating the relative contributions of multiple factors or forcings to a change with some statistical confidence. In general, a detected change is attributed to a specific forcing if the change is consistent with the projected responses to that specific forcing or combination of forcings and is inconsistent with the responses that exclude this specific forcing or combination of forcings. In both the evaluations, internal variability is taken into account. Thus, we need to compute how many different factors have contributed to recent observed climate change, with associated estimates of uncertainty. Figure 1-10 demonstrates the process of detection and attribution in a simple way. A change is first identified above noise. Response of the climate to various forcings such as volcanic, solar and carbon dioxide emissions is then determined. Contribution of these forcings to the identified change is then estimated and the cause of the detected change is determined. Detection is thus one component of the more complex and challenging process of

attribution. It is important to note here that attribution is an open-ended process as there is a possibility of an alternate explanation for the detected climate change, which may seem reasonable in future. Section 1.5.1 describes the components needed for detection and attribution study.

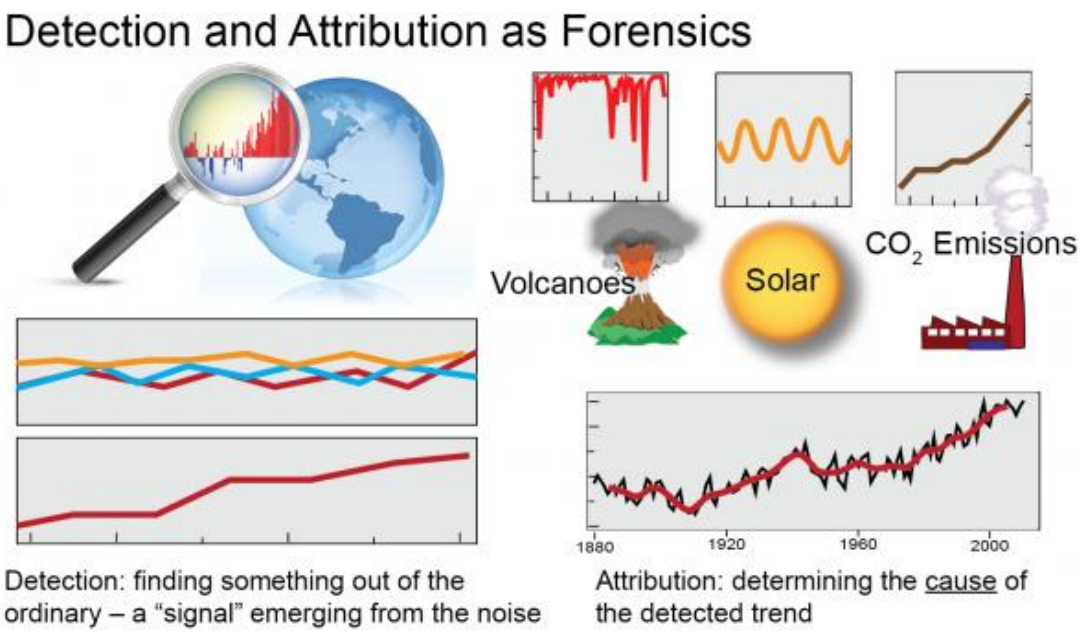

Figure 1-10. Detection and attribution of climate change in a climate variable (NOAA NCDC /CICS-NC).

1.5.1 Elements of Detection and Attribution

1.5.1.1 Observations

Detection and attribution studies require long records of observed data for the climate parameter being studied. The observations should have sufficient spatial coverage to ensure that the main features of variability whether natural or climate changes can be identified and monitored. Another vital factor is to have high-quality data for example, observations made with minimum instrumental errors, with correct computation algorithms, implementation of corrections such as atmospheric corrections in case of satellite ocean color data. This refers to the uncertainties such as due to instrumental errors. Also, homogeneous data series are required which account for changes in observing system technologies and observing

practices. For example, satellite ocean colour measurements began in October 1978 with the CZCS. Since then, many sensors have been launched and measurements of ocean colour have been made. To get a longer time series of any ocean colour derived variable, in our case chlorophyll, we would need to blend datasets from different sensors. In order to do so we would have to take into account the fact that sensors differ in the instruments used for measurements, calibration techniques used, the spatial and temporal scales of the sensors and also the time period of operation. These dissimilarities affect the homogeneity, coverage and quality of the data.

1.5.1.2 Internal Climate Variability

It has been discussed that detection and attribution is a statistical “signal-in-noise” problem. Accurate knowledge of "noise" is required which is termed as the internal climate variability. Ideally, long records of observed data provide internal variability, but there are certain problems associated with it. Firstly, instrumental records of observed data can be short relative to the longer time-scales that are needed for detection and attribution of climate change (Barnett et al., 1999). Secondly, the instrumental record contains influences of external anthropogenic and natural forcing in addition to the naturally occurring change in the internal cycle. Paleo-reconstructions do not provide information on chl concentration as they do for past temperatures. Hence, internal variability of chl concentration cannot be estimated from paleo data. Long-run control simulations of coupled climate models provide the best estimate for the internal climate variability in chlorophyll, but we must always bear in mind that models are not the same as reality. However, there is no possibility to validate the model output against real observations as there are no long-term records of chl concentration in which we can detect climate change. There is a method for checking the consistency between natural internal variability constructed by removing the simulated estimates of the response to external forcing from observations and natural internal variability estimated from control simulations (Allen and Tett, 1999). Uncertainty in the consistency check is introduced by incomplete knowledge

of the forcings and by the accuracy of the climate model used to estimate the response to the forcings.

1.5.1.3 Response to the Forcings

Since the pre-industrial era, there has been a change in the global mean radiative forcing. This has increased the significance of the relative impacts of different forcings on the climate. To detect the influence of these forcings on the climate we require estimates of the anticipated pattern of the response of the observed climate. For example, the projected pattern of the response of chl concentration due to various forcings needs to be estimated. Variations in the observations of the climate parameter being studied due to different external forcings are superimposed on each other and on internal climate variability. Hence, to estimate the contribution from each forcing to the change in the climate variable, climate models are used. Climate models provide estimates of natural internal variability and variability due to climate forcings separately i.e. as separate simulations. Climate models range from simple energy balance models to complex coupled models that simulate the spatial and temporal variations of many climate parameters. With the rapid development of computer technology, processing power has increased which has led to the development of models from simple energy balance models to coupled complex general circulation models (Manabe and Stouffer, 1980). Most of the detection and attribution studies use coupled atmosphere ocean general circulation models (AOGCMs) or atmospheric general circulation models (GCMs) coupled to mixed layer ocean models. The response pattern estimated for a specific forcing from different models may be different therefore, for consistent results of signal detection for a climate forcing, output from several climate models is used in the analysis. On the other hand, response patterns estimated from a specific model may be similar for different forcings ((Hegerl and North, 1997); (North and Stevens, 1998); (Allen and Tett, 1999)). This makes it difficult to separate the signal patterns for different forcings i.e. greenhouse gas, sulphate, volcanic and solar forcings.

1.5.1.4 Uncertainties

Detection and attribution studies are affected by uncertainties in observations and models. Uncertainty in observations may arise due to several factors such as -

- Autocorrelation;
- Bias in space, time, instrument, sampling and reporting;
- Measurement errors;
- Limited number of observations.

Uncertainties in models arise due to a number of factors. These can be due to fundamental errors in the model itself, such as the inability to generate a reliable ENSO cycle (Capotondi, 2013) or to parameterize ocean mixing, clouds, etc. Some errors arise due to forcings that are included such as sulphate aerosol direct effects, or from inadequate specification of poorly known anthropogenic or natural forcings. Another source of uncertainty arises due to internal model variability, for example nonlinear interactions within the models that produce large variability even when run in control mode (Gupta et al., 2013). Sea-ice plays an important role in the global biogeochemical cycle, however, currently models represent sea ice as biologically and chemically static which may lead to increased uncertainty in models (Vancoppenolle et al., 2013). These uncertainties affect the climate change signal that we hope to find in the observations. Careful assessment of all potential error sources in both observations and models needs to be made and their influence should be included in the detection study. Thus, there are two stages to detection and attribution: First, we need to know if we can detect a climate change signal, given all the uncertainties in model and observations. Second, if we can detect the change then we need to know if the change can be attributed to specific forcing, given all the level of uncertainty.

1.6 Summary

This introduction has demonstrated the following-

- Ocean primary production is an important element of the marine food web and global carbon cycle. It strongly influences marine ecosystem functioning and fishery yields. As it is also part of the biological pump, it is critical for transfer of carbon from atmosphere into the deep ocean.
- The Earth system is made up of various components and interacting processes. Changes in the climate system are caused by internal or external forcing mechanisms. Greenhouse gas emissions by anthropogenic activities is one of the internal forcings and is a major cause of increased radiative forcing on Earth.
- Climate change evidence is found by studying the changes in the climate variables such as temperature of the Earth's atmosphere and the oceans, atmospheric and oceanic circulation patterns and ocean acidification. These have cascading effects on the climate system such as increased evaporation, increased precipitation, increased sea-level, melting of sea-ice, change in the marine biogeochemical cycles and change in the chl concentration in the ocean.
- Chl concentration in the ocean has a strong natural variability which makes detection of climate change signal in chl concentration very difficult.
- A formal detection and attribution study needs to be done in order to detect climate change signal in chlorophyll.
- Elements needed for a detection and attribution study are obtained from observed data and the output from Earth system models.

1.7 Thesis Outline

Chapter 2 describes the optimal fingerprint (OF) method used for detection and attribution (D&A) of climate change signal in chlorophyll concentration in the ocean. The procedure to estimate the elements needed

for the OF method is also described in detail. Pre-processing of the datasets before they are implemented in the OF method are also explained. Details of the datasets i.e. the observed data and the output from the climate models are given along with a discussion of the sources of limitations and errors associated with it.

Chapter 3 illustrates the results of OF method implementation using a two dimensional climate change pattern. The Climate change signal is defined as the spatial pattern of linear trend of chlorophyll in the ocean. Discussion of the results of the D&A of this two dimensional pattern for the global and other regions of the ocean is presented. Interpretation and implementation of the results are described at the end of the chapter.

The Climate change signal is defined as the linear trend of zonal average of chlorophyll in the ocean. OF method is implemented using this climate change signal and the results for the global and other regions of the ocean are shown in chapter 4. Comparison of the climate change signal pattern for all the regions of the ocean from all the datasets is made. Results of the OF method, its interpretation and the implications are described as well.

The OF method is implemented to detect and attribute a climate change signal in the time series of the size of the subtropical gyres. Results of the D&A for all the gyres of the ocean are illustrated in Chapter 5. Comparison of the trend in the gyre size from all the datasets is shown and the amplitude of the contribution of the response of the forcings is demonstrated as well. Interpretation of the results and its implications are described at the end of the chapter.

Chapter 6 summarizes the results from chapter 3, 4 and 5. Conclusions regarding the D&A of climate change signal in chlorophyll are made. Discussion of the future work and the possible implications of the study are presented as well.

2 Data, Methods and model evaluation

The chapter mainly describes the various datasets that have been used in the analysis and the detection and attribution method. The data section (section 2.1) contains details of the dataset that has been chosen to represent observations and the climate models used in the analysis. Details such as the components, spatial and temporal resolution, time period of availability and limitations and advantages of the data and model are discussed.

The second section of the chapter is the 'method' part (section 2.2). A brief description of the various methods of detection and attribution is followed by the description of the optimal fingerprint method and the various steps used to compute the components needed for the detection and attribution analysis.

Several pre-processing steps are applied to the datasets prior to implementing the optimal fingerprint method. These steps are described in the third section of the chapter (section 2.3).

2.1 Data

Phytoplankton contain chlorophyll which initiates photosynthesis i.e. in the presence of sunlight chl produces energy by absorbing atmospheric carbon dioxide and nutrients in the water. Chlorophyll (chl) concentration describes the first order changes in the phytoplankton biomass and also reflects the photo acclimation state of phytoplankton (Ryther and Yentsch, 1957) therefore, it is used as an indicator of phytoplankton biomass and primary production (PP). Measurement of chl is much simpler and instantaneous. Chl is also available on a much wider spatial and temporal resolution than PP. Therefore, in this study, detection and attribution of climate change in chlorophyll is studied. Climate change detected in chlorophyll would suggest climate change in primary production as well.

More than two-thirds of the Earth's surface is covered by Oceans. The physical and biological variability in the oceans occurs over a wide range of

space and time scales (Steele, 1978). Measurement of chl is made using various platforms depending on the space, time scale and the accuracy of the estimation required. Shipboard measurements provide an accurate point measurement but they have limited spatial coverage. Estimation of chl by moored buoys has even less spatial coverage than ships but they can provide a long time-series of data. Aircrafts and satellites provide large spatial coverage impossible to obtain from ships and buoys, but the measurements are limited to the upper few meters of the surface ocean. Sampling platforms have been developed to cover intermediate space/time scales such as autonomous underwater vehicles (AUVs), drifters and floats (Dickey, 2003). Optical sensors are deployed on these platforms to measure optical properties of the water from which chl is derived.

2.1.1 Observations

Detection of a climate change signal requires accurate, detailed and good quality observations of the climate parameter. Data should also be corrected for biases and gaps. There are many ways biases are introduced in the data, one of them being 'inhomogeneity'. Changes in observing system technologies and measurement techniques cause inhomogeneity in the data. For example, to study long-term changes in chl, Boyce et al. (2010) blended in-situ chl data obtained from two different measurement techniques. One of the data series was obtained by deriving chlorophyll values from ocean transparency data, which is measured by a Secchi disk. Secchi depth measurements are available since 1899. Another data series was the shipboard measurements of chl made since 1950s, using spectrophotometry, high performance liquid chromatography (HPLC), and fluorometry. As the techniques used to obtain the two chl data series are different, they are not homogeneous. Blending the two data series would require to account for this inhomogeneity and correction of the bias introduced by it (Mackas, 2011, Rykaczewski and Dunne, 2011, McQuatters-Gollop et al., 2011). Spatial coverage is another important aspect of the observations. In-situ measurements of chl have in-homogeneous spatial coverage, with many observing stations near the coast and few in the open ocean. Remote sensing

observations overcome this drawback by providing chl data through ocean color sensors for the global ocean. Gaps in the data still occur due to clouds, but this gap in the coverage is still small compared to the gap in spatial coverage of in-situ data. Satellite data also needs correction for orbital and atmospheric transmission effects and for instrumental biases. Satellite ocean colour measurements began in October 1978 with the Coastal Zone Color Scanner (CZCS). Since then, many sensors have been launched and measurements of ocean colour have been made. To get a longer time series of chlorophyll, we need to blend datasets from different sensors. In order to do so we have to take into account the fact that sensors differ in the instruments used for measurements, calibration techniques used, the spatial and temporal scales of the sensors and also the time period of operation. These dissimilarities affect the homogeneity, coverage and quality of the data.

Another way to obtain homogeneous and coherent data for the global ocean is by combining observations and their temporal and spatial statistics with model information. This is known as the data assimilation system. Output of this assimilative model has good spatial and temporal coverage and it also produces a dataset consistent with the physics and biology of the model. One such assimilation system has been developed by Global Modeling and Assimilation Office (GMAO). In this assimilation system, chlorophyll data from Sea-viewing Wide Field-of-view Sensor (SeaWiFS) is assimilated with coupled general circulation, biogeochemical and radiative model of the global oceans using the method of Nerger and Gregg (2007). This three dimensional model is known as NASA Ocean Biogeochemical Model (NOBM).

Components of the model and the pathways and interactions among those components are shown in Figure 2-1. The ocean general circulation model (OGCM), shown in blue box in the Figure, is the Poseidon version 2. The model is global and has a latitude span from -84° to 72° in increments of 1.25° longitude by 2/3° latitude, including only open ocean areas where bottom depth is deeper than 200 meters (Schopf and Loughe, 1995). This model is forced with wind stress, sea-surface temperature and shortwave

radiation. The biogeochemical model, shown in green box in the Figure, has four phytoplankton groups - diatoms, chlorophytes, cynobacteria and cocolithophores; four nutrient groups - silica, nitrate, ammonia and iron; one grazing group and three detrital pools - nitrogen/carbon detritus, silica detritus and iron detritus (Gregg et al., 2003b). This model is forced with aerosol composition and sea-ice. The Ocean Atmosphere Spectral Irradiance Model (OASIM) provides underwater light fields that drive photosynthesis. The model includes spectral and directional properties of light transfer in the ocean and also accounts for clouds (Gregg, 2002). The forcing fields for this model are winds, precipitable water, surface pressure, humidity, ozone, cloud cover and cloud liquid water path. Outputs of the NOBM model are chlorophyll, nutrients, phytoplankton groups, primary production and spectral radiance.

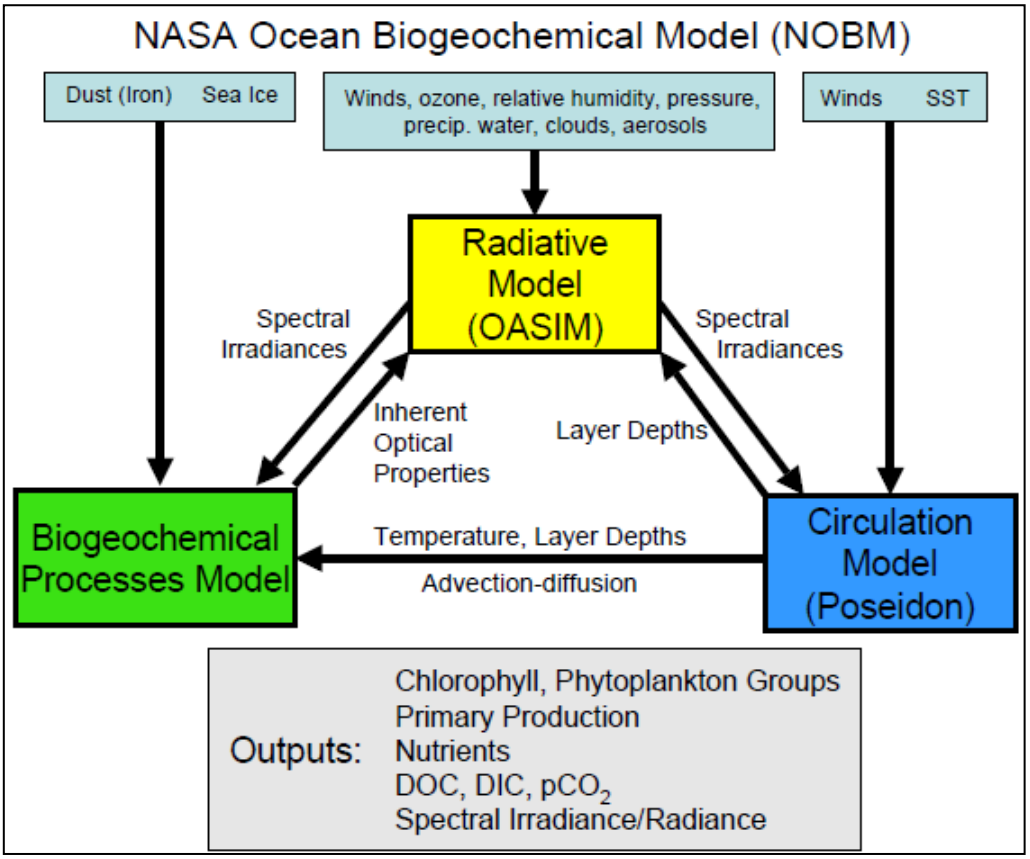

Figure 2-1. Pathways and interactions among the components of the NASA Ocean Biogeochemical Model (NOBM) (Nerger and Gregg, 2007).

Monthly chlorophyll data from NOBM were downloaded from the Ocean's Portal of the Giovanni application run by NASA's Goddard Earth Sciences Data and Information Services Center (GES DISC) (http://disc.sci.gsfc.nasa.gov/giovanni). The chl files downloaded are in netCDF (Network Common Data Form) format and chl values are in mg m^{-3}. Chl data is available from January 1997 to December 2007. Missing data is identified by a floating point value of $9.99x10^{11}$.

Model performance is evaluated by comparing the time series of global mean chl from NOBM model with the SeaWiFS data. Figure 2-2a below shows the monthly time series of global mean chl from NOBM (blue) and SeaWiFS (red). From the graph it can be seen that chl concentration increases in winter and decreases in summer whereas, in SeaWiFS chl concentration decreases in winter and increases in summer. This difference in phase is also indicated by the negative correlation coefficient between the two time series (-0.5834). The reason of this might be the patchiness in SeaWiFS data in the southern hemisphere due to clouds which makes the seasonal cycle of the southern hemisphere as the dominant signal globally when assimilated by NOBM. However, comparison of monthly time series of regional chl for example, comparison of North Atlantic (NA) (Figure 2-2b) and South Pacific (SP) region (Figure 2-2c) of the ocean shows that chl from NOBM model and SeaWiFS are in phase with each other. Correlation coefficient between the two is 0.965 and 0.915 for NA and SP regions of the ocean respectively. These results show that chl from NOBM model should not be used on a global scale however, regional chl can be used as it is in phase with the SeaWiFS data. In this study, NOBM data would be referred to as observations even though it is a combination of satellite data and model output.

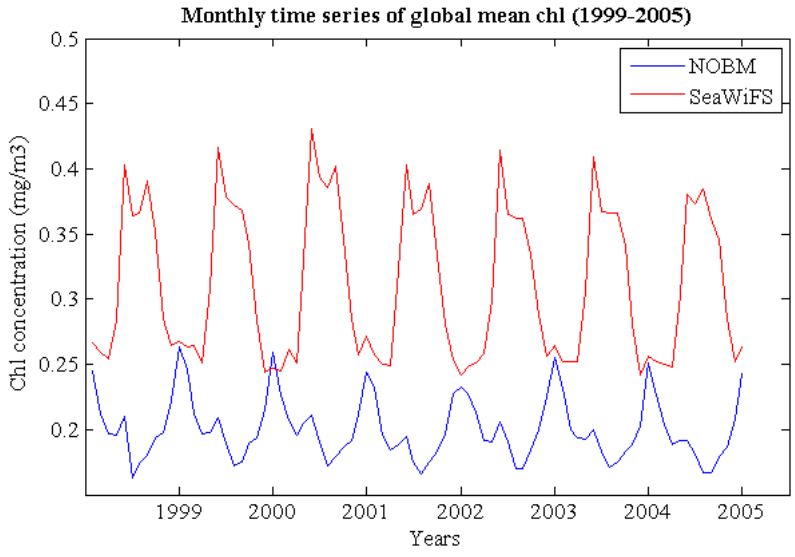

a).

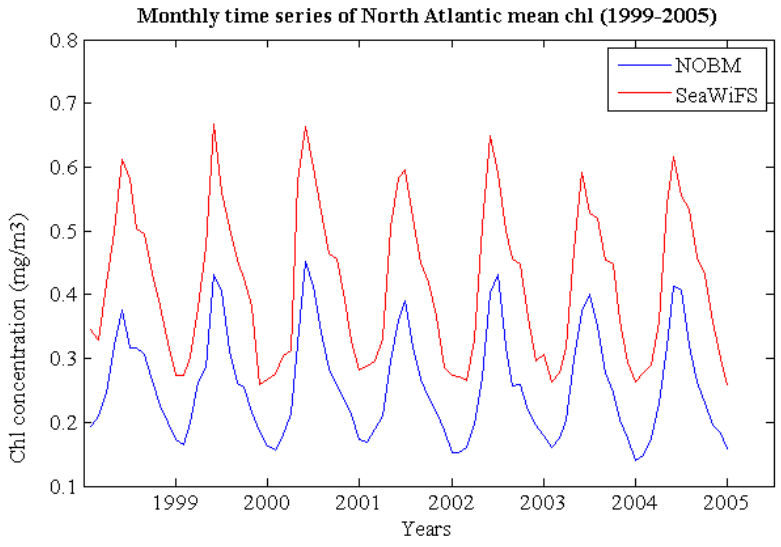

b).

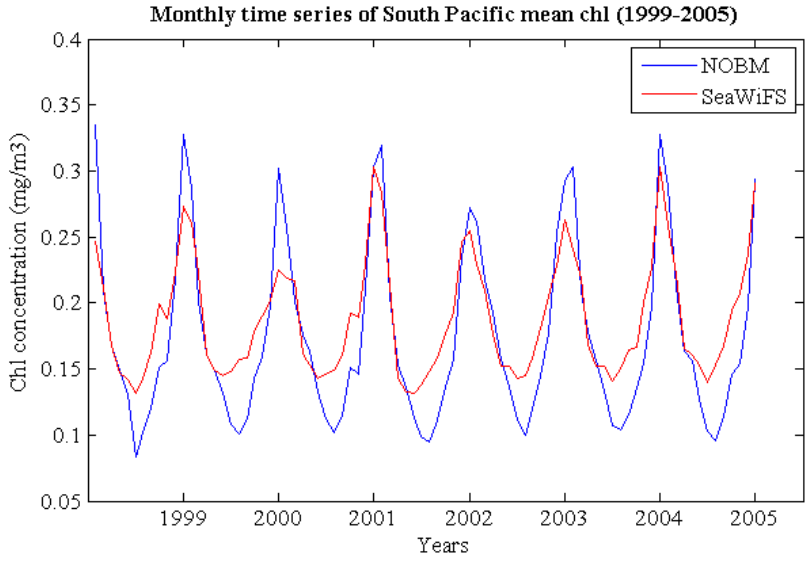

c).

Figure 2-2. Monthly time series (1999-2005) of a). Global, b). North Atlantic and c). South Pacific mean chl from NOBM model (blue) and SeaWiFS data (red).

2.1.2 Climate Models

Climate models simulate the interactions between the components of the climate system. The objective of climate models is to understand the important physical, chemical and biological processes of the climate system. Understanding the climate system helps in better understanding of the past climate by comparison with the observations. Climate models also help in predicting future climate i.e. how the climate system will behave in the future. Climate models range from simple Energy Balance Models (EBMs), to complex General Circulation Models (GCMs) and to Earth System Models (ESMs). When the GCMs are coupled to the biogeochemical components that account for the carbon fluxes in the atmosphere, ocean and land, they are known as the ESMs. Earth System Models represent global biogeochemical cycles of elements within and between the components of the climate system i.e atmosphere, ocean and land. Sensitivity and feedback of these components to climate and human activities is also included in these models. In this study, chl output from ESMs is used to determine the internal climate variability and climate parameter response to external forcing.

In climate change detection and attribution studies, apart from the observations of the climate parameter, internal variability of the climate parameter and the response of the climate parameter to climate forcings is also needed. Internal climate variability or noise is the record of the climate parameter without the influence of external climate forcings, mainly greenhouse gases. Noise can be obtained from long records of observations of the climate parameter before the industrial revolution (before 1750) i.e. before the emission of anthropogenic greenhouse gases in the atmosphere. In the previous sections it has been pointed out that there is lack of homogeneous long-term records of chlorophyll. Due to this, output from control run simulations of climate models are used to compute the internal variability of chlorophyll. Control run simulation of a climate model is the simulation in which there is no change in the forcing parameters i.e. the climate forcings are held at constant levels which represent a time period before anthropogenic climate change for example, 1850 or 1860. For

example, in a control simulation there would be no change in the solar irradiation, greenhouse gas concentration and aerosols concentration in the atmosphere. No change in the climate forcings ensures that all the climate parameters are following their natural cycles and there is no external influence on them.

To detect the climate change signal, we also need estimates of the space-time pattern of the response of the climate parameter to the climate forcings. This can be obtained if the response of the observed climate to each climate forcing (natural and anthropogenic) can be separated i.e. spatial and temporal variations caused due to each forcing can be distinguished. These patterns of response cannot be determined from the observations as the variations caused due to different climate forcings are superimposed on each other and also on internal variability of the climate parameter. Therefore, we need climate models to estimate the pattern of response of chlorophyll to each climate forcing. In this study, five climate models have been used to obtain internal climate variability and climate forcing response of chlorophyll (see section 2.1.2.3 to 2.1.2.5).

Many climate models have been developed by various modelling groups all over the world to study and understand the past, present and future climate. In order to study the climate in a multi-model context, the Coupled Model Intercomparison Project (CMIP) was started in 1995 under the auspice of Working Group on Coupled Modelling (WGCM). The objective of CMIP is to study the internal variability of the climate system and response of the climate to natural and anthropogenic forcings in various space and time scales in a multi-model framework. Another important objective of CMIP is to standardize the output from various models and make them available to the public. CMIP experiments involve simulating models using different scenarios such as increase in carbon dioxide by 1% per year, increase in greenhouse gas only, changes in aerosol concentration only, changes in solar and volcanic forcings and projections of climate response in future. On the basis of the time period of simulations these experiments are divided into two types. These are long-term integrations with time periods of century scale

and near-term integrations with time periods of 10-30 years. Various phases of CMIP have been developed since it started in 1995.

In this study, climate model output for chl concentration from several models from the latest phase of the CMIP i.e. CMIP5 have been used. Apart from studying the climate system in a multi-model framework and standardizing the output from various models, objective of CMIP5 was to inform and support Intergovernmental Panel on Climate Change (IPCC) Fifth Assessment Report (AR5). CMIP5 was started in 2008, with 20 modelling groups from around the world performing CMIP5 simulations using more than 50 models (Taylor et al., 2012). Due to large number of simulations in the CMIP5 framework, integrations are divided into a "core" set and one or two "tiers" (Figure 2-3). The core integrations located in the innermost circle in both the Figures are the set of simulations to be completed for any model performing experiments on any time-scale chosen by the modelling group. As we move up the tier i.e. the circle shaded yellow and green in the Figures, simulations become more specialized.

a).

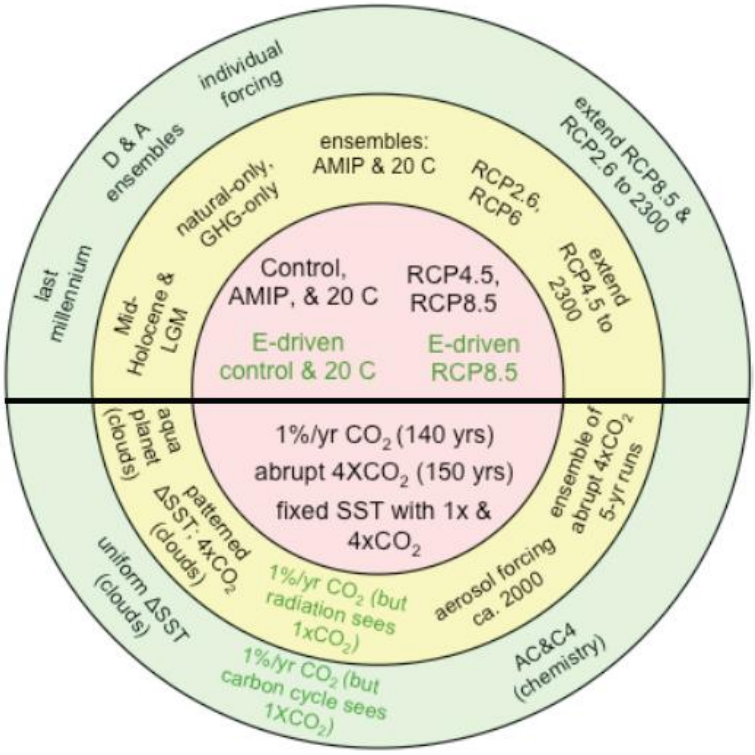

b).

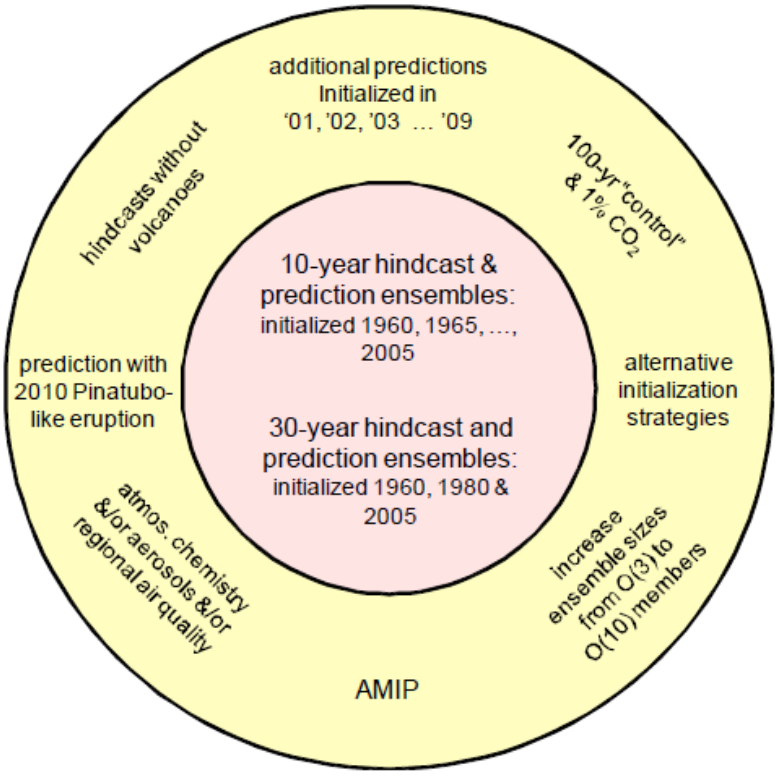

Figure 2-3. a). Schematic of the CMIP5 long-term experiments divided into 3 sets with tier 1 and tier 2 set of experiments organized around a central core. b). Schematic summary of CMIP5 decadal prediction integrations (Taylor et al., 2012).

2.1.2.1 Climate simulations

From Figure 2-3, it can be seen that there are many scenarios for which climate models have been simulated to study the climate system and its variability. For detection and attribution study, only few of these simulations are used. These are -

Preindustrial Control run

This is a long-term simulation of models (500 years) forced with pre-industrial conditions. In pre-industrial conditions atmospheric concentrations of well-mixed gases (including CO_2) and natural aerosols are fixed. Also, the land use is undisturbed for the time period of simulations. In this simulation, there are no changes in the climate parameters due to anthropogenic activities, such as increase in greenhouse gases. Output from this simulation is therefore used to obtain the internal variability of climate parameters.

Historical

These simulations have a time period of more than 150 years (1850 to 2005). This simulation is forced with changing climate conditions which are obtained from observations. For example, observed change in the atmospheric concentration of gases due to both anthropogenic and volcanic activities, observed change in the solar forcing and observed change in land use is included in the simulations. Thus, the output of the model is consistent with the observations.

Historical Natural Only

These simulations are similar to preindustrial control run simulations but are forced with only natural forcings i.e. changes in the climate system due to volcanic and solar forcings. For example, the simulation is forced with observed change in the concentration of aerosols due to volcanic activity.

Historical Greenhouse gas only

These simulations are imposed with the same conditions as the preindustrial control run simulations but they are forced with greenhouse gas forcing i.e. changes in the climate parameters caused due to change in the concentration of greenhouse gases in the atmosphere. For example, observed changes in the greenhouse gas concentration in the atmosphere acts as a forcing field in the model simulation.

Historical Miscellaneous

These are simulations which are again similar to the control run simulations but are forced with other individual forcings or a combination of forcings. For example, land-use changes only, or anthropogenic aerosols concentration changes only, or volcanic aerosols only and so on.

Future projection

These simulations are model experiments that predict the future conditions of the climate. The simulations are forced with emission scenarios such that the approximate target radiative forcing at year 2100 would be 4.5 or 8.5 W m^{-2}. These simulations are known as "representative concentration pathways" (RCPs). They are simulated from 2006 to 2100 and sometimes extended to the year 2300. In this study RCP8.5 simulation has been used as it is the "business as usual" highest level of forcing scenario which would give a high signal-to-noise ratio and hence has an increased possibility of signal detection.

2.1.2.2 Obtaining CMIP5 model output

CMIP5 involves models and experiments run by 20 modelling groups located all over the world. Model output from different groups is converted to a standard format and this process of data standardization is known as CMORization (Climate Model Output Rewriter). Users can download CMIP5 model output according to their specific interest through any Earth System Grid (ESG) federated data portals (for example http://pcmdi9.llnl.gov/esgf-web-fe/).

For this study monthly chl data from five climate models have been downloaded. The CMIP5 variable name is "mass_concentration_of_phytoplankton_expressed_as_chlorophyll_in_sea_water" and it is described as the Total Chlorophyll Mass Concentration at Surface. Data from CMIP5 is available in netCDF-3 format and conforms to the net-CDF "classic" data model. Chlorophyll data is in kg/m3 units which was later converted to mg m^{-3} for the analysis. Five models from CMIP5 archive have been simulated for historical_greenhouse gas and historical natural scenarios. These models are GFDL-ESM2G, GFDL-ESM2M, IPSL, CanESM2 and HadGEM2. Control run simulation from these climate models was checked for drift. Mean of chl was computed for the time period of the control run and the trend was checked for its significance. It was found that except chl in NP region from CanESM2 model, all the models showed no drift in any region of the ocean (NA, SA, NP, SP and IO). Details of the model output downloaded for this study are given in Table 2-1 and summary of the main characteristics of the models is given in table 2-2.As can be seen from table 2-2 there are several differences between the models. One of the differences is in the determination of chl by models i.e. the constant or variable redfield ratios. These differences between the models may lead to varying output (chl) from the models.

Table 2-1. Model simulations and their time periods

Simulation/Model	**GFDL ESM2G**	**GFDL ESM2M**	**IPSL**	**CanESM2**
Preindustrial Control	500 years	500 years	1800-2099 (300 years)	2015-3010 (995 years)
Historical	1861-2005	1861-2005	1850-2005	1850-2005
Historical Greenhouse gas only		1861-2005	1850-2005	1850-2012
Historical Miscellaneous		1861-2005		
Historical Natural only		1861-2005	1850-2012	1850-2012
Representative Concentration Pathway (RCP) 8.5		2006-2100	2006-2100	2006-2100

Table 2-2. Table below gives a summary of the main characteristics of the models. Fixed redfield and variable ratios are represented by R and V respectively.

Models	**Atmosphere**	**Ocean**	**Marine Biogeo-chemical component**	**Redfield**	**No. of phytoplankton groups**	**No. of zooplankton groups**	**Limiting nutrients**
GFDL-ESM2G	24 levels, $2.5^o/2.0^o$	63 levels, $0.3–1^o$	TOPAZ2	R (C : N) and V (P, Si, Chl, Fe)	3 (large separated into diatoms and other eukaryotes, small, diazotrophs) implicit calcification in small	1	5 (NO3, NH4 PO4, SiO4, Fe)
GFDL-ESM2M	24 levels, $2.5^o/2.0^o$	50 levels, $0.3–1^o$					
IPSL	39 levels, $1.2^o/2.5^o$	31 levels, $0.5–2^o$	PISCES	R (C :N: P) and V (Si, Chl, Fe)	2 (diatoms and nanophyto-); implicit calcification in nanophyto-	2 (micro- and mesozooplankton)	5 (NO3, NH4 PO4, SiO4, Fe)
CanESM 2	35 levels, $2.81^o/2.81^o$	40 levels, $0.94^o/1.41^o$	NPZD	R (C:N)	1	1	1 (N)

2.1.2.3 GFDL-ESM

NOAA's (National Oceanic and Atmospheric Administration) first Earth System Models (ESMs) were developed by the Geophysical Fluid Dynamics Laboratory (GFDL) (Dunne et al., 2012a, Dunne et al., 2012b). GFDL's ESMs are similar to GFDL's previous climate model CM2.1. The atmospheric component of GFDL-ESM is Atmospheric Model, version 2 (AM2.0). The horizontal resolution of the AM2 is 2^o latitude by 2.5^o longitude and it has 24 vertical level. It uses a 0.5 hour time step for atmospheric physics and 3 hour time step for atmospheric radiation (Lin, 2004). The land component of GFDL-ESM is the Land Model, version 3 (LM3.0) (Dunne et al., 2012a, Dunne et al., 2012b, Shevliakova et al., 2009). The horizontal resolution of the LM3.0 is the same as that of the AM2.0. The

sea-ice component of the GFDL-ESM is the GFDL Sea Ice Simulator (SIS) (Winton, 2000). The model has three vertical layers of which one is for snow and two are for ice and it has five different ice thickness categories. To reduce the uncertainty in ocean biogeochemical response to increased CO_2 and climate change coming from the ocean physical representation, GFDL developed two earth system models ESM2G and ESM2M. ESM2M uses Modular Ocean Model version 4.1 (MOM4) (Murray, 1996, Griffies, 2009) in which vertical coordinates are based on depth, whereas ESM2G uses Generalized Ocean Layer Dynamics (GOLD) in which vertical coordinates are based on density (Hallberg, 1995). Ocean model resolution is 1° in latitude and longitude, with meridional resolution becoming progressively finer towards the equator i.e. starting with 1^{o} resolution at 30° latitude; it gets to 1/3° at the equator (Delworth et al., 2006). Both the ocean models have 50 vertical levels. The ocean component uses a tripolar grid with poles over Eurasia, North America, and Antarctica to avoid polar filtering over the Arctic (Murray, 1996). The ocean biogeochemical and ecological component of the GFDL ESMs is Tracers of Ocean Phytoplankton with Allometric Zooplankton code version 2.0 (TOPAZ2). TOPAZ2 includes 3 explicit phytoplankton classes; small, large, and diazotrophs comprising 4 phytoplankton functional types; small, nitrogen fixers, large non-diatom, and large diatom (Dunne et al., 2005, Dunne et al., 2007, Dunne et al., 2012a, Dunne et al., 2012b). Figure 2-4 shows the schematic of the biogeochemical and carbon cycle in the ocean as represented by TOPAZ2 model.

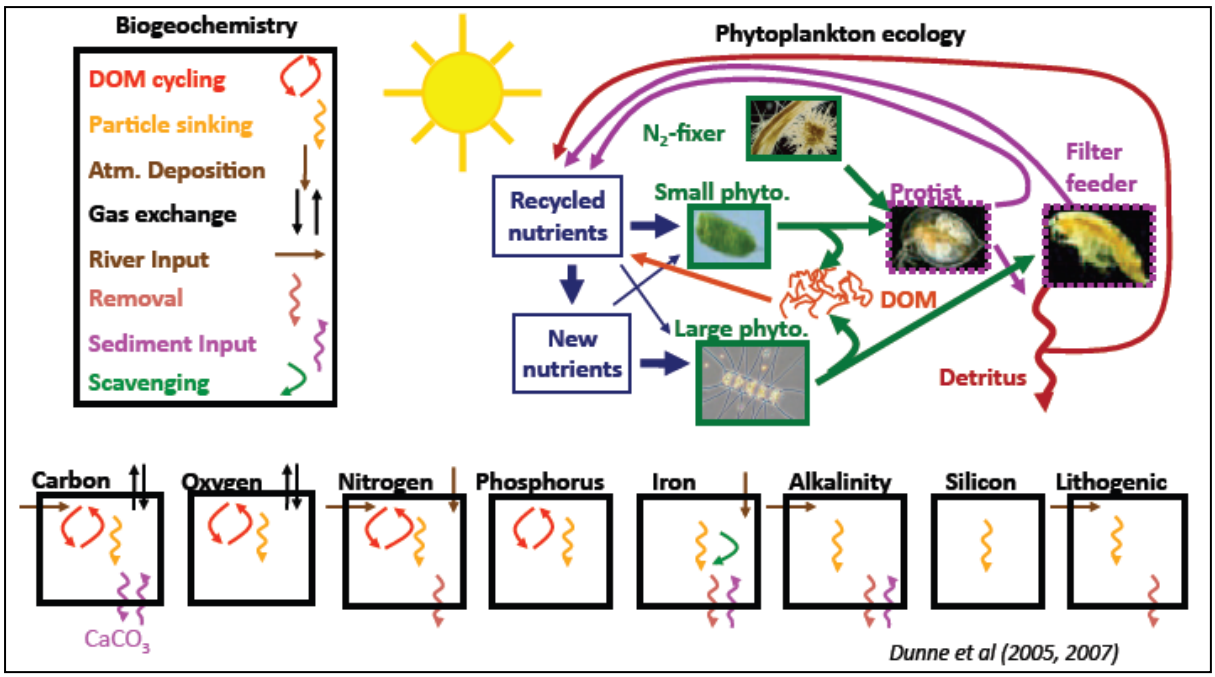

Figure 2-4. Schematic of the biogeochemical and carbon cycle in the ocean as represented by TOPAZ2 model (Dunne et al., 2005, Dunne et al., 2007).

2.1.2.4 IPSL

For the 5th phase of the Coupled Model Intercomparison Project (CMIP5), Institut Pierre Simon Laplace (IPSL) developed a full Earth System Model (ESM) known as IPSL-CM5. As an ESM, IPSL-CM5 has a basic physical core that includes atmosphere, land, ocean and sea-ice. Apart from this, it also includes biogeochemical processes through different models: stratospheric and tropospheric chemistry, aerosols, terrestrial and oceanic carbon cycle (Dufresne et al., 2013). Various components of the model are shown in Figure 2-5.

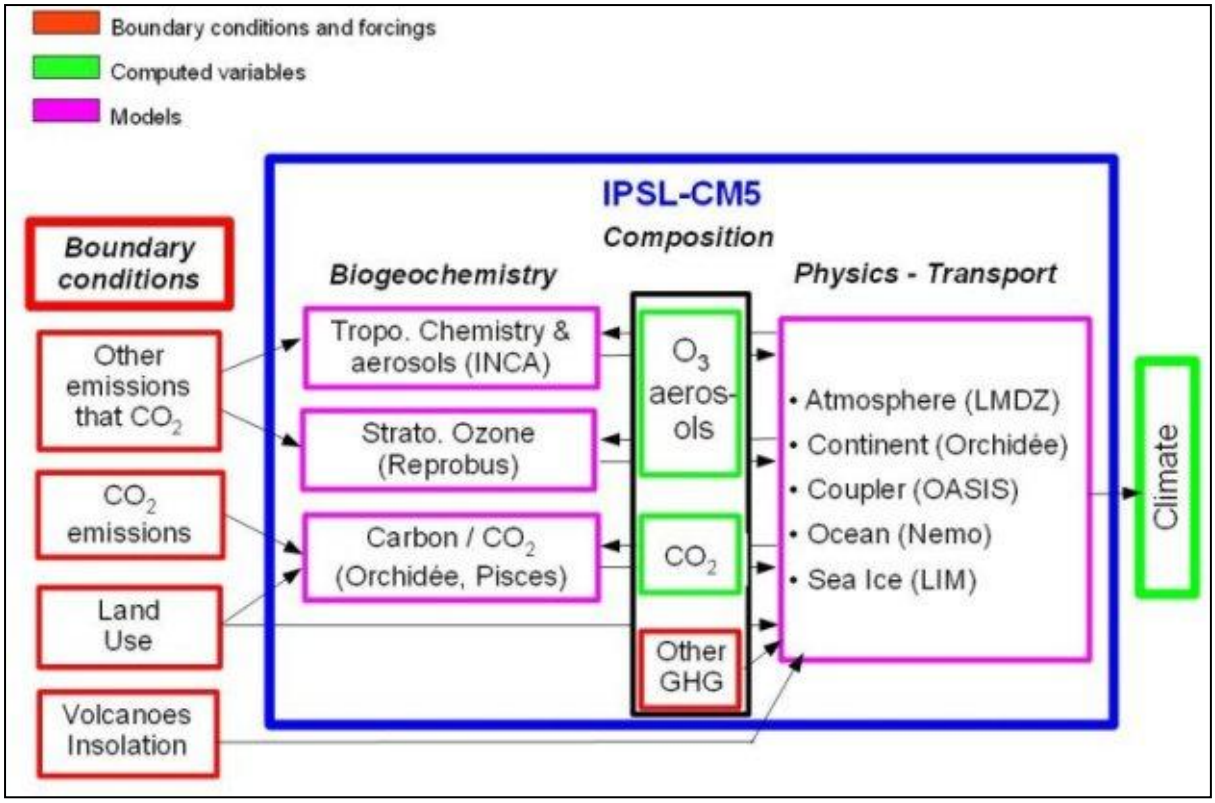

Figure 2-5. Various components of the IPSL model for CMIP5. Figure downloaded from http://icmc.ipsl.fr/index.php/icmc-models/icmc-ipsl-cm5.

The atmospheric general circulation model is LMDZ developed by Laboratoire de Me´te´orologie Dynamique (Hourdin et al., 2006). The atmospheric model LMDZ of IPSL-CM5 has two standard resolutions. The low resolution is 1.9° in latitude and 3.75° in longitude. The mid-resolution is 1.25° in latitude and 2.5° in longitude. In this study, simulations from IPSL-CM5 with medium resolution atmospheric model have been used for the analysis. The land-surface model is ORganizing Carbon and Hydrology In Dynamic EcosystEms (ORCHIDEE) that simulates the energy and water cycles of soil and vegetation, the terrestrial carbon cycle, and the vegetation composition and distribution (Krinner et al., 2005). Distribution of aerosols and gaseous reactive species in the troposphere is simulated by the INteraction with Chemistry and Aerosol (INCA) model (Schulz, 2007, Szopa et al., 2013). Global distribution of trace gases, aerosols, and clouds within the stratosphere are computed by a part of the LMDZ model which is known as Reactive Processes Ruling the Ozone Budget in the Stratosphere (REPROBUS) (Lefevre et al., 1994, Lefevre et al., 1998). The ocean model is

the Nucleus for European Modelling of the Ocean (NEMO) version 3.2 which also includes sea ice and marine biogeochemistry (Madec, 2008). Sea-ice model is Louvain-la-Neuve (LIM) (Fichefet and Maqueda, 1997). Resolution of the Ocean model NEMO is 2° in latitude and longitude, with a meridional increased resolution of 0.5° near the equator. A tripolar grid is used in this model to avoid polar filtering over the Arctic. Pelagic Interaction Scheme for Carbon and Ecosystem Studies (PISCES) is the ocean biogeochemical model (Aumont and Bopp, 2006) (Figure 2-6). Phytoplankton are represented by two functional groups - nano-phytoplankton and diatoms; zooplankton is distinguished into two size classes - meso- and micro-zooplankton. Phytoplankton growth is limited by five nutrients - ammonium, nitrate, phosphate, iron and silicate. In the Figure, DOM is the dissolved organic matter and POM is the particulate organic matter.

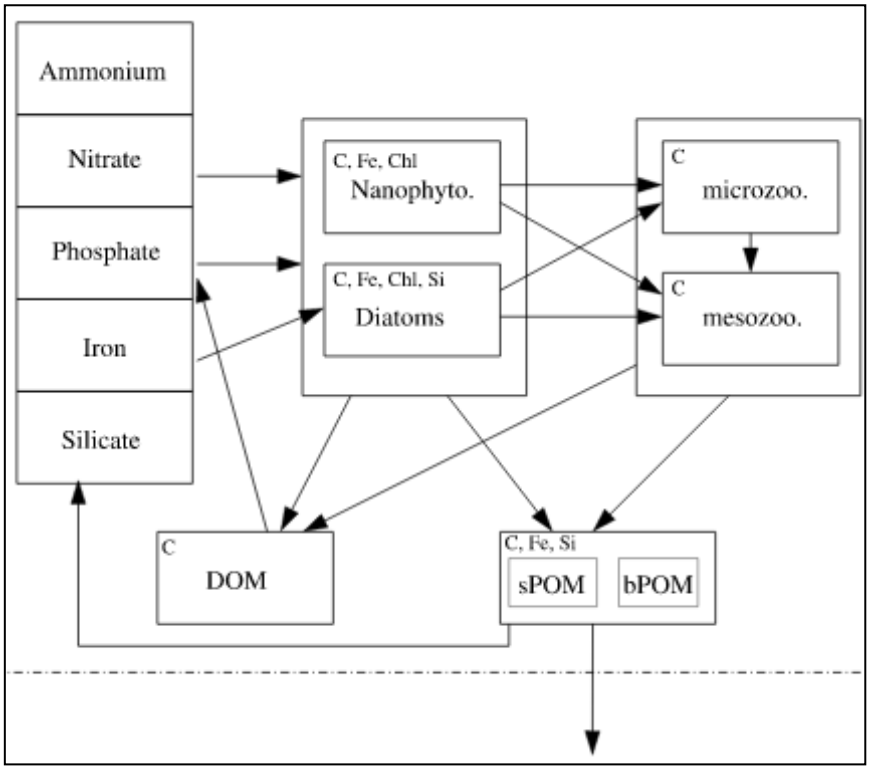

Figure 2-6. Schematic of the PISCES biogeochemical model (Aumont and Bopp, 2006).

2.1.2.5 CanESM2

Developed by Canadian Centre for Climate Modelling and Analysis (CCCma) Canadian Earth System Model 2 (CanESM2) is similar to the first generation of Canadian Earth System Model (CanESM1) (Arora and Matthews, 2009). It is a fully carbon-climate model based on third version of the CCCma Coupled Global Climate Model (CGCM3). The atmospheric component of the CanESM2 model is the fourth generation of the CCCma atmospheric general circulation model (CanAM4) (Scinocca et al., 2008). It has horizontal resolution of approximately 2.81^{o} in both latitude and longitude. The terrestrial carbon component of the model is provided by Canadian Terrestrial Ecosystem Model (CTEM) (Arora and Matthews, 2009, Arora and Boer, 2010) and the ocean carbon component of the model is provided by Canadian Model of Ocean Carbon (CMOC) (Christian et al., 2010). The ocean component of the CanESM2 model is the National Centre for Atmospheric Research Community Ocean Model (NCOM1.3) (Gent, 1998). Horizontal ocean resolution is approximately 0.94^{o} latitude by 1.41^{o} longitude (Arora and Boer et al. 2014). The ecosystem component of CMOC is based on the Nutrient, Phytoplankton, Zooplankton and Detritus (NPZD) model of Denman and Pena (Denman and Pena, 1999) as shown in Figure 2-7.

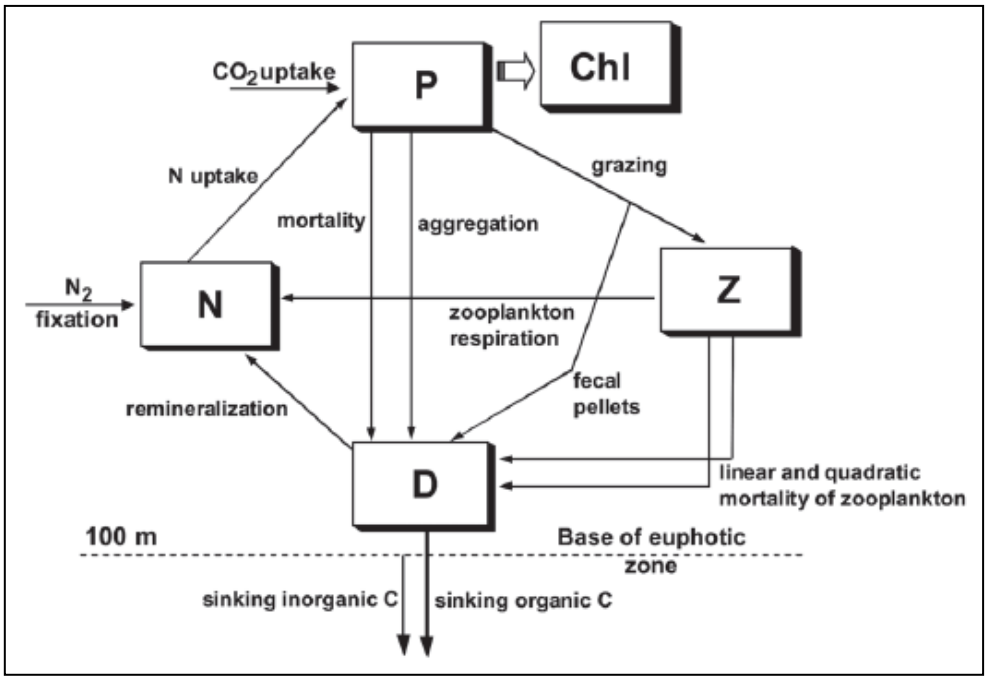

Figure 2-7. NPZD model by (Denman and Pena, 1999).

Figure 2-7 shows a simple representation of the components of the ocean biogeochemical cycle and the various interactions between the components such as grazing of phytoplankton by zooplankton and remineralization of detritus to nutrients which are taken up by phytoplankton for photosynthesis.

Hadley Centre Global Environment Model version 2 - Earth System (HadGEM2-ES) was also considered to be used in this study but it was observed that HadGEM2 data had negative chlorophyll values for certain regions of the ocean. Therefore, blank spaces were observed in map of linear trend of global chl from HadGEM2 dataset (1859-2005) (Figure 2-8) as trend was computed after replacing negative values with NaN. Apart from this problem, HadGEM2 also had negative chlorophyll values at different grid points for different time steps. This causes problems in the implementation of the detection and attribution analysis. Hence, HadGEM2 dataset was not used in this study.

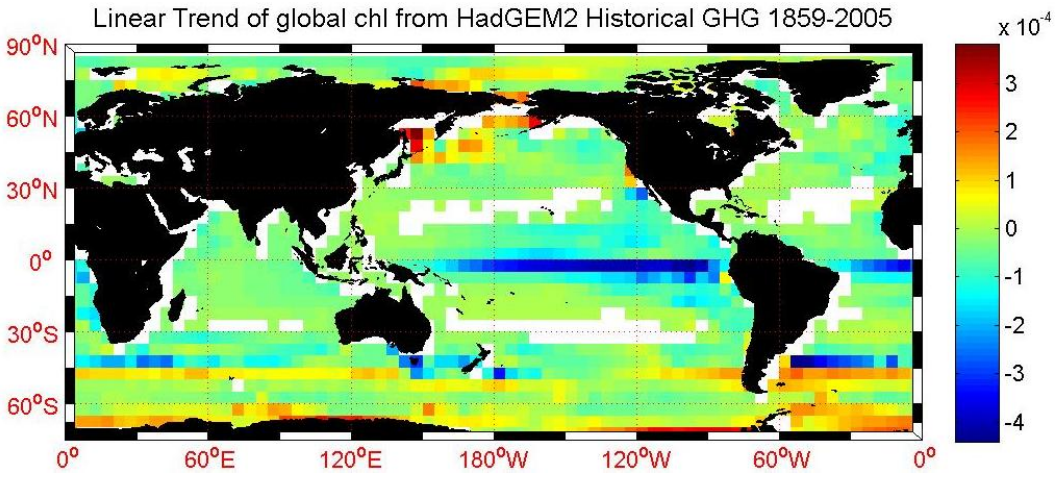

Figure 2-8. Linear trend of global chl (mg m^{-3}) from HadGEM2 Historical greenhouse gas simulation from 1859-2005.

2.1.2.6 Limitations of NOBM

Comparison of NOBM output with SeaWiFS in section 2.1.1 showed that seasonal cycle of global mean chl from NOBM is not in phase with SeaWiFS data. On the other hand, regional mean of chl from NOBM is in phase with SeaWiFS data. Thus, global chl from NOBM data cannot be used

in the analysis. Also, even though seasonal cycle from NOBM for regional chl is represented well with respect to timing but absolute values differ from the SeaWiFS chl.

2.1.2.7 Limitations of Climate Models

Climate models are mathematical representations of the interactions between the components of the climate system. They help us understand the current and past climate and also help to predict the future climate. But models are limited in several ways. It is important to know these limitations before using model output in the analysis.

Incomplete understanding of the climate system

The climate system is very complex and involves many processes and interactions among the components of the system which are not completely understood. Even if scientists understand these complex processes it is difficult to express them mathematically. For example, precipitation and passage of weather fronts are difficult to represent; complex weather events such as hurricanes, thunderstorms and tornadoes are not properly represented and climate patterns such as El Niño, La Niña, Pacific Decadal Oscillation (PDO) and North Atlantic Oscillation (NAO) are not efficiently reproduced i.e. the frequency of the oscillations, the magnitude of the climate parameters associated with it for example, SST or the spatial pattern of the oscillation may not be reproduced by the model correctly (Landsea and Knaff, 2000, Walsh and Pittock, 1998, Fedorov and Philander, 2000, Lienert et al., 2011). Climate oscillations play a major part in chlorophyll variability in the ocean, hence incorrect representation of the climate oscillations may result in inaccurate chl concentration in the ocean.

Limited power of computers

Climate processes and interactions occur over broad range of spatial and temporal scales i.e. climate variations occur over molecular, regional and global spatial scale and these variations can occur instantaneously or they

can take weeks, months, year, decades or millennia to develop. Computers and programs that run the models are limited in their computing power and therefore the spatial and temporal resolution of models is limited. Many of the important climate phenomenon are not included in the models due to low resolution or these phenomenon are represented in the model equations by parameterizations. In some models if the resolution is increased, there is error introduced in the model output due to contamination caused by boundary interactions.

Failure when compared to observations

To test climate model predictions of the future climate it is not possible to wait 20-30 years to see if the model prediction is correct. Therefore, models are tested against the past observations. This is known as 'Hindcasting'. If the models predict the trends in the past correctly then it gives us some confidence that they can be used to predict the future trends correctly as well. Imperfections are introduced in the models due to various reasons such as distortion of the Earth's topography in the model, approximation of the effect of clouds or simplified representation of a certain complex climate processes. Due to imperfections in the model, large differences can sometimes be observed when model outputs are compared with past climate observations (Pincus et al., 2008, Reichler and Kim, 2008, Zhang et al., 2005, Zhou et al., 2007, Henson et al., 2009a, Henson et al., 2009b, Kim et al., 2012).

Thus, we can see that models have several limitations. In spite of these limitations they provide the most detailed projections of climate parameters which help us in understanding of the climate.

2.1.2.8 Comparison of model output with NOBM

Output from climate models was compared with observations i.e. NOBM. This comparison was made using three statistical terms. These are - correlation coefficient, root mean square (RMS) difference and standard deviation. For example, consider observations is 'f' and a model output is 'r',

both having N independent discrete points in space or in time. Correlation coefficient between f and r is

Eq 2-1. $$R = \frac{\frac{1}{N}\sum(f-\bar{f})(r-\bar{r})}{\sigma_f \sigma_r}$$

where, $\bar{f}$ and $\bar{r}$ are the mean values and σ_f and σ_r are the standard deviations of f and r respectively. Standard deviation of f and r is computed as follows -

Eq 2-2 $$\sigma_f = \sqrt{\frac{1}{N}\sum(f-\bar{f})^2} \quad \& \quad \sigma_r = \sqrt{\frac{1}{N}\sum(r-\bar{r})^2}$$

RMS difference E is

Eq 2-3. $$E = \left[\frac{1}{N}\sum_{n=1}^{N}(f-r)^2\right]^{1/2}$$

RMS difference is a measure of the difference between model output 'r' and observations 'f'.. Lower the RMS difference, closer the model output to observations and vice-versa. To know whether the error is due to amplitude difference or phase difference between patterns, four statistical terms R, E, σ_f and σ_r are needed. Using these four statistical terms, a diagram is made which quantifies the similarity between f and r. The diagram was developed by Taylor (2001). Taylor diagram is a way of graphically representing how closely patterns match with observations. Figure 2-9 shows comparison of monthly time series of mean chl for NA region (1999 to 2005) from four climate models with observations (NOBM). Table 2-3 shows the values for the statistical terms used in the Figure.

Table 2-3. Statistical terms computed for Taylor diagram

Model/statistical term	**Standard Deviation**	**RMS difference**	**Correlation Coefficient**
IPSL	0.289	0.244	0.648
GFDL-ESM2G	0.060	0.063	0.649
GFDL-ESM2M	0.126	0.071	0.852
CanESM2	0.101	0.154	-0.396

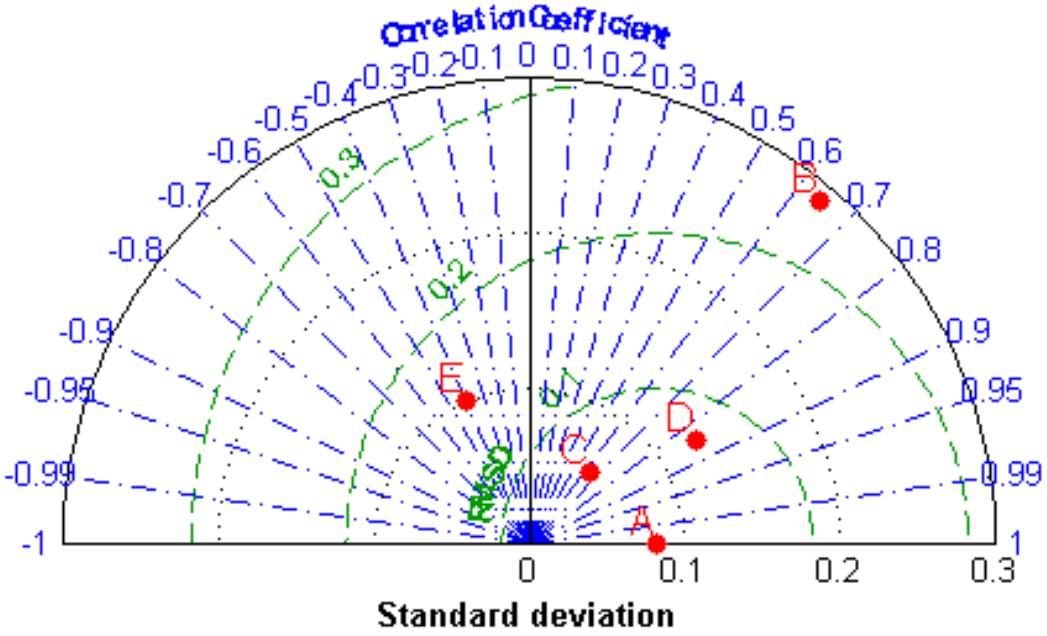

Figure 2-9. a). Pattern statistics describing the monthly time series of mean chl (mg m^{-3}) for NA region (1999-2005) simulated by 4 models compared with the observed.

In Figure 2-9, data from NOBM, IPSL, GFDL-ESM2G, GFDL-ESM2M and CanESM2 is represented by A, B, C, D and E points. X-axis is the standard deviation, Y-axis is the RMS difference and Z-axis is the correlation coefficient. Model outputs that agree well with the observations will lie closer to the point 'A' on the x-axis. From the Figure, it can be seen that the correlation coefficient between NOBM and all the models is moderate (0.648 to 0.852) except for CanESM2 model it is negative (-0.396). This indicates that the phase of the all the models except CanESM2 is same as the observations. From the Figure, it can also be seen that the standard deviation of GFDL-ESM2G is less than NOBM, whereas, standard deviation of other models is larger than NOBM. This indicates that GFDL-ESM2G underestimates the amplitude of the chl values and the other models exaggerate the amplitude of chl values. The RMS difference between models GFDL-ESM2G and GFDL-ESM2M and NOBM is between 0 and 0.1 whereas, RMS difference is more than 0.1 for models IPSL and CanESM2. Lower RMS difference for GFDL-ESM2G and GFDL-ESM2M climate models is due to lower difference in amplitudes of the models and observations. Lower RMS difference indicates that these models perform well in simulating the chl. On

the other hand, IPSL and CanESM2 models performs poorly as the RMS difference is higher which is due to larger difference in the amplitude of patterns.

A similar comparison for the other regions of the ocean i.e., South Atlantic (SA), North Pacific (NP), South Pacific (SP) and Indian Ocean (IO) is also made. The Table of statistical terms for all the models and the diagrams associated with them are shown in Appendix I. In summary it can be said that GFDL-ESM2G and GFDL-ESM2M models perform well in simulation the chl in the ocean.

2.2 Method

2.2.1 Detection and attribution methods

Several techniques have been used to detect the climate change signal such as simple indices and time-series methods, pattern correlation method and optimal detection technique. A brief discussion of these techniques is presented in the following sections.

2.2.1.1 Simple Indices and Time-series methods

This technique uses an index of climate change that is obtained from the climate system variable used for detection. For example, to find a climate change signal in surface temperature, linear trend in surface temperature can be used as an index. The spatial pattern of the index is obtained in observed trends and compared with that obtained from long control model simulations and simulations that incorporate greenhouse gases, sulphate aerosol forcing and natural forcings. The level of agreement between these trends will indicate whether the trend in observations can be explained by internal variability, by anthropogenic variability, by a combination of internal and anthropogenic, by natural forcing variability or a combination of all three variabilities. Studies have incorporated this technique to detect climate change signal in surface temperature records (Knutson, 2000, Boer et al.,

2000). The studies observe an increased agreement between observed and simulated trends when trends are obtained from simulations that include greenhouse gases and aerosols forcings. An extension of this technique is to examine the differences in the correlation structures of observed and simulated climate variable. Wigley et al. (1998) compared correlation structures of observed and model hemispheric mean temperature and found that the differences between the structures can be explained by combined influences of anthropogenic and solar forcing and internal variability. Another extension to the technique is to use statistical models. Global mean near-surface temperature was obtained from time series model and a strong statistical relationship was found between atmospheric CO_2 and observed global mean temperature (Tol and De Vos, 1998).

2.2.1.2 Pattern Correlation Methods

This technique correlates the large-scale patterns of response due to different forcings obtained from model simulations, with the pattern of climate change in observations to distinguish between different causes of climate change. The statistic of this technique can be either centered or uncentered. Centered statistic correlates observed and signal anomalies after removal of their global means whereas the uncentered statistic correlates these fields without removing global mean (Barnett and Schlesinger, 1987). In a study by Tett et al. (1996) to observe changes in atmospheric temperature, simulations from climate models were obtained for increased CO_2 and sulphate aerosols, and reduction in stratospheric ozone and compared with observations. They found that when all three factors were included, the agreement between observations and models was the highest.

2.2.1.3 Optimal Fingerprint (OF) Methods

Optimal Fingerprint technique of detection and attribution was developed by Hasselmann (1979). The technique is a regression based approach to increase the signal-to-noise ratio by looking at the component of the response away from the direction of highest internal variability. Since its

development in 1979 several authors have developed new approaches to the technique. It has been applied to detect climate change signal in surface temperatures (Hegerl et al., 1996, Barnett et al., 1999). Studies have used data other than surface air temperature, such as vertical profiles of zonal mean temperature (Allen and Tett, 1999) and lower tropospheric mean temperature (Paeth and Hense, 2001). Signals from simulation with greenhouse gas plus sulphate plus stratospheric ozone was consistent with the observations of zonal mean temperature whereas, greenhouse gas only fingerprint was detected for lower tropospheric mean temperature. These studies used a single-pattern approach i.e. detection of one signal at a time. Hegerl et al. (1997) developed a two signal approach using a greenhouse gas signal and the sulphate aerosol signal. The two signals are made spatially independent of each other and are regressed with observations. Influence of both the signals was detected in the 50-year trends in northern summer temperatures Some studies have applied this technique to detect a climate change signal in land precipitation trends (Zhang et al., 2007), meridional overturning circulation (Stuart et al., 2007, Baehr et al., 2008), ocean wind waves (Dobrynin et al., 2014), surface salinity of the oceans (Terray et al., 2012) and oceanic oxygen (Andrews et al., 2012). All these studies have detected the anthropogenic signal in the observations i.e. anthropogenic forcing has contributed significantly to the changes in land precipitation trends, surface salinity of the oceans and oceanic oxygen; and the observed changes could not be explained by internal variability or natural forcings.

Advantages of OF method

- The OF method analyses the datasets in a reduced dimension which increases the strength of the climate change signal in the observed data stream. Dimension of the dataset can be reduced in several ways such as reducing the spatial resolution of the data, computing the weighted average of the data and selecting a limited number of empirical orthogonal functions to represent the data.

- The OF technique suppresses noise or internal variability and this again increases the strength of the climate change signal which enhances the possibility of its detection.
- The OF method provides a quantitative estimate of the detected climate change signal and it also provides a technique to detect and quantify more than one signal simultaneously.

Considering the advantages of OF method over conventional detection techniques, OF technique of detection and attribution has been implemented in this study to detect climate change signal in chl concentration in the ocean.

2.2.2 Optimal Fingerprint Method

The principle of this technique is to increase the signal-to-noise ratio by looking at the component of the response of the climate parameter due to climate forcings away from the direction of the highest internal variability (Hasselmann, 1979, Hasselmann, 1993, Hasselmann, 1997). The component of the response of the climate parameter due to climate forcings is defined as the climate change signal or the fingerprint which we need to detect. Figure 2-10 illustrates the principle of OF method. In the Figure, it is assumed that the climate parameter has two modes for example a spatial pattern. The amplitude of the two modes of the climate parameter vary in time along OX and OY. The shaded area in the Figure represents the natural variability of the climate parameter. The climate change signal or the fingerprint lies along OB. This is the fingerprint that is to be detected. OBn represents the part of the signal that is overlapped by noise i.e. natural variability. Thus, OB/OBn is the signal-to-noise ratio. As the signal is in the direction of the main component of the noise, the overlapping by noise on signal is large. Due to this the signal-to-noise ratio OB/OBn is small. To get a higher signal-to-noise ratio, OB is projected in the direction of OD which has less overlap by the main component of the natural variability. Even though the new signal OD is smaller than the full signal OB, the new signal-to-noise ratio OD/ODn is higher than OB/OBn. Thus, there are two main components of the optimal detection technique. First, is to have a good estimate of the noise or the

natural variability. Second, is to choose the direction of the projected signal (OD) such that it maximizes the signal-to-noise ratio.

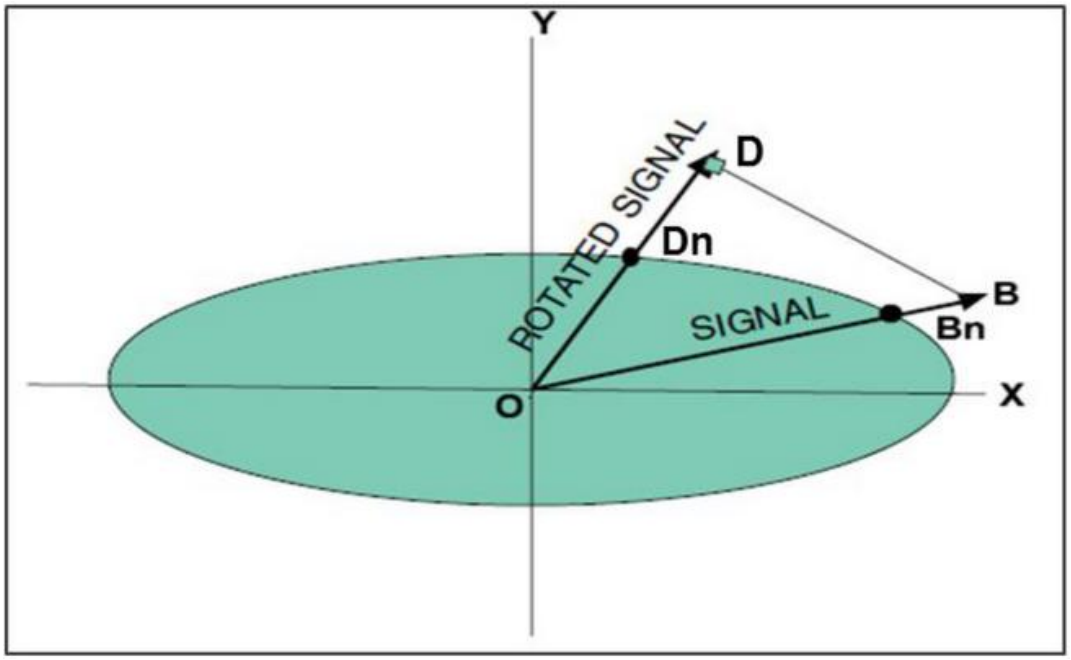

Figure 2-10. Representation of the principle of Optimal Detection technique (Mitchell et al., 2001).

Statistically, the optimal fingerprint approach is a multiple regression problem with respect to generalised least squares. The data is expressed as a linear combination of signal patterns.

Eq 2-4. $$Y=\sum_{i=1}^{m} x_i\beta_i + n = X\beta+n$$

Where Y is a field of 'N' data elements/observations, in which it is assumed that m signals are present, the ith signal is expected to have a pattern of x_i, as seen in the data, the unknown amplitude of the i^{th} signal is β_i (beta) and n is the noise. Equation 2-3 represents the Ordinary Least Squares (OLS) approach which does not account for errors in X. The procedure consists of effectively estimating the unknown amplitudes beta. In matrix form, estimates of the signal amplitude (beta) is give by -

Eq 2-5. $$\beta=(X^TC^{-1}X)^{-1}X^TC^{-1}Y$$

Where C is the NxN covariance matrix of the noise and N is the number of observations (Berliner et al., 2000, Allen and Tett, 1999, Hasselmann, 1997). Positive value of β_i would indicate detection of the signal x_i. If beta value is approximately 1 ($\beta \sim 1$), then it would mean that the model output is representing the observations perfectly. If beta value is more than 1 ($\beta > 1$), it indicates that the model output is underestimating the climate change response in observations. If beta value is less than 1 ($\beta < 1$), it indicates that the model output is overestimating the climate change response in observations. The optimal fingerprint technique has three approaches depending on the time evolution of the signal amplitude and structure:

Fixed pattern approach

In this approach it is assumed that the spatial structure of the climate change signals does not change during the time period of observations (Hegerl et al., 1996, Hegerl et al., 2000, Berliner et al., 2000, Barnett et al., 2001). Hegerl et al. (1996) computed spatial pattern of 50-year trends in northern summer temperatures from observations and model simulations. This spatial pattern does not evolve with time but the amplitude of this spatial pattern may change i.e. increase or decrease. Increasing amplitude of the fixed anthropogenic signal pattern with time would be the evidence of climate change due to anthropogenic forcings in the climate parameter being studied.

Space-time approach

In this approach the signal patterns evolve within the time period of observations. For example, Tett computed spatial pattern of decadal mean for five-decades and formed signal vectors. This five-decade window is then moved one decade at a time and the evolution of the signal amplitudes is obtained (Tett et al., 1999).

Space-frequency approach

In this approach annual or monthly mean signal patterns are used. These patterns evolve throughout the analysis period (North and Wu, 2001). Signal vector is formed by first converting the temporal variation of each signal to frequency domain by Fourier transformation and then selecting the low-frequency Fourier coefficients. Selecting the low-frequencies is a way to reduce the dimension of the signal in time domain. Dimension of the signal is also reduced in spatial domain by reducing the resolution. Dimension of the dataset can be reduced in space and time by Empirical Orthogonal Function (EOF) analysis and Truncation (Appendix II).

2.2.2.1 Components of the OF method

2.2.2.1.1 Guess Signal

In order to detect the influence of climate forcings on chl concentration, space-time pattern of the response of chl in the ocean due to climate forcings needs to be estimated. Observations of chl are a combination of internal variability of chl and response of chl due to climate forcings. Measurement of response of chl to each climate forcing separately is not possible, therefore simulations for specific climate forcing in climate models is used. Having chl data from model simulations alone is not sufficient for detection of climate change signal. In order to detect a signal in a climate parameter, search for the climate change should be in the right direction. For this, a guess signal (Hegerl et al., 1996) is defined and estimated from model simulations. This guess signal is assumed to be representing signal of climate change (Hegerl et al., 1996). For example, a guess signal can be defined as (1) a difference between chl concentration in the beginning of the industrial era from the chl concentration in some arbitrary time in the future, (2) a trend increase in the amount of chl from the beginning of industrial era to some arbitrary time in the future, (3) a trend increase in the size of the subtropical gyre, (4) spatial pattern of the mean of chl, (5) time series of the peak of chl bloom in spring or (6) time series of the average chl in a certain region for a particular month and so on. It might happen that we define the guess signal as time series of the peak of chl bloom in spring and not detect

any climate change whereas, if we define the guess signal as spatial pattern of the mean of chl we might detect a climate change signal. This means that looking in the right direction is important but knowing which direction is the right one is not possible. Hence, defining a guess signal is a trial and error method. Thus, even though defining a guess signal is an important element for a detection study it is still a subjective choice with the possibility of it being a wrong one.

In this study the first guess signal was chosen as the first Empirical Orthogonal Function (EOF) of the model output. EOF analysis is a technique to decompose the data into different modes of variability (Venegas and Bjornsson, 1997). Apart from getting different modes of variability of the data, another purpose of EOF analysis is to reduce the dimension of the data, so that it becomes easier to get the climate change signal and it also makes data handling easier. The procedure to compute EOFs of a dataset is given in Appendix II. Output of the EOF analysis are eigenvectors (spatial structure of the variability/mode), eigenvalues (amount of variance explained by each mode), time-series of each mode and new time-series of data. The new time-series of data can be obtained with reduced dimensions by truncating the eigenvectors matrix at some number N, where N is less than the number of eigenvectors. Various methods to determine the truncation level are discussed in Appendix II.

For a detection and attribution study, the first EOF of model output from climate forcing simulations was regressed using the optimal fingerprint method with first EOF of observations. Noise was computed from long-run control simulations. All the datasets were regridded to $5x5^{o}$ resolution as has been explained later in section 2.2.3.1 which describes the pre-processing of the datasets. Figure 2-11 and Figure 2-12 show the spatial pattern and time series of the first EOF from greenhouse gas (GHG) simulation of GFDL-ESM2M model output and observations from monthly chl time series for the North Atlantic Ocean.

a).

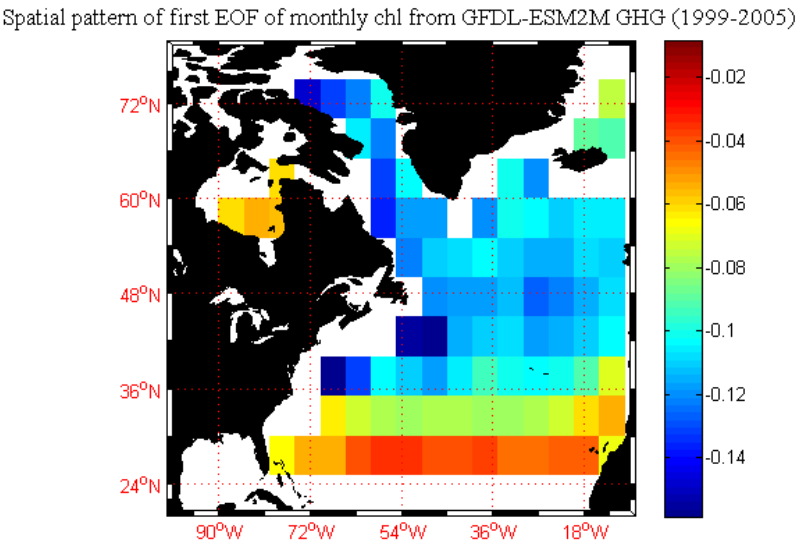

b).

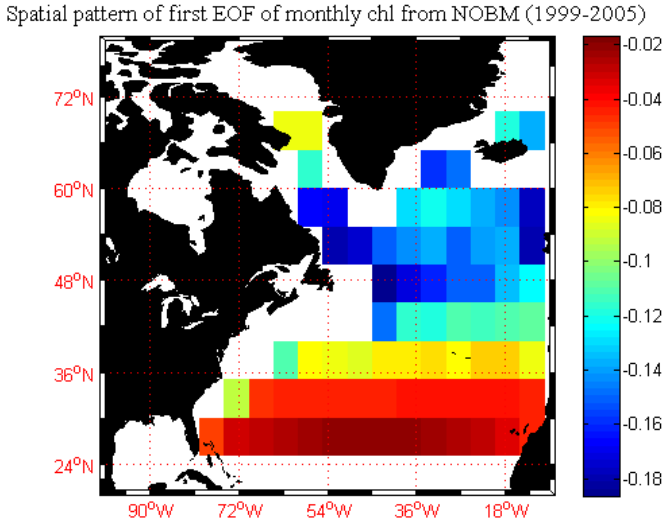

Figure 2-11. First EOF spatial pattern from time series of monthly chl (1999-2005) for North Atlantic from a). GFDL-ESM2M historical greenhouse gas simulation and b). NOBM. Spatial resolution of both the datasets is 5° x 5°.

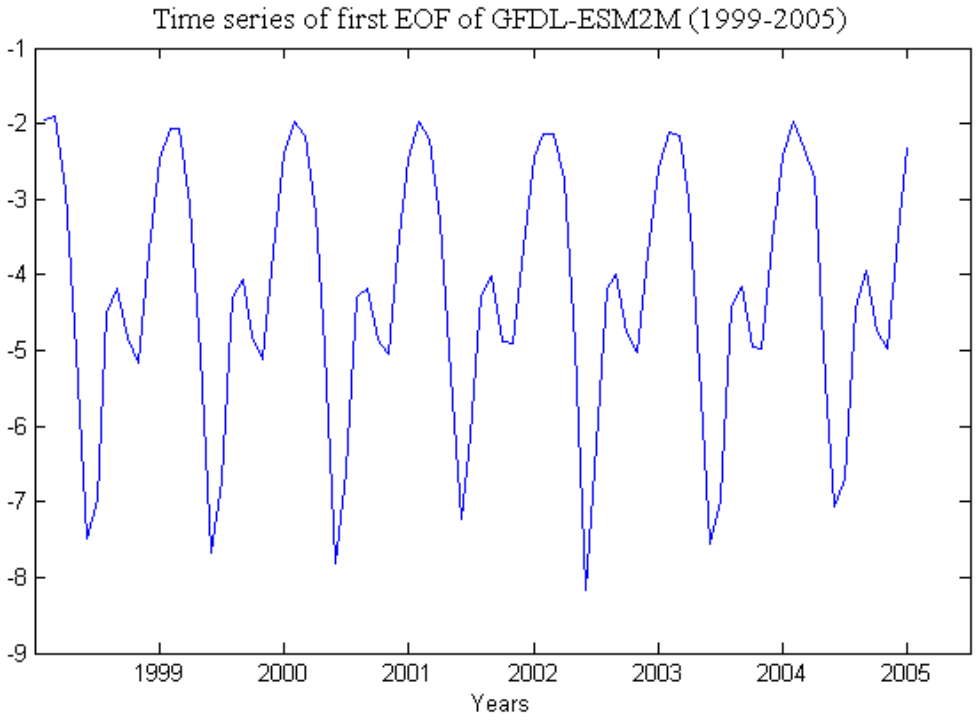

a).

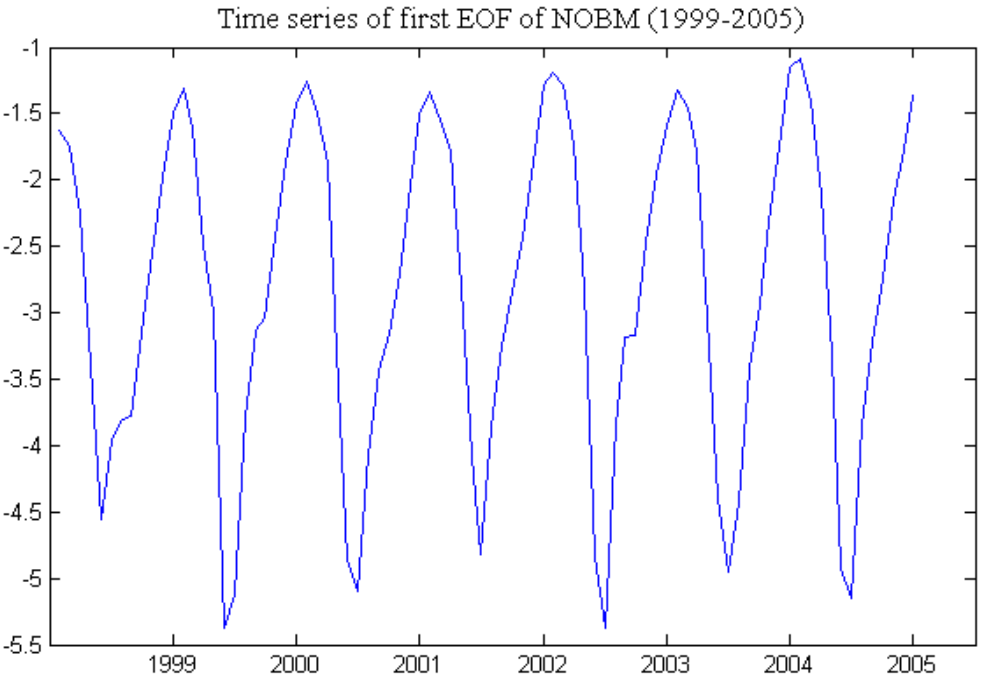

b).

Figure 2-12. Time series of first EOF from time series of monthly chl (1999-2005) for North Atlantic from a). GFDL-ESM2M historical greenhouse gas simulation and b). NOBM.

From the Figure 2-11, it can be seen that increase in chl is observed in lower latitudes (26^{o} N to 36^{o} N in GFDL-ESM2M model and 26^{o} N to 42^{o} N in NOBM) and decrease in chl is observed in latitudes higher to 36^{o} N in

GFDL-ESM2M and 42^{o} N in NOBM. Time series of the two EOFs (Figure 2-12) show a seasonal cycle of the pattern of variability. Hence, the first EOF is a seasonal cycle of chl in North Atlantic and forms part of the internal variability of chl. Similarly, to get the climate change signal, 2nd EOF or any other EOF can be the representation of climate change signal. It cannot be confirmed as to which EOF represents the variability in chl due to climate change, therefore taking EOFs as the climate change signal is not the right direction to look for climate change. Also, in the case when the selected EOF pattern from NOBM does represent the climate change signal (as is expected), the same number of EOF pattern from the model may not represent the climate change signal. It might represent variability in chl due to NAO index or variability in chl due to change in spring bloom period. Therefore, comparing the EOF from greenhouse gas simulation with EOF from observations for climate change detection in chl would be like comparing apples with oranges and then determining the similarity between the two. Hence, it was concluded that defining first EOF as the guess signal is not the right direction to look for climate change in chl concentration in the ocean.

There were three more definitions of guess signals for which detection and attribution study was done. These are -

- Spatial pattern of the Linear Trend of Chlorophyll.
- Linear trend of the zonal average of chlorophyll.
- Time series of the size of subtropical gyres.

It is assumed here that changes in chl due to climate change will be linear and therefore, linear trend of chl is chosen in this study. However, climate change may cause non-linear changes in chl concentration. In that case, climate change will not be detected in the signals chosen in this study. Details of the computation and the results of detection and attribution for these three guess signals is presented in Chapter 3, 4 and 5.

The time period chosen for computation of the guess signal from the model historical simulations is the same as the time period of the observations. For example if observations have the time period from 1997 to

2007, output from the model simulations will be chosen for the same time period. In matrix form, the guess signal is presented as a vector g (Nx1) and it becomes a column of matrix X in Eq 2-3. The number of columns of matrix X depends on the number of climate forcing simulations for which the attribution analysis is being done. In this study guess signals have been computed for the historical simulation, the historical-greenhouse gas simulation, the historical natural simulation and the historical miscellaneous simulation (section 2.1.2.2). The guess signals for each climate forcing simulation represents the influence of the respective climate forcing on chl concentration in the ocean for that time period and for that region.

2.2.2.1.2 Observations

Chl data from NOBM have been taken as the observations in this study. NOBM data for the global ocean is available from 1997 to 2007. This gives us 132 months of data. Figure 2-13 shows the map of global chl averaged over the years 1997 to 2007 and the time series of global chl from 1997 to 2007. For data analysis purpose, when the size of the subtropical gyre was computed (section 5.2), it was observed that there was a spike in the first year (or year and a half for some gyres) (Figure 2-14). This spike may be due to the El Niño event in 1997-1998 or it may be because of the time taken for NOBM model to stabilize from the initial point. Therefore, the first two years of the NOBM data were removed from the analysis.

a).

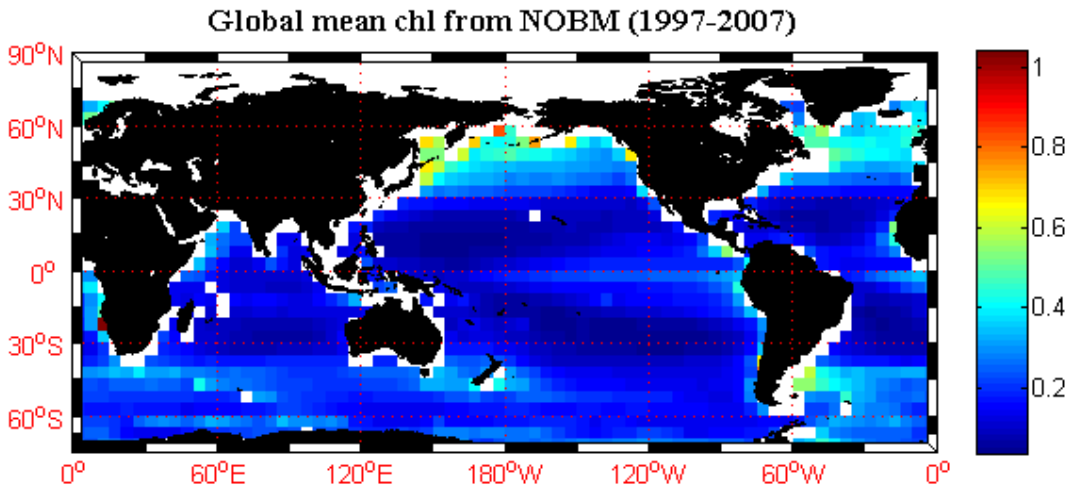

b).

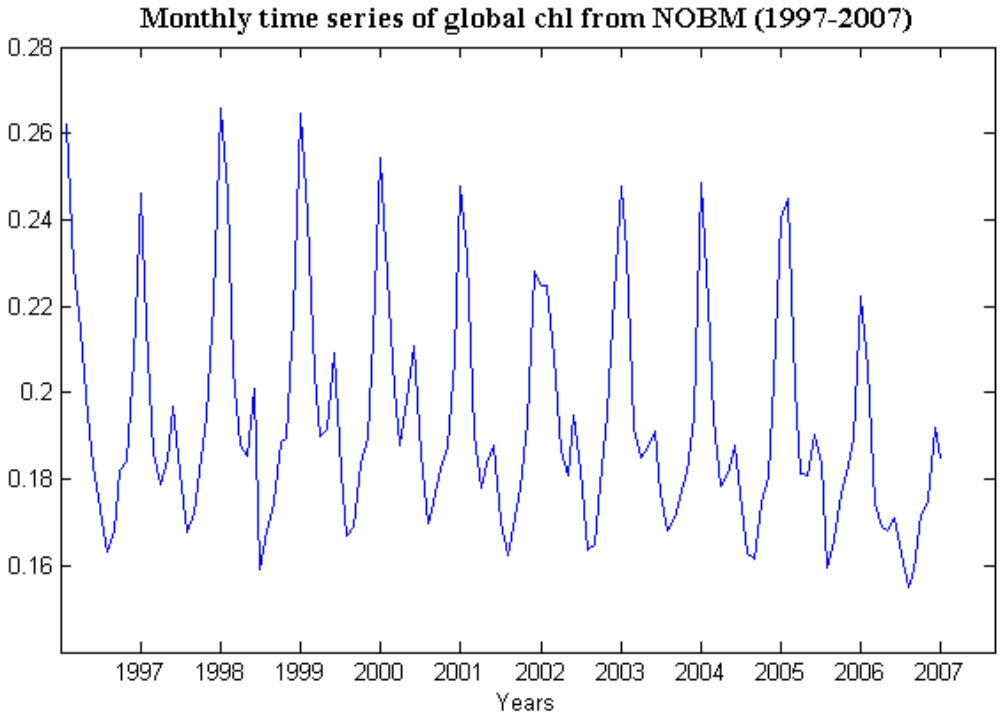

Figure 2-13. a). Map of global chl obtained by averaging monthly chl over 1997-2007 from NOBM and b). Time series (1997-2007) of monthly chl from NOBM, averaged globally. Chl values are in mg m^{-3}.

a).

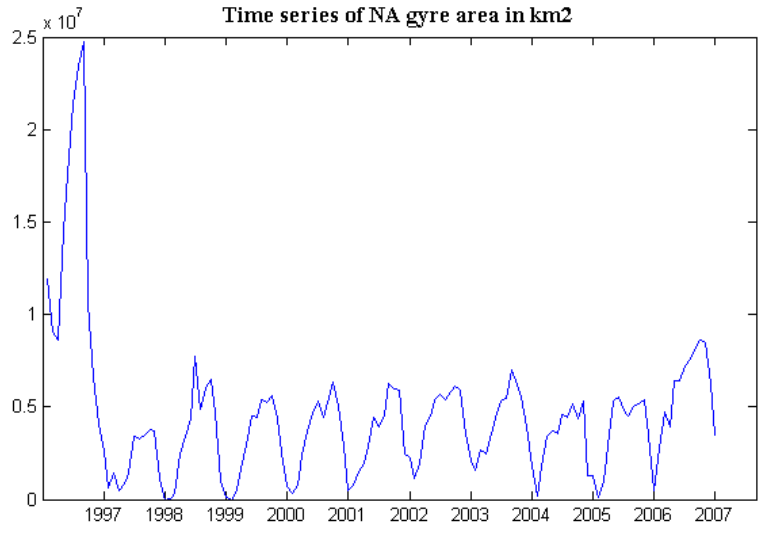
Time series of NA gyre area in km2
x 10^7
2.5
2
1.5
1
0.5
0
1997
1998
1999
2000
2001
2002
2003
2004
2005
2006
2007

b).

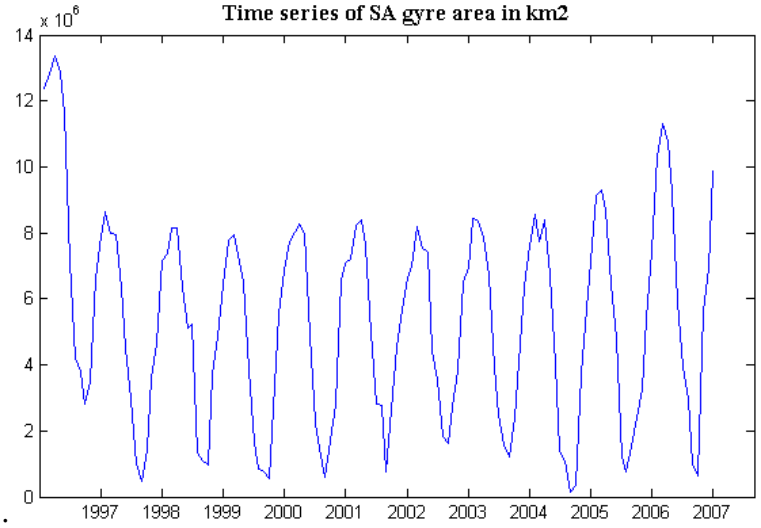
Time series of SA gyre area in km2
x 10^6
14
12
10
8
6
4
2
0
1997
1998
1999
2000
2001
2002
2003
2004
2005
2006
2007

c).

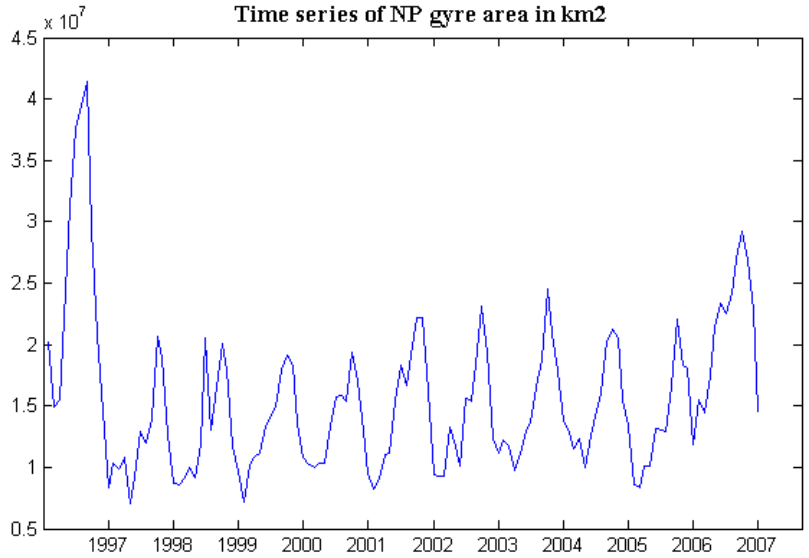
Time series of NP gyre area in km2
x 10^7
4.5
4
3.5
3
2.5
2
1.5
1
0.5
1997
1998
1999
2000
2001
2002
2003
2004
2005
2006
2007

d).

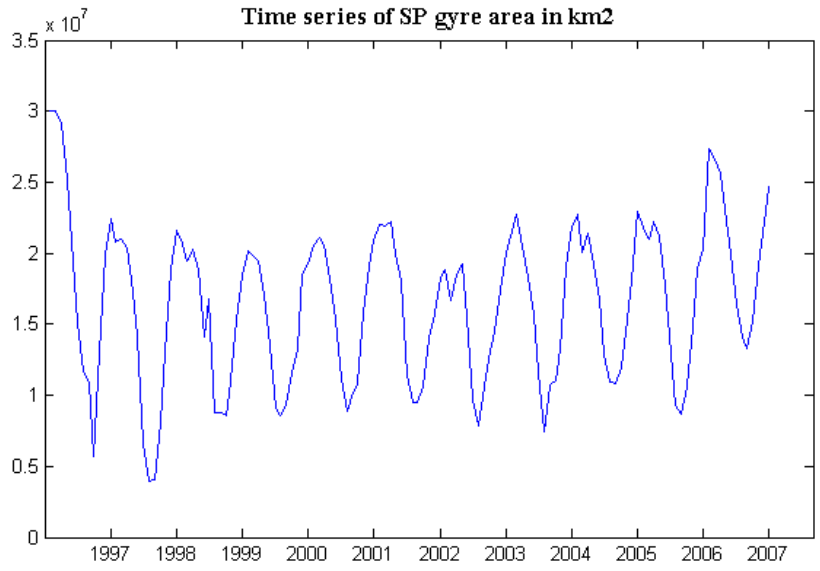

e).

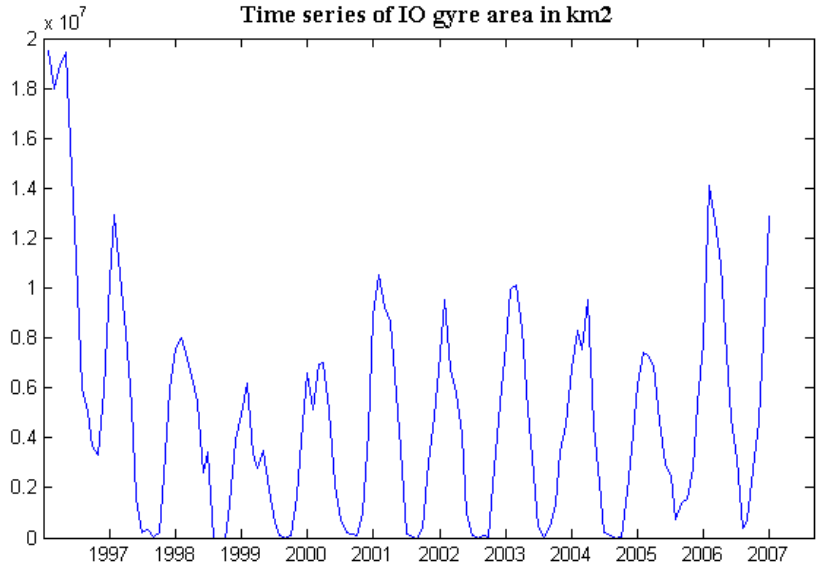

Figure 2-14. Monthly time series of gyre area (km^2) from 1997-2007 for a). North Atlantic, b). South Atlantic, c). North Pacific, d). South Pacific and e). Indian Ocean

Most of the models used in the analysis have historical and historical greenhouse gas simulations starting at 1850 and ending in 2005 (Table 2-1). To match this time period, the last two years of NOBM were removed from the analysis. Therefore, the time period of NOBM used for the study is 1999 to 2005. This gives us 84 months of data.

Vector Y of Eq 2-3 is computed in a similar way as vector X i.e. as the guess signal is defined. For example if the guess signal is defined as the

spatial linear trend of chl then the same function is computed from the observations as well. Thus, matrix Y is also a vector with N rows i.e. Nx1.

2.2.2.1.3 Internal climate variability/noise

Noise is another important element of optimal fingerprint method. As it has been discussed previously, internal climate variability is the natural variability of the climate system. It is this natural variability which is termed as noise 'n' in Eq 2-3. Variability in chl occurs on seasonal, annual and decadal time scales. Chl concentration in the ocean varies with latitude as well. These changes observed in chl concentration are superimposed on the natural cycle of chl and the influence of climate forcings on chl. To obtain the natural cycle of chl, long-term records of chl prior to industrial revolution are needed i.e. those records which have not been influenced by climate forcings. Since there are no long-term chl observations, the control runs of climate models are used to obtain the natural variability of chl. There is no reference to which this estimate of natural variability of chl can be compared with, as there are no long-term records of chl prior to industrial revolution. Therefore, the record obtained from the model control run is divided into two parts. One part is used to obtain the noise covariance matrix i.e. 'n' of Eq 2-3 and is used in optimization and the other is used for comparison with the residuals obtained after the removal of the optimized climate forcing signals. This process is known as the residual consistency test (Allen and Tett, 1999). Apart from verifying that the noise is correct, it is necessary to reduce the dimensions of the noise covariance matrix. The process to reduce the dimensions is known as truncation and the various methods to determine the truncation level are explained in Appendix II. In this study, the method developed by Hegerl et al. (1996) is used to determine the truncation level of the noise covariance matrix.

The step-by-step process of computing the noise covariance matrix is described below. Assume that chl from control run is in matrix C with M rows and T columns, where M represents the number of grid points and T represents the number of time steps. Matrix C is then divided into two parts

C1 and C2 with M rows and T/2 columns. Matrix C1 is used for computing the noise covariance matrix and C2 for the residual consistency test.

Computing the noise covariance matrix

1. Divide C1 into chunks of length equal to the time period of observations. For example, if time period of observations is 84 and C1 has 1000 time steps then C1 is divided into chunks of length 84. This gives 11 chunks of C1 with length 84. In matrix form each chunk will have dimensions as Mx84.
2. For each chunk, a vector of dimension Nx1 is computed in the same way as the guess signal was computed. As we have 11 chunks, there will be 11 vectors of length Nx1. One single matrix 'C1_chunks' is made with these vectors i.e. a matrix with dimensions Nx11. The spatial and temporal dimensions of this matrix are reduced by EOF analysis and the Hegerl et al. (1996) method of truncation (Appendix II).
3. Twice the standard deviation of matrix C1_chunks gives us the noise matrix 'noise_1' which has Nx1 dimensions.
4. The same process is repeated for matrix C2 without the truncation step and the noise matrix obtained is 'noise_2'.
5. Noise covariance matrix 'C' in Eq 2-4 is computed as C = noise_1*noise_1T where noise_1T is the transpose of the noise_1 matrix. Thus, C has dimensions NxN.
6. The noise covariance matrix is used to solve for β values using Eq 2-5. This gives the amplitude of the climate forcing signal in observations. It is a scalar quantity.
7. The β value is implemented in Eq 2-6 and residual is computed as follows:

   Eq 2-6. $R = Y - X\beta$

   R is a vector with dimensions Nx1.

8. The residual is compared with noise_2 computed with the second matrix of control simulation C2. Comparison of these two vectors is made using an F-test. The F-test tests the null hypothesis that the data in the two vectors (residual and noise_2) come from normal distributions with the

same variance. If the result of the test is 1, then it means that the null hypothesis is rejected at 5% significance level. If the result of the test is 0, then it would indicate that the two vectors come from normal distributions with the same variance. Residual consistency test can also be performed to compare residual with noise_2 as described in point 8, section 8.1.2 of Appendix II - Allen & Tett method of truncation.

The process chart associated with steps to compute noise covariance method is given in section 9.2 of Appendix III.

2.2.2.1.4 Implementing Optimal Fingerprint method

After computing all the elements needed for OF method amplitudes of the climate forcing signals i.e. beta is computed using Eq 2-5. Two sided Confidence interval (CI) for the beta values is also estimated. Equation used to estimate CI is

Eq 2-7. $CI=t_{\alpha/2,n-p}*\sqrt{\sigma}$

Where σ is variance of beta and t-score for the critical value α/2 is computed with n-p degrees of freedom.

Eq 2-8. Alpha (α) = 1 - (percent confidence interval/100)

For example, for 95% confidence interval α = 1 - (95/100) = 0.05.

'n' is the number of independent observations. In this study n will be equal to N i.e. the length of the guess signal. 'p' is the number of response patterns for which beta is to be estimated. Equation to estimate Variance of beta is

Eq 2-9. $\sigma = (X^T C_1^{-1} X)^{-1}$

The process chart for implementing OF method is given in section 9.4 of Appendix III.

2.2.3 Pre-processing of the datasets

All the data from NOBM and the five climate models is provided in netCDF format. Chl values and latitude and longitude values are extracted from this file using Matlab. Prior to estimating the elements of OF method i.e. estimating guess signal, internal variability and observations as described in section 2.2.2.1, there are some pre-processing steps that need to be implemented for all the datasets. A brief description of these steps is as presented below:

2.2.3.1 Gridding & Regridding

The data files from the different models are not all gridded in the same way. For example, longitudes can be in 0 to 360 or -180 to 180 degrees format. To make the computation simple every file was arranged with respect to the 0 to 360 degrees grid orientation. Furthermore, all datasets were re-gridded or interpolated to the regular traditional longitude-latitude Cartesian grid where necessary by keeping the resolution of the grid in accordance to the number of latitudes and longitudes in the original grid. For example, if the model output from IPSL is in tripolar grid with 211 number of latitudes and 360 number of longitudes then, the re-gridded Cartesian grid would have the same number of latitudes and longitudes. All the datasets were regridded to $5x5^{o}$ resolution. This resolution was also used by Hegerl et al. (1997) to detect climate change in near-surface temperature. This resolution was chosen in this study as it is big enough to eliminate small-scale varaibilities which add to the noise and make the detection of climate change signal difficult, and it is small enough to not remove or neglect relevant changes in chl due to climate change.

2.2.3.2 Compute Anomalies

Climate change studies are interested in long-term changes in the climate parameter under study. Since seasonal variability is on short time scales and forms part of the internal variability, seasonal cycle is removed from the datasets. Procedure to remove the seasonal mean is as follows: take

the mean of all the Januarys for all the years; subtract this mean from all the January data; repeat this process for all the other months. This removes seasonal mean from the whole time-series.

2.2.3.3 Handling missing values

The grid of the model data and the data from observations (NOBM) should be same for further analysis. Observations grid is usually not changed. Therefore, the model data is re-gridded to match the observations grid. The dataset used here consists of firstly, the data itself, in this case chl values for the ocean; secondly, the land component, which may be represented as a negative value, or null value or some arbitrary large value in the dataset; and thirdly, during some months, in some regions the data will be missing, the missing data may be represented as a negative value, or null value or some arbitrary large value. Negative or large values would skew the mean or calculation of any metrics and are also not useful for our analysis. Therefore these values (other than the chl values) need to be represented as one standard value, which in this study is NaN. The model data and observations should have NaNs at the same position. This is to make the computation easier because missing values are normally removed from the data for any statistical analysis. Therefore, when missing values are removed from observations and model data, the resulting matrices should be the same size. For this, the position of missing values is made similar in both the datasets before removing them. Missing values are made similar in two matrices by cross-multiplication.

The process chart for the pre-processing of the datasets is given in section 9.1 of Appendix III.

3. Climate Change Detection and Attribution for Spatial Linear Trend in Chlorophyll

One of the key constraints on detecting a climate change signal in a climate parameter is the time period of availability of observations. Industrial revolution has lead to emission of greenhouse gases in the atmosphere and this is causing global warming which is the cause of climate change. If the observations are available since the pre-industrial era (~1750) then it would be easier to distinguish between variability before climate change (internal variability) and variability due to climate change. Another important factor is the homogeneity of the observations i.e. the method used to measure the parameter should be same and the measurement techniques used should also be the same so that the observations have similar space and time resolution and their computation is also same. Also, the errors and uncertainties due to different measurement techniques are also same and would give homogenous datasets which would make it easier to use them in any analysis. Otherwise, datasets will have different errors and uncertainties and might not be similar enough to be used together in the analysis. In the case of chlorophyll, there is no homogenous long-term (~100 year) observations which make the detection of climate change in chl difficult. An attempt was made by Boyce et al. (2010) to study long-term (~100 year) trend in chl by blending in-situ chl data obtained from two different shipboard measurement techniques. The study observed a declining trend in global median chl of 1% per year. The results of the study were questioned by several authors as the detected trend was observed in datasets obtained from different measurement techniques (Mackas, 2011, Rykaczewski and Dunne, 2011, McQuatters-Gollop et al., 2011). Studies made on shorter time scales of data (20-50 years) with limited spatial coverage have observed an increase in chl by observing the trends in in-situ measurements made at Bermuda Atlantic Time Series (BATS) station, Hawaii Ocean Time-Series (HOT) station (Saba et al., 2010b) and Cooperative Oceanic Fisheries Investigations (CalCOFI) (Kahru et al., 2009). Studies have also been made to observe trends in global ocean chl from satellite ocean color sensors (Gregg, 2005, Behrenfeld et al., 2006, Vantrepotte and Mélin, 2011, Siegel et al., 2013).

However, none of these studies take into account or remove the effect of internal variability (noise) of chl on the observed trends. Thus, the observed trend in these studies may be due to climate change or may be due to internal variability.

In order to detect a climate change signal in chl using short data records a formal detection and attribution study needs to be implemented. This study focuses on implementing the optimal fingerprint (OF) method of detection and attribution on satellite records of chlorophyll. The method optimizes the observations and the response of chl to climate forcings from model simulations, with the noise obtained from the control simulations. Thus, by increasing the signal-to-noise ratio and even though the time period of availability of observations is less, there is a possibility of a climate change signal to be detected.

An important element of the optimal detection method is to determine the metric of climate parameter or the definition of guess signal in which climate change is likely to be detected. In this chapter, the guess signal is defined as the spatial linear trend of chl in a region. This gives a fixed spatial pattern of climate change signal i.e. we assume that the observed trend in chl in a certain time period is representative of the climate change. Spatial structures have been used before in detection of climate change in near surface temperatures (Hegerl et al., 1996, Hegerl et al., 2000, Berliner et al., 2000, Barnett et al., 2001, Antoine et al., 2005). For example, Hegerl et al. (1996) defined the climate signal as the spatial pattern of near-surface trends defined for time intervals of 15-30 years; Hegerl et al. (2000) computed the climate change signal as the first EOF of the summertime near surface temperature and Hegerl et al. (1997) defined the climate change signal as the difference between the average of two time periods.

Linear trend of chl over a certain time period is related to the change in chl in that region. This change may happen due to internal variability or due to climate forcings such as increase in greenhouse gases, change in solar radiation and change in aerosols in the atmosphere. To detect whether greenhouse gases contribute towards the observed change or not, optimal

fingerprint method is used. In this, spatial pattern of change is computed from observations and the model forced simulations. Noise is computed from the control simulations of the model and is removed from the observations and the model forced simulations.

The first section of the chapter gives the details of the dataset used and the regions of the ocean where the signal is to be detected. For the purpose of presentation of results, the North Atlantic region is used here as a case study. Previous studies have found decadal variability in the timing and magnitude of the phytoplankton bloom in North Atlantic (Barton et al., 2003, Henson et al., 2006, Henson et al., 2009a). Long-term declining trend in chl in North Atlantic has also been observed by Boyce et al. (2010). Decline of 1.3% per year was also observed in anomalies of chl concentration in North Atlantic ocean from SeaWiFS ocean color data (1998-2007) (Beaulieu et al., 2013). These studies are indicative of a climate change trend in chl in North Atlantic and hence, OF analysis is implemented in this region with the possibility of detecting a climate change signal. The second section of the chapter describes some of the basic statistics performed on the datasets for different regions of the ocean. Comparison of the results is made for different datasets and for different time periods. Methodology used to implement the OF method on the spatial linear trend in the data is described in the third section. Results from comparison of datasets, consistency checks on noise covariance matrix and estimation of scaling factors are presented in the fourth section of the chapter. Interpretation of the results takes place in the discussion section which is the fifth section and chapter is completed with summary and conclusions of the analysis in the sixth section.

3.1. Data

The datasets used for the analysis are as mentioned in chapter 2 (Table 2.1). As observations, chl from NOBM is used in the analysis and simulations from GFDL-ESM2G, GFDL-ESM2M, IPSL and CanESM2 models are used to compute the signal and the noise.

Regions of the ocean for which spatial linear trend of chl is computed are listed in Table 3-1 along with their latitude and longitude limits. These latitude and longitude limits were chosen with reference to the division of ocean regions made by Boyce et al. (2010) although in this study, the equatorial region is not included for the analysis and there is no separate division for Southern Ocean instead the latitude limits of the South Atlantic, South Pacific and Indian Ocean are extended further south than those in Boyce et al. (2010). Figure 3-1, shows the regions of the ocean (red boxes) chosen for OF analysis.

Table 3-1. Latitude and longitude limits of the regions of the ocean chosen for the analysis

Region	**North Atlantic (NA)**	**South Atlantic (SA)**	**North Pacific (NP)**	**South Pacific (SP)**	**Indian Ocean (IO)**
Latitude	20^o to 80^o	-85^o to -15^o	20^o to 80^o	-80^o to -20^o	-80^o to -20^o
Longitude	260^o to 352^o	295o to 25o	120^o to 280^o	150^o to 300^o	30^o to 120^o

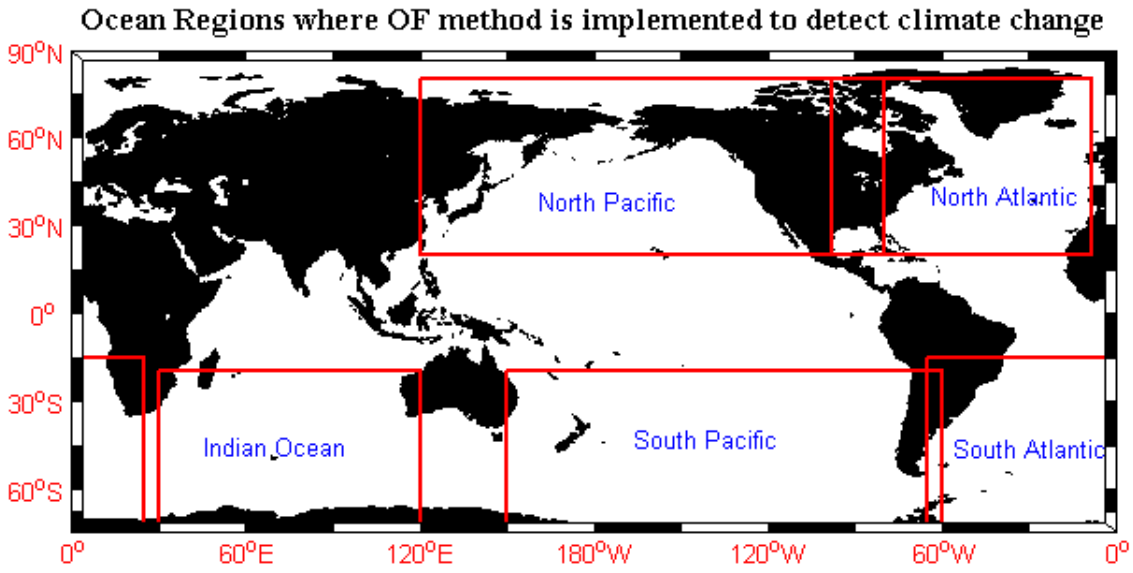

Figure 3-1. Regions of the ocean chosen for analysis. Each region is represented by a box in red.

For ease of presentation, each of the model simulations used in the analysis is represented as a letter of the alphabet in the Figures and tables in

the chapter. The letter associated with each model simulation is as in Table 3-2.

Table 3-2. Model simulations and letter of the alphabet designated to each simulation

Model Simulation		**Alphabet**
NOBM		A
GFDL-ESM2G	Historical	B
GFDL-ESM2M	Historical	C
	Historical Greenhouse gas	D
	Historical Natural	F
	RCP85	G
IPSL	Historical	H
	Historical Greenhouse gas	I
	Historical Natural	J
	RCP8.5	K
CanESM2	Historical	L
	Historical Greenhouse gas	M
	Historical Natural	N
	RCP8.5	O

3.2. Pre-processing of the datasets

Prior to estimating the elements of OF method i.e. estimating guess signal, internal variability and observations as described in section 2.2.2.1 of chapter 2 and implementing the OF method, there are some pre-processing steps that need to be implemented for all simulations of the model and the observations (NOBM).

1. A summary of some of the steps is provided here, see section 2.2.3 of chapter 2 or section 9.1 of Appendix III for details. Chl values are extracted from the netcdf files, rearranged and regridded, invalid values in the data are replaced by NaNs, values are converted to mg m^{-3} and seasonal mean is removed from the dataset.
2. Remove NaNs from the data and regress data with time. This gives several statistical terms of importance. These are -

    - Slope at each grid point for the time period of the dataset. This gives the spatial linear trend of chl in a region of the ocean. Spatial linear

trend is also the guess signal for the analysis, hence this step gives us the guess signal for each model simulation.

- r^2 statistic, i.e. coefficient of determination gives an indication as to how well the regression line fits the real data points. The value of r^2 varies between 0 and 1 with 0 being 'no fit' and 1 being 'perfect fit' to the data.
- F-statistic and its p-value - F-statistic tells whether the linear fit, i.e. the linear trend, is significant or not. If p-value is less than 0.05 then the linear trend is significant at the 95% level and if it is more than 0.05 then the linear trend is not significant at the 95% level.

3. Perform Lilliefors test on the residuals obtained by regressing the chl values against time. Lilliefors test is used to test the null hypothesis that the residuals come from a normally distributed population. The result of the test is 1 if the null hypothesis is rejected at 5% significance level, otherwise it is 0.
4. For forced run of the model, steps 2 and 3 are computed for two time periods. One is the 'whole time period' i.e. the time period for which the data is available as given in Table 2.1. For example, if model output is available from 1861-2005, spatial linear trend is computed for this time period. Longer time period used for computing linear trend may give a significant trend of chl, which may increase the possibility of climate change signal detection. Another time period is the 'reduced time period' i.e. 1999-2005. This time period is chosen to match the time period of models with that of observations (NOBM). As an example of the signal, global map of linear trend computed for 1999-2005 from NOBM dataset is shown in Figure 3-2.

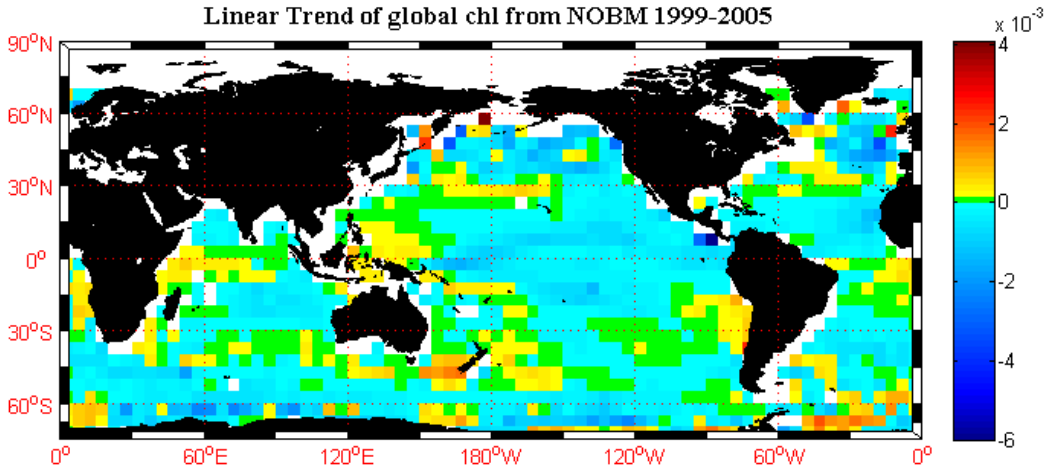

Figure 3-2. Linear trend of global chl (mg m^{-3} per month) from NOBM (1999-2005)

5. Linear trend from all the forced model simulations is compared with the NOBM and presented in a Taylor Diagram. The statistics needed for the diagram are correlation coefficient (R) between observations and model output, root mean square difference (E), standard deviation of observations and standard deviation of model output.

3.3. Implement OF method

Steps to implement OF method are as follows -

1. Guess signal for the forced model simulations has already been obtained in the pre-processing step 2.
2. Noise covariance matrix needs to be computed from the control run of models. Steps used are as described in section 2.2.2.1.3 or as in section 9.2 of Appendix III. In brief, the data from the control simulation is divided into two parts, one part is used to optimize the observations and the signals from the model forced simulations and the other part is used to check the consistency of the noise matrix computed from the first part. Each part of the control simulation is divided into chunks of length (time period) equal to the length of observations and for each chunk signal (spatial linear trend) is computed. These chunks are also known as pseudo observations as they are masked to imitate the pattern of missing values found in the observations. Twice the standard deviation of the matrix obtained from the signal of the chunks is the noise covariance matrix.

3. Dimension of the noise covariance matrix needs to be reduced so as to make the computation easier to handle and also to increase the strength of the climate change signal in the observations. One way to reduce the dimension of a dataset is to reconstruct the dataset using a selective number of empirical orthogonal functions of the data Hence, for every region of the ocean using forced model simulations, noise covariance matrix is truncated. The method is described in detail in section 1.2.2 of Appendix II or as in 9.3 of Appendix III using Method 1. In this method correlation coefficient is computed between optimal fingerprint ($OF = C^{-1}*g$, where C is the noise covariance matrix and g is the signal from the model forced simulation) and the guess signal (g). This is plotted against the level of truncation used to reconstruct the noise covariance matrix. The point in the graph where there is a drop in the correlation coefficient, is chosen as the level of truncation. This point is chosen because this number of EOFs give maximum correlation and beyond this correlation coefficient is either decreasing or stabilizing. Figure 3-3 shows the graph for determining the truncation level when the guess signal is spatial linear trend of North Atlantic (NA) region of the ocean computed from the greenhouse gas simulation of GFDL-ESM2M model. Level of truncation determined from the graph is 28 (shown by the red line).

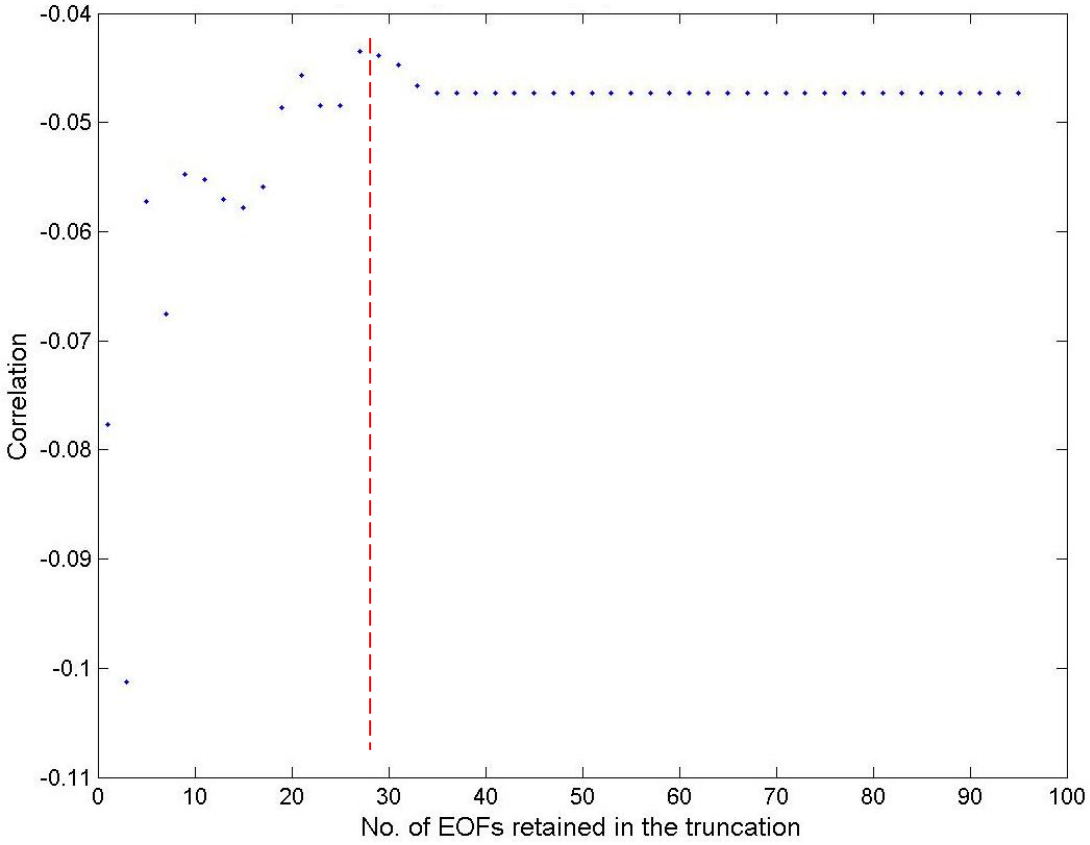

Figure 3-3. Example of a graph to determine the level of truncation of the noise covariance matrix. The chosen truncation level is 28 as at values greater than this, the correlation coefficient is invariant.

4. At this step, all the elements needed for OF method implementation have been obtained i.e. the guess signal from the forced run, signal as in observations and the noise covariance matrix.
5. These three elements are input to the regression equation

Eq 3-1. $Y = X\beta + n$

where Y is signal from NOBM, X is signal from model forced simulation and n is the noise covariance matrix. Output of the OF method is the beta value with 5-95% confidence interval and residual of Eq 3-1. The method is described in detail in section 9.4 of Appendix III. Beta values are obtained for all the model forced simulations in all the regions of the ocean. If a positive beta value with confidence interval that exceeds zero is estimated, it is an indication of detection of the signal in the observations.

6. Residuals obtained in step 5 are compared with the noise matrix computed from the second part of the control simulation. This is to verify the consistency of the noise covariance matrices computed from the first and second part of the control simulation. This comparison is made using an F-test, the result of which is 0 when the vectors being compared come from normal distributions with the same variance and is 1 otherwise. The method is described in step 8 of section 2.2.2.1.3 of Chapter 2 or as in section 9.4 of Appendix III.

3.4. Results

3.4.1. Trend in chlorophyll

Linear trend at each grid point is computed for global chl from NOBM (1999-2005) and all the model simulations. Significance of these trends was determined by p-value of F-statistic (step2 of section 2.2). Figure 3-4a below shows the linear trend in global chl from NOBM (1999-2005). Negative trend in chl is presented by blue shades and positive trend in chl by yellow-red shades. Grid points with grey color are regions where trend was not significant ($p>0.05$) at 95% significant level. Figure 3-4b below shows the mean of chl at each grid point from NOBM (1999-2005). Percent of grid points where trend is significant is 21.47% of the total grid points for which linear trend is available. A small number of significant grid points is an indication that the strength of the signal is weak and that climate change signal will be difficult to detect. Out of the significant grid points, 70.54% of grid points have negative trend. Thus, regions of the global ocean where chl is declining are more numerous than the regions where trend is increasing. A strong negative trend is also observed in the Northeast region of North Atlantic and North Pacific oceans. These trends observed in global chl may be due to climate indices such as Pacific Decadal Oscillation and North Atlantic Oscillation (PDO and NAO) as observed by (Boyce et al., 2010), or to some other internal climate forcing or to external forcings such as greenhouse gas and natural or, they are just part of the natural variability of

chl. The results of the OF method implementation will clarify the reasons behind the observed trends.

a).

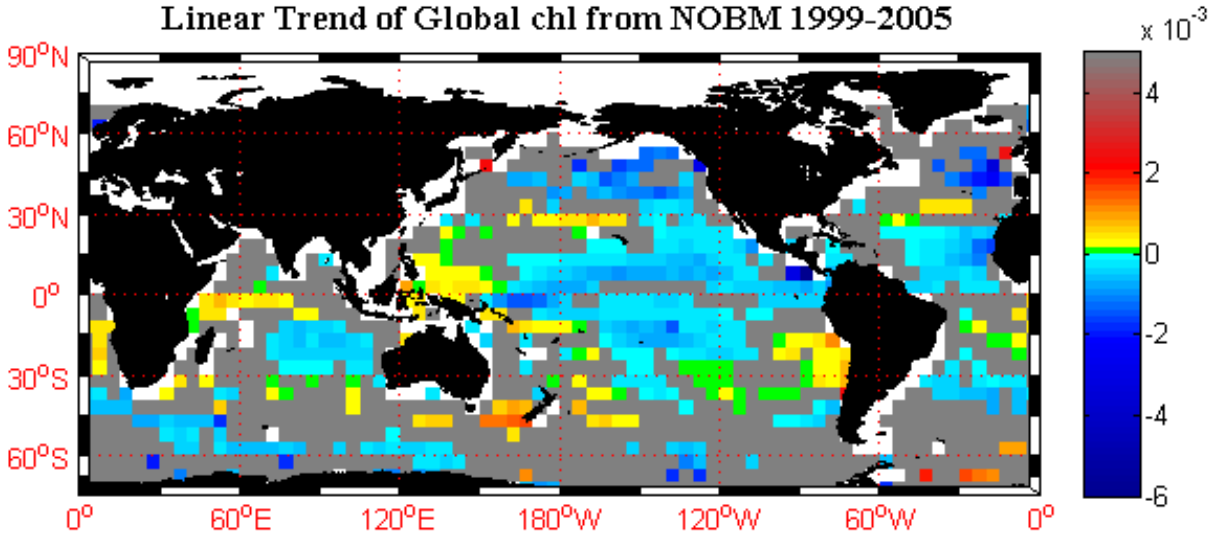

b).

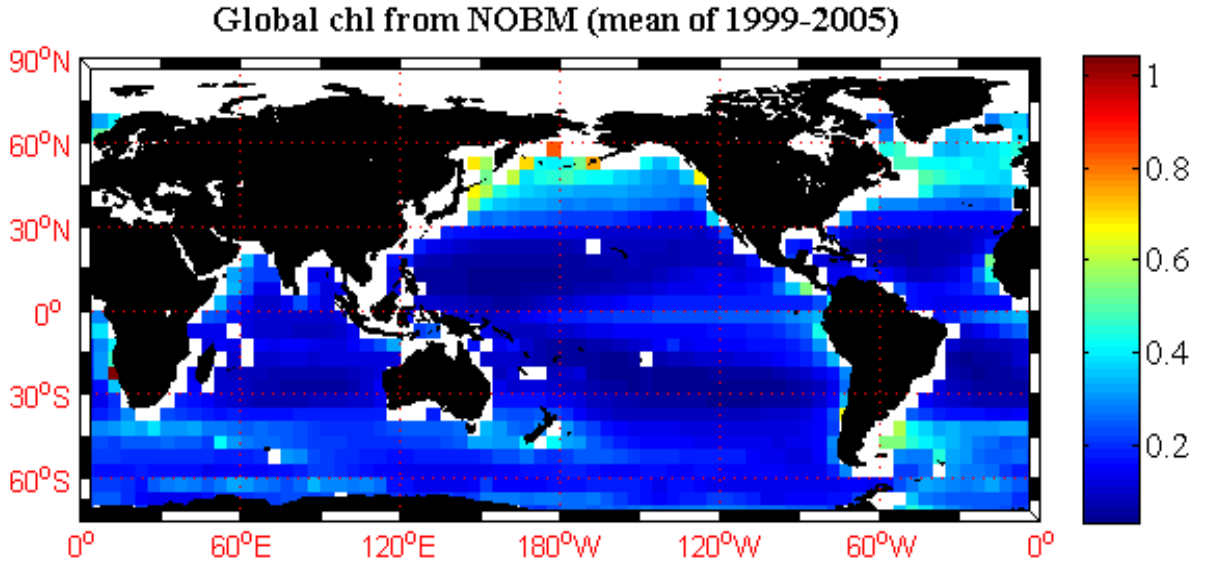

Figure 3-4. a). Linear trend at each grid point in global chl (mg m^{-3} per month) from NOBM (1999-2005). Grey areas represent grid points where trend is not significant ($p>0.05$). b). Mean of chl at each grid point from NOBM (1999-2005).

Spatial linear trend was computed for all the regions of the ocean from model forced simulations. Linear trend at each grid point was computed for two time periods i.e. whole and reduced. Reduced time period is from 1999-2005 which is the same as NOBM. Signal from model forced simulations is the response of chl to climate forcings, detection of which in observations

would indicate the influence of forcings in chl concentration in the ocean. A shorter time period of linear trend computation may not give a strong signal i.e. the signal-to-noise ratio may not be high enough to be detected. Therefore, linear trend was also computed for the whole time period of model forced simulations. Linear trend from whole time period of simulations was much smaller (10^{-2} to 10^{-3}) than the trends from reduced time period of simulations (10^{0} to 10^{-1}). Figure 3-5 below shows the percent of grid points where trend is significant for NA region of the ocean from all the model forced simulations. Percent of grid points for significant trend from whole time period of model simulations are represented by blue bars and percent of grid points for significant trend from reduced time period of model simulations are represented by red bars. From Figure 3-5, it can be seen that the percent of grid points where trend is significant is higher from whole time period than the reduced time period for most of the model simulations except for F (ESM2M historical natural simulation) and N (CanESM2 historical natural simulation). Thus, except for these simulations the possibility of climate change detection from whole time period of simulations will be higher than the reduced time period of simulations, suggesting that long time period of data capture the climate change more distinctly than short time period of data as short time series has a strong natural variability.

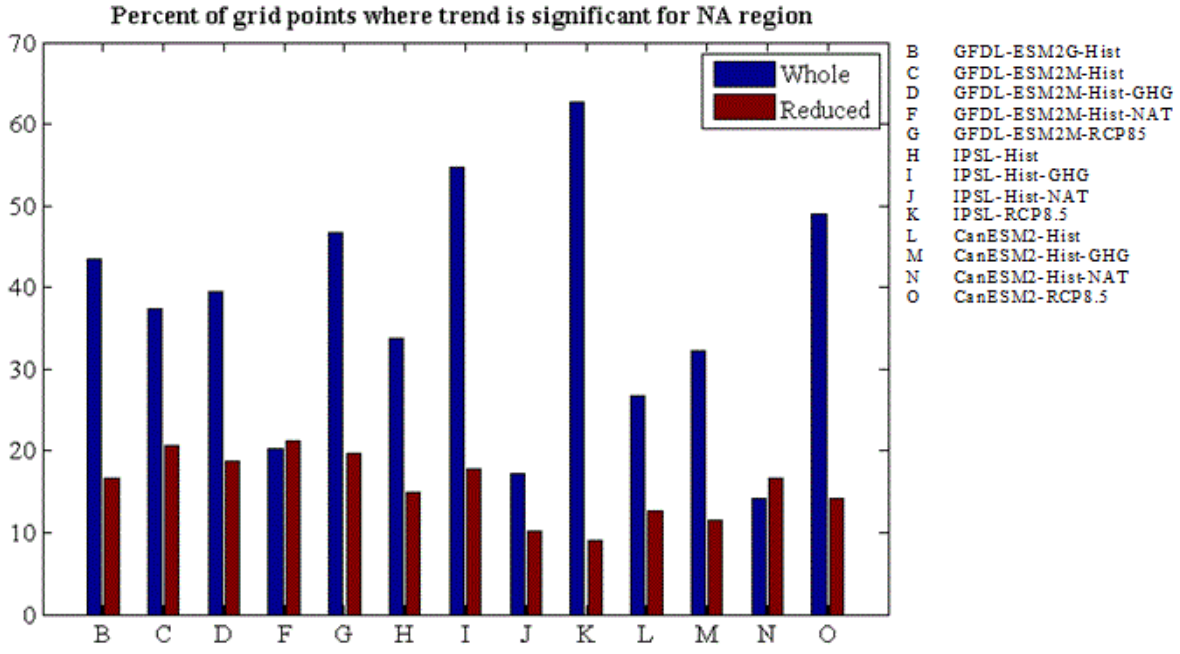

Figure 3-5. Percent of grid points in NA region where trend in chl is significant.

Similar comparison of percent of grid points from whole and reduced time period of model forced simulations has been made for other regions of the ocean as well (section 10.1 of Appendix IV). For most of the simulations percent of grid points from whole time period was higher than percent of grid points from reduced time period except IPSL historical natural simulation in SA, NP, SP and IO, CanESM2 historical natural in NP and ESM2M historical natural in IO. The results indicate that in some of the regions of the ocean historical natural simulations give a higher percent of significant grid points for reduced time period. This may be because the short time series happens to coincide with a period of strong monotonic natural variability, eg, El Niño to La Niña transition. Therefore, except for these simulations, the possibility of climate change detection from whole time period of simulations will be higher than the reduced time period of simulations.

3.4.2. Comparison of linear trend from model simulations with NOBM data

Spatial linear trend i.e. linear trend at each grid point was computed from the model forced simulations and from NOBM. Before implementing the OF method using these datasets, it is important to know how these modelled signals relate to observations.

Results for North Atlantic Region

Spatial linear trend for NA region from NOBM and greenhouse gas simulations of the reduced time period of model simulations is shown in Figure 3-6. Spatial linear trend from greenhouse gas simulations is chosen as an example for visual comparison because this is the signal that is of interest in this detection study. White spaces in the maps indicate grid points where there was no data from the model output. Location of these white spaces is different for each model as the maps were made before cross-multiplication of output from climate models with NOBM model output, for implementing the optimal fingerprint method. Visual comparison of the spatial trends from model simulations (Figure 3-6 b, c & d) indicates that there is partial

consistency in the signals obtained from the same model forcing simulation from different models. For example, increasing trend observed in north-eastern part of NA from CanESM2 (Figure 3-6 d) is also observed partially in spatial linear trend from ESM2M (Figure 3-6 b) and IPSL (Figure 3-6 c). Also, comparison of signals from model simulations (Figure 3-6 b, c & d) with NOBM (Figure 3-6 a) indicates that for some simulations patterns are similar to NOBM at some grid points but are completely opposite at other grid points. For example, declining trend observed in north-eastern part of NA from NOBM (Figure 3-6 a) is also observed in spatial linear trend from IPSL-Hist-GHG (Figure 3-6 c), but from CanESM2-Hist-GHG (Figure 3-6d) shows an increasing trend in north-eastern part of NA.

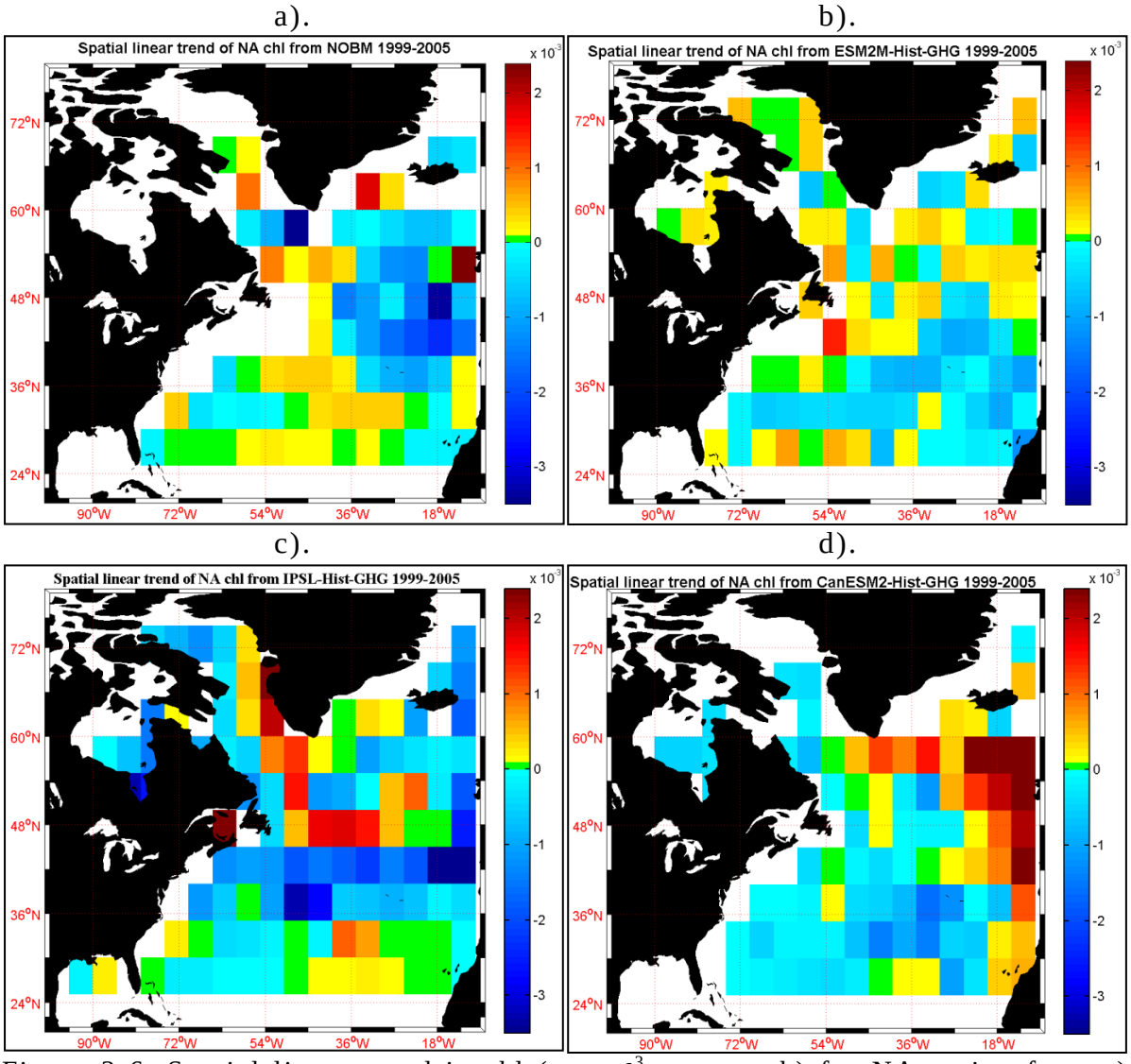

Figure 3-6. Spatial linear trend in chl (mg m^{-3} per month) for NA region from a). NOBM and reduced time period of b). GFDL-ESM2M Historical GHG c). IPSL Historical GHG and d). CanESM2 Historical GHG simulations. White spaces indicate gap in the data.

Statistical terms of comparison between spatial linear trend from model simulations and NOBM that were computed are correlation coefficient, centered root mean square difference and amplitude of the variation i.e. standard deviation The results are presented in the form of a Taylor Diagram (Taylor, 2001) (Figure 3-7). Table of values associated with the Figure are presented in (Table 10.1 in Appendix IV). Figure 3-7a shows statistical terms of comparisons when spatial linear trend was computed from whole time period of simulations. Figure 3-7b shows statistical terms of comparisons when spatial linear trend was computed from reduced time period of simulations.

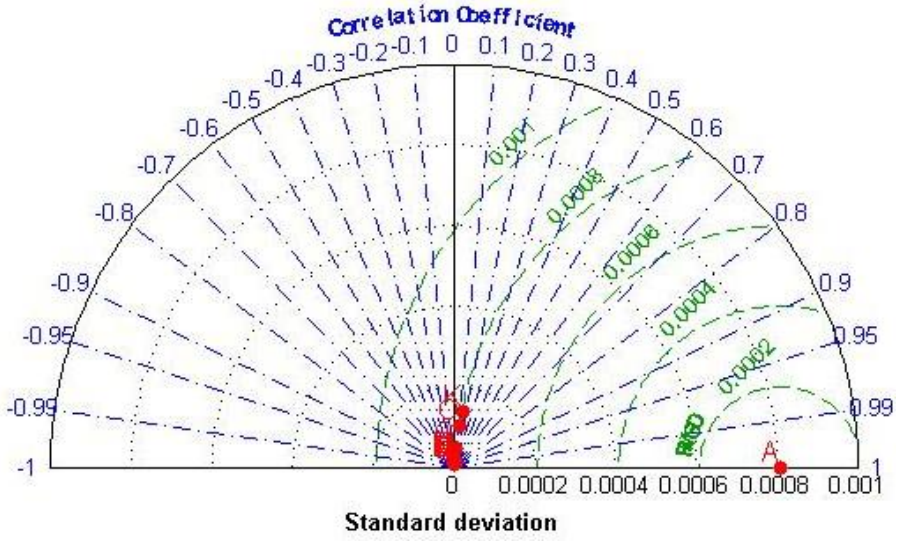

a).

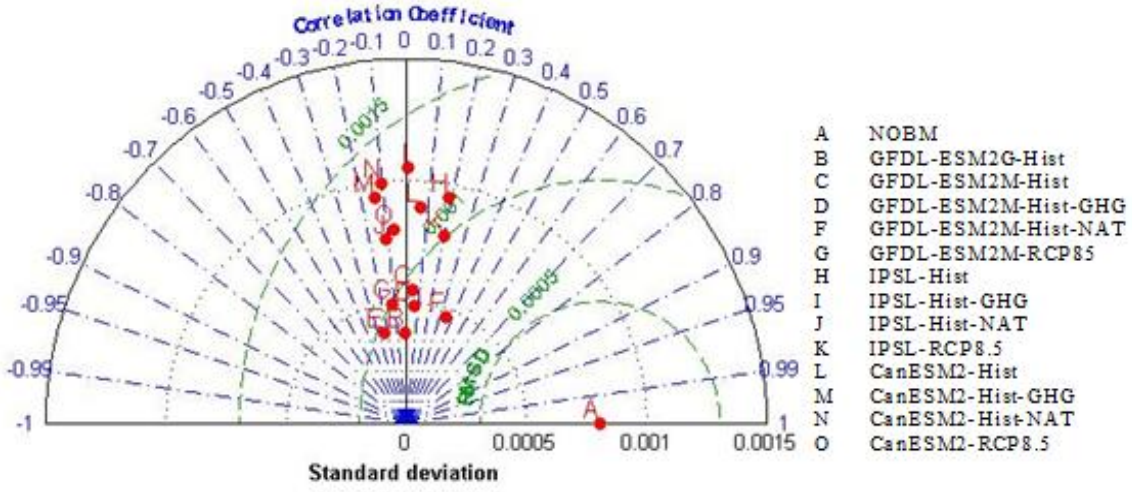

b).

Figure 3-7. Taylor diagrams associated with the comparisons of spatial linear trend for NA region computed from a). whole time period of simulations b). reduced time

period of simulations with spatial linear trend for NA region computed from NOBM.

From Figure 3-7, it can be seen that the correlation coefficient for all the model simulations is low (-0.2547 to 0.3477 in this study). Low correlation coefficient indicates that the spatial linear trend from model simulations is not correctly phased with NOBM. For most of the simulations correlation coefficient changes sign and magnitude for the two time periods for which linear trend is computed. This indicates that signal from whole time period of data is not the same as the reduced time period of data and they should be treated as two different metrics of signal computation. It should also be noted from Figure 3-7 that there is only partial consistency in the sign of correlation coefficient obtained from same forcing simulation from different models. For example, correlation coefficient obtained for whole time period of historical greenhouse gas simulation from ESM2M and IPSL model is negative but for CanESM2 model correlation coefficient is positive.

From Figure 3-7, it can also be seen that the standard deviation of all the model simulations is lower than NOBM for the 'whole time period'. On the other hand, for the reduced time period, standard deviation for some model simulations is larger than NOBM. The difference between the standard deviations of NOBM and model simulations for the whole time period (10^{-4}) is higher compared to the difference between the standard deviations of NOBM and the model simulations for the reduced time period (10^{-5}). From this it can be concluded that the amplitude of the spatial linear trend from the 'whole time period' of model simulations underestimates the amplitude of the spatial linear trend of chl and the 'reduced time period' of model simulations gives a much closer estimate to the amplitude of the spatial linear trend from NOBM.

Similar comparison of data has been made for other regions of the ocean as well and the result of the comparisons are presented in section 10.2 of Appendix IV. In summary it can be said that

- Signals (spatial linear trend) from model forcing simulations are not consistent with each other. This is indicated in the visual comparison of signals where increasing/decreasing trends observed in a part of an ocean region from one model simulation are not observed in another model simulation. Also, increasing/decreasing trends observed in a part of an ocean region from NOBM are not seen in all model simulations. Thus, there is lack of consistency in the signals from different models.
- Correlation coefficient between signal from NOBM and signals from both the time periods of model simulations is low for all the regions of the ocean. This indicates that model simulations are not correctly phased with observations. Low values of the correlation coefficient also indicate that it might be difficult to detect the signal from forcing simulations in the observations.
- For most of the model simulations correlation coefficient changes sign from whole to reduced time period of simulations. This indicates that signals from whole and reduced time period of simulations are not the same and are to be treated as different metrics of signal computation.
- For all the regions of the ocean, standard deviation of all the signals from model simulations for both the time periods is lower than standard deviation of signal from NOBM. This indicates that model simulations underestimate the amplitude of the spatial linear trend of chl.

3.4.3. Dimension reduction of noise component

One of the keys to detection of a signal is to reduce the dimensions of the elements of the OF method i.e. observations, model forcing simulations and noise from model control simulation. Reduced dimension of the datasets increases the signal-to-noise ratio and hence the possibility of signal detection increases. Dimension is reduced in several ways such as by reducing the spatial and temporal resolution of the datasets and selecting a limited number of empirical orthogonal functions to represent the data. Reduction of dimension needs to be done in a balanced way so as to not lose the relevant information and also to not increase the complexity by keeping more dimensions than necessary in the data. Out of the three elements of OF

method, noise/internal variability is the most complex element and its accurate estimation is significant in signal detection. For chl, internal variability cannot be derived from observations due to lack of long-term chl data and therefore it is computed from model control simulations. EOF analysis is used to reduce the dimension of the noise matrix. The methodology is described in step 3 of section 2.3 of this chapter. In this method, the noise matrix is reconstructed using a reduced number of eigenvectors known as the level of truncation.

Percent of EOFs chosen to reconstruct the noise covariance matrix for all the regions using model forced simulations for the 'whole time period' and the 'reduced time period' ranges from 4.9 to 48.91 (Table 10.6 of Appendix IV) and the variance represented by the chosen number of EOFs ranges from 96.14 to 100. This shows that more than 50% of the eigenvectors can be removed from the noise covariance matrices which reduces the dimension of the noise matrix considerably.

3.4.4. Consistency of internal variability

Due to lack of long-term homogeneous chl data, internal variability/noise is computed from the model control simulations. Accurate estimation of the noise is a crucial element to detection of a signal. If noise from the model simulations is underestimated or overestimated, significance of the estimated values of the scaling factors of the forcing signals in the observations would be questionable. Therefore, consistency check on the noise covariance matrix computed in step 2 of section 2.3 is performed. If the test fails then it indicates that the noise term is not accurate. If the test passes it indicates that the noise term has been estimated properly. Table 3-3 below shows result of the F-test for each OF method implementation i.e. signal detection for each region of the ocean using the forced model simulations. In the Table, passing of the test is represented as 'P' and failing of the test is represented as 'F'. Simulations for which the consistency test passes, are highlighted by green color.

Table 3-3. F-test result for each OF implementation. 'P' indicates Pass and 'F' indicates Fail. Green box indicates simulations where consistency test passes.

Model Simulation	**NA**		**SA**		**NP**		**SP**		**IO**	
	W	**R**	**W**	**R**	**W**	**R**	**W**	**R**	**W**	**R**
B	F	F	F	F	F	F	F	F	F	F
C	F	F	F	F	F	F	F	F	F	F
D	F	F	F	F	F	F	F	F	F	F
F	F	F	F	F	F	F	F	F	F	F
G	F	F	F	F	F	F	F	F	F	F
H	F	F	**P**	**P**	F	F	F	F	F	F
I	**P**	F	**P**	**P**	F	F	**P**	F	F	F
J	F	F	F	F	F	F	**P**	F	F	**P**
K	F	F	**P**	F	**P**	F	**P**	F	F	F
L	F	F	F	F	F	F	F	F	F	F
M	F	**P**	F	F	F	F	F	F	**P**	**P**
N	F	F	F	F	F	F	F	F	**P**	**P**
O	P	F	F	F	F	F	F	F	**P**	F

From Table 3-3 above it is seen that the internal variability is not consistent for most of the model simulations. This may be due to several reasons : inaccurate representation of noise from the control run; the control run itself may not represent the internal variability of the chl accurately and residuals may contain influence of the external forcing. Inaccurate internal variability affects the detection results as removal of noise is an important aspect of the OF method. It might lead to the failure of signal detection by the OF method as the signal-to-noise ratio may not be high enough to be detected. Therefore, possibility of a positive scaling factor i.e. detection of a signal would be high for the model forcing simulations for which the consistency test of the noise covariance matrix passes (highlighted in green above). Positive scaling factor may also be determined for the simulations for which the consistency test fails. However, inaccurate estimation of internal variability would tend to underestimation of the uncertainties in the estimated scaling factors. Therefore, only those model simulations for which

both the consistency test is passed (Table 3-3) and a positive and statistically significant beta is obtained should be considered to have detected a signal.

3.4.5. Detection of signals

Optimal fingerprint method described in section 2.3 is applied to evaluate the detection of observed changes in response to external forcings. Statistically significant scaling factors (β) determined as a result of the fingerprint analysis are indicative of the detection of an external signal in observations. Scaling factors are considered to be significant when their values are positive and their confidence intervals are different from 0. In the case where the scaling factor is negative it indicates that the signal is not detected. There may be several reasons for a negative scaling factor. First, there is no climate change signal present in the observations. Second, the signal-to-noise ratio is not strong enough to be detected. This may be due to misrepresentation of the noise from the control run. Third, there may be too much small-scale variability in observations for them to be compared to the smoothed model fields.

Scaling factors obtained as a result of the implementation of the OF method in spatial linear trend of chl in NA region of the ocean (using spatial linear trend from model forced simulations as the signal) is shown in Figure 3-8.

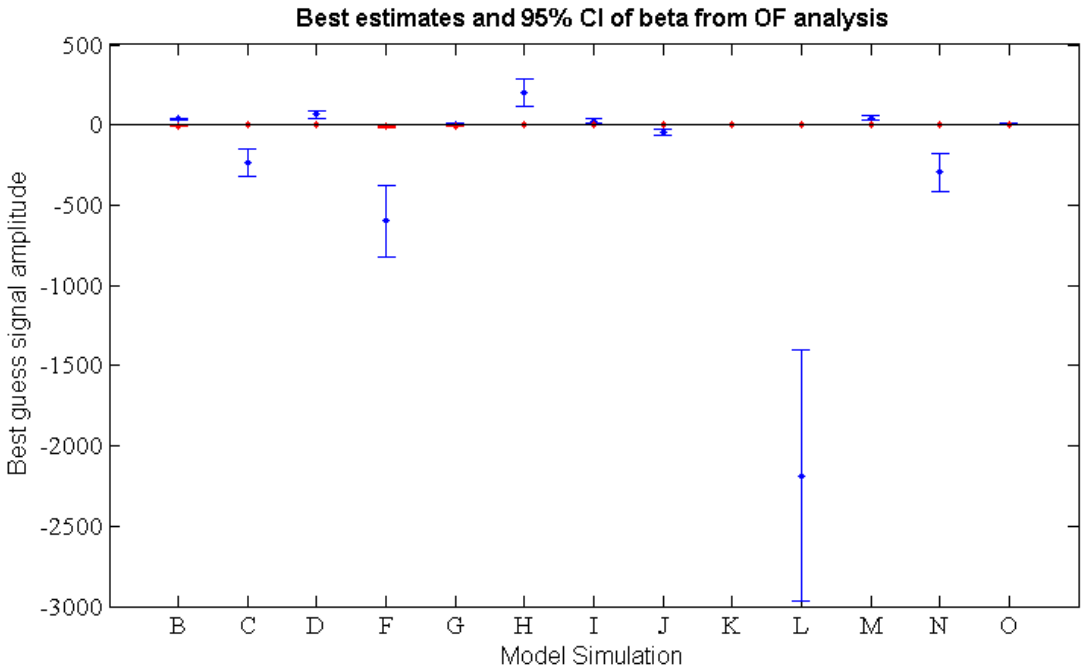

a).

B GFDL-ESM2G-Hist
C GFDL-ESM2M-Hist
D GFDL-ESM2M-Hist-GHG
F GFDL-ESM2M-Hist-NAT
G GFDL-ESM2M-RCP85
H IPSL-Hist
I IPSL-Hist-GHG
J IPSL-Hist-NAT
K IPSL-RCP8.5
L CanESM2-Hist
M CanESM2-Hist-GHG
N CanESM2-Hist-NAT
O CanESM2-RCP8.5

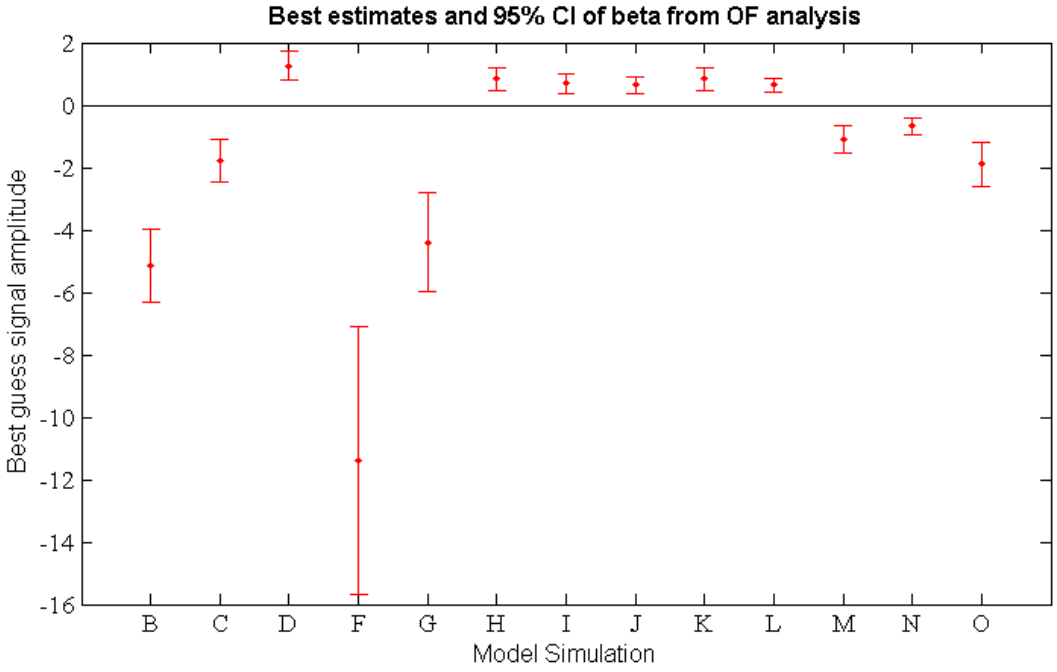

b).

Figure 3-8. Graph of signal amplitude along with the Confidence Interval (CI), obtained for OF implementation in NA region using signals from whole and

reduced time period of model simulations. a). result for both whole (blue) and reduced (red) time period of model simulations used to compute the signal. b). result for only reduced time period of model simulations.

Table associated with Figure 3-8 is given in (Table 10.7, Appendix IV). Figure 3-8 above shows the beta values obtained in NA region for signals obtained from model forced simulations along with the confidence interval (CI) associated with each beta value. For the whole time period of model simulations, it can be seen from the Figure 3-8a (blue dots and CI lines) that positive beta values are obtained for signals from whole time period of GFDL-ESM2G historical, GFDL-ESM2M historical GHG, GFDL-ESM2M RCP8.5, IPSL historical, IPSL historical GHG, IPSL RCP8.5, CanESM2 historical GHG and CanESM2 RCP8.5 simulations. This indicates that signals from these model simulations are detected in the observations. For the reduced time period of model simulations, it can be seen from Figure 3-8b (red dots and CI lines) that positive beta values are obtained for signals from reduced time period of GFDL-ESM2M historical GHG, IPSL historical, IPSL historical GHG, IPSL historical natural, IPSL RCP8.5 and CanESM2 historical simulations. As there is no consistency in the estimation of scaling factor values from the four models, it is difficult to judge the result of the detection of a signal from particular model simulation in the observations. For example, for the signals from the whole time period of model simulations, positive scaling factors are obtained for historical simulation from GFDL-ESM2G and IPSL models. For the other two models (GFDL-ESM2M and CanESM2) scaling factors are negative. Thus, it is difficult to conclude the detection result of the signal from historical forcing simulation in the observations.

Significance of the scaling factors for the simulations for which the consistency test failed (Table 3-3) is questionable and therefore, only those results are considered significant where the consistency test passed. Thus, the graph below (Figure 3-9) shows results for the OF implementation using the signals from the model simulations where the consistency test passed.

Simulations from whole and reduced time period of model simulations is represented with a 'W' and 'R' respectively.

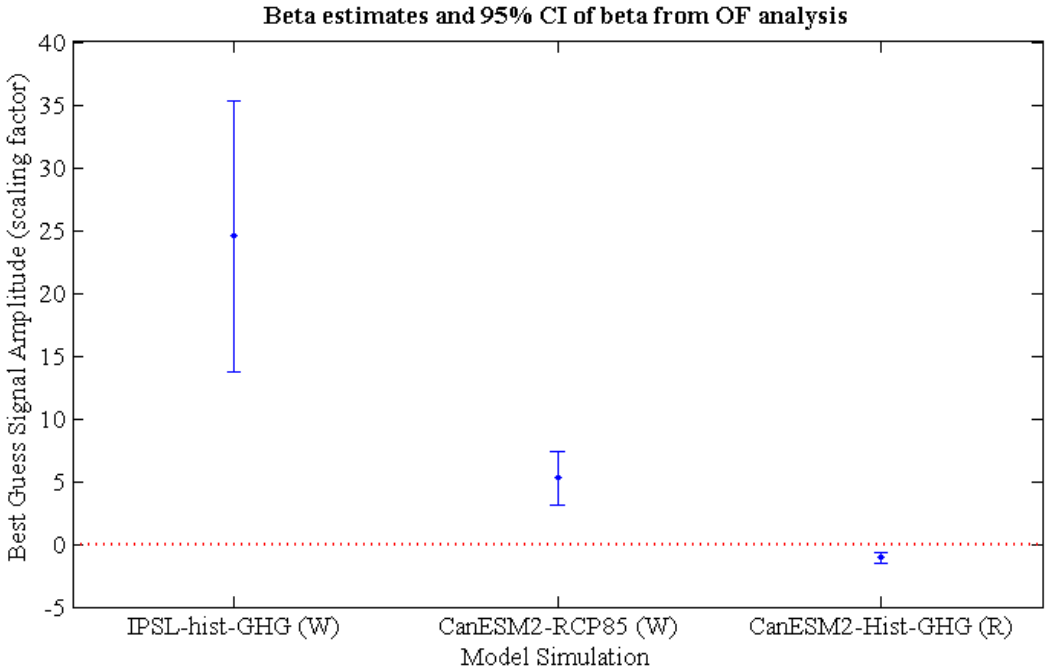

Figure 3-9. Scaling factor and their 5-95% CI for signals from model forced simulations for which consistency test passes in NA region.

As it can be seen from the Figure 3-9 above, scaling factors for whole time period of greenhouse gas simulation from IPSL model and RCP8.5 simulation from CanESM2 model is 24.516 and 5.253 which are significantly different from 0 with 5-95% confidence interval. This indicates that the effect of greenhouse gas forcing is detected in the observations and the effect of future emissions too is large enough to be detected. Since, the beta values are greater than unity, it can be inferred that the model simulated response of chl to external forcings is significantly underestimated and it needs to be amplified (by a factor of ~24 and ~5) to be consistent with observations. Trends from observations and model simulations for which signal is detected are shown in Figure 3-10. The difference in the scale of trends from observations and models is (10^{-1}). It can be observed that in the observations (Figure 3-10a) there is a declining trend in northeast region of NA which is also observed in RCP8.5 simulation from CanESM2 model (Figure 3-10c). On the other hand, in the greenhouse gas simulation from IPSL model (Figure

3-10b) there is a region of increasing trend in chl in northeast region surrounded by a region of decreasing trend.

a). b).

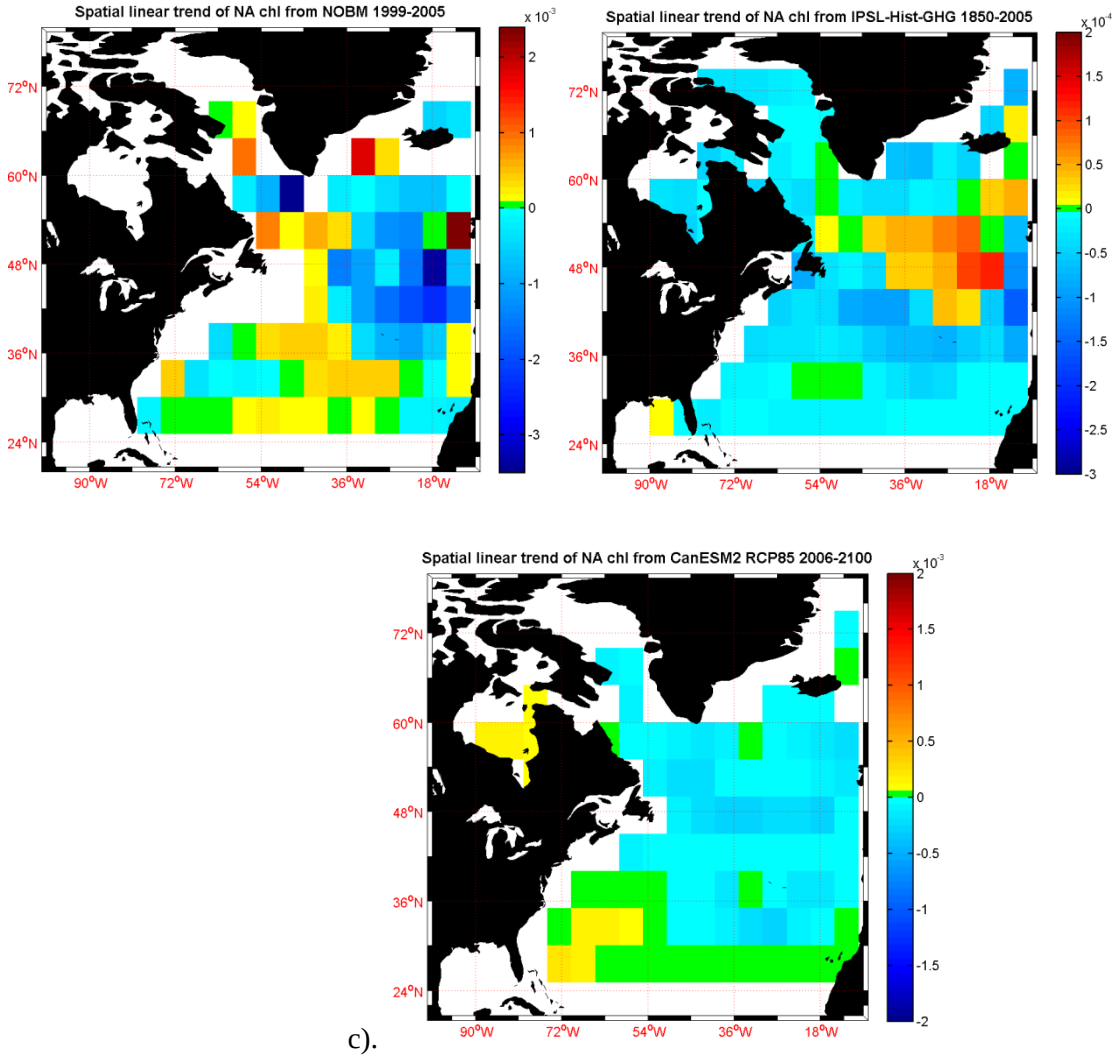

c).

Figure 3-10. Spatial linear trend of chl (mg m^{-3} per month) in NA region of the ocean from a). NOBM, b). whole time period of greenhouse gas simulation from IPSL model and c). whole time period of RCP8.5 simulation from CanESM2 model. b and c maps are from model simulations for which a signal is detected.

Results of the OF method of detection and attribution in other regions of the ocean are presented in section 10.4 of Appendix IV. The global map below (Figure 3-11) shows the model simulations for which the signal was detected in the regions of the ocean. Signals from whole and reduced time

period of model simulations are represented with a 'W' and 'R' at the end of their name.

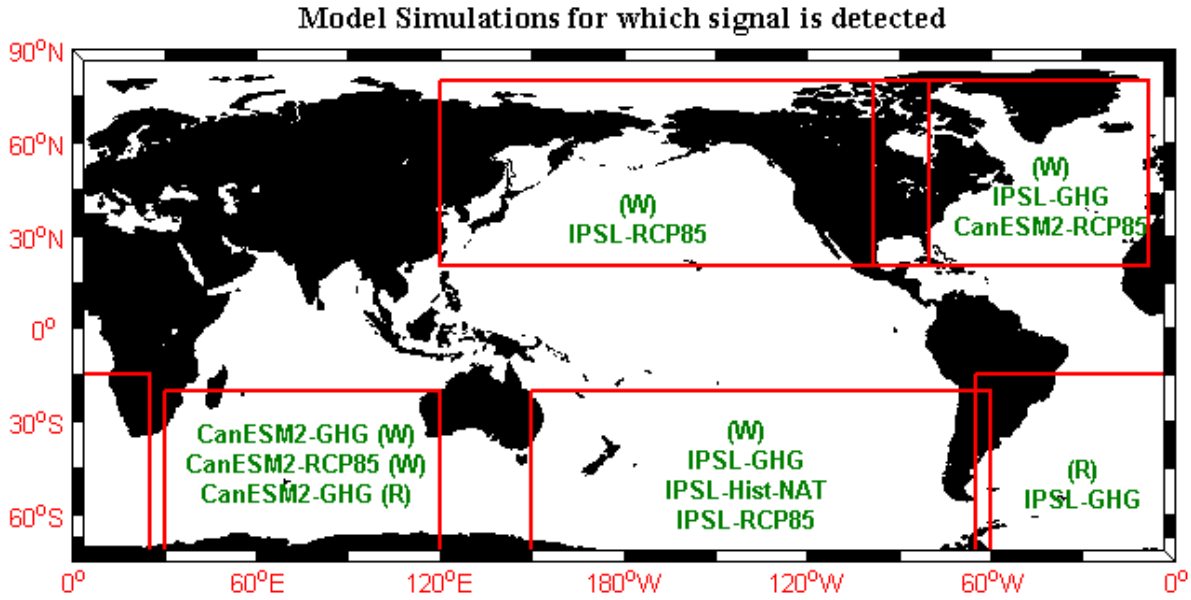

Figure 3-11. Global map showing the model simulations for which the signal was detected in the regions of the ocean

Summarizing the results of the OF analysis it is found that in SA region of the ocean signal from reduced time period of greenhouse gas simulation from IPSL model is detected. Scaling factor determined is 1.218 which is significantly different from 0 with 5-95% confidence interval. This indicates that the effect of greenhouse gas forcing is detectable in the observations. As the beta value is ~1, it can be inferred that model simulated response of chl to external forcing is consistent with observations. Trends from observations and model simulations for which signal is detected are shown in Figure 3-12. It can be observed that in the observations (Figure 3-12a) there is a declining trend in the lower latitudes and an increasing trend in upper latitudes. This pattern of spatial trends is also observed in greenhouse gas simulation from IPSL model (Figure 3-12b).

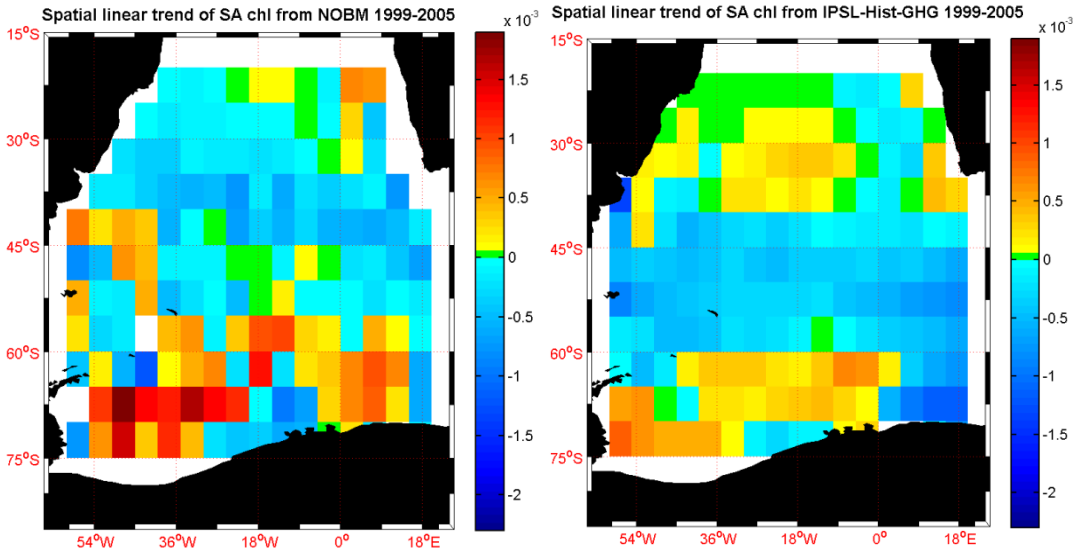

Figure 3-12. Spatial linear trend of chl (mg m^{-3} per month) in SA region of the ocean from a). NOBM and b). reduced time period of greenhouse gas simulation from IPSL model. b is map from model simulation for which signal is detected.

In NP region of the ocean, signal from whole time period of RCP8.5 simulation from IPSL model is detected. Scaling factor determined is 6.924 which is significantly different from 0 with 5-95% confidence interval. This indicates that the effect of future emissions is large enough to be detectable. Since, the beta value is greater than unity, it can be inferred that the model simulated response of chl to external forcings is significantly underestimated and it needs to be amplified (by a factor of ~6) to be consistent with observations. Trends from observations and model simulations for which signal is detected are shown in Figure 3-13. The difference in the scale of trends from observations and models is (10^{-1}). It can be observed that in the observations (Figure 3-13a) there is a declining trend in the higher latitudes and increasing trend in lower latitudes. On the other hand, in the RCP8.5 simulation from IPSL model (Figure 3-13b) the whole region has declining trend except for a small patch of increasing trend in chl.

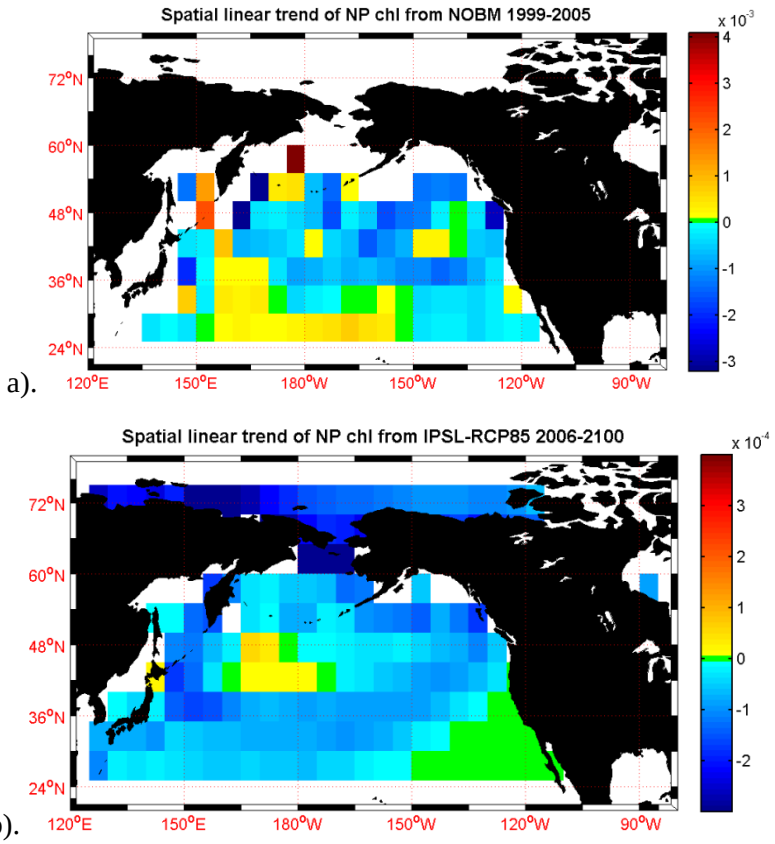

Figure 3-13. Spatial linear trend of chl (mg m^{-3} per month) in NP region of the ocean from a). NOBM and b). whole time period of RCP8.5 simulation from IPSL model. b is map from model simulation for which a signal is detected.

In SP region of the ocean, signal from whole time period of greenhouse gas, natural and RCP8.5 simulation from IPSL is 5.679, 19.524 and 3.129 respectively. As can be seen that the confidence intervals of the scaling factors are not different from 0 therefore it indicates that changes in the chl observations in SP region are also caused by internal variability. Trends from observations and model simulations for which signal is detected are shown in Figure 3-14. The difference in the scale of trends from observations and models is (10^{-1}). It can be observed that in the observations (Figure 3-14a) there is a increasing trend in most of the regions in SP except for a small region in higher latitudes where declining trend is observed. On the other hand, in model simulations (Figure 3-14b, c& d) a declining trend is observed in lower latitudes and an increasing trend is observed in higher latitudes.

a). b).

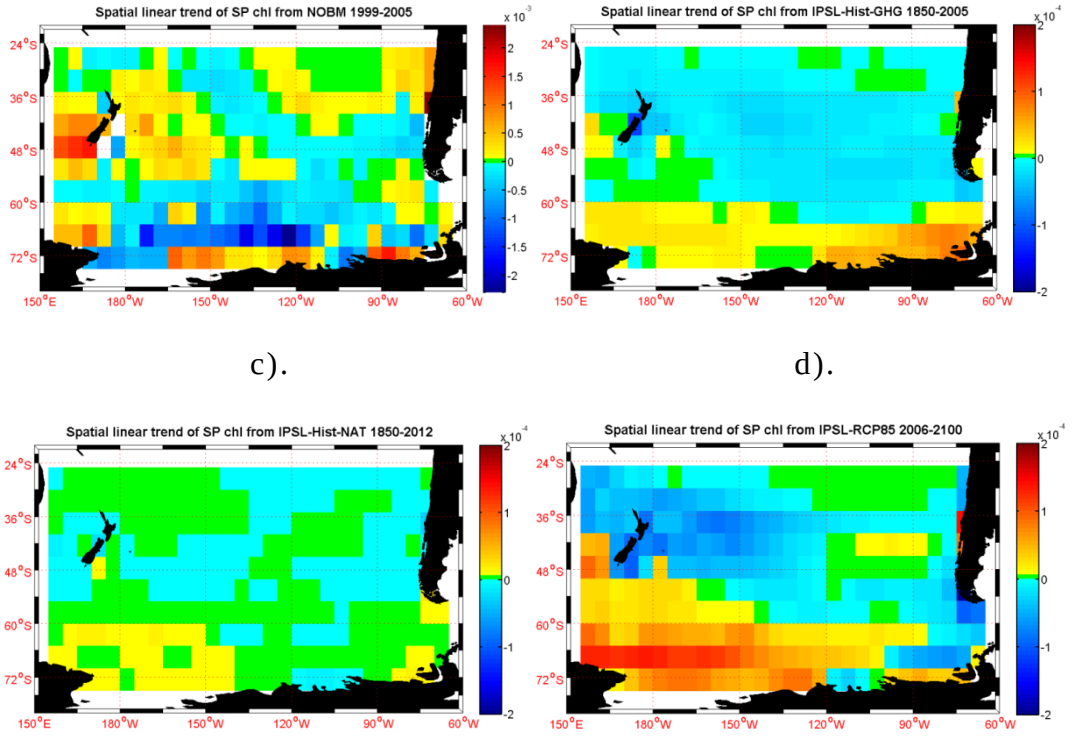

Figure 3-14. Spatial linear trend of chl (mg m^{-3} per month) in SP region of the ocean from a). NOBM, whole time period of b). greenhouse gas simulation c). natural forcing simulation and d). RCP8.5 simulation from IPSL model. b, c and d maps are from model simulations for which a signal is detected.

In IO region of the ocean, signals from whole time period of greenhouse gas and RCP8.5 simulation from CanESM2 model and reduced time period of greenhouse gas from CanESM2 model are 5.534, 1.524 and 0.352. As can be seen (Figure 10-15 in Appendix IV) that the confidence intervals of the scaling factors is not different from 0 therefore it indicates that changes in the chl observations in IO region are also caused by natural internal variability. Trends from observations and model simulations for which signal is detected are shown in Figure 3-15. From the Figure 3-15a & b it is observed that the pattern of increasing or decreasing trend is patchy in both NOBM and model.

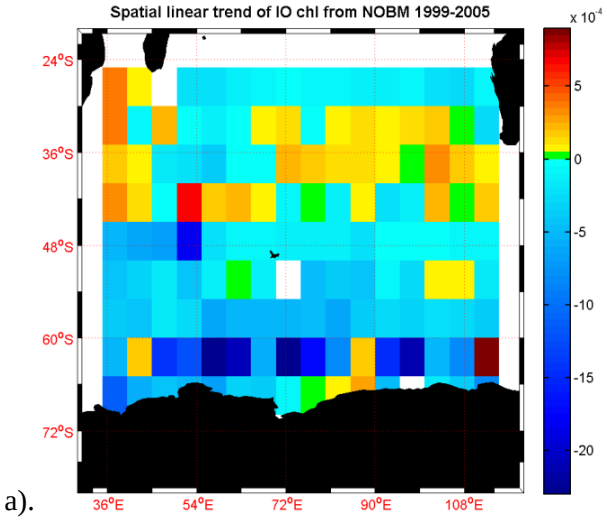

a).

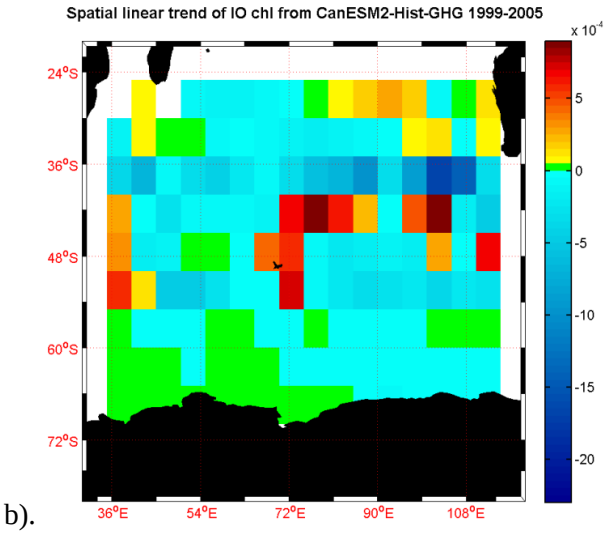

b).

Figure 3-15. Spatial linear trend of chl (mg m^{-3} per month) in IO region of the ocean from a). NOBM and whole time period of b). greenhouse gas simulation from CanESM2 model. b is map from model simulation for which signal is detected.

3.5. Discussion

This study presents, for the first time, an optimal fingerprint analysis detecting statistically significant changes in chl in the regions of the ocean, in response to external forcing, as different from internal variability. Chl concentration in the ocean is regulated by solar energy and nutrients available to phytoplankton for photosynthesis. Availability of solar energy and nutrients to phytoplankton is driven by mixing and water column stratification which are in turn driven by ocean circulation, wind patterns and surface ocean temperatures (Sarmiento et al. 2004). Impact of climate

forcings (natural or anthropogenic) on any of these parameters leads to an impact on chl in the water as well.

Several studies have investigated global trends in chl concentration (Gregg et al., 2003b, Gregg, 2005, Behrenfeld et al., 2006, Boyce et al., 2010). Boyce observed long-term trends in chl (1899 to 2008) by blending chl derived from transparency and direct in-situ optical measurements. Declining trend in chl was observed in eight out of ten ocean regions, and global rate of decline was estimated at 0.006 mg m^{-3} yr^{-1}, which is approximately 1% of the global median per year. The changes observed by Boyce were questioned (Mackas, 2011, Rykaczewski and Dunne, 2011, McQuatters-Gollop et al., 2011) but most other studies have also concluded that a decline in global average chl is occurring (Gregg et al., 2003b, Behrenfeld et al., 2006, Sommer and Lengfellner, 2008, Mackas, 2011). However none of the studies have distinguished between changes observed in chl due to internal variability and climate forcings. This study attempted to make this distinction by implementing optimal fingerprint method of detection and attribution in chl concentration in different regions of the ocean.

Spatial linear trend computed from whole time period of model simulations had more grid points where trend was significant than the spatial linear trend from reduced time period of model simulations. This indicates that the signal from the whole time period is stronger and hence the possibility of its detection in observations increases. This is reflected in the significant scaling factors estimated for the signals from model simulations. Only SA and IO (Figure 10-11 and 10-16 in Appendix IV) had signals detected from reduced time period of model simulations. Other regions of the ocean (Figure 10-14 in Appendix IV and Figure 3-9) had signals detected from the whole time period of model simulations. This indicates that the longer the time period from which signals are computed, the higher the signal-to-noise ratio and hence, the higher the possibility of signal detection. Also, longer time periods capture the change more accurately than shorter time periods.

Comparison of observations with model forcing simulations show that trend in chl from observations ranges globally from -0.0060 to 0.0041 (10^{-3}) mg m^{-3} per month which is much higher compared to the linear trend from model simulations which typically ranges from 10^{-4} to 10^{-5} mg m^{-3} per month. This shows that model simulations underestimate the trend in chl which is also reflected in the value of the scaling factors estimated for the trend in chl from model simulations. The reason for the underestimation of trends in chl may be that chl observations have too much small time-scale variability to be compared with smoother model fields or it may be due to model errors which cause weak signals from model forced simulations. The result of the comparison in all the chosen regions of the ocean show that correlation coefficient between trend obtained from model simulations and observations is very low (-0.5433 to 0.4206 in this study). Low correlation coefficient indicates that the strength of the signal from model simulations is very low signifying that the models don't do a good job of reproducing trends in data and hence it is challenging to detect the signal in observations. Also, there was no or partial consistency in the correlation coefficient obtained for same forcing simulation from different models or for signals from whole and reduced time period of model simulations indicating the uncertainties and unreliability of the spatial pattern of trends in chl obtained from climate models. Uncertainties in climate models can be removed to an extent by taking model ensemble mean. This may also improve the representation of noise from model control simulation.

Consistency check test of the internal variability/noise computed from the control simulations of GFDL-ESM2G and GFDL-ESM2M models failed for all the regions of the ocean and for all the signals from model forced simulations. However, consistency test of noise from control simulations of IPSL and CanESM2 model passed for some regions of the ocean and for some signals from model forced simulations. There are a number of potential explanations for failing of the consistency check. One possibility and the most probable cause is that there are elements of the observed chl variability which are not well captured by the model in the region of study. This is reflected in the results: for the same model simulation, the consistency check

of noise covariance passes in one region of the ocean but fails in another region. For example, for signal from whole time period of IPSL greenhouse gas simulation, consistency test for noise from IPSL control simulation passes in NA, SA and SP regions of the ocean but it fails in NP and IO regions (Table 3-3). This is indicative of the presence of external forcing in the residuals obtained from the linear regression i.e. the signal from model simulations does not capture the response of chl to external forcings accurately or response is not linear, or there isn't really a big trend. It is also concluded from here that representation of the noise matrix is accurate and the methodological choice made to compute the noise/internal variability is not the cause of biased results in different regions of the ocean from the same model simulation. Another possibility is that internal variability is not being estimated by the models accurately due to model errors or uncertainties. Due to failure of the consistency check, significance of the scaling factors estimated for the signals from model forced simulations is dubious. Therefore, results for only those simulations were considered significant where consistency check for noise covariance matrix passes.

Detection of the signal from model forced simulations is indicative of the patterns of change observed in the signal being present in observations as well. The magnitude of the pattern of change is represented by the deviation of the scaling factor from unity. In NA region, patterns of spatial linear trend from whole time period of greenhouse gas and RCP8.5 simulation from IPSL model are detected in the observations (Figure 3-10b). From Figure 3-10 it is observed that in NA region, there is a patch in the northeast region of subtropical and mid-latitudes (40-50^{o}N & 13-45^{o}W) where there is an increasing trend surrounded by region of decreasing trend. Also, decreasing trend in chl is observed in sub-tropical latitudes in NA (25-40^{o}N). These observed trends due to greenhouse gases were predicted by Doney (2006) (Figure 1.4). Increase in water surface temperature due to greenhouse gases would increase stratification and reduce mixing and hence the supply of nutrients to the upper ocean waters decreases, leading to a decrease in chl concentration. On the other hand, increased water surface temperature in higher latitudes results in shallowing of the mixed layer, which increases the

light availability to phytoplankton and hence chl concentration increases. This relationship of water column stratification to chl concentration in the water has also been observed in other studies (Behrenfeld et al., 2006).

In SA region, pattern of spatial linear trend from reduced time period of greenhouse gas simulation from IPSL model is detected in the observations (Figure 3-12b). From the Figure 3-12b it is observed that in SA region, a declining trend in chl occurs in sub-polar and mid-latitudes (40-60^{o}S) and an increasing trend is observed in sub-tropical (25-30^{o}S) and sub-polar to polar latitudes (60-75^{o}S). Declining trends in mid to high latitudes again may relate to the changes in stratification of the water column due to increased water temperature. However, increasing trends observed in low latitudes are not as expected in relation to the increased stratification due to increase in water temperature. This may be due to increase in the nitrogen fixing phytoplankton in these regions which may lead to increased chl concentration (Capone et al., 1997, Carpenter and McCarthy, 1975, Turk et al., 2011) however the models used here don't include these parameters (except GFDL) so the particular mechanism at work in the model is unclear. Another reason may be due to influx of nutrients in the upper ocean from some external source such as saharan dust or river input (Gallisai et al., 2014, Hamza et al., 2011, Ye et al., 2011, Resing and Barrett, 2014, Subramaniam et al., 2008).

In NP region, pattern of spatial linear trend from whole time period of RCP8.5 simulation from IPSL model is detected in the observations (Figure 3-13b). Since signals from historical simulations are not detected in the observations, it indicates that either chl concentration in NP is not affected by external forcings or the signal is not strong enough to be detected. As signal from future emission scenario is being detected it indicates that the enhanced level of emissions in the future may impact chl concentration in the NP ocean. In conclusion, as of the present time, chl concentration is not being affected by external forcings in NP region of the ocean.

In SP region, pattern of spatial linear trend from whole time period of greenhouse gas, natural and RCP8.5 simulation from IPSL is detected in the observations (Figure 3-14). From Figure 3-14 it is observed that in SP region,

declining trend is observed in eastern sub-tropical and mid-latitude region (25-60^{o}S and 85-165^{o}W). Increasing trend in chl is observed in western region of sub-polar and mid-latitudes (45-75^{o}S). Since the signal from natural forcing simulation is also detected in the observations, it indicates that greenhouse gases alone are not responsible for the observed change and natural forcings (solar and volcanic) are also impacting chl concentration in SP region. Declining trends in lower latitudes and increasing trends in higher latitudes are again related to the change in stratification due to increased water temperature as predicted by Doney (2006).

In IO region, pattern of spatial linear trend from whole and reduced time period of greenhouse gas and RCP8.5 simulation from CanESM2 model is detected in the observations (Figure 3-15). From Figure 3-15 it is observed that the pattern of increasing or decreasing trend is patchy. For example, there is a patch of increasing trend in eastern mid-latitudes, then there is a patch of decreasing trend in north-western latitudes and south-eastern latitudes. This patchiness makes it difficult to judge the probable cause of the trends in chl. Figure 10-16 in Appendix IV, shows that confidence interval for the scaling factors is not different than 0. This indicates that changes observed in chl are caused due to internal variability too i.e. internal variability was not removed completely from the signals or observations.

The magnitude of the scaling factors where the signal from model forced simulations is detected is greater than unity for most of the simulations except for reduced time period of greenhouse gas simulation from CanESM2 model (Table 10-11 of Appendix IV). Scaling factors less than unity indicate that the response of chl to external forcings is being overestimated by models and scaling factors greater than unity indicate that the response of chl to external forcings is being underestimated by models (Saba et al., 2011, Seferian et al., 2013). Climate system is a complex system and models attempt to represent this system simply, therefore there may be some variability in chl which may be difficult to simulate and hence the trends in chl concentration are being underestimated by the climate models.

3.6. Summary and conclusions

The spatial linear trend of chl in different regions of the ocean was taken as the guess signal to detect climate change in chl. Linear trend was computed for two time periods i.e. 'whole' and 'reduced' of model simulations. Internal climate variability was computed from the control run of the models. Optimal fingerprint method was then used to suppress the noise in observations and the forced simulations of the models. This enhanced the signal-to-noise ratio and the possibility of the climate change signal to be detected increased. Conclusions made by the study are -

1. Longer time periods used for computing the spatial linear trend from model forced simulations capture the change in chl more accurately than trends computed from shorter time period.
2. Models perform poorly in simulating the response of chl to external forcings and the internal variability of chl.
3. Distinct patterns of change are not observed in the signals from the models simulations.
4. Changes observed in the detected signals in the regions of the ocean mostly indicate decline in chl trends in lower latitudes and an increasing trend in higher latitudes which follows the predicted trend in chl by Doney (2006).
5. Natural forcing signal from IPSL model is detected in SP region of the ocean indicating that natural forcings are contributing towards the change in chl observed in this region.
6. No forcing signal from any model is detected in NP region of the ocean but detection of the signal from RCP8.5 simulation of IPSL model shows the possibility of the signal being detected in the future.
7. Greenhouse gas forcing signal from IPSL model is detected in North Atlantic, South Atlantic and South Pacific and from CanESM2 is detected in Indian Ocean region. This indicates that anthropogenic forcings are contributing towards the change in chl observed in these regions.

4. Climate Change Detection and Attribution for Linear Trend of Zonal Average of Chlorophyll

In the previous chapter, the metric of climate change detection was taken as the spatial linear trend of chl. The results of detection and attribution from two of the four models were considered insignificant as the consistency test failed for those models. A consistency test can fail due to several reasons; one is that the residuals may contain the influence of the external forcing; second is inaccurate estimation of the internal variability; third is that there are elements of the observed chl variability which are not well captured by the model. Another reason for failing to detect a signal or failing the consistency test for noise can be that the metric defined in chapter 3 (spatial linear trend) may not provide a distinct fingerprint of climate change in chl. Failure of a metric to capture climate change might be due to the small-scale variability present in the signal. This can be removed by reducing the dimension of the dataset spatially and temporally. Considering this, another metric was defined as the linear trend of the zonal average of chl in a region. Zonal average reduces the two-dimensional spatial chl values to one-dimensional values and linear trend reduces the time dimension; the signal produced is thus a one-dimensional vector. Zonal mean has been used before by studies in successfully detecting climate change in salinity (Terray et al., 2012) and oxygen (Andrews et al., 2012) fields.

This chapter mainly describes the results of the implementation of Optimal Fingerprint method when the guess signal is the linear trend of the zonal average of chl in a region. The first section of the chapter gives the details of the dataset used and the regions of the ocean where the signal is to be detected. For the purpose of presentation of results with clarity, North Atlantic region is used here as a case study. Results for other regions of the ocean are presented in the Appendix and the summary of those results is presented in the main chapter text. Second section of the chapter describes some of the basic statistics performed on the datasets for different regions of the ocean. Comparison of the results is made for different datasets and for different time periods. The third section of the chapter describes the methodology used to implement OF method on linear trend of zonal average

of data. Fourth section of the chapter is the results section along with the interpretation of the results. Fifth section summarizes the conclusions of the analysis.

4.1. Data

The datasets used for the analysis are as mentioned in chapter 2. As observations, chl from NOBM is used in the analysis and simulations from GFDL-ESM2G, GFDL-ESM2M, IPSL and CanESM2 models are used to compute the signal and the noise (Table 2.1). Regions of the ocean for which linear trend of zonal average of chl is computed are the same that were used in chapter 3 (see Table 3.1 and Figure 3.1). Also, as in chapter 3, each dataset i.e. observations and model simulations are represented by a letter of the alphabet (see Table 3.2).

The pre-processing steps in this chapter are the same as in chapter 3 (section 2.2) with the difference in the signal computation. Instead of computing the spatial linear trend as in chapter 3, linear trend of zonal average is computed in this chapter. Steps to compute linear trend of zonal average are as follows-

- Compute zonal average for each time step of the dataset.
- Compute linear trend at each grid point. This gives the linear trend of zonal average of chl from every dataset for each region of the ocean. Thus, the guess signal is obtained for the analysis from each model simulation.

For the forced run of the model, the linear trend of the zonal average is computed for two time periods. These are the same as described in chapter 3 i.e. the 'whole' and 'reduced' time period. Comparison of signals from all the forced model simulations is done with NOBM in a similar manner as in chapter 3.

After pre-processing of the datasets, OF method is implemented following the same steps as described in chapter 3 (see section 3) i.e. signal from observations and model simulations and noise from control run is

computed and input to the regression equation (eq 3.1) to solve for scaling factors i.e. β. Scaling factor values are obtained for all the model forced simulations in all the regions of the ocean. If positive beta value with confidence interval that exceeds zero is estimated, it is an indication of detection of the signal in the observations.

4.2. Results

4.2.1. Comparison of linear trend of zonal average from model simulations with NOBM data

Linear trend of zonal average i.e. linear trend at each grid point was computed from the model forced simulations and from NOBM. Before implementing the OF method using these datasets i.e. to detect the signals from model simulations in observations, it is important to know how these signals relate to observations. A comparison of linear trend of zonal average from the model simulations with linear trend of zonal average from NOBM was done.

Results for North Atlantic Region

Linear Trend of zonal average for NA region from NOBM and greenhouse gas simulations of the whole and reduced time period of model simulations is shown in Figure 4-1. Linear trend of zonal average from greenhouse gas simulations is chosen as an example for visual comparison because this is the signal that is of interest in this detection study. Trends from NOBM and reduced time period of simulations were 10 times higher than the trends from whole time period of simulations, therefore for clarity in presentation; trends from NOBM were plotted after dividing them by 10. From Figure 4-1 it can be seen that in observations (blue line in graph), the linear trend of zonal chl decreases in the mid-latitudes (35^o to 55^o N) in NA region. This decrease in trend is also observed in all the model forced simulations from whole time period (Figure 4-1a) and reduced time period (Figure 4-1b) but with a slight shift toward the south compared to the

observations. For example, the declining trend from whole and reduced time period of greenhouse gas simulation from IPSL is from 25^{o} to 50^{o} N which is shifted southward compared to the declining trend in NOBM (35^{o} to 55^{o} N). From Figure 4-1 it can also be seen that the pattern of trends from ESM2M-Hist-GHG and CanESM2-Hist-GHG follow each other closely in all the latitudinal zones. The pattern of trend from IPSL-Hist-GHG also follows the other two models except in northern latitudes (55^{o} to 65^{o}N) where the pattern is much more similar to the observations (NOBM). Thus, visual comparisons of the trends from model simulations indicate consistency between signals obtained from the same model forcing simulation from different models. Also, pattern of trends from model simulations are similar to patterns from NOBM. Statistical terms of comparison such as correlation coefficient are also computed and presented in the form of Taylor diagram (Figure 4-2).

a).

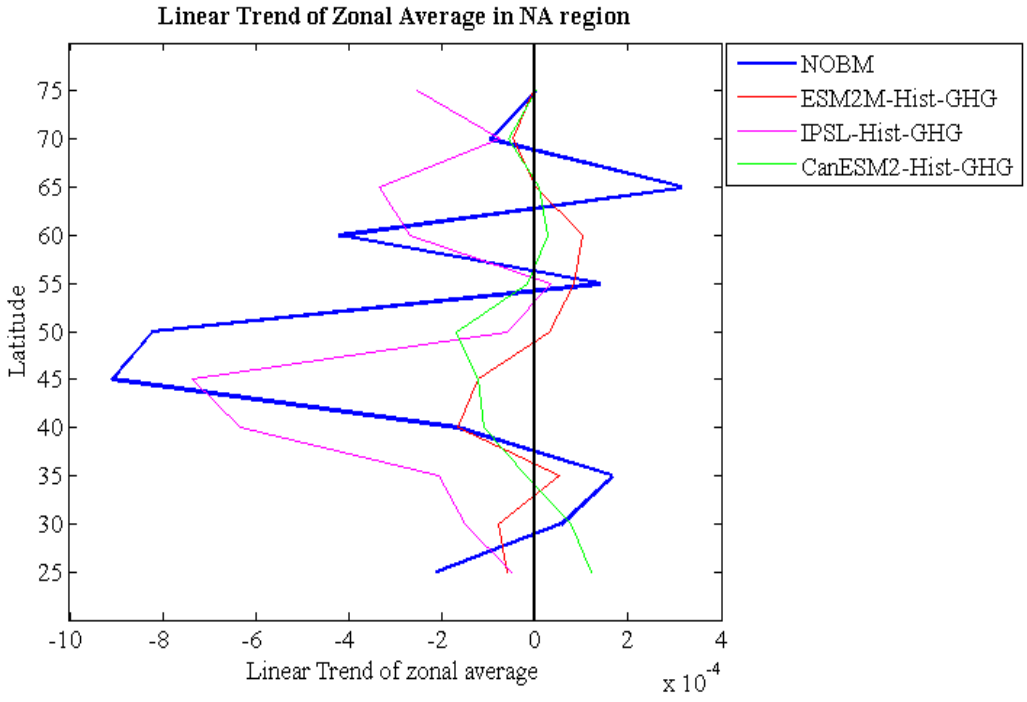

b).

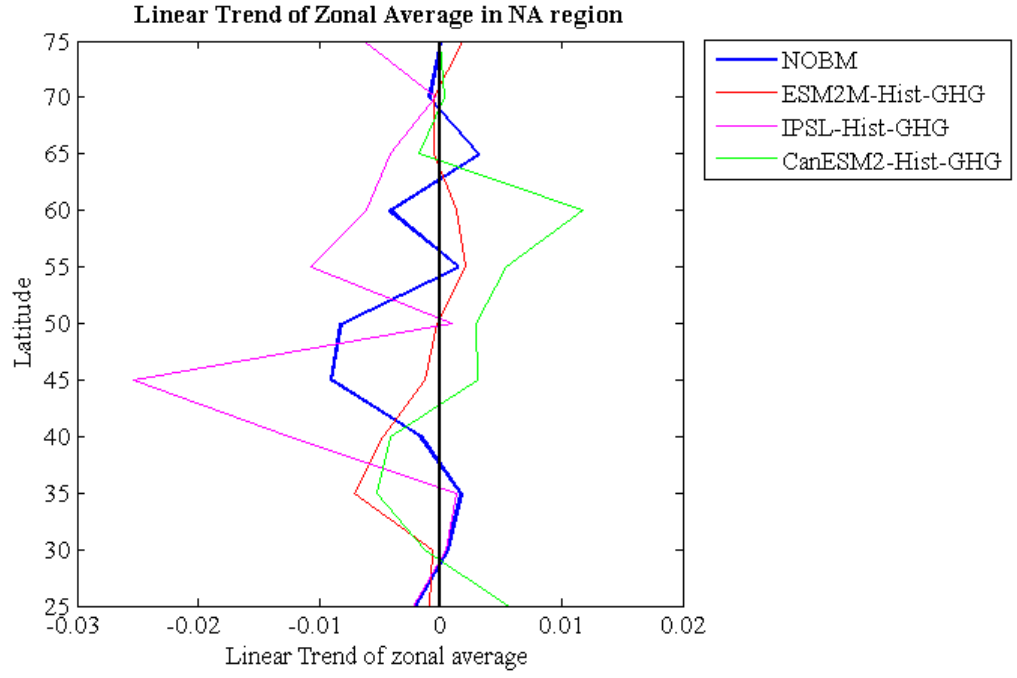

Figure 4-1. Linear Trend of zonal average (mg m^{-3} per month) for NA region from NOBM (data x 10^{-1}) and greenhouse gas simulations from models. a). Linear trend computed for whole time period and b). Linear trend computed for reduced time period.

Statistical terms of comparison between linear trend of zonal average from model simulations and NOBM that were computed are correlation coefficient, centered root mean square difference and amplitude of the variation i.e. standard deviation. Linear trend of zonal average for model

simulations was computed for two time periods i.e. whole and reduced. The results are presented in the form of a Taylor Diagram (Taylor, 2001) (Figure 4-2). Table of values associated with the Figure are presented in Table 1 of section 11.1 in Appendix V. Figure 4-2a shows statistical terms of comparison when linear trend of zonal average was computed from whole time period of simulations. Figure 4-2b shows statistical terms of comparison when linear trend of zonal average was computed from reduced time period of simulations.

a).

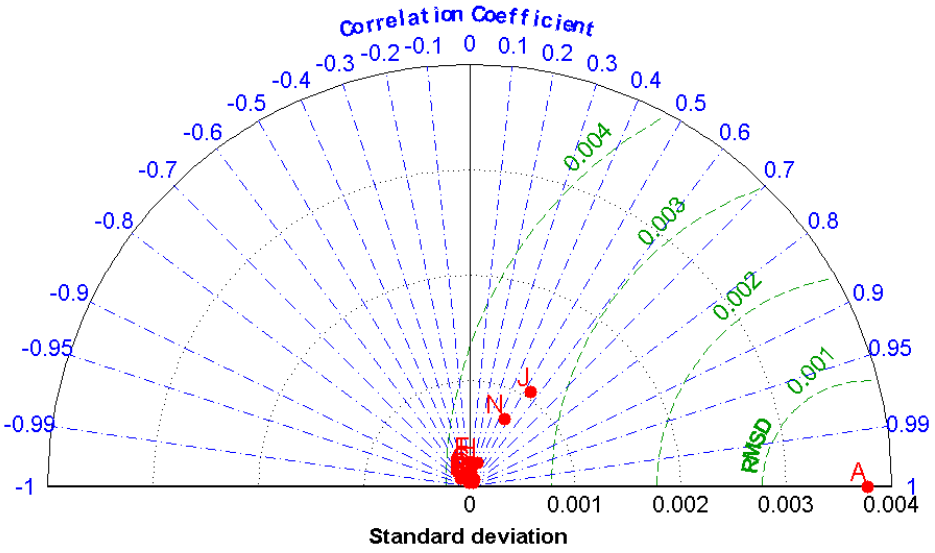

b).

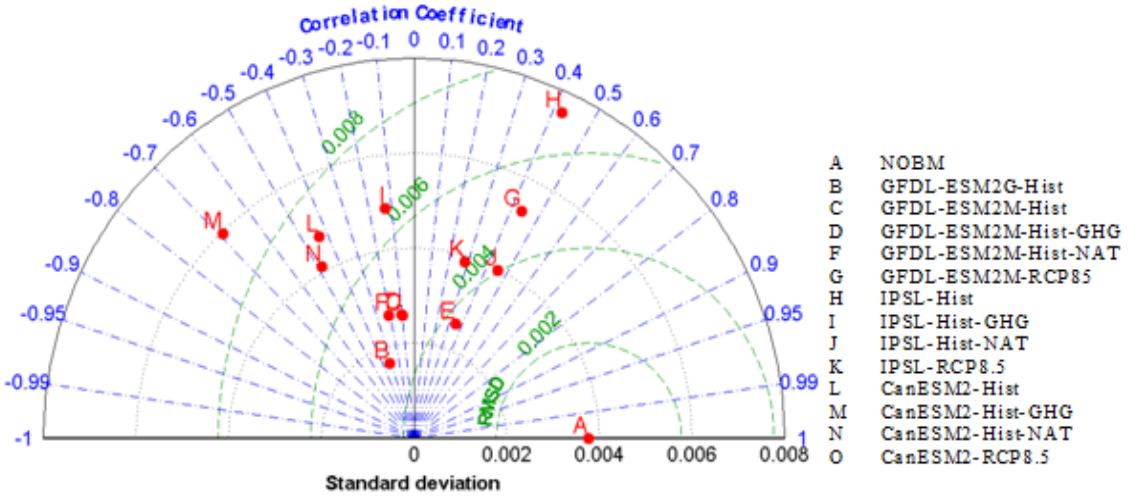

Figure 4-2. Taylor diagrams associated with the comparisons of linear trend of zonal average for NA region computed from a). whole time period of simulations and b). reduced time period of simulations, with linear trend of zonal average for NA region computed from NOBM.

From Figure 4-2, it can be seen that the correlation coefficient for all the model simulations is moderate (-0.74059 to 0.72513 in this study). This indicates that linear trend of zonal average from some model simulations is partially phased with NOBM. For most of the simulations correlation coefficient changes sign and magnitude for the two time periods for which linear trend is computed. This indicates that signal from whole time period of data is not the same as the reduced time period of data and they should be treated as two different metrics of signal computation. It should also be noted from Figure 4-2 that the sign of the correlation coefficient from same forcing simulation for different models is consistent for whole time period of simulations. For example, correlation coefficient obtained for whole time period of historical greenhouse gas simulation from ESM2M, IPSL and CanESM2 is positive but for reduced time period correlation coefficient is positive for greenhouse gas simulation from IPSL and is negative for greenhouse gas simulation from ESM2M and CanESM2.

From Figure 4-2, it can also be seen that the standard deviation of all the model simulations is lower than NOBM for the 'whole time period'. On the other hand, for the reduced time period, standard deviation for some model simulations is larger than NOBM. The difference between the standard deviations of NOBM and model simulations for the whole time period (10^{-3}) is higher compared to the difference between the standard deviations of NOBM and the model simulations for the reduced time period (10^{-5}-10^{-3}). From this it can be concluded that the amplitude of the linear trend of zonal average from the 'whole time period' of model simulations underestimates the amplitude of the linear trend of zonal average of chl from NOBM and the 'reduced time period' of model simulations gives a much closer estimate to the amplitude of the linear trend of zonal average from NOBM.

Similar comparison of data has been made for other regions of the ocean as well and the result of the comparisons are presented in section 11.1 of Appendix V. In conclusion it can be said that

- Signals (linear trend of zonal average) from model forcing simulations are consistent with each other. This is indicated in the visual comparison of signals where increasing/decreasing trends observed in a latitudinal zone from one model simulation are also observed in the pattern of trends from another model simulation. Also, increasing/decreasing trends observed in a latitudinal zone from NOBM are sometimes observed in pattern of trend from model forcing simulation from one model but are not observed in another model i.e. not all models agree with the observations.
- Correlation coefficient between signal from NOBM and signals from both the time periods of model simulations is high for all the regions of the ocean. This indicates that model simulations are correctly phased with observations. High value of correlation coefficient indicates increased possibility of the signal from forcing simulation to be detected in the observations.
- For most of the model simulations correlation coefficient changes sign from whole to reduced time period of simulations. This indicates that signals from whole and reduced time period of simulations are not the same and are to be treated as different metrics of signal computation.
- For all the regions of the ocean, standard deviation of all the signals from model simulations for both the time periods is lower than standard deviation of signal from NOBM. This indicates that model simulations underestimate the amplitude of the spatial linear trend of chl.

4.2.2. Dimension reduction of noise component

Dimension reduction of the noise covariance matrix is an important part of the OF method as noise or internal variability is the most complex element and its accurate estimation is significant in signal detection. The method to reduce the dimensions is described in chapter 3 (see section 2.3). In this method, the noise matrix is reconstructed using a selective number of eigenvectors known as the level of truncation. Percent of EOFs chosen to reconstruct the noise covariance matrix for all the regions using model forced simulations for the 'whole time period' and the 'reduced time period' ranges from 33.33 to 81.82 (Table 11-6 of Appendix V) and the variance represented

by the chosen number of EOFs ranges from 91.24 to 100. This shows that more than 20% of the eigenvectors can be removed from the noise covariance matrices.

4.2.3. Consistency of internal variability

Consistency test is done on the noise covariance matrix to determine if the internal variability estimated from model control simulations is accurate or not. Significance of the estimated values of the scaling factors of the forcing signals would be questionable if the consistency test fails for the noise computed from that model. The method to conduct the consistency test is described in chapter 3 (step 6 of section 2.3). Table 4-1 below shows result of the F-test for each OF method implementation i.e. signal detection for each region of the ocean using the forced model simulations. In the Table, passing of the test is represented as 'P' and failing of the test is represented as 'F'. Simulations, for which the consistency test passes, are highlighted in green.

Table 4-1. F-test result for each OF implementation

Model Simulation	**NA**		**SA**		**NP**		**SP**		**IO**	
	W	**R**	**W**	**R**	**W**	**R**	**W**	**R**	**W**	**R**
B	F	F	**P**	F	**P**	**P**	F	F	F	F
C	F	F	F	F	**P**	**P**	F	F	F	F
D	F	F	F	F	**P**	**P**	F	F	F	F
F	F	F	F	F	**P**	**P**	F	F	F	F
G	F	F	F	F	**P**	**P**	F	F	F	F
H	**P**	**P**	**P**	**P**	**P**	**P**	F	**P**	F	**P**
I	**P**	**P**	**P**	**P**	**P**	**P**	**P**	**P**	F	**P**
J	F	**P**	**P**	F	**P**	**P**	**P**	F	**P**	**F**
K	F	**P**	**P**	F	**P**	**P**	**P**	**P**	**P**	**P**
L	**P**	**P**	F	F	F	F	**P**	**P**	**P**	**P**
M	**P**	**P**	F	F	F	F	**P**	**P**	**P**	**P**
N	F	**P**	F	F	**P**	F	**P**	**P**	**P**	**P**
O	**P**	F	F	F	F	F	**P**	**P**	**P**	**P**

From Table 4-1 above it is seen that the internal variability is consistent for most of the model simulations except for ESM2G and ESM2M in NA, SA, SP and IO region of the ocean and CanESM2 in SA and NP region of the ocean. This may be due to several reasons: inaccurate representation of noise from the control run; the control run itself may not represent the internal variability of the chl accurately and residuals may contain influence of the external forcing. Inaccurate internal variability affects the detection results as removal of noise is an important aspect of the OF method. It might lead to the failure of signal detection by the OF method as the signal-to-noise ratio may not be high enough to be detected. Therefore, possibility of a positive scaling factor would be high for the model forcing simulations for which the consistency test of the noise covariance matrix passes (highlighted in green above). Positive scaling factor may also be determined for the simulations for which the consistency test fails. However, inaccurate estimation of internal variability would tend to underestimate the uncertainties in the estimated scaling factors. Therefore, only those estimated values of scaling factors would be significant for which the consistency test passes.

4.2.4. Detection of signals

Optimal fingerprint method described in section 2.3 is applied to evaluate the detection of observed changes in response to external forcings. Statistically significant scaling factors (β) determined as a result of the fingerprint analysis are indicative of the detection of an external signal in observations. Scaling factors are considered to be significant when their values are positive and their confidence intervals are different from 0. In the case where the scaling factor is negative it indicates that the signal is not detected. There may be several reasons for a negative scaling factor. First, there is no climate change signal present in the observations. Second, the signal-to-noise ratio is not strong enough to be detected. This may be due to misrepresentation of the noise from the control run. Third, there may be too much small-scale variability in observations for them to be compared to the smoothed model fields.

Scaling factors obtained as a result of the implementation of the OF method on linear trend of zonal average of chl in NA region of the ocean using linear trend of zonal average from model forced simulations as the signal are shown in Figure 4-3.

a).

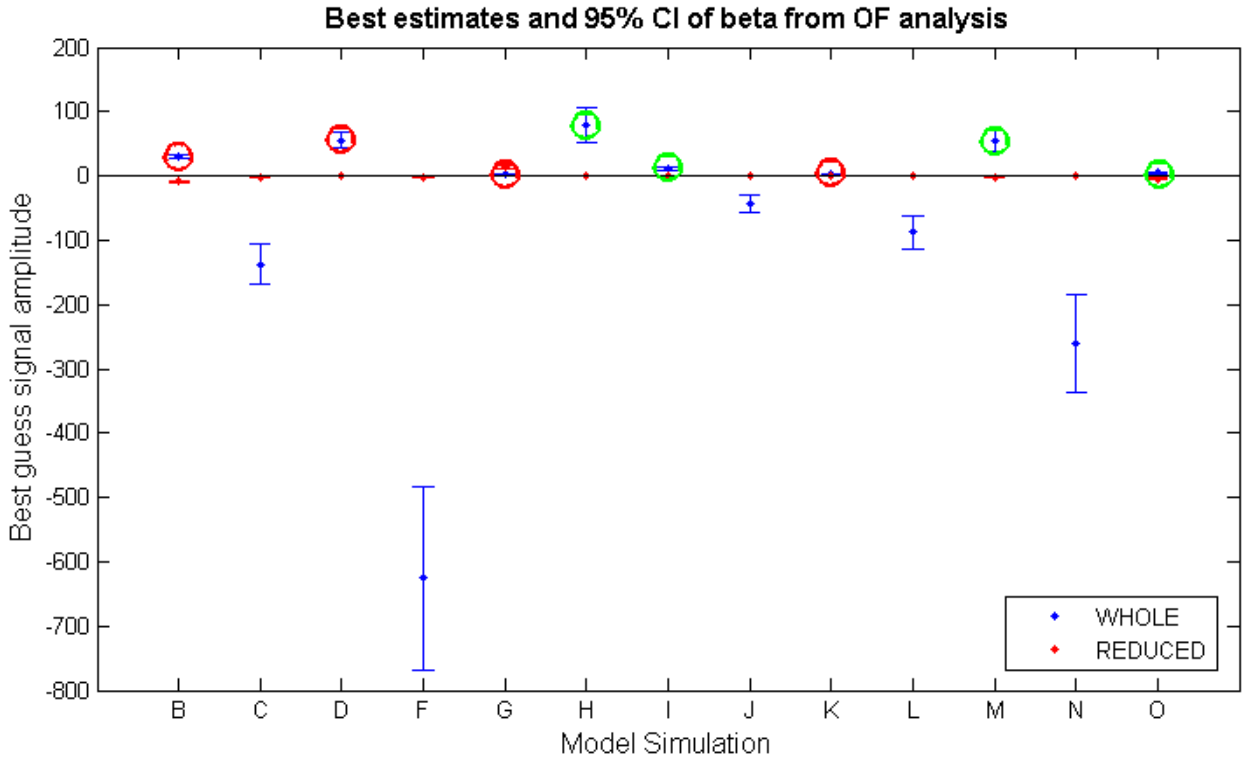

B	GFDL-ESM2G-Hist
C	GFDL-ESM2M-Hist
D	GFDL-ESM2M-Hist-GHG
F	GFDL-ESM2M-Hist-NAT
G	GFDL-ESM2M-RCP85
H	IPSL-Hist
I	IPSL-Hist-GHG
J	IPSL-Hist-NAT
K	IPSL-RCP8.5
L	CanESM2-Hist
M	CanESM2-Hist-GHG
N	CanESM2-Hist-NAT
O	CanESM2-RCP8.5

b).

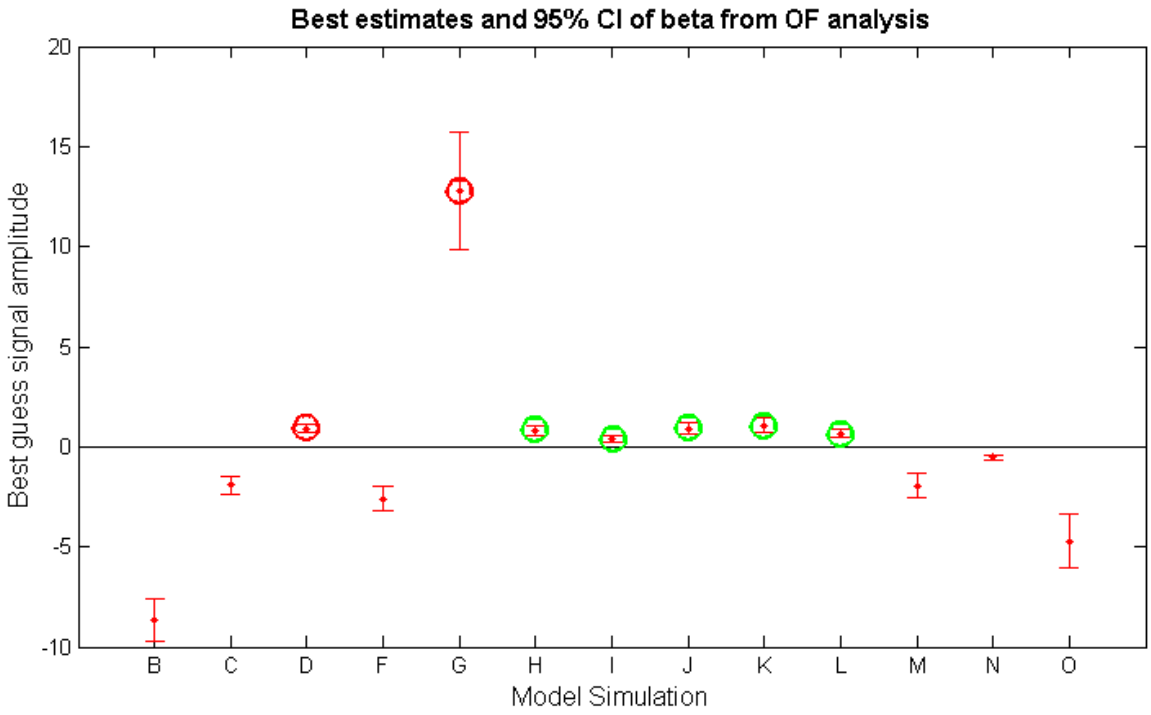

Figure 4-3. Graph of signal amplitude along with the confidence interval (CI) obtained for OF implementation in NA region using signals from whole and reduced time period of model simulations. a). Result for both whole (blue) and reduced (red) time period of model simulations used to compute the signal. b). Result for only reduced time period of model simulations. Green circles indicate scaling factors which are positive and are obtained for the simulations for which consistency test passed. Red circles indicate scaling factors which are positive and are obtained for the simulations for which consistency test failed. Circles in a) are drawn only for whole time period of simulations.

The Table of β values associated with Figure 4-3 is given in Table 7 of section 11-3 of Appendix V. Figure 4-3 shows the beta values obtained in NA region for signals obtained from model forced simulations along with the confidence interval (CI) associated with each beta value. For the whole time period of model simulations, it can be seen from Figure 4-3a (blue dots and CI lines) that positive beta values are obtained for signals from whole time period of GFDL-ESM2G historical, GFDL-ESM2M historical GHG and RCP8.5, IPSL historical, historical GHG and RCP8.5, CanESM2 historical GHG and RCP8.5 simulations. This indicates that signals from these model simulations are detected in the observations. For the reduced time period of

model simulations, it can be seen from Figure 4-3b (red dots and CI lines) that positive beta values are obtained for signals from reduced time period of GFDL-ESM2M historical GHG and RCP8.5, IPSL historical, historical GHG, historical natural and RCP8.5 simulations and CanESM2 historical. As there is no consistency in the estimation of scaling factor values from the four models, it is difficult to determine the result of the detection of a signal from a particular model simulation in the observations. For example, for the signals from the whole time period of model simulations, positive scaling factor is obtained for historical simulation from GFDL-ESM2G and IPSL model. For the other two models (ESM2M and CanESM2) scaling factors are negative. Thus, it is difficult to conclude that a historical GHG forcing signal has been detected in the observations.

Significance of the scaling factors for the simulations for which the consistency test failed (Table 4-1) is questionable and therefore, only those results are considered significant where the consistency test passed. Green circles in Figure 4-3 indicate scaling factors which are positive and are obtained for the simulations for which consistency test passed. Red circles in Figure 4-3 indicate scaling factors which are positive and are obtained for the simulations for which consistency test failed. As can be seen from Figure 4-3 above, scaling factors for whole time period of historical and historical greenhouse gas simulation from IPSL model and historical greenhouse gas and RCP8.5 simulation from CanESM2 model are 79.47, 10.75, 55.18 and 5.36 respectively, which are significantly different from 0 with 95% confidence. Also, scaling factors for reduced time period of historical, historical greenhouse gas, natural and RCP8.5 simulation from IPSL model and historical simulation from CanESM2 model are 0.77, 0.39, 0.91, 1.08 and 0.67 respectively, which are significantly different from 0 with 95% confidence. Thus, signal detection is not consistent between models for same forcing simulations but it is consistent between whole and reduced time period of simulations from all models. For example, historical simulation from whole time period and reduced time period of IPSL model is detected in observations but historical simulation from whole time period of CanESM2 model is not detected. Beta values are greater than unity for the whole time

period of model simulations, which implies that the model simulated response of chl to external forcings is significantly underestimated and it needs to be amplified (by a factor of ~79 to ~5) to be consistent with observations. Beta values are ~1 or less than unity for reduced time period of model simulations, which implies that the model simulated response of chl to external forcings is being overestimated and it needs to be decreased to be consistent with observations. Trends from observations and model simulations for which signal is detected are shown in Figure 4-4. Signals from whole and reduced time period of model simulations are represented as (W) and (R) respectively. Trends from whole time period of simulations are 10 times smaller than trends from NOBM and reduced time period of simulations. Therefore for observing the pattern of trends clearly, linear trend of zonal average from NOBM and reduced time period of model simulations is divided by 10 for plotting. From Figure 4-4, it can be seen that there is a declining trend in observations from 35-55^{o}N. This pattern is also observed in signals from model simulations except that for some simulations there is a slight shift in the declining trend zone either towards the north (eg. as in CanESM2-RCP8.5 in Figure 4-4c) or towards the south (eg. as in IPSL-Hist-GHG in Figure 4-4a). The scaling factor for signal from reduced time period of IPSL-RCP8.5 simulation is ~1 which is also seen in Figure 4-4c as the linear trend of zonal average from IPSL-RCP8.5 follows linear trend of zonal average from NOBM closely in pattern and magnitude. Thus, the pattern of the trends from model simulations is similar to that from NOBM with a slight latitudinal shift and difference in amplitude for some simulations. This was also observed by computing the correlation coefficient between NOBM and model simulations, which was found to be in the range of -0.7406 to 0.7251.

a).

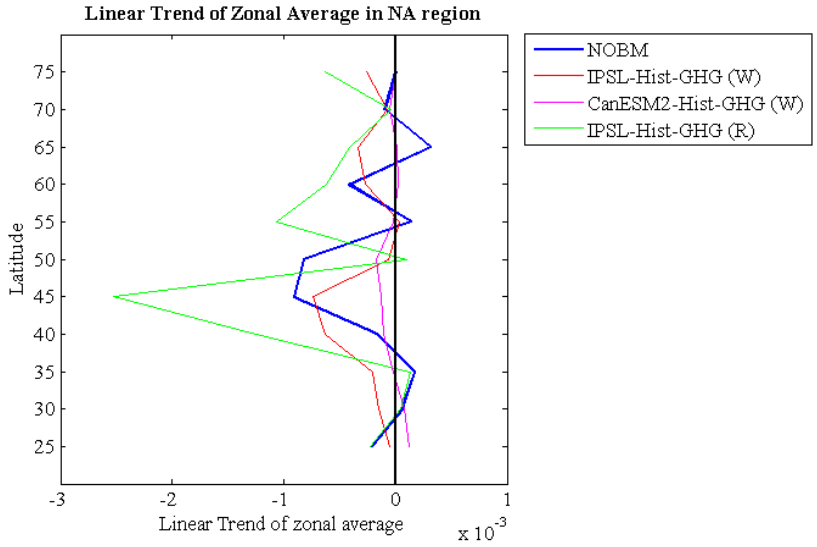

b).

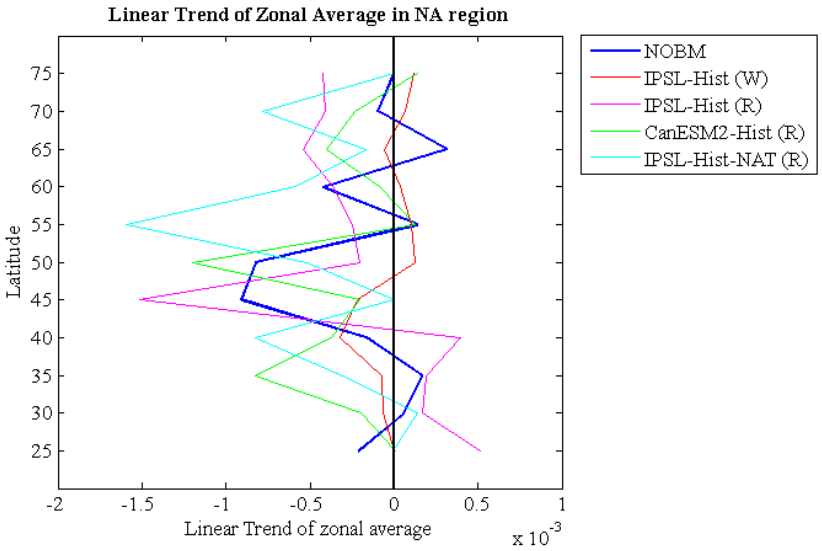

c).

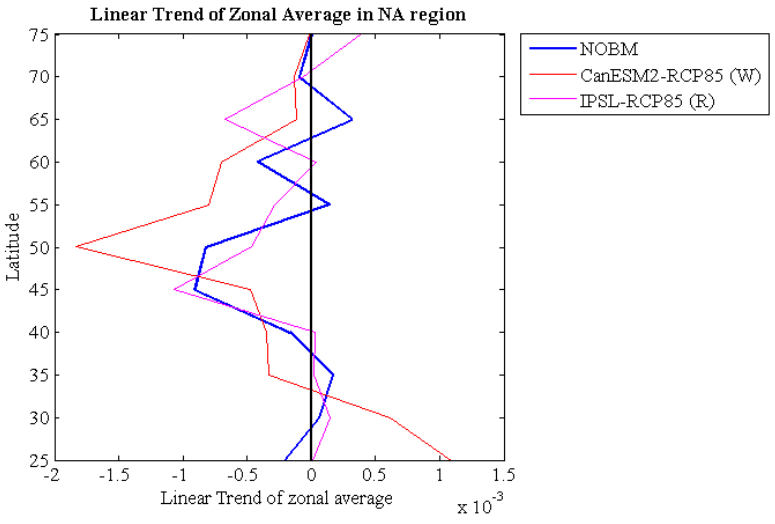

Figure 4-4. Linear trend of zonal average of chl (mg m^{-3} per month) in NA region of the ocean from NOBM and b). greenhouse gas simulation, b). historical and historical natural simulation and c). RCP8.5 simulation.

Results of the OF method of detection and attribution in other regions of the ocean are presented in section 11-3 of Appendix V. The global map below (Figure 4-5) shows the model simulations for which the signal was detected in the regions of the ocean. Signals from whole and reduced time period of model simulations are represented with a 'W' and 'R' at the end of their name.

a).

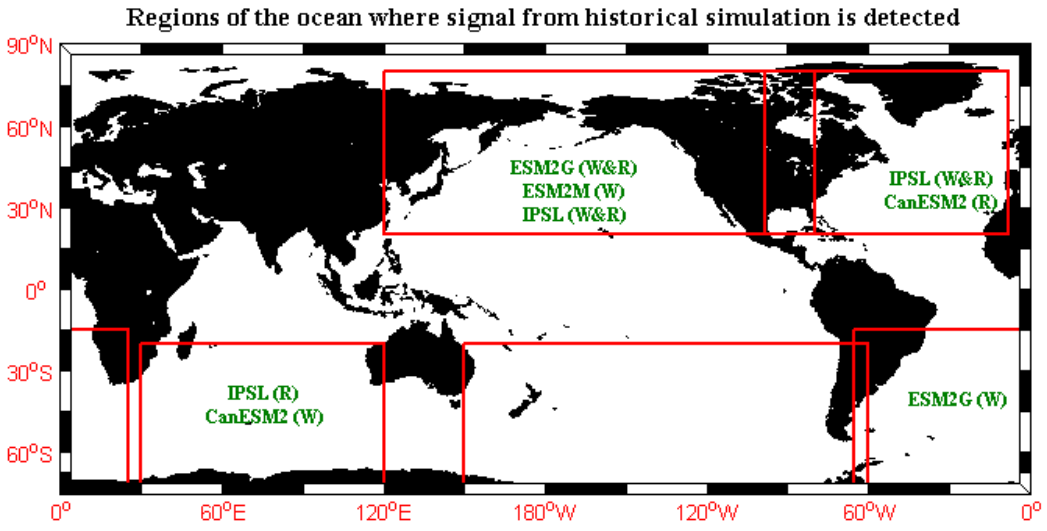

b).

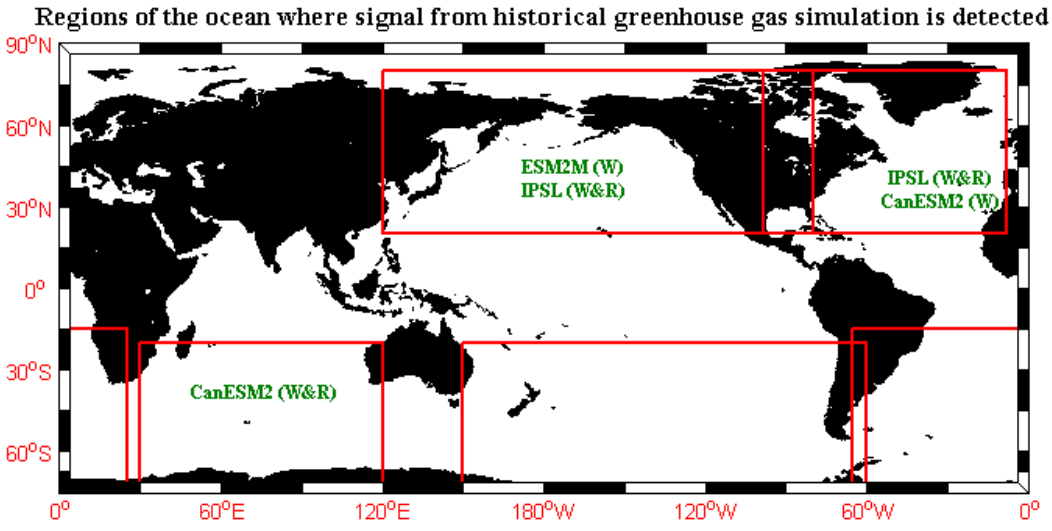

c).

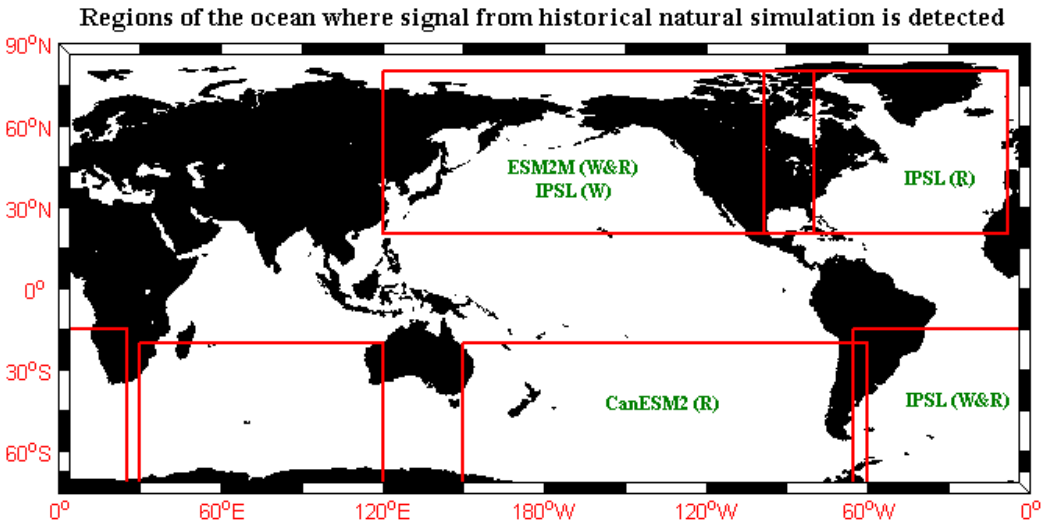

d).

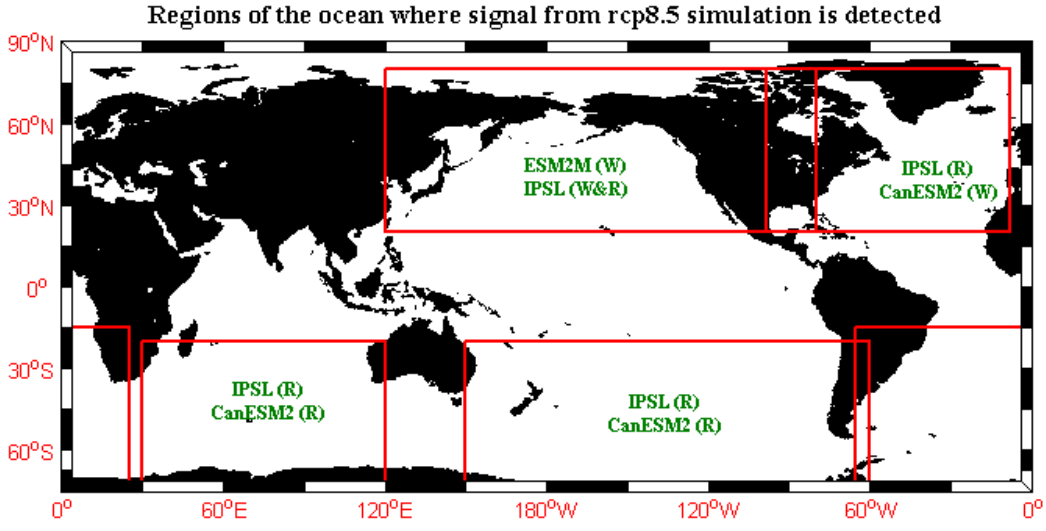

Figure 4-5. Global map showing the regions of the ocean where signals from a). historical, b). historical greenhouse gas, c). historical natural and d)RCP8.5 simulation of the models is detected. If a signal is blank, then no signals were detected in that from any model.

Summarizing the results of the OF analysis it is found that in SA region of the ocean signal from whole time period of historical simulation from GFDL-ESM2G model and historical natural simulation from IPSL model and reduced time period of historical greenhouse gas simulation from IPSL model are detected. Signal detection is not consistent between the models for any forcing simulation and is also not consistent between whole and reduced time period of simulations from the models. Beta values are greater than unity for whole time period of model simulations, which implies that the model simulated response of chl to external forcings is significantly

underestimated and it needs to be amplified (by a factor of ~30 and ~75) to be consistent with observations. Beta value is less than unity for reduced time period of model simulation, which implies that the model simulated response of chl to external forcings is overestimated and it needs to be decreased to be consistent with observations.

Trends from observations and model simulations for which signal is detected in the SA region is shown in Figure 4-6. Signals from whole and reduced time period of model simulations are represented as (W) and (R) respectively. Trends from whole time period of simulations are 100 times smaller than trends from NOBM and reduced time period of simulations. Therefore for observing the pattern of trends clearly, linear trend of zonal average from NOBM and reduced time period of model simulations is divided by 100 for plotting. From the Figure, it can be seen that there is an increasing trend in observations from -70 to -50^{o}S. This pattern is also observed in signals from model simulations except that for some simulations (ESM2G-hist (W) and IPSL-hist-NAT (W) there is a slight shift in the increasing trend zone towards the north. It is also observed that there is a declining trend in observations from -50 to -25^{o}S. This pattern is also observed in signals from model simulations from ESM2G-hist (W) and IPSL-hist-NAT (R). Thus, the pattern of the trends from model simulations is similar to that from NOBM with a slight latitudinal shift and difference in amplitude for some simulations. This was also observed by computing the correlation coefficient between NOBM and model simulations, which was found to be in the range of -0.6722 to 0.8370.

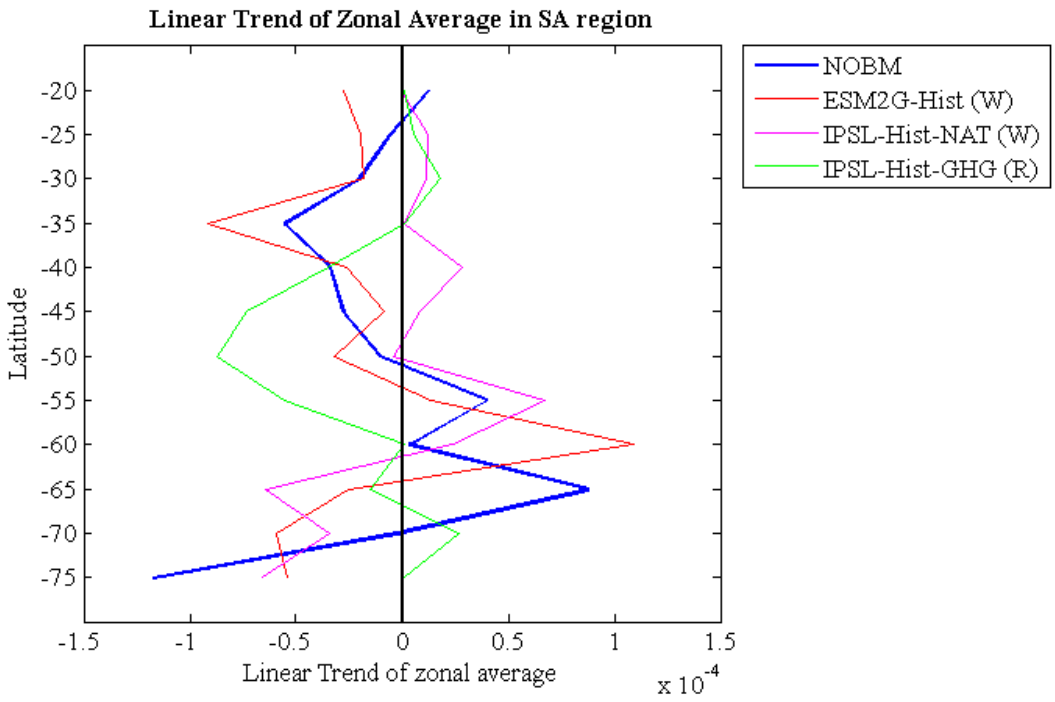

Figure 4-6. Linear trend of zonal average of chl (mg m^{-3} per month) in SA region of the ocean from NOBM and model forced simulations.

In NP region of the ocean, signal from the whole time period of all the forcing simulations from ESM2G, ESM2M and IPSL model and only historical natural simulation from CanESM2 model and reduced time period of ESM2G historical, ESM2M historical natural, IPSL historical, historical GHG and RCP8.5 simulations is detected. Detection of signal is consistent between the models from whole time period of forcing simulations but are not consistent from reduced time period of forcing simulations. Trends from observations and model simulations for which signal is detected is shown in Figure 4-7. From Figure 4-7, it can be seen that there is a declining trend from 35-60^{o}N. This pattern is clearly observed in signals from whole time period of historical simulation from ESM2G and ESM2M (Figure 4-7a), historical natural simulation from ESM2M and IPSL (Figure 4-7c), RCP8.5 simulation from IPSL (Figure 4-7d) and also from reduced time period of historical simulation from ESM2G (Figure 4-7a) and historical natural simulation from ESM2M (Figure 4-7c). From other model forcing simulation the declining pattern is not clearly evident but if the signal from model simulation is shifted either north or south, the declining trend may become evident. For example, if signal from whole time period of IPSL-GHG

simulation (Figure 4-7b) is shifted towards north, then the declining trend will be in the same latitudes as that in observations (NOBM) (Figure 4-7b). Thus, the pattern of the trends from model simulations are similar to that from NOBM but in some there is a slight latitudinal shift in the pattern and also there is a difference in amplitude of the trend from some model simulations. This was also observed by computing the correlation coefficient between NOBM and model simulations, which was found to be in the range of -0.7958 to 0.5220.

a). b).

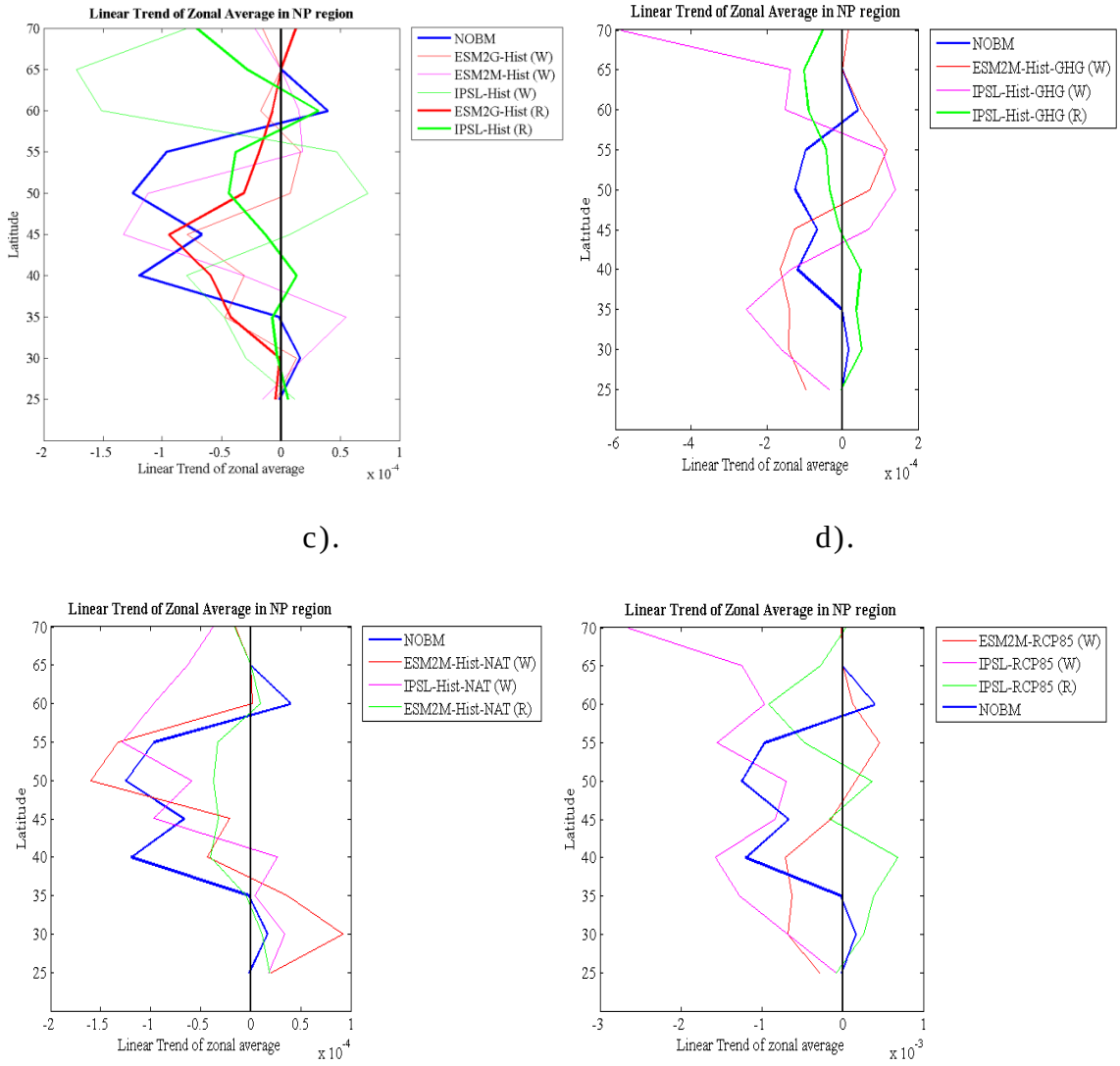

c). d).

Figure 4-7. Linear trend of zonal average of chl (mg m^{-3} per month) in NP region of the ocean from NOBM and a). historical, b). historical greenhouse gas, c). historical natural and d). RCP8.5 simulations from the model. Signals from NOBM and reduced time period of model simulations are divided by 100 before plotting.

In the SP region of the ocean, signal from reduced time period of IPSL RCP8.5 and CanESM2 historical natural and RCP8.5 simulations is detected. Detection of signal is consistent between the models from reduced time period of forcing simulations. Trends from observations and model simulations for which signal is detected are shown in Figure 4-8. From Figure 4-8, it can be seen that there is a declining trend from -70 to -52°N and an increasing trend from -52 to -25°S in observations. An increasing trend pattern is observed in trends from model simulations as well (Figure 4-8) but the declining trend pattern is observed only in IPSL-RCP8.5 simulation with a decline from -52 to -40°S. Thus, the pattern of the trends from model simulations is similar for some latitudinal zones to the pattern of trends from NOBM but is dissimilar for other latitudinal zones. This was also observed by computing the correlation coefficient between NOBM and model simulations, which was found to be in the range of -0.8140 to 0.5350.

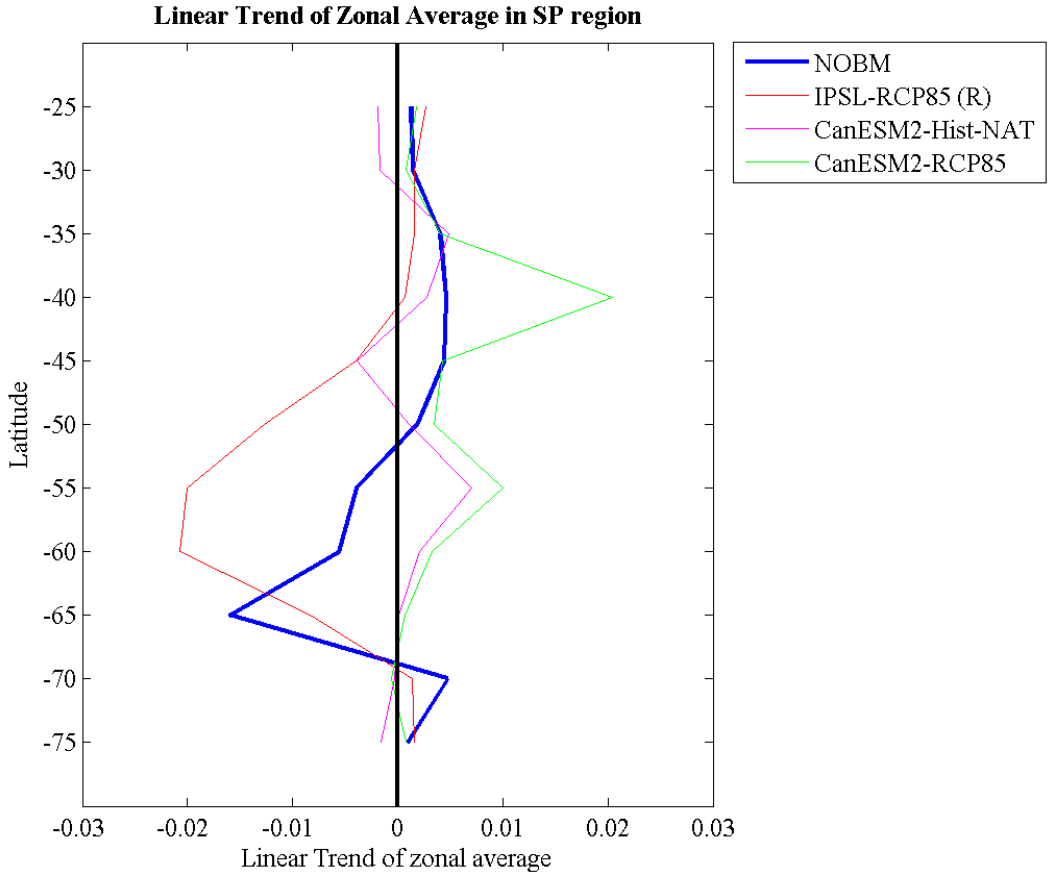

Figure 4-8. Linear trend of zonal average of chl (mg m^{-3} per month) in SP region of the ocean from NOBM and model forced simulations.

In IO region of the ocean, signal from whole time period of CanESM2 historical, historical GHG and RCP8.5 simulations and reduced time period of IPSL historical and RCP8.5 and CanESM2 historical GHG simulations is detected. Detection of signal is not consistent between the models from whole and reduced time period of forcing simulations. Trends from observations and model simulations for which signal is detected are shown in Figure 4-9. Trends from whole time period of simulations are 100 times smaller (except for CanESM2-RCP8.5 simulation) than trends from NOBM and reduced time period of simulations. Therefore for observing the pattern of trends clearly, linear trend of zonal average from NOBM and reduced time period of model simulations is divided by 100 and then plotted in Figure 4-9. From Figure 4-9, it can be seen that there is a declining trend in observations from -70 to -42^{o}S and an increasing trend from -42 to -30^{o}S. This pattern is clearly observed in signals from reduced time period of historical and RCP8.5 simulations from IPSL model (Figure 4-9). Thus, the pattern of the trends from model simulations is similar to that from NOBM. This was also observed by computing the correlation coefficient between NOBM and model simulations, which was found to be in the range of -0.9357 to 0.8747.

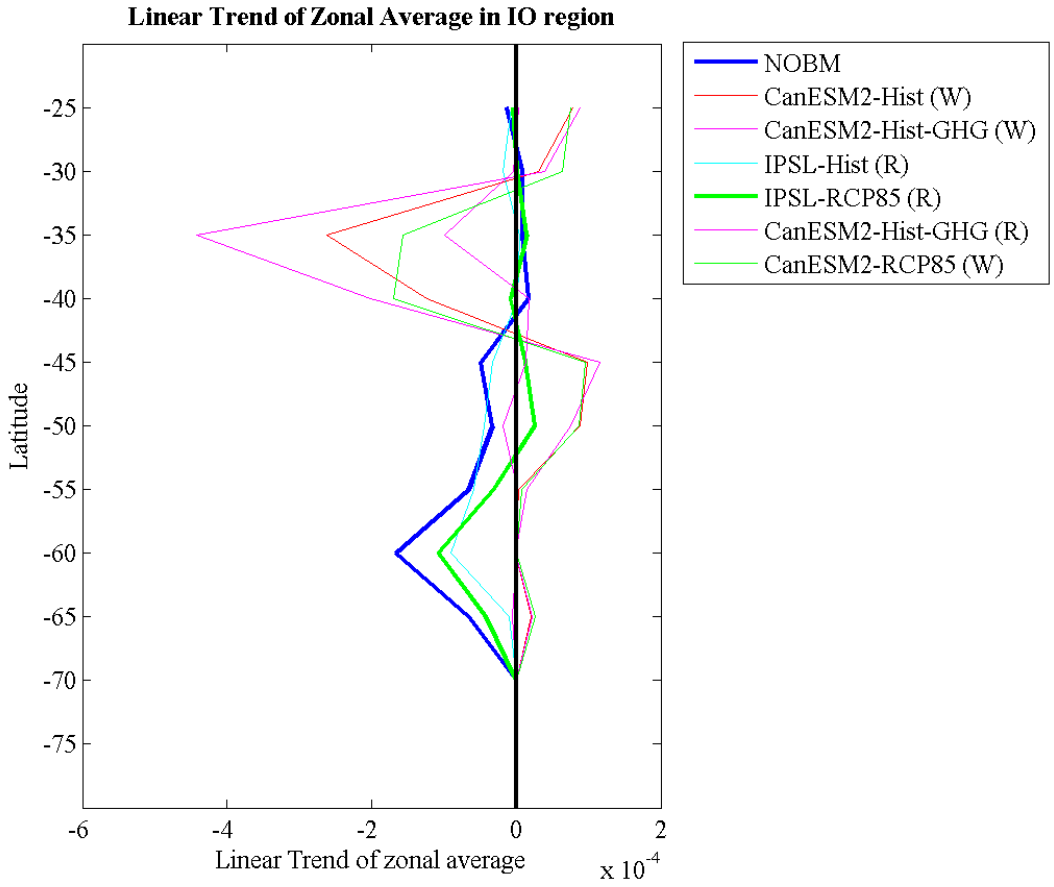

Figure 4-9. Linear trend of zonal average of chl (mg m^{-3} per month) in IO region of the ocean from NOBM and model forced simulations.

4.3. Discussion

In the previous chapter optimal fingerprint method of detection and attribution was implemented to detect climate change influence on chl concentration in the ocean, using spatial linear trend of chl in the region of study as the metric of signal computation. The Principle of the OF method is to increase the signal to noise ratio by changing the direction of the signal to a direction where the overlap with internal variability is less compared to the previous direction. One of the ways to reduced the overlap of the internal variability is by reducing the spatial and temporal variability in the signal. Presence of small scale variability in the signal would reduce the possibility of its detection and might also result in failure of the consistency check of the noise matrix. Spatial linear trend is a 2-dimensional metric which may contain small scale spatial variability due to which the climate change signal

may not be represented distinctly. This may cause a low signal-to-noise ratio which might have been the cause of failure of consistency test of the noise matrix computed for several forcing simulations in different regions of the ocean (Table 3.3). It might also have been the cause of failure of detection of a signal in a region of the ocean even when the consistency test passed (for eg, reduced time period of CanESM2-GHG simulation). Thus, a new metric was defined as the linear trend of the zonal average which has reduced spatial variability and is a 1-dimensional metric. OF method was implemented to detect and attribute statistically significant changes in chl in the regions of the ocean, in response to external forcing, as different from internal variability using linear trend of zonal average as the metric of signal computation.

Linear trend in zonal average was computed from NOBM for different regions of the ocean. Declining trends in subtropical to mid-latitudes was observed in NA, SA and NP regions of the ocean. On the other hand, increasing trend in chl was observed in subtropical to mid-latitudes in SP and IO regions. However, in these regions (SP and IO), decreasing trends in chl were observed in sub-polar to mid-latitudes. Increasing trends in chl were also observed in sub-polar to mid-latitudes in SA region. These trends in the regions of the ocean were observed by some other studies too although the methods used to compute trends is not similar to the method used in this study. For example, Boyce et al. (2010) estimated chl trends (1899-2010) as continuous log-linear functions of time from the blended chl data (ocean transparency and in-situ chl measurements). He observed a declining trend in chl in NA, SA and NP regions of the ocean. Wernand et al. (2013) derived chl from Forel-Ule (FU) scale record and found a declining trend in mean chl concentration per year in NP region. FU scale is the colour comparator method used since 1889 to establish the colour of the sea. Beaulieu et al. (2013) observed a declining trend in average chl from SeaWiFS data (1998-2007) in NA region. Trends were estimated from generalized least squares regression (GLS) model.

Water temperature and stratification of the water column affect the nutrient supply to phytoplankton and therefore, changes in water temperature and stratification result in changes in chl concentration (Behrenfeld et al., 2006, Doney, 2006). Declining trends in chl observed in lower latitudes of NA, SA and NP regions of the ocean follow the expected trend due to global warming. It has been predicted that at lower latitudes (nutrient limited waters), as the water temperature increases due to global warming, stratification increases, which hinders the nutrient entrainment to the euphotic zone resulting in decline of production and hence low chl concentrations (Doney, 2006). Increasing trend in chl observed in higher latitudes of SA region also follows the expected trend due to global warmingi.e. as water temperature increases due to global warming, stratification increases, which reduces the mixed layer depth and hence the light availability to phytoplankton increases which results in higher chl concentrations (Doney, 2006, Bopp et al., 2001). However, this phenomenon of decreasing and increasing trend in chl in lower and higher latitudes respectively, is not followed in SP and IO regions. This may be due to an increase in the nitrogen fixing phytoplankton in lower latitudes which may lead to increased chl concentration (Capone et al., 1997, Carpenter and McCarthy, 1975, Turk et al., 2011) however the models used here don't include the nitrogen fixing phytoplankton (except GFDL) so the particular mechanism at work in the model is unclear. Another reason may be due to influx of nutrients in the upper surface of the ocean from some external source such as saharan dust or river input (Gallisai et al., 2014, Hamza et al., 2011, Ye et al., 2011, Resing and Barrett, 2014, Subramaniam et al., 2008) or changes in direction and strength of winds (Swart and Fyfe, 2012). A study by Behrenfeld et al. (2008a) suggested that primary production decreases with increasing sea surface temperature. Phytoplankton growth and metabolic rate are influenced by water temperature therefore, as temperature increases, primary production (PP) increases until a threshold is reached, beyond which PP decreases (Eppley, 1972). The threshold of maximum PP is species dependent. This decline in PP beyond a threshold temperature might be the reason for observed decline in chl in higher latitudes in some regions of the ocean. Another reason for decline in chl in higher latitudes may be due to the

expansion of warm water phytoplankton species (small picoplankton) from low to high latitudes (Hegseth and Sundfjord, 2008) and migration of cold water phytoplankton species (large phytoplankton) towards the pole (Michaels and Silver, 1988).

In this study, it was found that correlation coefficient between linear trend in zonal average in all the chosen regions of the ocean from NOBM and several model forced simulations is high with maximum value as 0.8747. This indicates that these model simulations are correctly phased with observations and they do a good job of reproducing the observations. High value of correlation coefficient indicates increased possibility of detection of the signal from forcing simulations in the observations.

Consistency check test of the internal variability/noise computed from the control simulations of GFDL-ESM2G and GFDL-ESM2M models failed for NA, SA, SP and IO region of the global ocean and for all the signals from model forced simulations except for historical simulation from GFDL-ESM2G in SA region. Also, consistency check test of the noise computed from the control simulations of CanESM2 model failed for SA and NP region of the global ocean and for all the signals from model forced simulations except for historical natural simulation in NP region. However, consistency test of noise from control simulations of IPSL and CanESM2 model passed for some regions of the ocean and for some signals from model forced simulations. There are a number of potential explanations for failing of the consistency check. One possibility and the most probable cause is that there are elements of the observed chl variability which are not well captured by the model in the region of study. This is reflected in the results as for the same model simulation the consistency check of noise covariance passes in one region of the ocean but fails in another region. For example, for signal from whole time period of IPSL greenhouse gas simulation, consistency test for noise from IPSL control simulation passes in NA, SA, NP and SP regions of the ocean but it fails in the IO region (Table 4-1). This is indicative of the presence of external forcing in the residuals obtained from the linear regression i.e. the signal from model simulations does not capture the

response of chl to external forcings accurately. It is also concluded from here that representation of the noise matrix is accurate and the methodological choice made to compute the noise/internal variability is not the cause of biased results in different regions of the ocean from the same model simulation. Another possibility is that internal variability is not being estimated by the models accurately due to model errors or uncertainties. Due to failure of the consistency check, significance of the scaling factors estimated for the signals from model forced simulations is dubious. Therefore, results for only those simulations were considered significant where consistency check for noise covariance matrix passed.

Detection of the signal from model forced simulations indicates that the patterns of change observed in the signal are present in observations as well. The magnitude of the patterns of change is represented by the deviation of the scaling factor from unity. If the value of scaling factor is greater than unity then it indicates that the signal is underestimating the change in chl and if the value is less than unity then it indicates that the signal is overestimating the change in chl. Greenhouse gas and natural forcing signals were detected in NA, SA and NP regions. In SP region, only natural forcing signal is detected and in IO region, only greenhouse gas forcing signal is detected. Patterns of change observed in these regions are due to the forcing signals detected in these regions. The pattern of change observed in model forcing simulations are not always the same as the change observed in observations. For some model simulations the increasing or decreasing trend is shifted towards the north or south relative to the observations. Trends from observations are the response of chl to a combination of forcings but trends from a specific forcing simulation portray changes in chl only due to that particular forcing and therefore, the patterns of change do not match the observations completely. For example, in SA region, a declining trend is observed from NOBM in subtropical to mid-latitudes. This pattern of declining trend is observed in greenhouse gas simulation from IPSL model but it is shifted by 10 degrees towards to south. However, patterns of change from historical simulation which are expected to be the same as observations, also do not follow the pattern of change in chl from NOBM completely

(Figure 4.7, 4.8 and 4.9). Climate models in their representation of the climate system simplify the complex phenomenon of the climate system. Therefore even though they help understand the climate system and the interactions between the components better they still might not capture some biological processes thoroughly such as the complete range of phytoplankton species, dynamics of higher trophic levels and adaption of primary producers to climate change, and hence the pattern of trends in chl concentration is not captured by the models.

The findings of this study indicate that greenhouse gas forcing is affecting chl concentration in most of the regions of the ocean (NA, SA, NP and IO). As chl is an indicator of phytoplankton biomass (Steele, 1978, Cullen, 1982), changes in the chl concentration in the ocean would suggest changes in the phytoplankton biomass and hence alterations in primary production in the ocean (Blanchard et al., 2012). This would affect the carbon cycle of the ecosystem as the quantity of carbon fixed by the phytoplankton and the carbon exported to the bottom of the ocean will change (Falkowski et al., 1998, Passow and Carlson, 2012). Shift in the composition of the phytoplankton species would alter the carbon export for example, if large phytoplankton (diatoms and coccolithophores) which contribute to the majority of carbon export (Michaels and Silver, 1988, Brzezinski et al., 1998) are replaced by small phytoplankton then the magnitude of the carbon export would decrease. Change in marine primary production and composition of phytoplankton species indicates change in the food availability to the higher trophic levels i.e. zooplankton and fish, and therefore affecting the marine ecosystem, primarily the food chain and fishery yields (Iverson, 1990, Chavez et al., 2003, Ware and Thomson, 2005, Cheung et al., 2009, Cheung et al., 2010).

4.4. Summary and conclusions

Linear trend of zonal average of chl in different regions of the ocean were taken as the guess signal to detect climate change in chl. Linear trend was computed for two time periods i.e. 'whole' and 'reduced' of model

simulations. Internal climate variability was computed from the control run of the models. Optimal fingerprint method was then used to suppress the noise in observations and the forced simulations of the models. This enhanced the signal-to-noise ratio and the possibility of the climate change signal to be detected increased. Conclusions made by the study are -

1. Models underestimate the trend in chl when compared to the observations.
2. Consistency of noise from the control simulation of the model improved from the noise consistency that was observed in the previous chapter when signal was take as the spatial linear trend of chl. This shows that dimension reduction removes the small-scale variability and improves the signal-to-noise ratio and hence, the estimation of the noise/internal variability improves as well.
3. Greenhouse gas and natural forcing signal from climate models is detected in North Atlantic, South Atlantic and North Pacific regions. This indicates that anthropogenic and natural forcings are contributing towards the change in chl observed in these regions.
4. Natural forcing signal is detected in SP region of the ocean indicating that natural forcings are contributing towards the change in chl observed in this region.
5. Greenhouse gas forcing signal is detected in IO region of the ocean indicating that anthropogenic forcings are contributing towards the change in chl observed in this region.
6. Changes observed in the detected signals in the regions of the ocean mostly indicate decline in chl trends in lower latitudes and an increasing trend in higher latitudes which follows the predicted trend in chl by Doney (2006). This norm is not followed in some latitudinal zones in SP and IO region of the ocean. This might be due to changes in these regions which are caused by phenomena not yet completely understood.

5. Climate Change Detection and Attribution for size of the gyres.

In chapter 3 and 4, the signal of climate change in chl is defined as the spatial linear trend in chl and linear trend of zonal average of chl respectively. Linear trend in chl is a direct representation of change in chl. However, climate change in chl can also be studied using indirect metrices such as, change in the size of the subtropical gyres and change in the timing of the annual bloom. In this chapter, climate change detection and attribution is carried out for the metric of the size of the gyres. Gyres are formed due to wind-driven currents which are deflected due to Coriolis effect in clockwise and anticlockwise pattern in northern and southern hemispheres respectively (Huang and Russell, 1994). Westerly winds on northern side and easterly winds on the southern side cause downwelling at the center of the gyres and supply of nutrients to the euphotic zone decreases. This reduces productivity in the water and results in low chl concentration in the gyres. Increase in sea surface temperature due to climate change would increase stratification in the gyres and would further reduce the supply of nutrients to the surface ocean. This would reduce the chl concentration in the gyres. In satellite-based studies the gyre area has been determined by the region where surface chl is below 0.07 mg m^{-3} (McClain et al., 2004). In this study, the same threshold is assumed to be true in computation of gyre area from observations and climate model simulations. Gyres occupy approximately 40% of the Earth's surface and therefore, even though productivity within the gyres is low (Hayward, 1987a, Hayward, 1991, Jenkins and Goldman, 1985, Jones et al., 1996, Karl and Lukas, 1996) they likely contribute more than 30% of the total marine primary production (Longhurst, 1995). Thus, they form a significant part of the marine ecosystem and also of the carbon cycle. Change in the size of the gyres, i.e. change in the regions of low chl concentration in the ocean due to climate change would affect the carbon cycle as the quantity of carbon fixed by the phytoplankton and the carbon exported to the bottom of the ocean will change (Falkowski et al., 1998, Passow and Carlson, 2012). Variability in the size of the gyres has been observed by several studies (McClain et al., 2004, Gregg, 2005, Polovina et al., 2008). For example, Polovina et al.

(2008) ENREF 133 observed monthly mean area of surface chlorophyll in oligotrophic gyres by using satellite ocean color data from SeaWiFS (1998 to 2006). The North Atlantic Gyre (NAG), South Atlantic Gyre (SAG), North Pacific Gyre (NPG) and South Pacific Gyre (SPG) were observed to have an increase in size by 4.3, 0.8, 2.2 and 1.4% per year respectively. Increase in the size of the gyres indicates that low chlorophyll concentration regions of the ocean are increasing and therefore concluding that there is a decline in productivity in the ocean. However, none of the studies take into account or remove the effect of internal variability (noise) of chl on the observed trends. Thus, the observed trend in gyre size observed in these studies may be due to climate change or may be due to internal variability. In this study the optimal fingerprint technique is implemented to detect and attribute climate change signal in the size of the gyres.

The climate change signal is defined as the time series of the gyre area. This is a one-dimensional signal in which climate change is to be determined. The first section of the chapter gives the details of the dataset used and the regions of the ocean where the signal is to be detected. For the purpose of presentation of results with clarity, the North Atlantic region is used here as a case study. Results for other regions of the ocean are presented in the Appendix V and the summary of those results is presented in the main chapter text. The second section of the chapter describes some of the basic statistics performed on the datasets for different regions of the ocean. A comparison of the results is made for different datasets. The third section of the chapter describes the methodology used to implement OF method on the size of the gyres. The fourth section of the chapter is the results section along with the interpretation of the results. The fifth section discusses the results and summarizes the conclusions of the analysis.

5.1. Data

The datasets used for the analysis are as mentioned in chapter 2. As observations, gyre area from NOBM is used in the analysis and simulations

from GFDL-ESM2G, GFDL-ESM2M, IPSL and CanESM2 models are used to compute the signal and the noise (Table 2.1).

Regions of the ocean from which size of the gyres is computed are listed in Table 5-1 along with their latitude and longitude limits and are also shown in Figure 5-1. As it can be seen from the latitude limits of the regions, equatorial belt of -5°S to 5°N is not included in the analysis as chl concentration in this region is strongly influenced by El Niño and La Niña events. Therefore, any changes in chl observed in this region would be difficult to detect as there have been several El Niño and La Niña events during the time period of study. Also, the equatorial region is not a part of the oligotrophic gyre region.

Table 5-1. Latitude and longitude limits of the regions of the ocean chosen for the analysis

Region	**North Atlantic (NA)**	**South Atlantic (SA)**	**North Pacific (NP)**	**South Pacific (SP)**	**Indian Ocean (IO)**
Latitude	5° to 50°	-50° to -5°	5° to 50°	-50° to -5°	-50° to -5°
Longitude	260° to 352°	-60° W to 20° E	120° to 280°	150° to 300°	30° to 120°

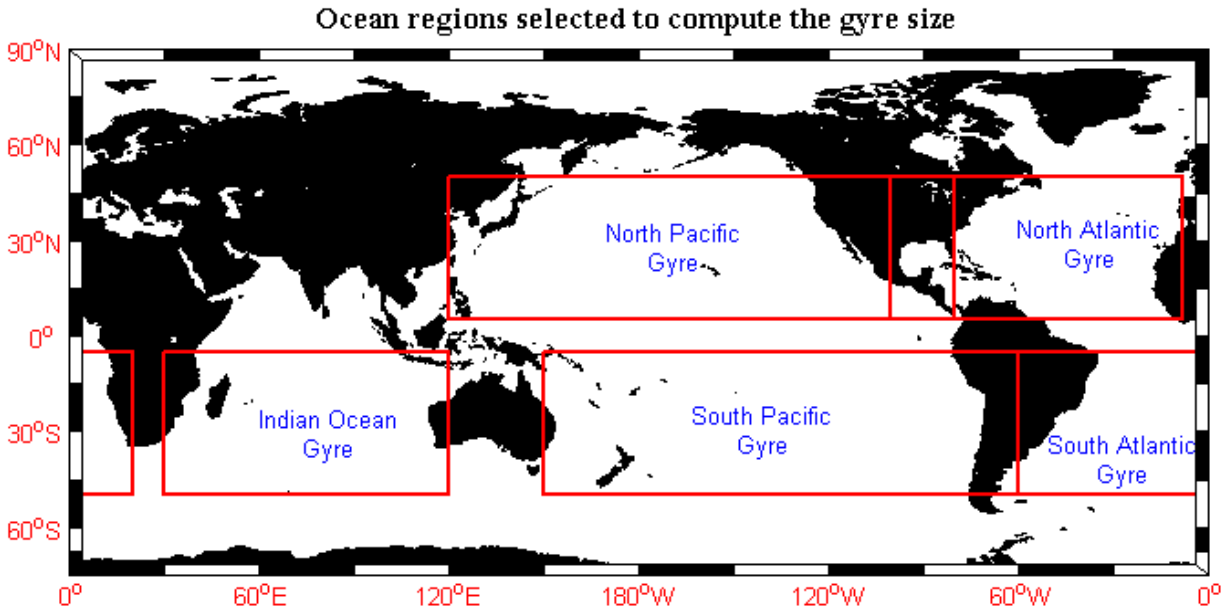

Figure 5-1. Regions of the ocean chosen for analysis. Each region is represented by a box with red boundary.

As in chapter 3, each dataset i.e. observations and model simulations are represented by a letter of the alphabet (see Table 3.2).

5.2. Processing of the Datasets

Prior to estimating the elements of OF method i.e. estimating guess signal, internal variability and observations as described in section 2.2.2.1 of chapter 2 and implementing the OF method, there are some pre-processing steps that need to be implemented for all simulations of the model and the observations (NOBM).

1. Implement the pre-processing steps mentioned in chapter 2, section 2.2.3 or as in flowchart in section 9.1 of Appendix III except the step to remove seasonal mean. In these steps, chl values are extracted from the netcdf files, chl data is rearranged and regridded, invalid values in the data are replaced by NaNs and values are converted to mg m^{-3}.
2. Compute gyre area for every region from each dataset. Steps to do that are as follows -
    - Extract the grid points where chl values are less than 0.07 mg m^{-3}.
    - Compute the area (in km^2) for each time step using the extracted grid points. This gives the time series of the size of the gyre from every dataset for each region of the ocean. Thus, the guess signal is obtained for the analysis from each model simulation.
    - Remove seasonal cycle from the datasets as described in section 2.2.3 of chapter 2 or section 9.1 of Appendix III.
3. For forced run of the model, size of the gyres is computed for the same time period as the observations (NOBM) i.e. 1999-2005.
4. Guess signal from all the forced model simulations is compared with the signal from the observations. This comparison is done by computing the correlation coefficient between the observations and model output, root mean square difference, standard deviation of observations and standard deviation of model output and is presented in a taylor diagram.
5. After pre-processing of the datasets, OF method is implemented following the same steps as described in chapter 3 (see section 3) i.e. signal from

observations and model simulations and noise from control run is computed and input to the regression equation (Eq 3.1) to solve for scaling factors i.e. β. Scaling factor values are obtained for all the model forced simulations in all the regions of the ocean. If positive beta value with confidence interval that exceeds zero is estimated, it is an indication of detection of the signal in the observations.

5.3. Results

5.3.1. Comparison of size of the gyres from model simulations with NOBM data

The size of the gyres in the time period of the dataset was computed from the model forced simulations and from NOBM. Before implementing the OF method using these datasets i.e. to detect the signals from model simulations in observations, it is important to know how these signals relate to observations. A comparison of time series of gyre area from model simulations with gyre area from NOBM was done.

Results for North Atlantic Region

Time series of the NA Gyre area from NOBM and greenhouse gas simulations of the models is shown in Figure 5-2. Size of the gyres from greenhouse gas simulations is chosen as an example for visual comparison because this is the signal that is of interest in this detection study. From Figure 5-2, it can be seen in observations (NOBM) that there is a peak in the size of the gyres in mid 1999 after which there is a decline in the size from 1999 to mid 2002 with occasional peaks. There is then an increase in the size of the gyre from mid 2002 to 2004 which is followed by a decrease. This pattern of change in the gyre area is may be due to the North Atlantic Oscillation (NAO) (Curry and McCartney, 2001). This pattern of increase and decrease in size of the gyre is followed partially by greenhouse gas simulations of the model. Linear trend in the gyre size is computed for all the datasets and the values are presented in (Table 12-1 of Appendix VI). It is

observed that there is an increasing trend (6576.80 km^2 per month) from NOBM, which is also observed in greenhouse gas simulations from ESM2M (6772.59 km^2 per month) and IPSL (5663.54 km^2 per month). However, greenhouse gas simulation from CanESM2 model shows a declining trend (-10852.44 km^2 per month) in the size of the gyres. Trend in gyre size from NOBM and greenhouse gas simulations are significant at 95% level but trends from several other model forced simulations are not significant (Table 12-1 of Appendix VI). This shows that models are not always consistent with the outputs from the same forcing simulations and also, model outputs are not always consistent with observations in pattern and trend.

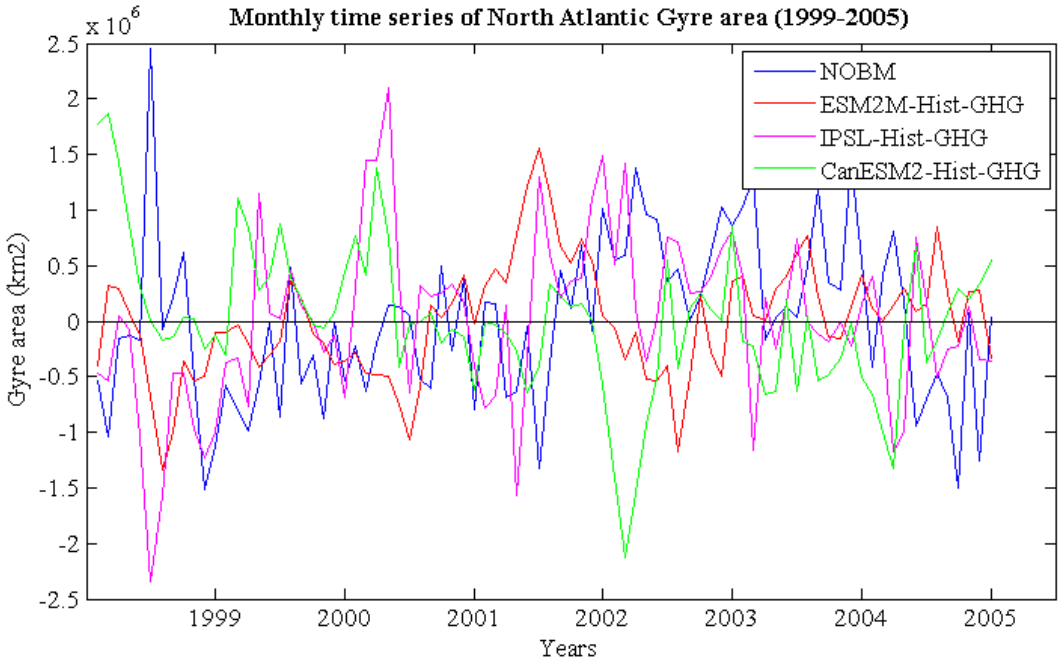

Figure 5-2. Monthly time series of anomalies in the size of the NA gyre i.e. gyre area in km^2.

Statistical terms of comparison between size of the gyres from model simulations and NOBM that were computed are correlation coefficient, centered root mean square difference and amplitude of the variation i.e. standard deviation. The results are presented in the form of a taylor diagram (Taylor, 2001) (Figure 5-3). The Table of values associated with the Figure is presented in (Table 12-2 in Appendix VI).

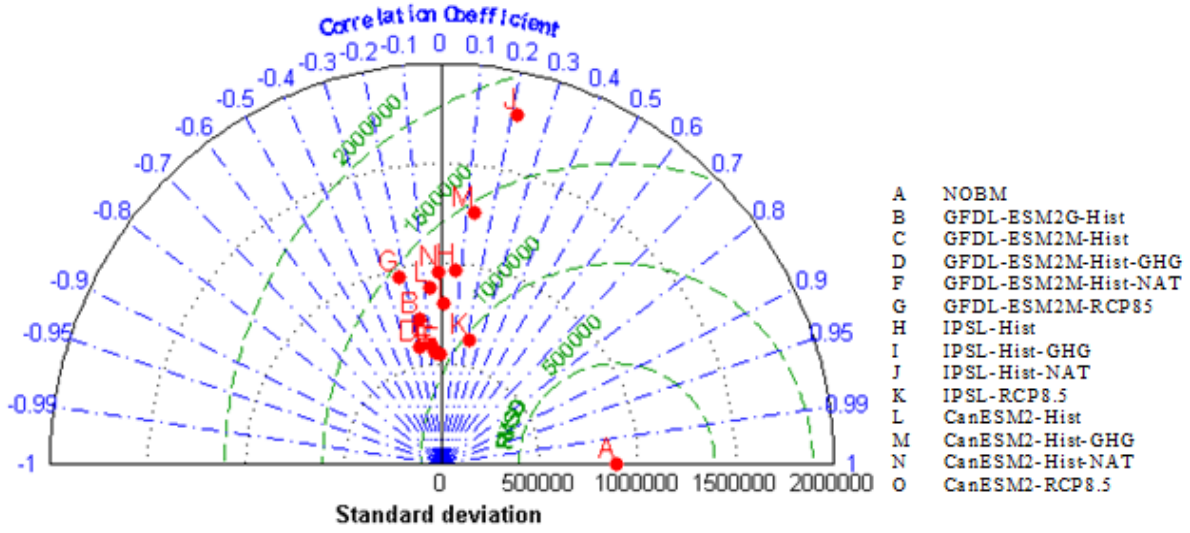

Figure 5-3. Taylor diagram associated with the comparisons of time series of gyre area for NA gyre computed from model simulations with time series of gyre area from NOBM.

From Figure 3-7, it can be seen that the correlation coefficient for all the model simulations is low (-0.2264 to 0.2181 in this study). This indicates that time series of the size of the gyre from model simulations is not correctly phased with NOBM. It should be noted from Figure 3-7 that sign of the correlation coefficient from same forcing simulation from different models is not consistent. For example, correlation coefficient obtained for historical greenhouse gas simulation from ESM2M and CanESM2 is negative but is positive for greenhouse gas simulation from IPSL.

From Figure 3-7, it can also be seen that the standard deviation of some model simulations is lower than NOBM and for some it is higher than NOBM. This shows that some simulations overestimate the gyre area and some under estimate the gyre area when compared to the gyre area from observations. Variation in the estimation of the gyre area from different models may be due to dissimilarity between the models in representation of some physical or biological phenomena in the ocean such as stratification of the water column, mixed layer depth and classification of phytoplankton and zooplankton species or it may be due to the assumed common threshold of chl (0.07 mg m^{-3}) for determining the gyre size in all the models. The difference

in the estimation of gyre area from models would affect the scaling factors obtained for model forced simulations from the implementation of OF method. Simulations which underestimate the gyre area give high scaling factor (>1) and simulations which overestimate the gyre area give lower scaling factor (<1).

Similar comparison of data has been made for other gyres of the ocean as well and the result of the comparisons are presented in section 12.1 of Appendix VI. In summary -

- Trend in gyre size from NOBM is positive and significant at 95% level in NA, NP, SP and IO gyre. Trend is positive but not significant in SA gyre.
- Signals (time series of the size of the gyre) from model forcing simulations are not always consistent with each other. This is indicated in the comparison of the trend of gyre area during the time period of study (1999-2005).
- Correlation coefficient between signal from NOBM and signals from model simulations is low for all the regions of the ocean. This indicates that model simulations are not correctly phased with observations. Low value of correlation coefficient indicates reduced possibility of the signal from forcing simulation to be detected in the observations.
- For all the regions of the ocean, standard deviation of all the signals from model simulations is lower than standard deviation of signal from NOBM except for some model simulations. This indicates that model simulations underestimate the amplitude of the size of the gyres except for some model simulations which may be due to difference in threshold of chl used for computation of gyre area.

5.3.2. Dimension reduction of noise component

Dimension reduction of the noise covariance matrix is an important part of the OF method as noise or internal variability is the most complex element and its accurate estimation is significant in signal detection. The method to reduce the dimensions is described in chapter 3 (see section 2.3).

In this method, the noise matrix is reconstructed using a selective number of eigenvectors known as the level of truncation. Percent of EOFs chosen to reconstruct the noise covariance matrix for all the regions using model forced simulations ranges from 17.86 to 50% (Table 12-11 of Appendix VI) and the variance represented by the chosen number of EOFs ranges from 98.02 to 100%. This shows that approximately 50% of the eigenvectors can be removed from the noise covariance matrices.

5.3.3. Consistency of internal variability

To determine the accuracy of the internal variability estimated from model control simulations, the consistency test is implemented on the noise covariance matrix. Significance of the estimated values of the scaling factors of the forcing signals would be questionable if the consistency test fails for the noise computed from that model. The method to conduct the consistency test is described in chapter 3 (step 6 of section 2.3). Table 5-2 below shows result of the F-test for each OF method implementation i.e. signal detection for each region of the ocean using the forced model simulations. In the Table, passing of the test is represented as 'P' and failing of the test is represented as 'F'. Simulations, for which the consistency test passes, are highlighted in green.

Table 5-2. F-test result for each OF implementation

Model Simulation	NA	SA	NP	SP	IO
B	F	F	F	F	F
C	F	F	F	F	**P**
D	F	F	F	F	**P**
F	F	F	F	F	F
G	F	F	F	F	F
H	**P**	F	F	F	F
I	**P**	F	F	F	F
J	**P**	F	F	F	F
K	**P**	F	F	F	F
L	F	F	F	F	F
M	F	F	F	F	F
N	F	F	F	F	F
O	F	F	F	F	F

From Table 5-2above it is seen that the consistency test fails for most of the model forced simulations in all the regions of the ocean except for all the simulations from IPSL model in NA region and for historical and historical greenhouse gas simulation from ESM2M model in IO region. This may be due to several reasons : inaccurate representation of noise from the control run; the control run itself may not represent the internal variability of the chl accurately and residuals may contain influence of the external forcing. In this study, second and third reason are more likely to be the cause of failure of consistency test as correlation coefficient between gyre area from NOBM and model simulations is low. Inaccurate internal variability affects the detection results as removal of noise is an important aspect of the OF method. It might lead to the failure of signal detection by the OF method as the signal-to-noise ratio may not be high enough to be detected. Thus, results of the detection and attribution for the size of the gyres will be dubious for all the regions of the ocean.

5.3.4. Detection of signals

The optimal fingerprint method described in section 2.3 is applied to evaluate the detection of observed changes in response to external forcings. Statistically significant scaling factors (β) determined as a result of the fingerprint analysis are indicative of the detection of an external signal in observations. Scaling factors are considered to be important when their values are significantly different from 0. In the case where the scaling factor is negative it indicates that the signal is not detected. There may be several reasons for a negative scaling factor. First, there is no climate change signal present in the observations. Second, the signal-to-noise ratio is not strong enough to be detected. This may be due to misrepresentation of the noise from the control run. The second reason is the most probable cause of failure of signal detection as correlation coefficient between gyre area from NOBM and model simulations is low which cause both the signal and the noise to be misrepresented by the models.

Scaling factors obtained as a result of the implementation of the OF method on time series of the gyre area in NA region of the ocean is shown in Figure 3-8.

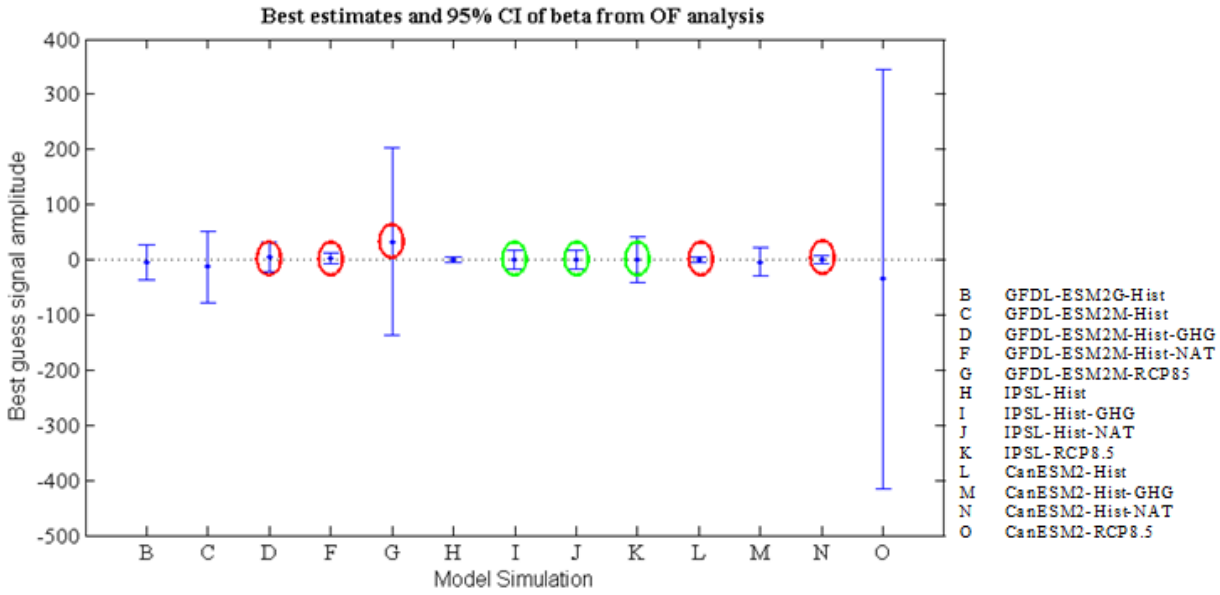

Figure 5-4. Graph of signal amplitude along with the CI, obtained for OF implementation in NA gyre using signals from model forced simulations. Green circles indicate scaling factors which are positive and are obtained for the simulations for which consistency test passed. Red circles indicate scaling factors which are positive and are obtained for the simulations for which consistency test failed.

The Table associated with Figure 5-4 is given in Table 12-12 of Appendix VI. Figure 5-4 above shows the beta values obtained in NA region for signals obtained from model forced simulations along with the confidence interval (CI) associated with each beta value. From the Figure 5-4a it can be seen that even though there are some model simulations for which scaling factors are positive, none of the scaling factors are significantly different from 0 with 95% confidence interval. This indicates that the effect of external forcings is not being detected in the NA gyre and the null hypothesis that changes in size of the gyres is caused by internal variability cannot be rejected.

The OF method was implemented for other gyres as well and the results are presented in section 12.3 of Appendix VI. Summarizing the results of the OF analysis it is found that for all the gyres, scaling factors estimated for some of the signals from model forced simulations are positive but none of them are significantly different from 0 with 95% confidence interval. This

indicates that changes observed in the size of the gyres from NOBM are most likely due to internal variability in gyre size.

5.4. Discussion

In this chapter optimal fingerprint method of detection and attribution is implemented to detect climate change influence on chl concentration in the ocean, using time series of the size of the gyres as the metric of signal computation. Seasonal anomalies of the gyre area were estimated for each month from 1999-2005 for all the datasets. As monthly data of gyre area for the years 1999-2005 is used in the analysis, the signal (time series of the gyre size) contains small time-scale variability which makes it difficult to identify any distinct patterns of change in the gyre area over the years 1999-2005. Linear trend in the size of the gyres was estimated from NOBM and model forced simulations. Increasing trend in size of all the gyres was observed from NOBM where SA gyre had the slowest trend (1408.74 km^2 per month) and NP gyre had the fastest trend (29324.35 km^2 per month) in size. However, percent increase in gyre area of NA, SA, NP, SP and IO gyres computed with reference to the yearly mean of gyre area in 1999 is faily consistent and is 1.98, 1.9, 1.71, 1.75 and 1.8 percent per year respectively. This indicates that NP gyre has the slowest increasing rate and NA gyre has the fastest rate. Positive linear trends in gyre area (NA, SA, NP and SP gyres) were also obtained by Polovina et al. (2008) where gyre size was computed from a 9-year time series (1998-2006) of SeaWiFS ocean color data and the trends were estimated by fitting a generalized additive model (GAM) (Hastie and Tibshirani, 1990). Percent increase in gyre area observed by Polovina et al. (2008) of NA, SA, NP and SP gyres computed with yearly mean of gyre area in 1998 is 4.3, 0.8, 2.2 and 1.4 percent per year respectively. The percent increase in gyre size obtained by Polovina et al. (2008) _ENREF_133was lowest in SA region and highest in NA region. This difference in increase in gyre size between this study and (Polovina et al., 2008) _ENREF_133may be due to different length of the dataset used and also due to the different approach used to compute linear trend in the gyre size. McClain et al. (2004) also observed increasing trends in size of the NA, SA,

NP and SP gyres where values were derived from OCTS (November, 1996 to June, 1997) and SeaWiFS (September, 1997 to October, 2003) ocean color data. However, a decreasing trend in the IO gyre size was observed by McClain et al. (2004) which is in contradiction to the increasing trend estimated in IO gyre size in this study from NOBM data. These contradicting trends in IO gyre area are may be due to the different time period used by McClain et al. (2004) to compute the trend. Also, McClain et al. (2004) used data from two different satellite sensors which differ in the instruments used for measurements, calibration techniques, the spatial and temporal scales of the sensors and also the time period of operation. These differences in sensors may give rise to uncertainties when datasets from these sensors are blended in an analysis.

Increase in the size of the gyres is an indication of decline in the chl concentration in the oligotrophic region of the ocean. Simultaneous increase in the sea surface temperature (SST) has been observed by some studies (Gregg, 2005, Polovina et al., 2008) which suggests that decrease in chl may be due to increase in SST. A study by Gregg (2005) _ENREF_61, observing chl concentration anomalies from SeaWiFS (1998-2008) found a declining trend in chl concentration in all the regions of the ocean. Gregg (2005) also simultaneously observed SST anomalies and found an increasing trend in SST in all the gyres except in NA gyre. However, Polovina et al. (2008) _ENREF_133observed an increasing trend in SST in all the gyres. Contradicting trends in SST in NA gyre from the two studies may be due to different time periods of study. Polovina et al. (2008) _ENREF_133studied 9 years of SeaWiFS data (1998-2006) whereas, Gregg (2005) studied 6 years of SeaWiFS data (1998-2003). Another reason for dissimilar SST trends may be that SST data used by Polovina et al. (2008) _ENREF_133is the NCEP Reynolds Optimally Interpolated SST product which incorporates both in-situ SSTs and satellite derived SSTs from NOAA Advanced Very High Resolution Radiometer (AVHRR) whereas, Gregg (2005) uses SST data from NOAA AVHRR only. Increasing SST results in increasing stratification in subtropical regions of the ocean (Barnett et al., 2001) which decreases net primary productivity in these regions (Behrenfeld et al., 2006). Thus, increasing in the size of the

gyres indicates the effect of global warming on chl concentration in the ocean.

Linear trend in gyre size from NOBM for all the gyres is significant at 95% level except for SA gyre, where trend is not significant. Also, there are several model simulations for which the trend in gyre size is not significant. Insignificant trends reduce the likelihood of signal detection. The possibility of signal detection is further reduced when the signals from NOBM and model simulations are not in phase i.e. correlation coefficient between time series of gyre size from model forced simulations and time series of gyre size from NOBM is low (-0.355 to 0.3778 in this study). Low correlation coefficient indicates that models don't do a good job of reproducing the size of gyres which makes it challenging to detect the signal in observations. Also, there was no or partial consistency in the correlation coefficient obtained for the same forcing simulation from different models indicating the uncertainties and unreliability of the size of the gyres estimated from climate models. Models also underestimate the amplitude of the size of the gyres which was indicated by the lower standard deviation obtained from all model forced simulations (but for some exceptions) when compared to the standard deviation from NOBM. The reason for the underestimation of size of the gyres by the models may be that there are probably some processes or parameters which have not been properly represented or are completely missing from the models. For example, models may be over simplifying the classification of phytoplankton and zooplankton species which might affect the phytoplakton growth and grazing rates and in-turn would affect the chl concentration or climate processes such as the decadal oscillations (NAO, PDO) may not be represented properly.

Consistency check test of the internal variability/noise computed from the control simulations of the models failed for all the gyres of the ocean and for all the signals from model forced simulations except for all the simulations from IPSL model in NA gyre and for historical and historical greenhouse gas simulation from ESM2M model in IO gyre (Table 5-3). The cause of the failure of the consistency test may be that signals do not

represent the change accurately and residuals may contain influence of the external forcing or noise may not be represented accurately from the control simulation or the control run itself may not represent the internal variability of gyres accurately. Improvement in the representation of climate processes by models may enhance the performance of the models. Failure of the consistency of the noise matrix makes the reliability and significance of the detection results questionable. Nonetheless, OF method was implemented to detect and attribute climate change in size of the gyres.

Detection of the signal from model forced simulations is indicative of the patterns of change observed in the signal being present in observations as well. The magnitude of the pattern of change is represented by the deviation of the scaling factor from unity. For all the gyres, there were some simulations in some of the gyres for which estimated scaling factors were positive but none of them were significantly different from 0 with 95% confidence interval. This indicates the presence of internal variability in the datasets i.e. the noise is not removed accurately from the datasets. This is indicated earlier as well in the failure of the consistency test for the noise covariance matrix. The reason of this may be that the metric defined to compute the signal (time series of the gyre) does not represent climate change and therefore, the OF method has failed to increase the signal-to-noise ratio and has also been unsuccessful in removing the internal variability from the datasets which led to the failure of detection and attribution. It can be argued that there is no climate change signal i.e. the changes observed in the size of the gyres are not due to climate forcings (external and natural) because of which the method has failed. In case of no climate change signal, scaling factors would be negative. In the detection results of this chapter, there are some simulations, for example greenhouse gas simulation in NA gyre, for which the scaling factor is estimated to be negative (Figure 5-4). It can be said for these simulations that there is no climate change signal, but since the detection results do have several simulations for which scaling factors is positive (Figure 5-4) but they are not significantly different from 0 with 95% confidence interval, it can be concluded that the method failed to remove internal variability from the

observations and model forced simulations. The results of this chapter leave the question of whether the increase in the size of the gyres is due to climate change or not, unanswered. Therefore, trends in the size of the gyres observed in this study and other studies (McClain et al., 2004, Polovina et al., 2008) might be due to climate change effect on chl or it may be due to internal variability of chl. In future, OF method can be implemented on a different metric for example, spatial pattern of the change in the gyre area which may be the representation of climate change and would be able to answer the question above.

5.5. Summary and conclusions

The time series of the gyre in different regions of the ocean was taken as the guess signal to detect climate change in chl. Monthly series of gyre area were computed for time period 1999-2005 of NOBM and model simulations. Internal climate variability was computed from the control run of the models. Optimal fingerprint method was then used to suppress the noise in observations and the forced simulations of the models. This enhanced the signal-to-noise ratio and the possibility of the climate change signal to be detected increased. Conclusions made by the study are -

1. Models underestimate the size of the gyres which may be due to the assumed threshold of 0.07 mg m^{-3} chl while computation of gyre size.
2. Increasing trend in size is observed in all the gyres (NA, SA, NP, SP and IO). NP gyre has the slowest percent of increase in size per year and NA has the fastest percent of increase in size per year.
3. Noise is not consistent for most of the signal detections performed using model forced simulations for the gyres except for some simulations in NA and IO gyres. This affects the signal-to-noise ratio and hence the detection of a signal may fail due to a lack of consistency of noise matrix. It also indicates the presence of external forcing in the residuals obtained from the regression of signals with observations.
4. Scaling factors for some of the model forced simulations are estimated to be positive but they are not significantly different from 0 with 95%

confidence interval. This indicates the presence of internal variability in the signals. Thus, the metric defined to detect the climate change signal in size of the gyres is incorrect.

6. Summary and Conclusions

This thesis aimed to perform a formal detection and attribution analysis on observed chl concentration using the optimal fingerprint method. The method projects response of chl to external forcings such as greenhouse gas forcing and solar forcing on the chl concentration from observations (assimilated satellite ocean colour data from three dimensional global ocean model i.e. NOBM). The amplitude of the responses are indicators of detection of a climate forcing signal in the observations. All the datasets, i.e. the observations and responses from model simulations, are optimized using the noise covariance matrix obtained from the control simulation of the models.

6.1. Assessment of signal metrics

One of the keys to detecting a climate change signal in a climate parameter is the 'direction' in which to look for the change. In the thesis this was represented by the metric defined for signal computation. The metric should be chosen such that it doesn't contain too much small scale variability which increases the noise in the signal and makes the detection of climate change signal difficult. At the same time the metric chosen should be able to capture the relevant change, i.e. the change due to climate forcings in the parameter. Three metrics defined in the thesis were: spatial linear trend of chl; linear trend of zonal average; and time series of the size of the oligotrophic gyres.

The first metric is a two-dimensional spatial pattern of change in chl. The second metric is also a spatial pattern of change in chl but is one-dimensional. The third metric is a one-dimensional time series representing change in chl. Out of the three metrics, this work demonstrated that the second metric is the best, and the third metric is the worst, 'direction' to look for a climate change signal in chl. This was indicated by the result of the consistency test for noise covariance matrix for these three metrics (Table 3-3, 4-1 and 5-2). The results show that for the first metric the test passed in some of the regions of the ocean, for some of the simulations; for the second

metric the test passed in more regions for more model simulations; and for the third metric the test failed in all the regions of the ocean for all the model forced simulations. Failure of the consistency test indicates that the noise was not removed completely from the datasets and the residuals may contain influence of the external forcing. One of the reasons for this failure would be the wrong definition of the metric, i.e. the wrong 'direction' to look for the climate change response.

The results also demonstrated that it is difficult to distinguish a temporal pattern of trend in the datasets (Figure 5-2) from the third metric. This might be because of high temporal variability introduced by using a monthly time series. In future, annual time series or a 3-year or a 5-year smoothed time series might be used as a metric to detect climate change. This would require a substantially longer time period of availability of observations. In the first metric, the spatial pattern of trend was obvious in some regions for some simulations but was not very apparent in other regions. This indicates that in some regions there is may be no distinguishing spatial pattern of trend or the 5° by 5° grid is still not large enough to provide a distinct pattern of trend. In the case of the second metric, the patterns of change were apparent in most of the regions for most of the simulations. This indicates that the reduction of the spatial resolution by computing the zonal average and the reduction of the temporal resolution by taking the linear trend gives a signal which captures the relevant trend in chl above the noise.

6.2. Evaluation of models

As mentioned in section 6.1 the consistency test failed for most of the simulations in most of the regions for the first and third metric. A possible reason for failure of the consistency test is that the models are not simulating the response of chl to external forcings correctly or the models are not simulating the noise properly. Incorrect representation of the response of chl or internal variability of chl might also lead to the failure of signal detection. Poor performance of models in simulating chl was observed in the values of

correlation coefficient between signals from observations and model simulations. Correlation coefficient was low for the signal in the first and third metric; it was higher for the signal in second metric. For some of the model simulations, correlation coefficient was even negative. Apart from the models being inconsistent with the observations, models are also inconsistent among themselves. For example, signal from the greenhouse gas forcing from one model is not consistent with the signal from greenhouse gas forcing from other models. This indicates uncertainty and unreliability of the signals from the model simulations. In future work, uncertainties in climate models can be removed to an extent by taking mean of the ensemble of runs of a climate model for a particular forcing scenario.

Out of the four models, consistency test failed for the first and second metric for most of the simulations from GFDL-ESM2G and GFDL-ESM2M model and passed for most of the simulations from IPSL and CanESM2 model in most of the regions of the ocean. One of the difference between the models that passed from those that failed is in their classification of phytoplankton. In GFDL models, phytoplankton are classified in three groups - small, large and diazotrophs. In IPSL model, phytoplankton are classified in two groups - nano phytoplankton and diatoms. In CanESM2 model, there is no classification of phytoplankton and a single component is used to represent phytoplankton. Another difference between the models is in their representation of grazing of phytoplankton. In the two models from GFDL, grazing of phytoplankton is specified through a size-based relationship (Dunne et al., 2005), i.e. grazing and in turn phytoplankton growth rate is dependent on the size of the phytoplankton. In IPSL and CanESM2 models, grazing of phytoplankton is controlled by the zooplankton. Models also differ in their representation of Redfield ratio and the variable ratios for organic matter production (table 2-2). This affects the derivation of chl in the model and hence models differ in their performance. These differences in the biological and carbon components might be one of the reasons why the model performance is poorer for GFDL. There may be other dissimilarities such as difference in representation of nutrient flux or in illustration of mixed layer depth or stratification of the water column.

Climate models simplify the complex phenomenon of the climate system therefore, even though they help understand the climate system and the interactions between the components better, they still might not accurately represent some the climate processes such as decadal oscillations (North Atlantic Oscillation and Pacific Decadal Oscillation). Alternatively, they may not capture some biological processes thoroughly such as dynamics of higher trophic levels and adaption of primary producers to climate change, and therefore the pattern of trends in chl concentration may not be captured by the models properly.

6.3. The need for longer term observations

Detection of a climate change signal in a particular parameter is easier if there are long records of the parameter available. This is because it becomes easier to remove the small-scale spatial and temporal variability. For example, if 30-50 years of chl observations were available then for the third metric, i.e. the size of the gyres, annual time series or a smoothed 5-year time series could be used to compute the signal. This would reduce the small-scale variability and might also give a more distinct pattern of change. In case of chl, global, multi-year data is available from satellite ocean color sensors. Satellite ocean colour measurements began in October 1978 with the Coastal Zone Color Scanner (CZCS) (1978-1986). Since then, many sensors have been launched such as SeaWiFS (1998-2010) and MODIS-Aqua (since 2002), and measurements of ocean colour have been made. To get a longer time series of ocean colour, observations from different sensors need to be blended, which is challenging as sensors differ in the instruments used for measurements, calibration techniques used, the spatial and temporal scales of the sensors and also the time period of operation. These dissimilarities affect the homogeneity, coverage and quality of the data. However, there are some merged ocean colour datasets available such as European Space Agency's (ESA) Climate Change Initiative (CCI) (1997-2013) and ESA's GlobColour (1997-present). Long-term in-situ measurements of chl are also available such as observations at Bermuda Atlantic Time Series (BATS) station and Hawaii Ocean Time-Series (HOT) station although they lack spatial coverage.

Formal detection and attribution can be implemented on these datasets to detect climate change signal in chl.

6.4. Detection results

A signal is considered to be detected if the value of the scaling factors for the climate forcing simulations is positive and significantly different from 0 with 95% confidence. For the third metric, i.e. the time series of the size of the gyres, there were some simulations where the scaling factor values were positive but all of these were not significantly different from 0 with 95% confidence. This indicates the presence of internal variability in the detected signal i.e. the internal variability/noise is not removed from the signals. This was also indicated by the failure of the consistency test for all the simulations for all the regions of the ocean. Thus, as has been mentioned before the reasons for this might be that the internal variability of chl and the response of chl to external forcings are not simulated by the models correctly; or the metric defined is not the correct 'direction' to look for the climate change response; or there is no climate change signal.

For the first metric i.e. spatial linear trend in chl, greenhouse gas forcing signal was detected in NA, SA, SP and IO regions and natural forcing signal was detected in SP region of the ocean. In NP region, no forcing signal was detected. Predicted patterns of change in chl with climate change (Doney, 2006), i.e. decline in chl in lower latitudes and increase in chl in higher latitudes, was observed in NA and SP regions. On the other hand, patterns of change in chl in the SA region were observed to be opposite to those expected, i.e. the trends in chl were increasing in lower latitudes and decreasing in higher latitudes. This might be due to the change in the species composition of phytoplankton with warming ocean i.e. expansion of warm water phytoplankton species (small picoplankton) from low to high latitudes and migration of cold water phytoplankton species (large phytoplankton) towards the pole (Michaels and Silver, 1988). Alternatively, it might be due to influx of nutrients in these regions from some external source such as saharan dust or river input (Gallisai et al., 2014, Hamza et al., 2011, Ye et

al., 2011, Resing and Barrett, 2014, Subramaniam et al., 2008). In IO region, there was no distinct pattern of change in chl. These results from the first metric indicate that chl in the ocean is being affected by greenhouse gas forcings and in some regions it is also affected by natural forcings but the pattern of change that was observed did not follow the predicted pattern of change in chl in all the regions i.e. Doney (2006)'s conceptual model is not universally correct for the future ocean. This signifies that changing climate is affecting chl in a way which is not yet completely understood and in future the effects of climate change to chl may be surprisingly different.

For the second metric i.e. linear trend of zonal average of chl, greenhouse gas and natural forcing signals were detected in NA, SA and NP regions of the ocean. In these regions the pattern of trends in chl followed the expected pattern of trend in chl i.e. decline in chl in lower latitudes and increase in trend in higher latitudes. On the other hand, SP and IO regions showed the opposite pattern i.e. there was an increase in chl in lower latitudes and decline in chl in higher latitudes. This might be because in these regions only one of the forcing signals was detected i.e. natural forcing signal was detected in SP region and greenhouse gas forcing signal was detected in IO region. These results indicate that the predicted pattern of change in chl is the change due to combination of two forcing signals i.e. greenhouse gas and natural forcings.

The detection results indicate that chl concentration in some regions of the ocean is already being affected by greenhouse gases. The results can further be verified by using more climate models or by applying the formal detection and attribution to another metric of climate change in chl, for example change in the timing of the phytoplankton bloom.

6.5. Future Work

This study focused on implementing a formal detection and attribution of climate change signal in chl by using the optimal fingerprint (OF) technique on three metrics of chl trend. Out of the three only one metric, i.e.

the linear trend of zonal average of chl, gave reliable results. The OF technique can be implemented using different metrics such as change in the timing of phytoplankton bloom or spatial representation of the change in the gyre area. The technique can also be applied on metrics with reduced spatial and temporal resolution. The OF technique can also be implemented on the primary production observations.

In this study, output from the NOBM model was used which assimilates SeaWiFS satellite chl observations. The time period of the data used was 7 years (1999-2005). Blended satellite ocean colour datasets such as ESA's CCI and GlobColour which provide long-term records could be used in detection and attribution analysis. The OF technique could also be implemented using long-term in-situ records of chl, such as records from BATS and HOTS stations. The temporal resolution of metrics is easier to reduce in long-term records of chl which would help in removal of small-scale temporal variability, which results in reduction of noise in the signal and hence, the possibility of signal detection increases.

As has been seen in this study, the fidelity of climate models play a major role in the detection and attribution method. Four models were used in this study and the correlation coefficient between model simulated chl and chl from NOBM was low for all the models. Taking mean of the ensemble of runs of a climate model for a particular forcing scenario might improve the model output. Also, output from more climate models with higher spatial resolution could be used in the detection and attribution as it may help in evaluating and improving model performance in simulating chl, as there may be certain meso and sub-meso scale processes affecting chl which may not be represented accurately in the models and there might be certain parameters which may not be simulated properly such as classification of phytoplankton functional groups or dynamics of higher trophic levels and adaption of primary producers to climate change.

Finally, I conclude that greenhouse gases have affected the chl concentration in some regions of the ocean and the signal is being detected in the observations. This indicates the need to act upon the prevention of further

effects by reducing the emission of greenhouse gases in the atmosphere, as changes in chl would affect the whole marine ecosystem and would also affect the biological pump and the carbon cycle.

7. Appendix I- Comparison of monthly mean chlorophyll time series from NOBM with climate models

7.1. Results for South Atlantic

Table 7-1. Statistical terms computed for Taylor diagram.

Model/statistical term	Standard Deviation	RMS difference	Correlation Coefficient
IPSL	0.109	0.111	0.386
GFDL-ESM2G	0.045	0.081	0.442
GFDL-ESM2M	0.061	0.087	0.383
CanESM2	0.037	0.124	-0.898

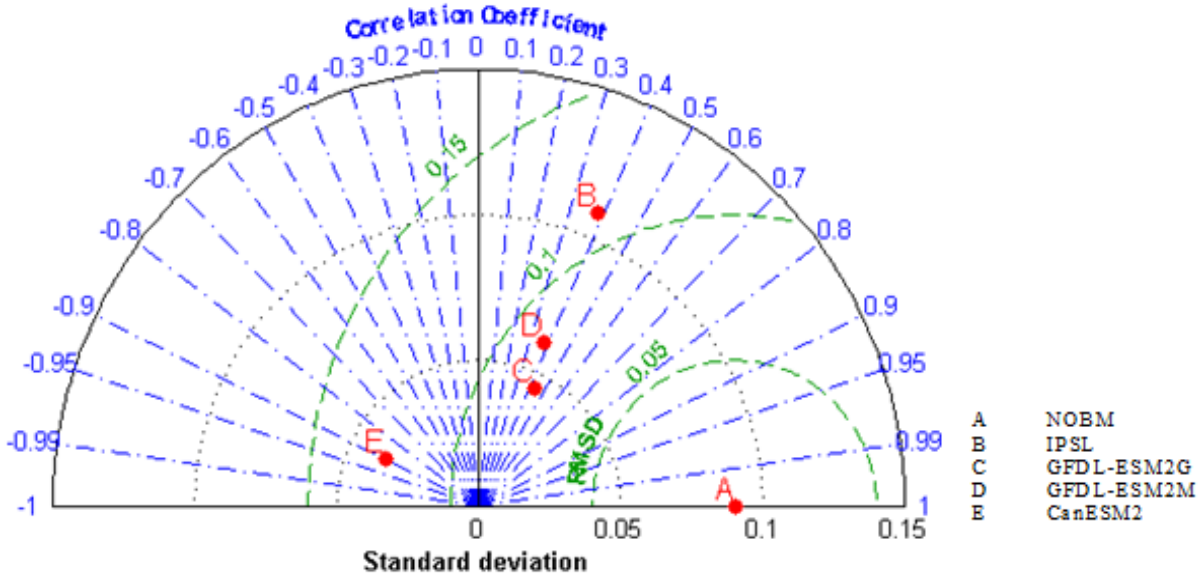

Figure 7-1. a). Pattern statistics describing the monthly time series of mean chl for SA region (1999-2005) simulated by 4 models compared with the observed.

From the Figure 7-1, it can be seen that the correlation coefficient between NOBM and IPSL, GFDL-ESM2G and GFDL-ESM2M is moderate (0.383 to 0.442) and for CanESM2 model it is negative (-0.898). This indicates that the phase of the all the models except CanESM2 is same as the observations. From the Figure 7-1, it can also be seen that the standard

deviation of all the models except IPSL model is less than NOBM. This indicates that all the models underestimate the amplitude of the chl values except for IPSL model which exaggerates the amplitude of chl values. The RMS difference between models GFDL-ESM2G and GFDL-ESM2M and NOBM is between 0 and 0.1 whereas, RMS difference is more than 0.1 for models IPSL and CanESM2. Lower RMS difference for GFDL-ESM2G and GFDL-ESM2M climate models is due to lower difference in amplitudes of the models and observations. Lower RMS difference indicates that these models perform well in simulating the chl. On the other hand, IPSL and CanESM2 models performs poorly as the RMS difference is higher which is due to larger difference in the amplitude of patterns.

7.2. Results for North Pacific

Table 7-2. Statistical terms computed for Taylor diagram.

Model/statistical term	**Standard Deviation**	**RMS difference**	**Correlation Coefficient**
IPSL	0.170	0.131	0.785
GFDL-ESM2G	0.056	0.051	0.587
GFDL-ESM2M	0.078	0.044	0.829
CanESM2	0.063	0.105	-0.556

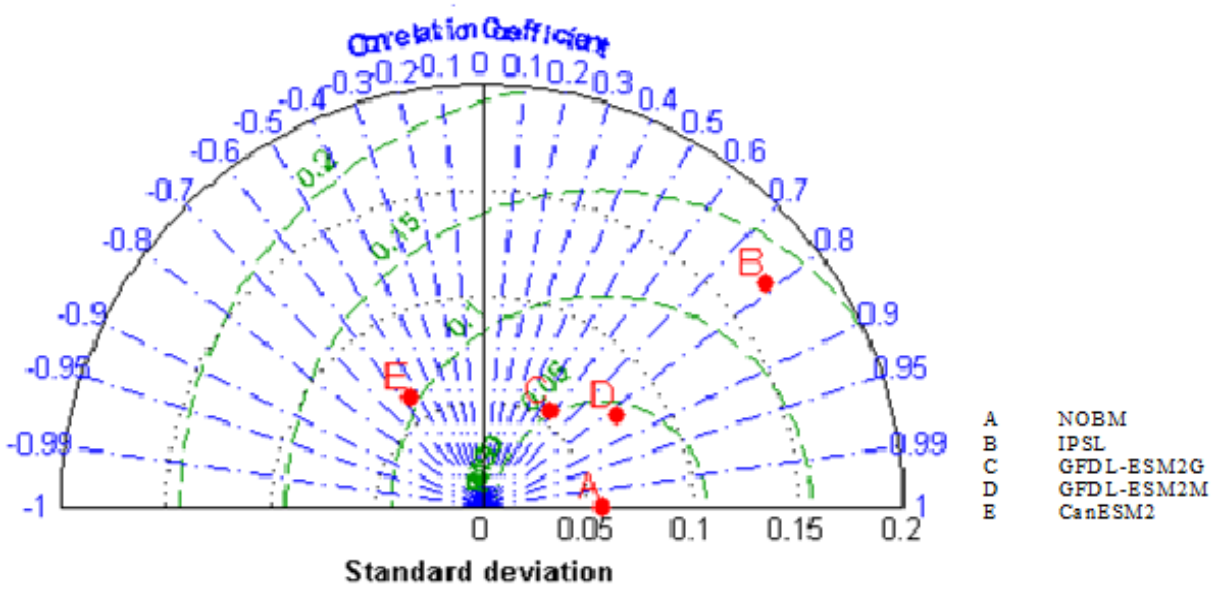

Figure 7-2. a). Pattern statistics describing the monthly time series of mean chl for NP region (1999-2005) simulated by 4 models compared with the observed.

From the Figure 7-2, it can be seen that the correlation coefficient between NOBM and IPSL, GFDL-ESM2G and GFDL-ESM2M is high (0.587 to 0.829 in this study) and for CanESM2 model it is negative (-0.556). This indicates that the phase of the all the models except CanESM2 is same as the observations. From the Figure 7-2, it can also be seen that the standard deviation of all the models except GFDL_ESM2G model is more than NOBM. This indicates that all the models exaggerate the amplitude of the chl values except for GFDL_ESM2G model which underestimates the amplitude of chl values. The RMS difference between models GFDL-ESM2G and GFDL-ESM2M and NOBM is between 0 and 0.1 whereas, RMS difference is more than 0.1 for models IPSL and CanESM2. Lower RMS difference for GFDL-ESM2G and GFDL-ESM2M climate models is due to lower difference in amplitudes of the models and observations. Lower RMS difference indicates that these models perform well in simulating the chl. On the other hand, IPSL and CanESM2 models performs poorly as the RMS difference is higher which is due to larger difference in the amplitude of patterns.

7.3. Results for South Pacific

Table 7-3. Statistical terms computed for Taylor diagram

Model/statistical term	Standard Deviation	RMS difference	Correlation Coefficient
IPSL	0.108	0.108	0.310
GFDL-ESM2G	0.048	0.057	0.549
GFDL-ESM2M	0.066	0.061	0.572
CanESM2	0.032	0.095	-0.850

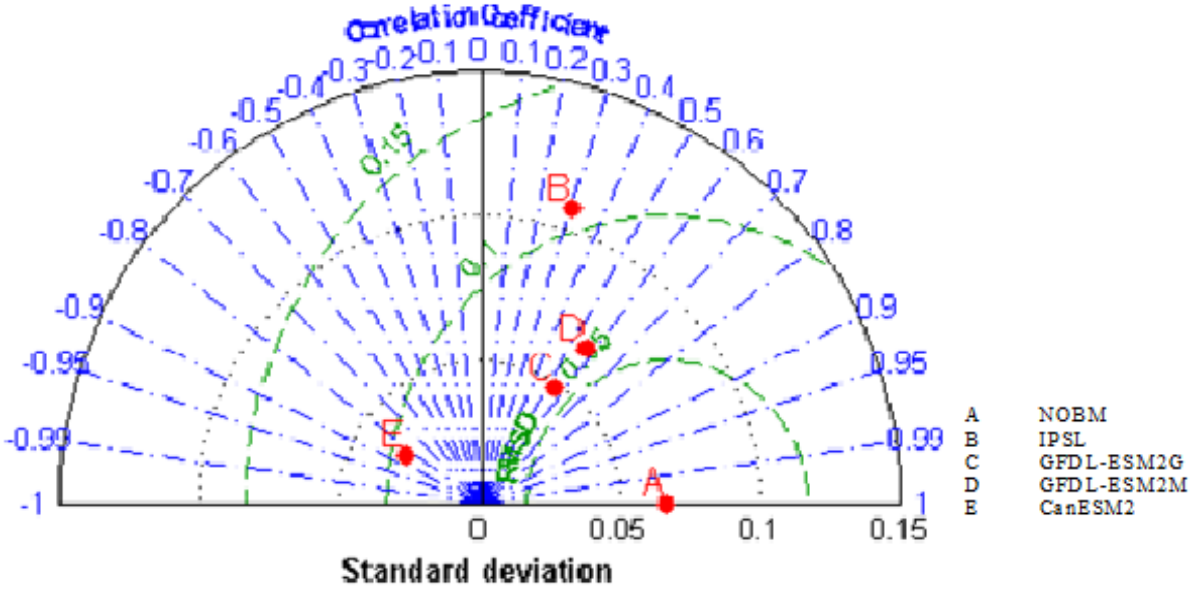

Figure 7-3. a). Pattern statistics describing the monthly time series of mean chl for NP region (1999-2005) simulated by 4 models compared with the observed.

From the Figure 7-3, it can be seen that the correlation coefficient between NOBM and IPSL, GFDL-ESM2G and GFDL-ESM2M is moderate (0.310 to 0.572 in this study) and for CanESM2 model it is negative (-0.850). This indicates that the phase of the all the models except CanESM2 is same as the observations. From the Figure 7-3, it can also be seen that the standard deviation of all the models except IPSL model is less than NOBM. This indicates that all the models underestimate the amplitude of the chl values except for IPSL model which exaggerates the amplitude of chl values. The RMS difference between models GFDL-ESM2G, GFDL-ESM2M and CanESM2 and NOBM is between 0 and 0.1 whereas, RMS difference is more than 0.1 for IPSL model. Lower RMS difference for GFDL-ESM2G, GFDL-

ESM2M and CanESM2 climate models is due to lower difference in amplitudes of the models and observations. Lower RMS difference indicates that these models perform well in simulating the chl. On the other hand, IPSL model performs poorly as the RMS difference is higher which is due to larger difference in the amplitude of patterns.

7.4. Results for Indian Ocean

Table 7-4. Statistical terms computed for Taylor diagram

Model/statistical term	Standard Deviation	RMS difference	Correlation Coefficient
IPSL	0.092	0.065	0.710
GFDL-ESM2G	0.0372	0.059	0.534
GFDL-ESM2M	0.056	0.045	0.764
CanESM2	0.029	0.074	0.070

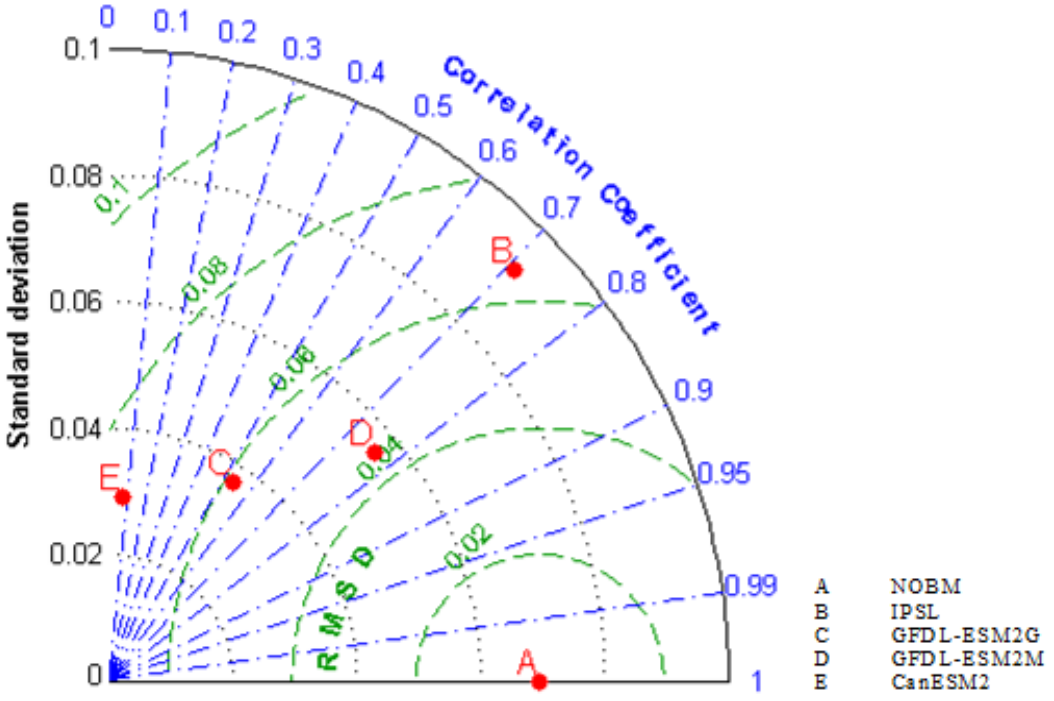

Figure 7-4. a). Pattern statistics describing the monthly time series of mean chl for IO region (1999-2005) simulated by 4 models compared with the observed.

From the Figure 7-4, it can be seen that the correlation coefficient between NOBM and all the models is moderate (0.534 to 0.764 in this study). This indicates that the phase of the all the models is same as the observations. From the Figure 7-4, it can also be seen that the standard deviation of all the models except IPSL model is less than NOBM. This indicates that all the models underestimate the amplitude of the chl values except for IPSL model which exaggerates the amplitude of chl values. The RMS difference between climate models and NOBM is between 0 and 0.1. Lower RMS difference for climate models is due to lower difference in amplitudes of the models and observations. Lower RMS difference indicates that these models perform well in simulating the chl.

8. Appendix II- EOF analysis and Truncation

8.1. Empirical Orthogonal Function (EOF) analysis

Statistically, EOF analysis is known as Principal Component Analysis (PCA). EOF analysis separates the data into 'modes' that are orthogonal to each other. These are not physical modes, but rather primarily data modes, i.e. data partitioned into orthogonal structures. EOFs are found by computing eigenvalues and eigenvectors of a spatially weighted anomaly covariance matrix. Eigenvalues represent the percent of variance explained by each mode. Projecting the eigenvector of each mode onto the spatially weighted covariance matrix derives the time series of each mode. EOF analysis can be applied in time domain and frequency domain. The procedure to perform EOF analysis on a dataset is presented as follows:

The data matrix F has n rows and p columns, where n is the number of time steps for which data is available and p is the number of locations for which measurements are taken at each time step. This way of arranging the data into a matrix is referred to as S-mode analysis. The covariance matrix of the data matrix F, is computed using the equation

Eq 8-1 $$R = F^T * F$$

Then solve the eigenvalue equation

Eq 8-2 $$RC = C*A$$

Where A (p by p) is a diagonal matrix, containing the eigenvalues E_i of R. The column vectors c_i of C (p by p) are the eigenvectors of R corresponding to the eigenvalues E_i. The percentage of variance explained by each mode can be found by dividing E_i by the sum of all the other eigenvalues. The eigenvector matrix C has the property $C^T*C = C*C^T = I$ (where I is identity matrix). This means that the eigenvectors or EOFs are orthogonal to each other. When EOF is plotted as a map, it represents a standing oscillation. To see how an EOF evolves in time, Eq 8-3 needs to be solved.

Eq 8-3 $\tilde{a}_i = F * \tilde{c}_i$

Where i represent the EOF. $\tilde{a}_i$ is a vector of length n. These are the principal component (PC) time series or the expansion coefficients of the EOFs. EOFs are uncorrelated in space; expansion coefficients are uncorrelated in time. As an example, Figure 2.12 and 2.13 shows map and time series of first EOF of GFDL-ESM2M historical greenhouse gas simulation and NOBM.

A new time-series of data can be created, by solving the Eq 8-4.

Eq 8-4 $F_n = \sum_{i=1}^{p} \tilde{a}_i (EOF)_i$

F_n has dimension of n x p. In order to obtain the new time-series data with reduced dimension space, the EOF matrix is truncated at some number N, where i = N <<p i.e. first few EOFs are used, as they represent the largest variance in the original data. There are techniques to determine the value of N, which are discussed in the next section.

8.2. Truncation

In order to reduce the dimension of the noise covariance matrix, EOFs are computed for the matrix C1_chunks (section 2.2.2.1.3 of chapter 2). Steps to compute EOFs have been discussed in the previous section. The result of the EOF analysis gives us a diagonal matrix (NxN) with eigenvalues and the matrix for eigenvectors (NxN). Time series of EOF can be obtained by solving Eq 8.3. A new data matrix can be created by using Eq 8.4, but to do that the matrix with eigenvectors needs to be truncated. The choice of the number of EOFs represents a compromise between a stable estimate of the noise covariance matrix and the need for a sufficiently large space for optimizing the fingerprint. There are several ways to decide the truncation level.

Random Choice

Randomly choosing a truncation level. It is not a very reliable way to choose the truncation level as there is no statistical basis to the choice.

Hegerl et al. (1996) Method

A simple method to choose the truncation level was developed by Hegerl et al. (1996). The steps to determine the truncation level are as follows:

1. Decompose C1_chunk matrix using EOF analysis and reconstruct matrix C1_chunk using various numbers of EOFs i.e. truncation levels. For example, if number of eigenvectors obtained after computing EOF analysis of C1_chunk matrix are 50, then choice of truncation level may be made by choosing multiples of 5. This will give us 10 truncation levels as 5, 10, 15 ....., 50. Choosing these truncation levels and for each level C1_chunk is reconstructed. This provides with 10 C1_chunk matrices.
2. For each of these C1_chunk matrices, noise covariance matrix C is computed. This provides with 10 noise covariance matrices.
3. Utilizing these noise covariance matrices, optimal fingerprint 'OF' is computed. Hegerl defined the optimal fingerprint as

   Eq 8-5 $OF = C^{-1}*g$

   Where, g is the guess signal as obtained in section 2.2.2.1.1. 10 noise covariance matrices give us 10 number of fingerprints.
4. Compute correlation between the guess pattern g and the fingerprint OF.
5. Plot the correlation coefficient against the number of EOFs chosen as truncation level.
6. The EOF number where there is a more dramatic decrease in the value of correlation coefficient indicates the number of EOFs chosen as truncation level.

Allen and Tett (1999) ENREF_2 ***Method***

Another method to determine the level of truncation was developed by Allen and Tett (1999).

1. Decompose C1_chunk matrix using EOF analysis and reconstruct matrix C1_chunk using various numbers of EOFs i.e. truncation levels. For example, if number of eigenvectors obtained after computing EOF analysis

of C1_chunk matrix are 50, then choice of truncation level may be made by choosing multiples of 5. This will give us 10 truncation levels as 5, 10, 15 ....., 50. Choosing these truncation levels and for each level C1_chunk is reconstructed. This provides with 10 C1_chunk matrices.

2. For each of these C1_chunk matrices, noise covariance matrix C is computed. This provides with 10 noise covariance matrices.
3. Utilizing these noise covariance matrices, beta is computed using equation 2. 10 noise covariance matrices give us 10 number of beta values.
4. Using these 10 beta values, 10 residuals are computed using Eq 2-5.
5. Using these 10 residual numbers, Eq 8-6 is solved

Eq 8-6 $r^2 = R'*(noise\_2*noise\_2')^{-1}*R$

This gives us 10 values of r^2. These values should be distributed as the sum of the square of k-m normally distributed random variables i.e. it can be chi-square (χ^2) or F distribution with k-m degrees of freedom. Here k is the level of truncation (in this case - 5,10....,50) and m is the number of response patterns for which beta is to be computed. For example, if OF is being implemented using only greenhouse gas signal then, m=1.

6. Plot $(k-m)/r^2$ against the level of truncation with lines of 5-95% range of $(k-m)/\chi^2$ and (1/F) distribution.
7. The EOF number where there is a more dramatic decrease in the value of correlation coefficient indicates the number of EOFs chosen as truncation level.
8. The line of $(k-m)/r^2$ should not cross the 5-95% range of $(k-m)/\chi^2$ and (1/F) distribution. This is the 'residual consistency check' for the noise matrix. If the line does not move outside the range it indicates that the control simulation does not include patterns which contain unrealistically low or high variance i.e. noise is represented correctly by the model.

The process chart for the truncation of a matrix by Hegerl et al. (1996) and Allen and Tett (1999) method is given in Appendix III.

9. Appendix III- Process Flowchart

9.1. Pre-processing

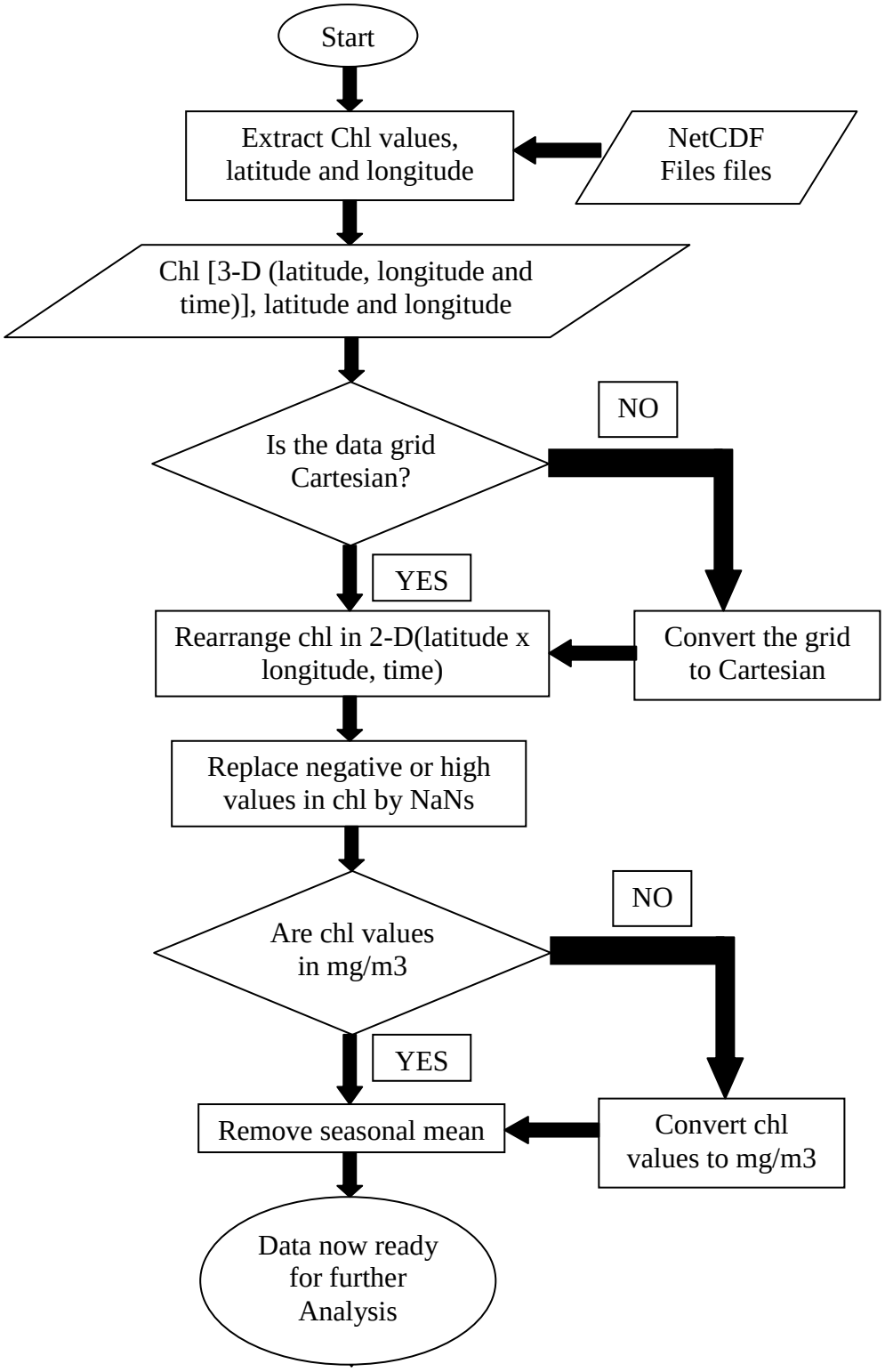

9.2. Compute noise covariance matrix

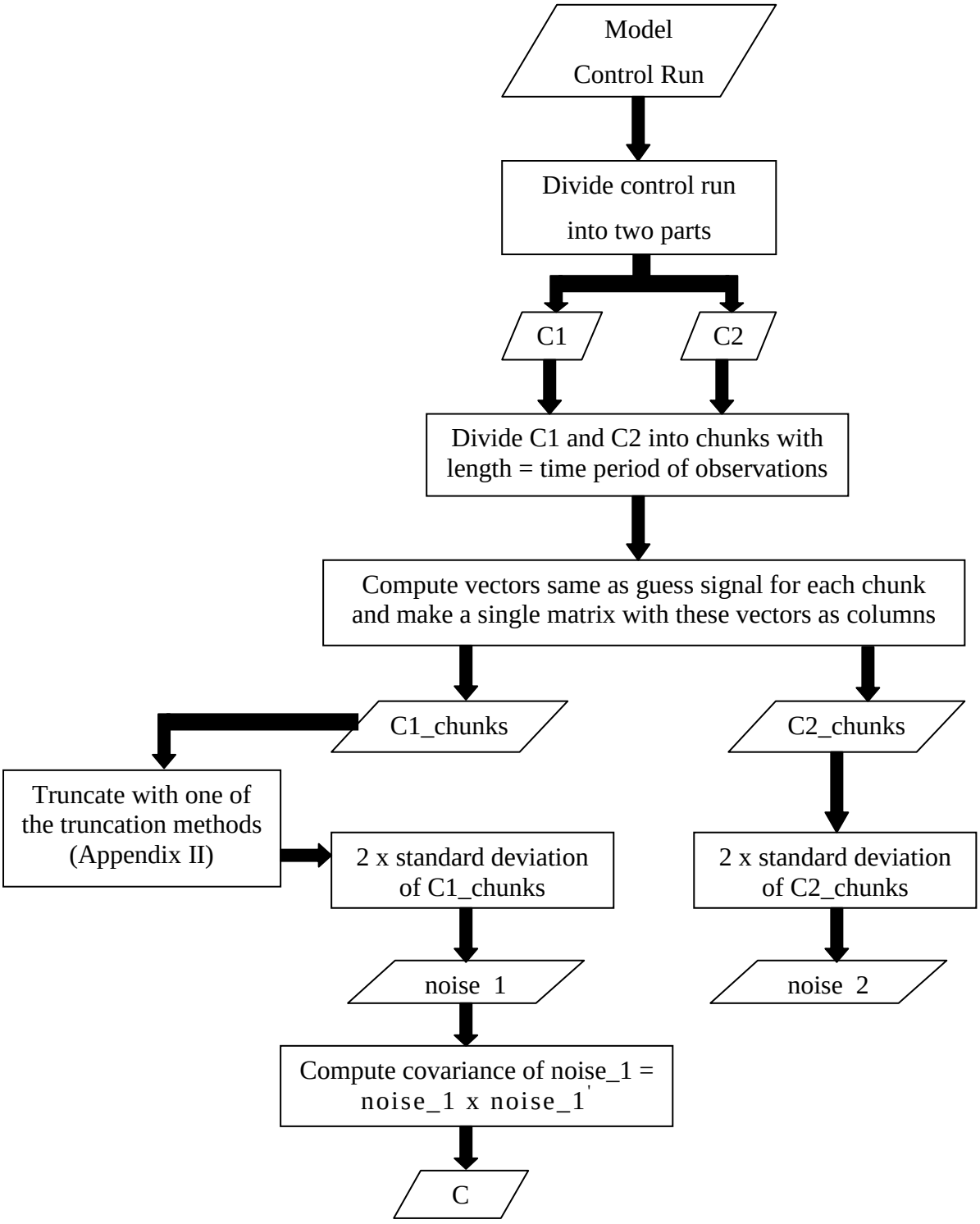

9.3. Truncation

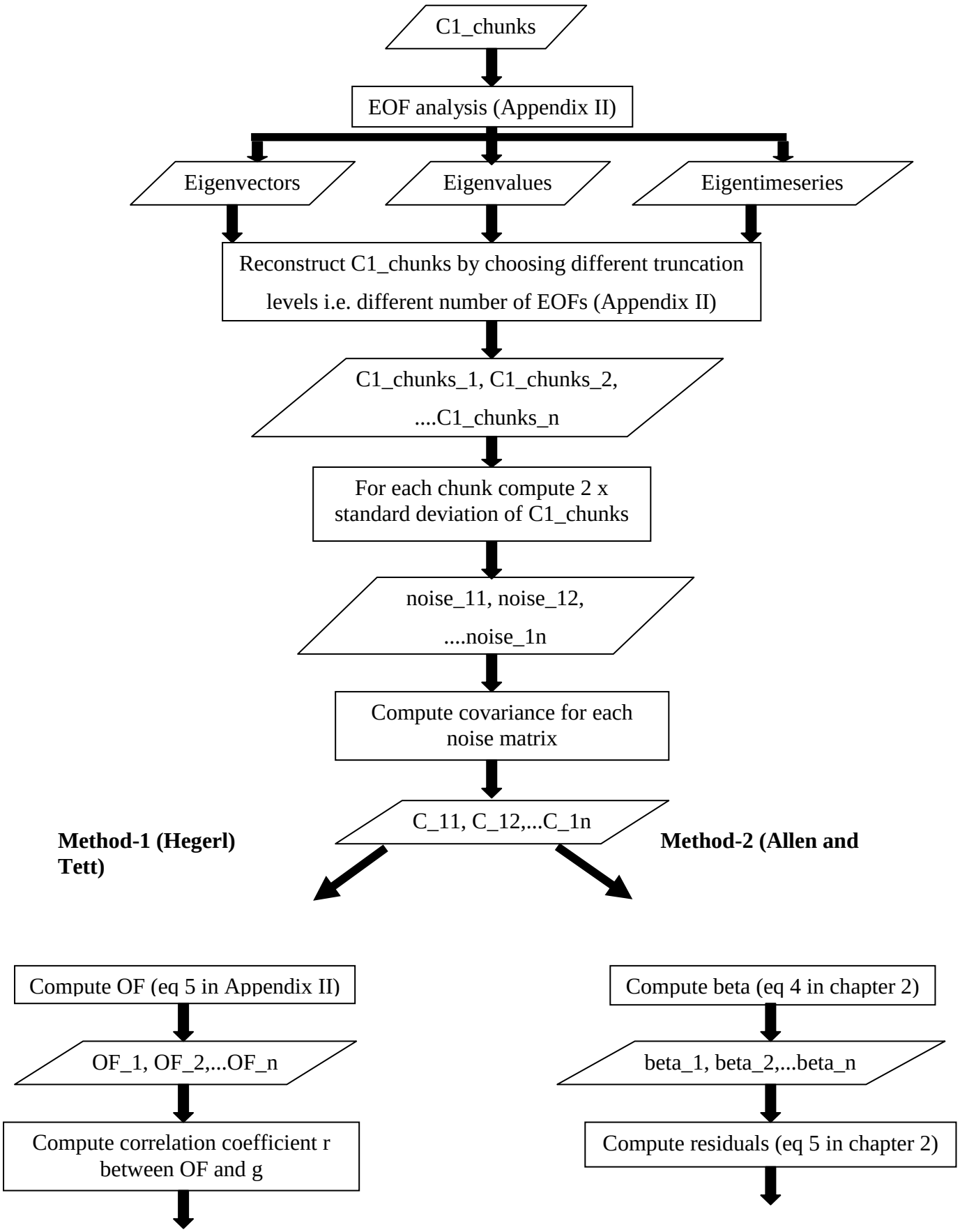

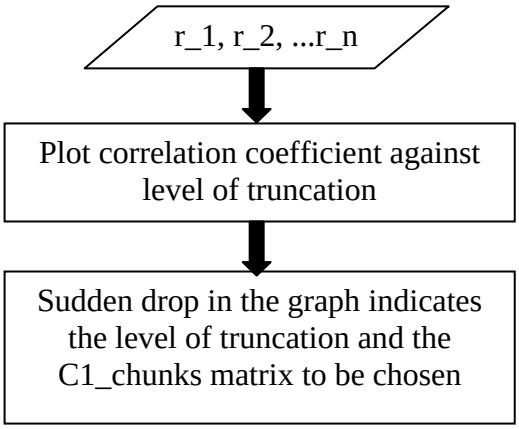
r_1, r_2, ...r_n
Plot correlation coefficient against level of truncation
Sudden drop in the graph indicates the level of truncation and the C1_chunks matrix to be chosen

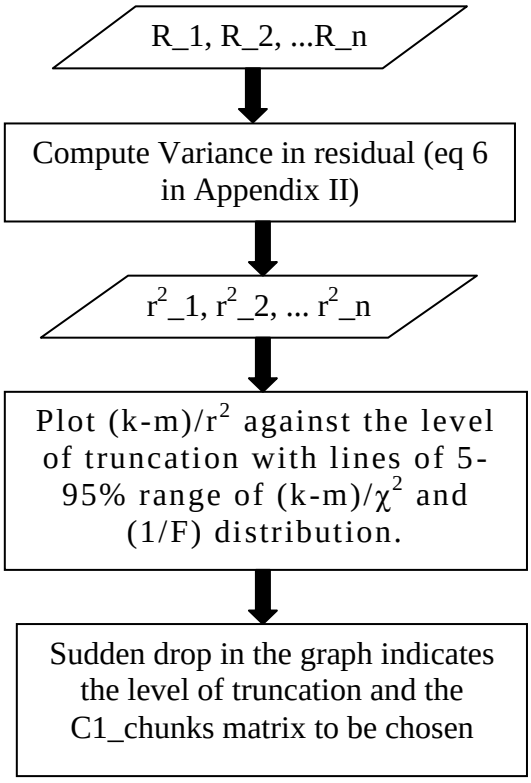
R_1, R_2, ...R_n
Compute Variance in residual (eq 6 in Appendix II)
r2_1, r2_2, ... r2_n
Plot (k-m)/r2 against the level of truncation with lines of 5-95% range of (k-m)/χ2 and (1/F) distribution.
Sudden drop in the graph indicates the level of truncation and the C1_chunks matrix to be chosen

9.4. Optimal Fingerprint Method

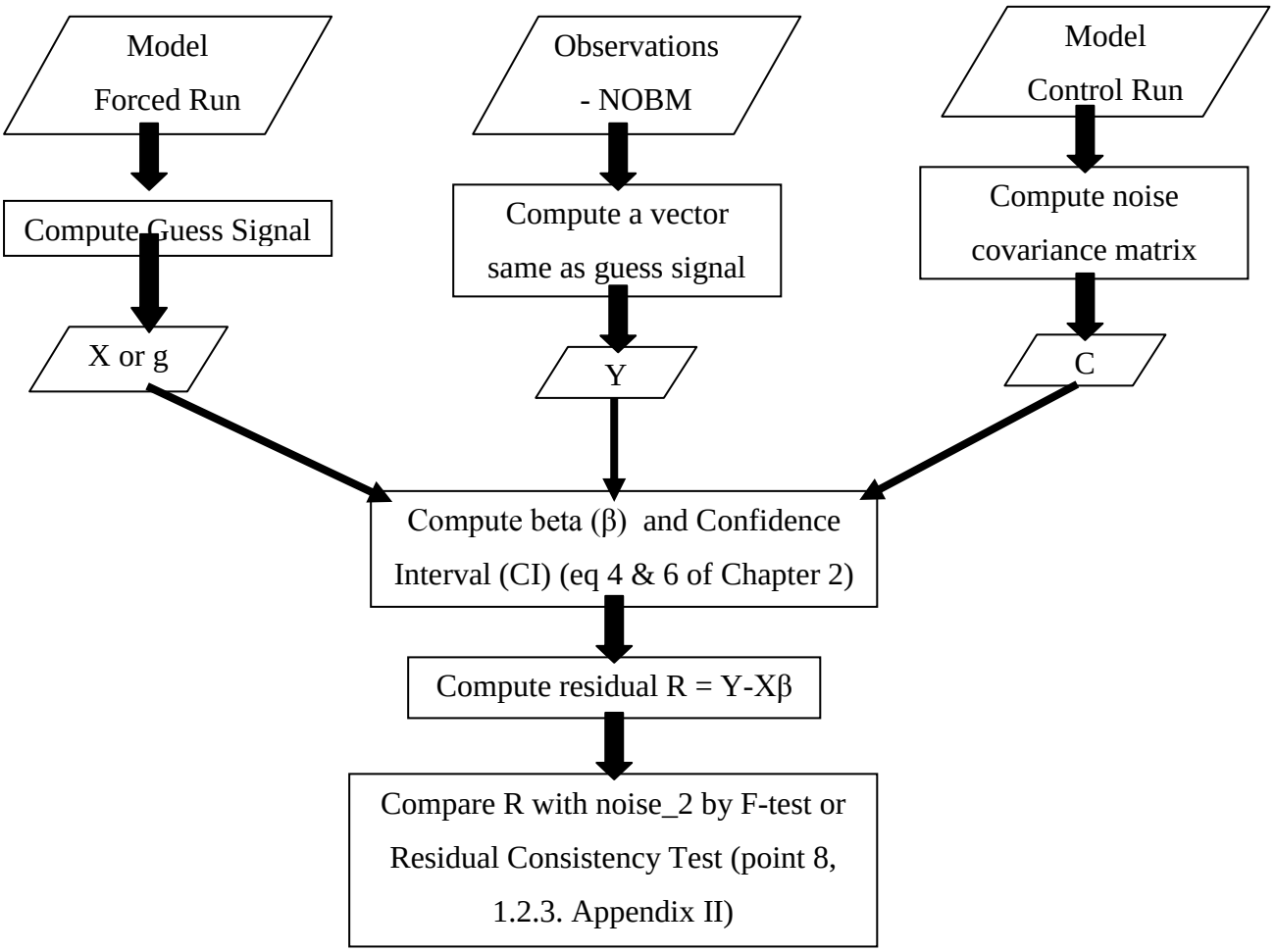

10. Appendix IV-Results for Chapter 3

10.1. Trend in chlorophyll

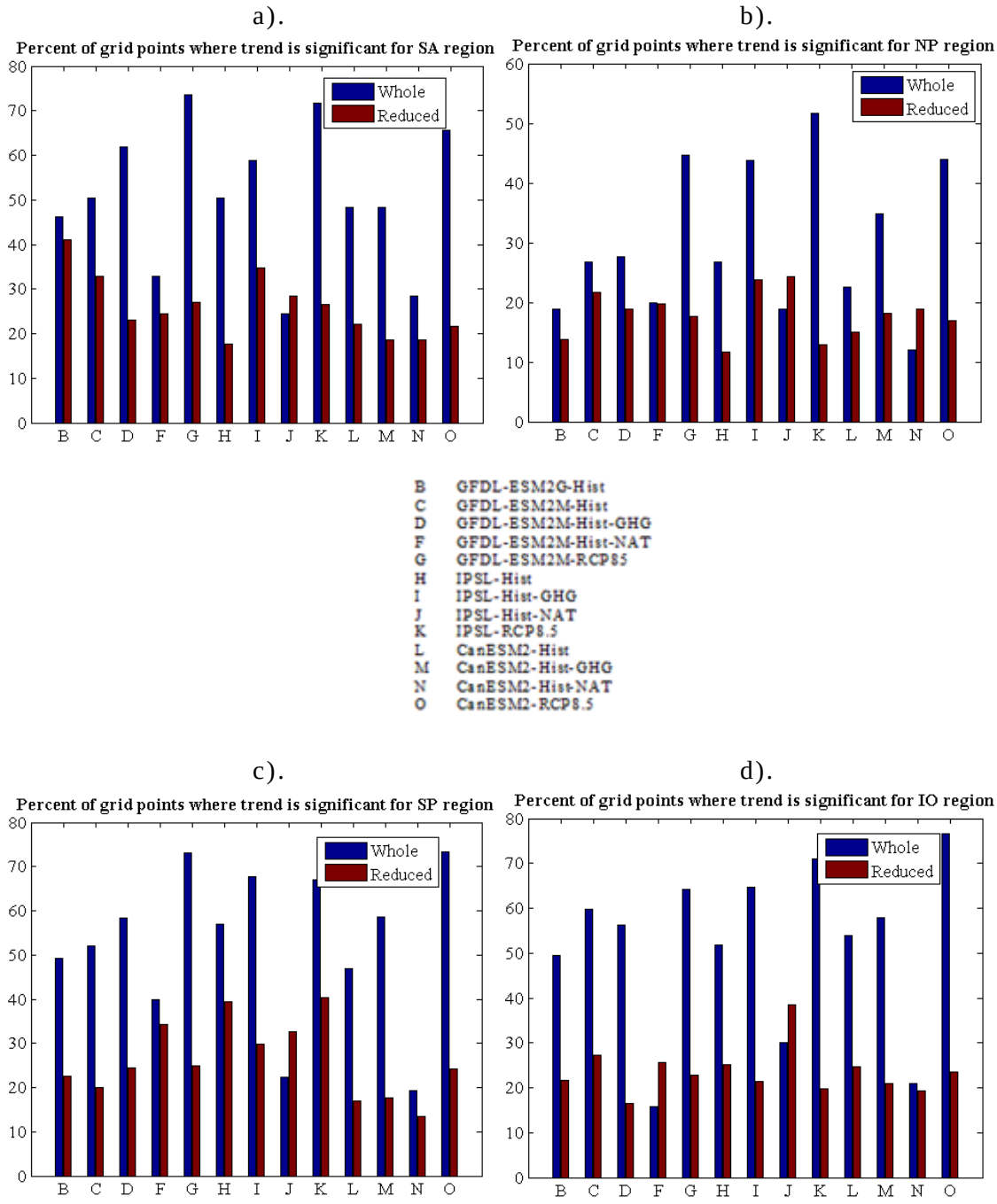

Figure 10-1. Percent of grid points where trend is significant from whole and reduced time period of simulations in a). SA region, b). NP region, c). SP region, d). IO region.

10.2. Results of comparison of linear trend from model simulations with NOBM data

Table 10-1. Statistical terms of comparison for North Atlantic region.

Model Simulation	Correlation Coefficient		RMS difference		Standard Deviation	
	W	R	W	R	R	R
B	0.04934	-0.01691	0.00081	0.00089	0.00002	0.00037
C	-0.06979	0.04906	0.00081	0.00095	0.00001	0.00055
D	-0.03241	0.06536	0.00081	0.00091	0.00001	0.00049
F	-0.05828	0.34773	0.00081	0.00078	0.00001	0.00047
G	0.12233	-0.11966	0.00080	0.00099	0.00004	0.00049
H	-0.16797	0.18849	0.00081	0.00112	0.00002	0.00094
I	-0.25468	0.009230	0.00082	0.00132	0.00004	0.00105
J	-0.15500	-0.11450	0.00081	0.00117	0.00001	0.00076
K	0.14964	0.19955	0.00080	0.00101	0.00014	0.00079
L	0.17773	0.06787	0.00080	0.00116	0.00001	0.00089
M	0.21221	-0.14225	0.00080	0.00132	0.00001	0.00094
N	0.09627	-0.10528	0.00081	0.00134	0.00001	0.00099
O	0.11607	-0.06839	0.00080	0.00117	0.00012	0.00079

10.2.1. Results for South Atlantic Region

Spatial linear trend for SA region from NOBM and greenhouse gas simulations of the reduced time period of model simulations is shown in Figure 10-2. Visual comparison of the spatial trends from model simulations (Figure 10-2b, c & d) indicates that models show some consistency in the patterns of linear trend in SA. For example, increasing trend observed in north-western part of SA from ESM2M historical greenhouse gas simulation (Figure 10-2b) is also observed in historical greenhouse gas simulation from IPSL (Figure 10-2c) and partially in CanESM2 (Figure 10-2d). On the other hand, there is a declining trend observed in north-western part of SA from

NOBM (Figure 10-2a) which is not consistent to that observed in spatial linear trend from model simulations. However, an increasing trend observed in south-western part of SA from NOBM (Figure 10-2a) is also observed in spatial linear trend from IPSL historical greenhouse gas simulation (Figure 10-2c). Thus, it can be concluded that there is partial consistency between signal from NOBM and model simulations and also among the signals from model simulations.

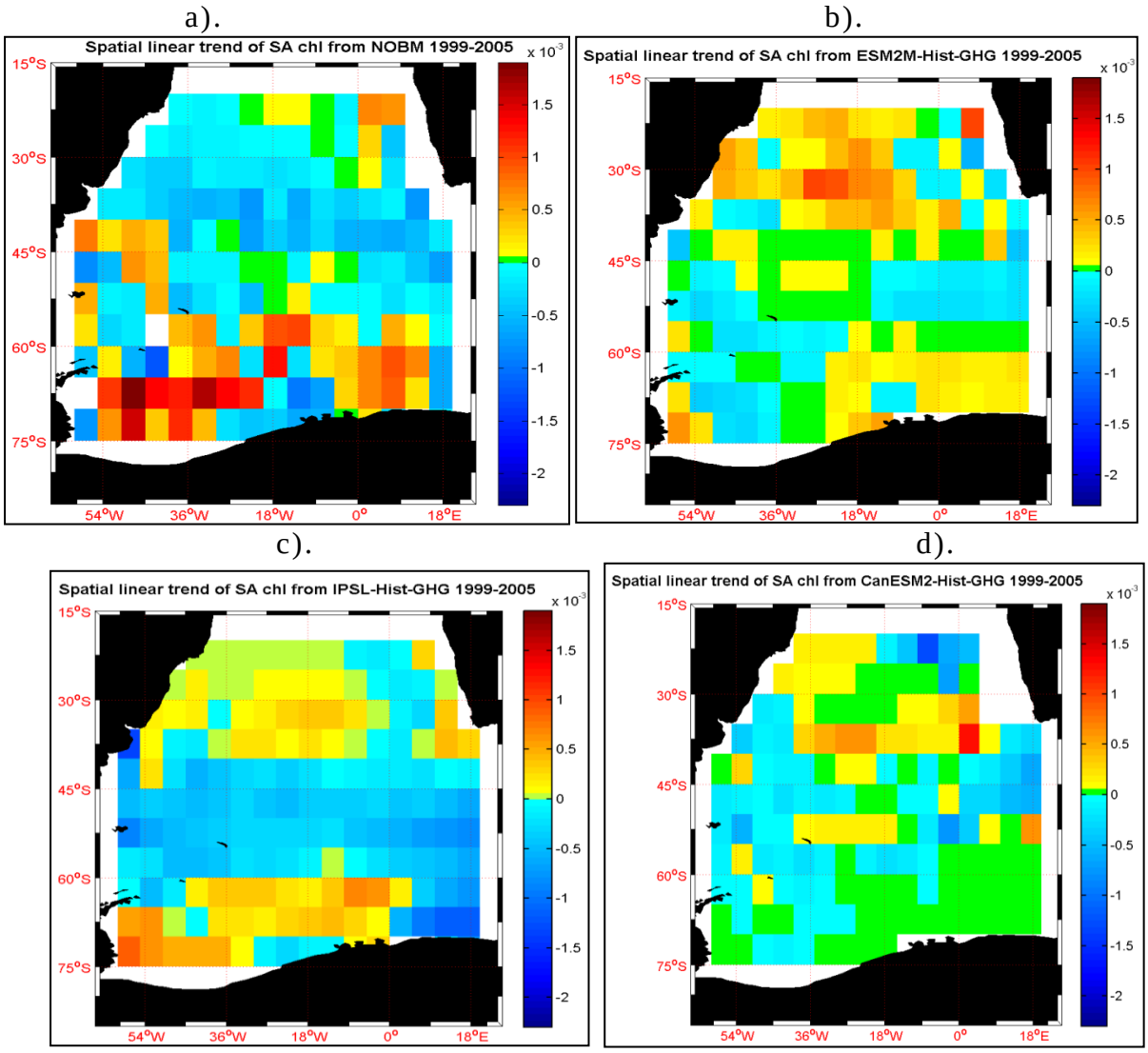

Figure 10-2. Spatial linear trend for SA region from a). NOBM and reduced time period of b). GFDL-ESM2M Historical GHG c). IPSL Historical GHG and d). CanESM2 Historical GHG simulations.

Table 10-2 below shows the value of the statistical terms of comparison i.e. the correlation coefficient, root mean square difference and standard deviation when spatial linear trend for SA region of the ocean

computed from different model simulations for two time periods (whole and reduced) was compared with linear trend from NOBM.

Table 10-2. Statistical terms of comparison for South Atlantic region.

Model Simulation	Correlation Coefficient		RMS difference		Standard Deviation	
	W	R	W	R	W	R
A					0.00060484	
B	-0.007740	-0.100784	0.000605	0.00088	0.00000598	0.000586
C	0.033665	0.005380	0.000605	0.00070	0.00000728	0.000366
D	0.071567	-0.116257	0.000604	0.00068	0.00000992	0.000237
F	0.140550	-0.026715	0.000604	0.00069	0.00000444	0.000307
G	-0.029908	0.170485	0.000608	0.00061	0.00000415	0.000245
H	0.350438	-0.201214	0.000603	0.00075	0.00000685	0.000344
I	0.235165	0.140842	0.000602	0.00067	0.00000120	0.000376
J	-0.002439	0.331355	0.000605	0.00060	0.00000423	0.000380
K	0.231753	0.232088	0.000595	0.00060	0.00005280	0.000053
L	0.023729	-0.036349	0.000605	0.00066	0.00000885	0.000241
M	0.054832	-0.062557	0.000605	0.00067	0.00000722	0.000260
N	-0.118415	0.063899	0.000605	0.00064	0.00000400	0.000264
O	0.103137	-0.000576	0.000602	0.00070	0.00004580	0.000351

Taylor diagrams associated with the comparisons are shown in Figure 10-3. Figure 10-3a shows statistical terms of comparisons when spatial linear trend was computed from whole time period of simulations. Figure 10-3b shows statistical terms of comparisons when spatial linear trend was computed from reduced time period of simulations.

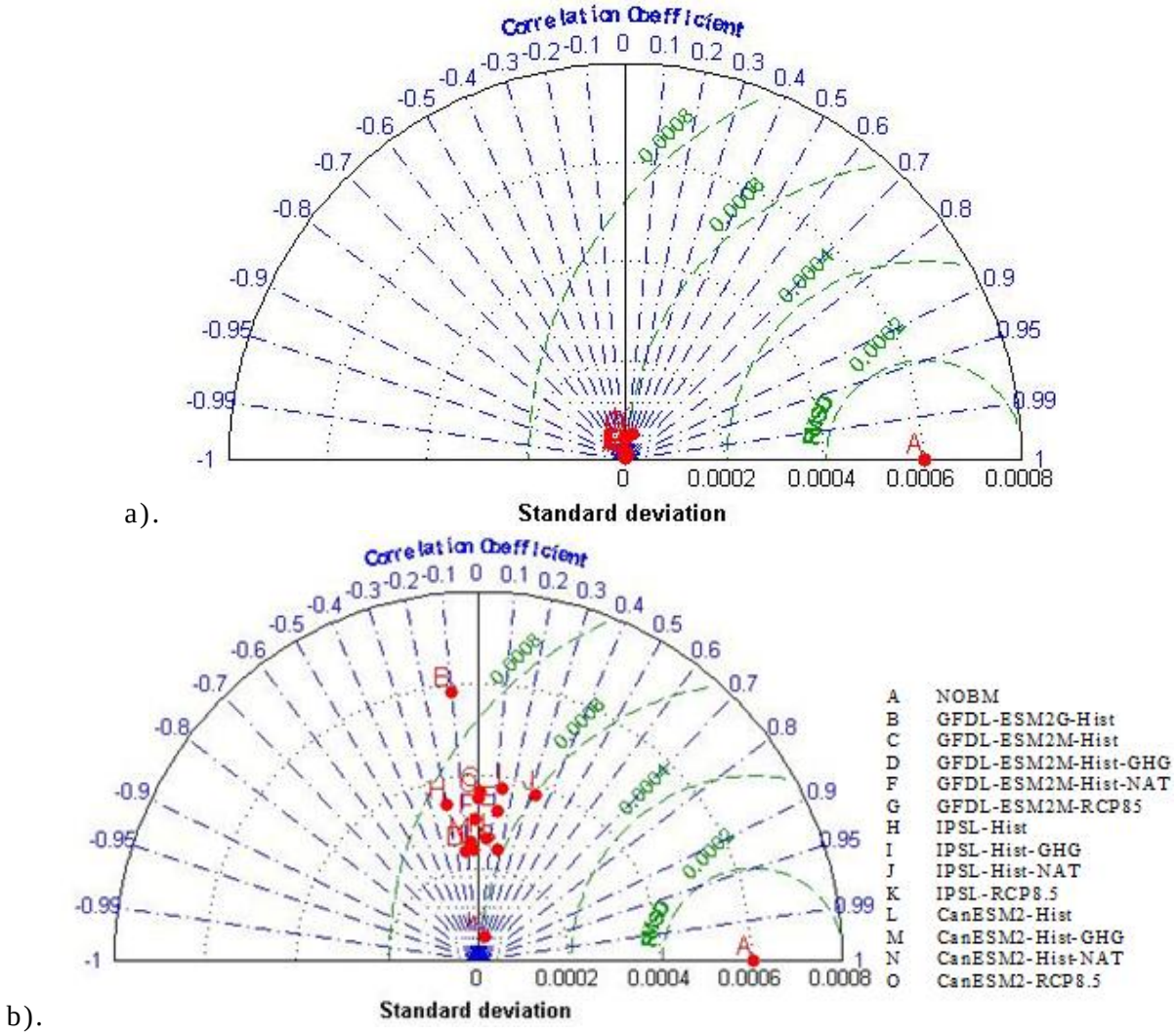

a).

b).

Figure 10-3. Taylor diagrams associated with the comparisons of spatial linear trend for SA region computed from a). whole time period of simulations b). reduced time period of simulations with spatial linear trend for SA region computed from NOBM.

From Figure 10-3, it can be seen that the correlation coefficient for all the model simulations is very low (-0.2012 to 0.3504 in this study). Low correlation coefficient indicates that the spatial linear trend from model simulations is not correctly phased with NOBM. For most of the simulations correlation coefficient changes sign and magnitude for the two time periods for which linear trend is computed. This indicates that signal from whole time period of data is not the same as the reduced time period of data and they should be treated as two different metrics of signal computation. It should also be noted from Figure 10-3 that there is only partial consistency in the sign of correlation coefficient obtained from same forcing simulation from different models. For example, correlation coefficient obtained for

whole time period of historical greenhouse gas simulation from ESM2M and IPSL model is positive but for CanESM2 model correlation coefficient is negative.

It can also be seen from Figure 10-3 that the standard deviation of all the model simulations for both the time periods is lower than NOBM. The difference between the standard deviations of NOBM and model simulations for the whole time period (10^{-4}) is higher compared to the difference between the standard deviations of NOBM and the model simulations for the reduced time period (10^{-5}). From this it can be concluded that the amplitude of the spatial linear trend from both the time period of model simulations underestimate the amplitude of the spatial linear trend of chl and the 'reduced time period' of model simulations gives a much closer estimate to the amplitude of the spatial linear trend from NOBM.

10.2.2. Results for North Pacific Region

Spatial linear trend for NP region from NOBM and greenhouse gas simulations of the reduced time period of model simulations is shown in Figure 10-4. Visual comparison of the spatial trends from model simulations (Figure 10-4b, c & d) indicates that models show some consistency in the patterns of linear trend in NP. For example, increasing trend observed in north-eastern part of NP from ESM2M historical greenhouse gas simulation (Figure 10-4b) is also partially observed in historical greenhouse gas simulation from IPSL (Figure 10-4c) and CanESM2 (Figure 10-4d). On the other hand, there is a declining trend observed in north-eastern part of NP from NOBM (Figure 10-4a) which is not consistent to that observed in spatial linear trend from model simulations. However, an increasing trend observed in south-western part of NP from NOBM (Figure 10-4a) is also observed partially in spatial linear trend from historical greenhouse gas simulation of ESM2M (Figure 10-4b) and IPSL (Figure 10-4c). Thus, it can be concluded that there is partial consistency between signal from NOBM and model simulations and also among the signal from model simulations.

a). b).

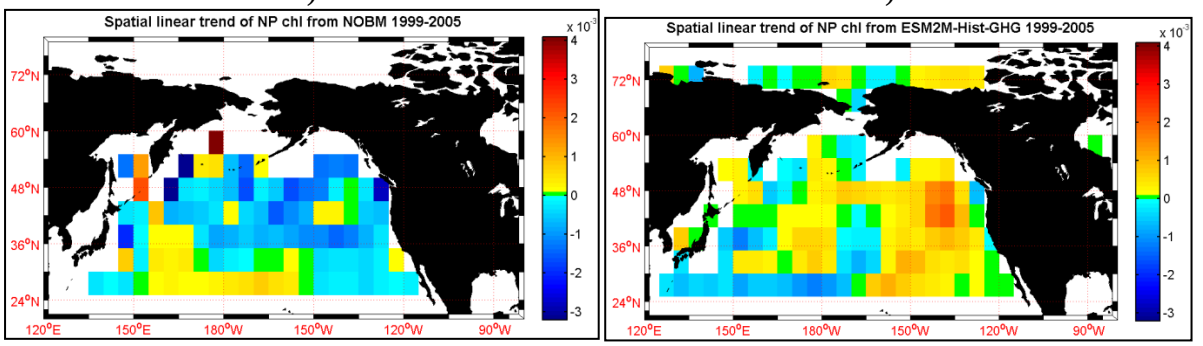

c). d).

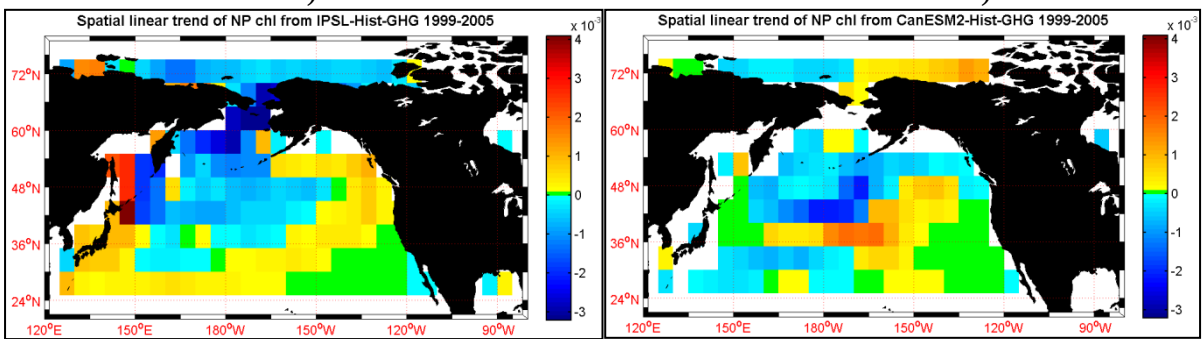

Figure 10-4. Spatial linear trend for NP region from a). NOBM and reduced time period of b). GFDL-ESM2M Historical GHG c). IPSL Historical GHG and d). CanESM2 Historical GHG simulations.

Table 10-3 below shows the value of the statistical terms of comparison i.e. the correlation coefficient, root mean square difference and standard deviation when spatial linear trend for NP region of the ocean computed from different model simulations for two time periods (whole and reduced) was compared with linear trend from NOBM.

Table 10-3. Statistical terms of comparison for North Pacific region.

Model Simulation	Correlation Coefficient		RMS difference		Standard Deviation	
	W	R	W	R	R	R
A					0.00083	
B	0.00807	0.06381	0.00082	0.00088	0.00000	0.00035
C	0.18908	0.05393	0.00082	0.00091	0.00001	0.00044
D	-0.11494	-0.02909	0.00083	0.00099	0.00001	0.00052
F	0.21524	0.28005	0.00082	0.00083	0.00001	0.00049
G	-0.08146	-0.13764	0.00083	0.00100	0.00003	0.00047
H	-0.28003	0.23434	0.00083	0.00086	0.00001	0.00049
I	-0.33647	-0.32976	0.00083	0.00115	0.00001	0.00058
J	0.12503	-0.25102	0.00082	0.00121	0.00001	0.00071
K	-0.01911	-0.03487	0.00083	0.00092	0.00004	0.00038
L	0.02224	0.02224	0.00082	0.00082	0.00001	0.00001
M	0.27757	0.27757	0.00082	0.00082	0.00001	0.00001
N	0.04087	0.04087	0.00082	0.00082	0.00001	0.00001
O	0.18145	0.18145	0.00082	0.00082	0.00004	0.00004

Taylor diagrams associated with the comparisons are shown in Figure 10-5. Figure 10-5a shows statistical terms of comparisons when spatial linear trend was computed from whole time period of simulations. Figure 10-5b shows statistical terms of comparisons when spatial linear trend was computed from reduced time period of simulations.

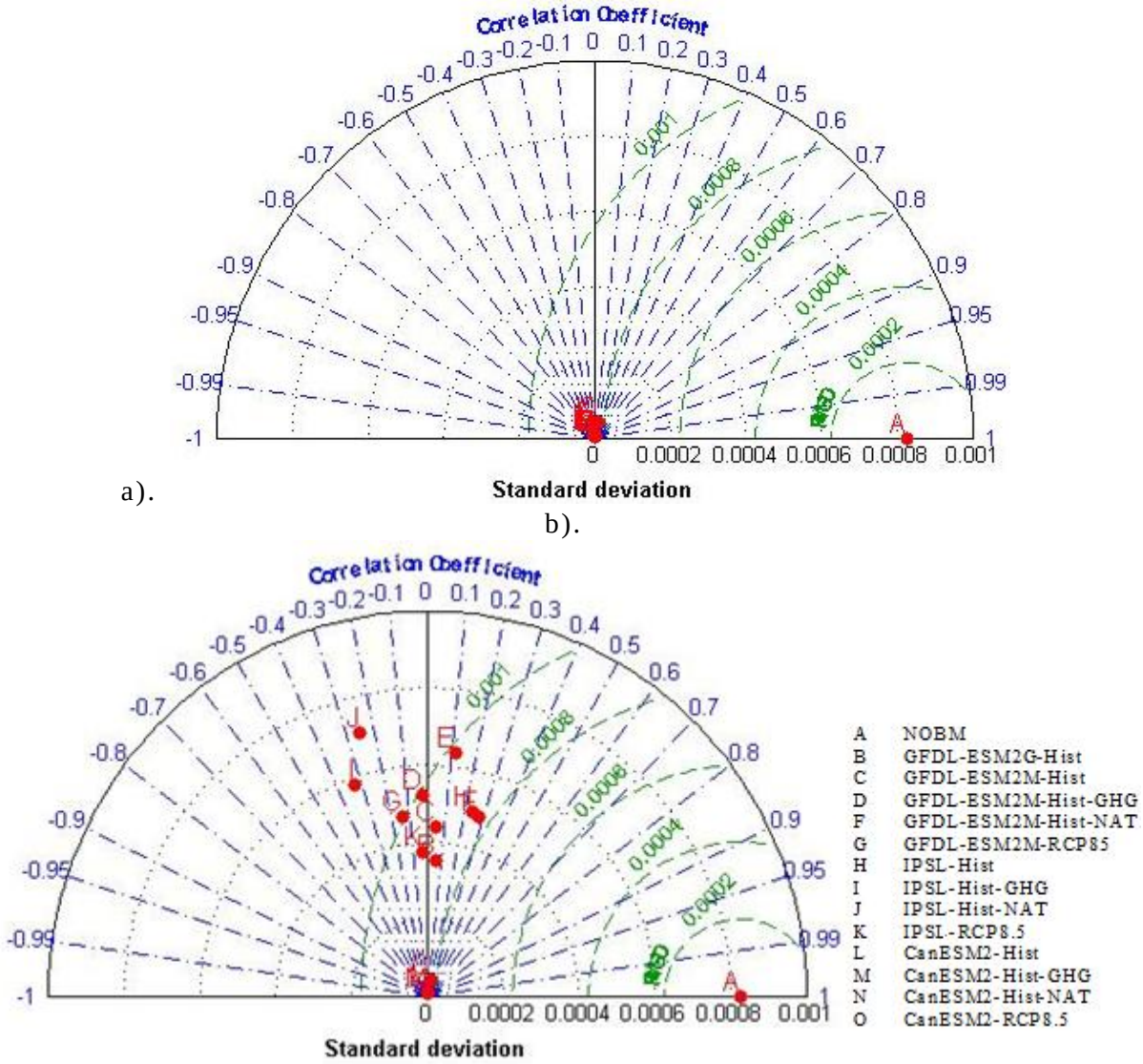

Figure 10-5. Taylor diagrams associated with the comparisons of spatial linear trend for NP region computed from a). whole time period of simulations b). reduced time period of simulations with spatial linear trend for NP region computed from NOBM.

From Figure 10-5, it can be seen that the correlation coefficient for all the model simulations is low (-0.3365 to 0.2801 in this study). Low correlation coefficient indicates that the spatial linear trend from model simulations is not correctly phased with NOBM. For most of the simulations, correlation coefficient does not change sign for whole time period to reduced time period of model simulations but the magnitude of correlation coefficient changes. This indicates that signal from whole time period of data has same phase as the signal from the reduced time period of data but due to difference in magnitude of correlation coefficient these two signals cannot be considered as same, therefore they should be treated as two different metrics

of signal computation. It should also be noted from Figure 10-5 that there is only partial consistency in the sign of correlation coefficient obtained from same forcing simulation from different models. For example, correlation coefficient obtained for whole time period of historical greenhouse gas simulation from ESM2M and IPSL model is negative but for CanESM2 model correlation coefficient is positive.

It can also be seen from Figure 10-5 that the standard deviation of all the model simulations for both the time periods is lower than NOBM. The difference between the standard deviations of NOBM and model simulations for the whole time period (10^{-4}) is higher compared to the difference between the standard deviations of NOBM and the model simulations for the reduced time period (10^{-5}). From this it can be concluded that the amplitude of the spatial linear trend from both the time period of model simulations underestimate the amplitude of the spatial linear trend of chl and the 'reduced time period' of model simulations gives a much closer estimate to the amplitude of the spatial linear trend from NOBM.

10.2.3. Results for South Pacific Region

Spatial linear trend for SP region from NOBM and greenhouse gas simulations of the reduced time period of model simulations is shown in Figure 10-6. Spatial linear trend from greenhouse gas simulations is chosen as an example for visual comparison because this is the signal that is of interest in this detection study. Visual comparison of the spatial trends from model simulations (Figure 10-6b, c & d) indicates that there is partial consistency in the signals obtained from the same model forcing simulation from different models. For example, a decreasing trend observed in mid-eastern part of SP from IPSL (Figure 10-6c) is also observed partially in spatial linear trend from ESM2M (Figure 10-6b) and CanESM2 (Figure 10-6d). Also, comparison of signals from model simulations (Figure 10-6b, c & d) with NOBM (Figure 10-6a) indicates that for some simulations patterns are similar to NOBM at some grid points but are completely opposite at other grid points. For example, declining trend observed in mid-eastern part of SP from NOBM is also

observed in spatial linear trend from IPSL-Hist-GHG, but CanESM2-Hist-GHG (Figure 10-6d) shows a partially increasing and partially decreasing trend in mid-eastern part of NOBM.

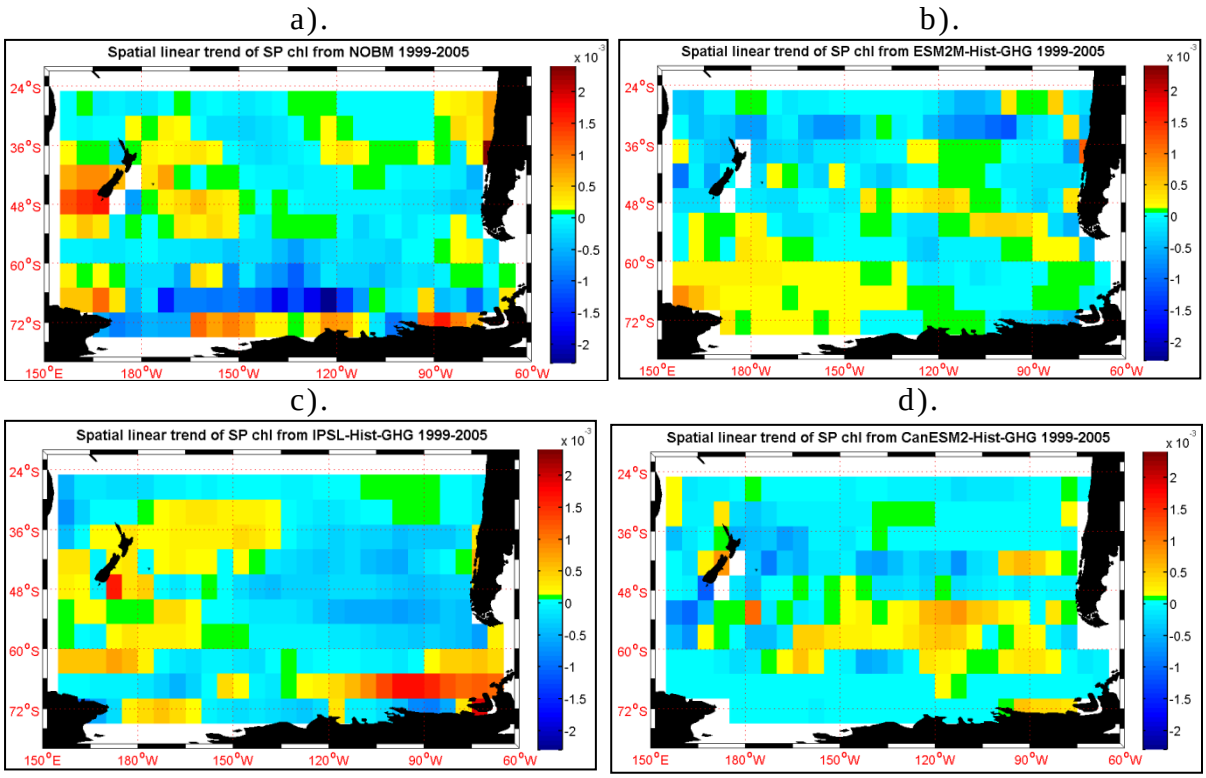

Figure 10-6. Spatial linear trend for SP region from a). NOBM and reduced time period of b). GFDL-ESM2M Historical GHG c). IPSL Historical GHG and d). CanESM2 Historical GHG simulations.

Table 10-4 below shows the value of the statistical terms of comparison i.e. the correlation coefficient, root mean square difference and standard deviation when spatial linear trend for SP region of the ocean computed from different model simulations for two time periods (whole and reduced) was compared with linear trend from NOBM.

Table 10-4. Statistical terms of comparison for South Pacific region.

Model Simulation	Correlation Coefficient		RMS difference		Standard Deviation	
	W	R	W	R	R	R
A					0.00051	
B	0.03721	0.08205	0.00051	0.00056	0.00001	0.00028
C	-0.05226	0.17997	0.00051	0.00052	0.00001	0.00023
D	-0.00808	-0.05678	0.00051	0.00059	0.00001	0.00028
F	-0.06027	0.14966	0.00051	0.00056	0.00001	0.00032
G	-0.00805	-0.03273	0.00051	0.00058	0.00003	0.00027
H	0.08920	-0.00490	0.00051	0.00070	0.00001	0.00048
I	-0.02951	-0.18956	0.00051	0.00070	0.00002	0.00039
J	-0.18843	0.20451	0.00051	0.00069	0.00000	0.00058
K	-0.16051	0.21961	0.00052	0.00063	0.00004	0.00051
L	0.08771	0.15587	0.00051	0.00057	0.00001	0.00035
M	0.05905	-0.08477	0.00051	0.00059	0.00001	0.00027
N	0.07870	-0.12158	0.00051	0.00064	0.00001	0.00034
O	0.01656	-0.00410	0.00051	0.00076	0.00004	0.00056

Taylor diagrams associated with the comparisons are shown in Figure 10-7. Part a of Figure 10-7 shows statistical terms of comparisons when spatial linear trend was computed from whole time period of simulations. Part b of Figure 10-7 is the zoomed in graph of part a to show the points more clearly. Part c of Figure 10-7 shows statistical terms of comparisons when spatial linear trend was computed from reduced time period of simulations.

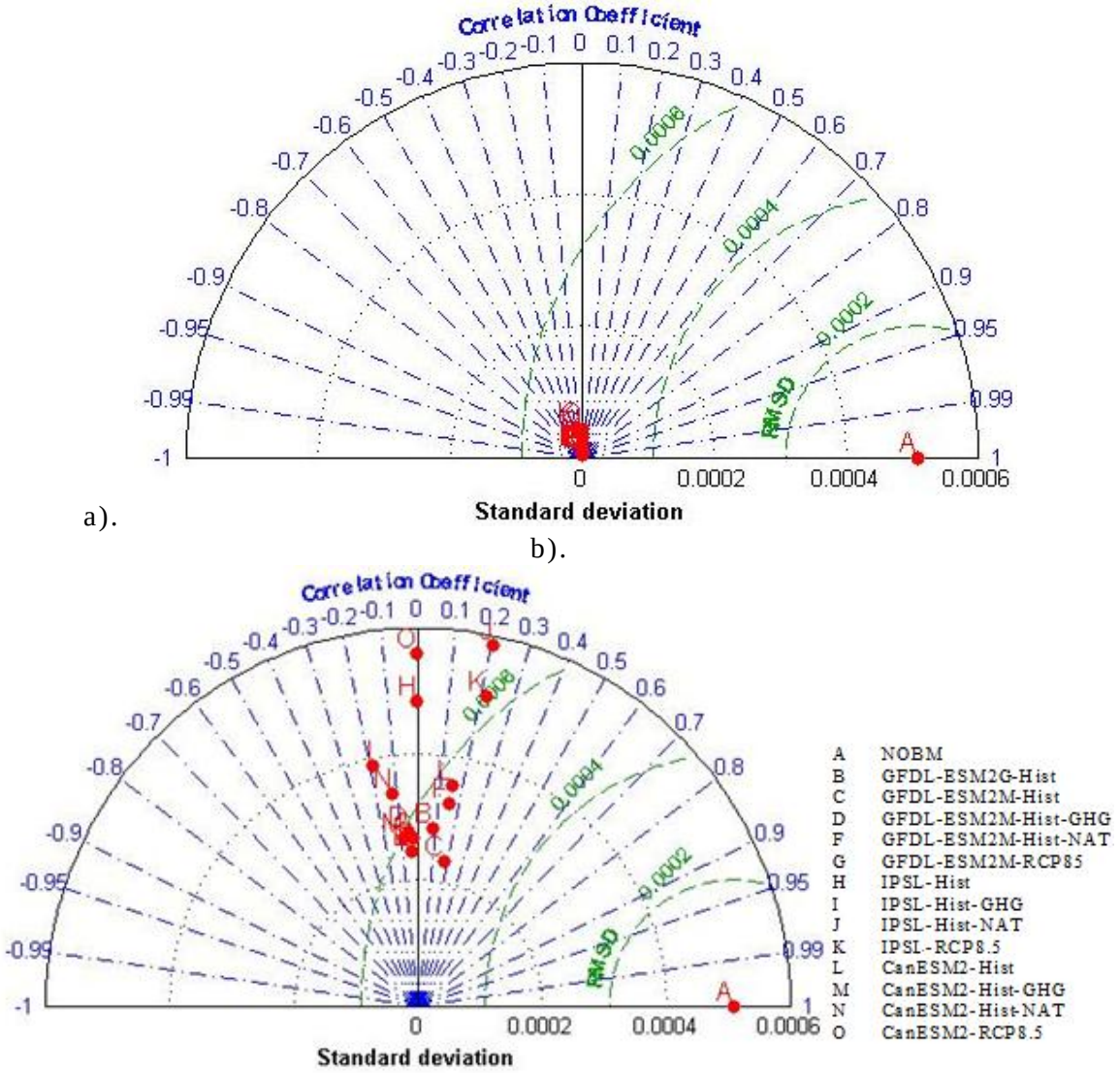

Figure 10-7. Taylor diagrams associated with the comparisons of spatial linear trend for SP region computed from a). whole time period of simulations b). reduced time period of simulations with spatial linear trend for SP region computed from NOBM.

From Figure 10-7, it can be seen that the correlation coefficient for all the model simulations is low (-0.1896 to 0.2196 in this study). Low correlation coefficient indicates that the spatial linear trend from model simulations is not correctly phased with NOBM. For most of the simulations correlation coefficient changes sign and magnitude for the two time periods for which linear trend is computed. This indicates that signal from whole time period of data is not the same as the reduced time period of data and they should be treated as two different metrics of signal computation. It should also be noted from Figure 10-7 that there is partial consistency in the sign of correlation coefficient obtained from same forcing simulation from

different models. For example, correlation coefficient obtained for whole time period of historical greenhouse gas simulation from ESM2M and IPSL model is negative but for CanESM2 model correlation coefficient is positive.

It can also be seen that the standard deviation of all the model simulations for both the time periods is lower than NOBM except for IPSL historical natural and CanESM2 RCP8.5 reduced time period simulation. The difference between the standard deviations of NOBM and model simulations for the whole time period (10^{-4}) is higher compared to the difference between the standard deviations of NOBM and the model simulations for the reduced time period (10^{-5}). From this it can be concluded that the amplitude of the spatial linear trend from both the time period of model simulations underestimate the amplitude of the spatial linear trend of chl and the 'reduced time period' of model simulations gives a much closer estimate to the amplitude of the spatial linear trend from NOBM.

10.2.4. Results for Indian Ocean Region

Spatial linear trend for IO region from NOBM and greenhouse gas simulations of the reduced time period of model simulations is shown in Figure 10-8. Spatial linear trend from greenhouse gas simulations is chosen as an example for visual comparison because this is the signal that is of interest in this detection study. Visual comparison of the spatial trends from model simulations (Figure 10-8b, c & d) indicates that there is partial consistency in the signals obtained from the same model forcing simulation from different models. For example, decreasing trend observed in eastern part of IO from ESM2M (Figure 10-8b) is also observed partially in spatial linear trend from IPSL (Figure 10-8c) and CanESM2 (Figure 10-8d). Also, comparison of signals from model simulations (Figure 10-8b, c & d) with NOBM (Figure 10-8a) indicates that for some simulations patterns are similar to NOBM at some grid points but are completely opposite at other grid points. For example, declining trend observed in southern part of IO from NOBM (Figure 10-8a) is also observed in spatial linear trend from CanESM2-

Hist-GHG (Figure 10-8d), but IPSL-Hist-GHG (Figure 10-8c) show an increasing trend in southern part of IO.

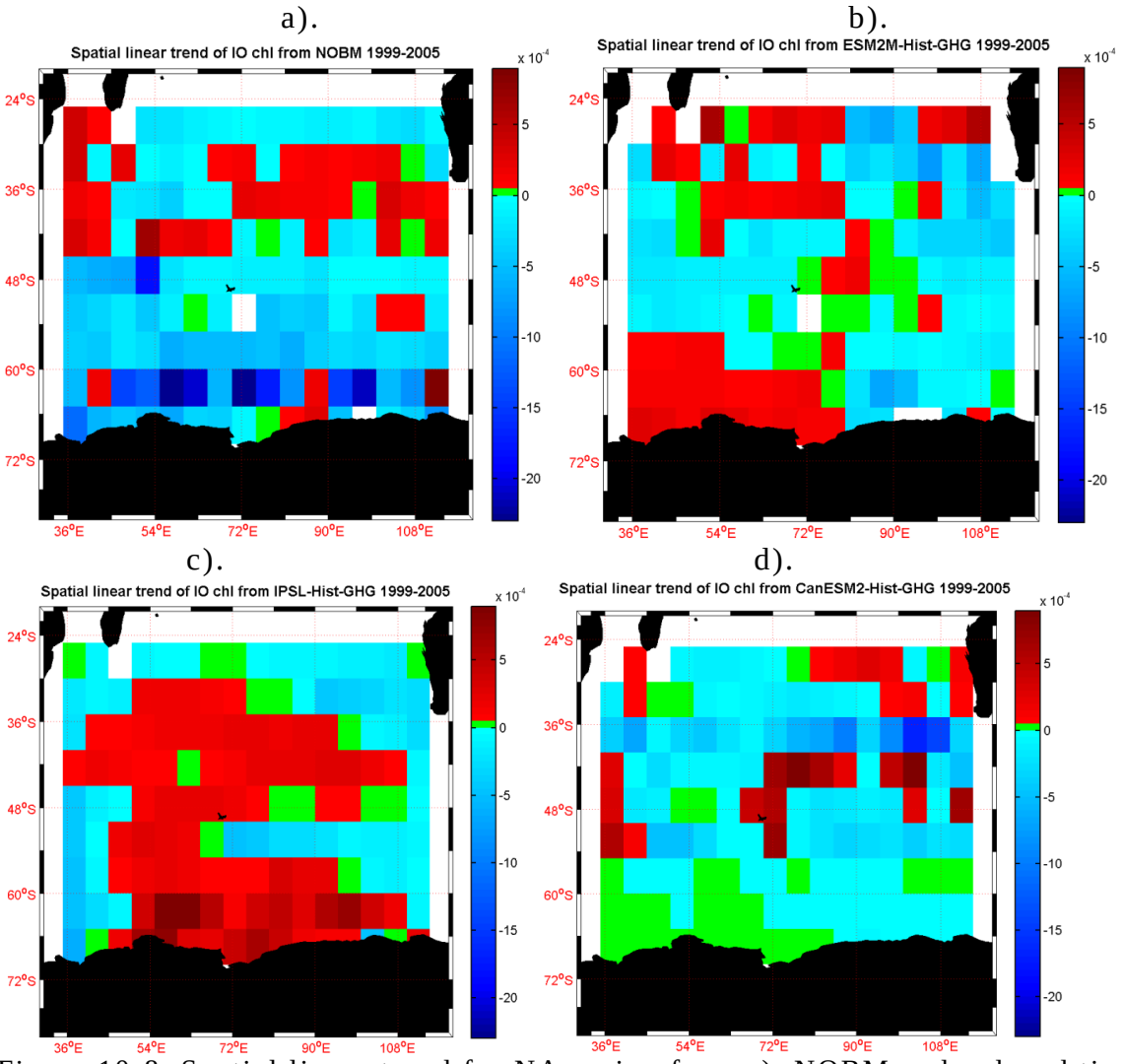

Figure 10-8. Spatial linear trend for NA region from a). NOBM and reduced time period of b). GFDL-ESM2M Historical GHG c). IPSL Historical GHG and d). CanESM2 Historical GHG simulations.

Table 10-5 below shows the value of the statistical terms of comparison i.e. the correlation coefficient, root mean square difference and standard deviation when spatial linear trend for IO region of the ocean computed from different model simulations for two time periods (whole and reduced) was compared with linear trend from NOBM.

Table 10-5. Statistical terms of comparison for Indian Ocean region.

Model Simulation	Correlation Coefficient		RMS difference		Standard Deviation	
	W	R	W	R	R	R
A					0.00083	
B	-0.39066	-0.02283	0.00053	0.00058	0.00001	0.00024
C	-0.32367	-0.06851	0.00053	0.00060	0.00001	0.00025
D	-0.18018	-0.15957	0.00052	0.00060	0.00001	0.00022
F	-0.02698	0.01947	0.00052	0.00060	0.00000	0.00031
G	-0.24593	-0.14413	0.00053	0.00064	0.00002	0.00030
H	-0.39887	0.42056	0.00053	0.00048	0.00001	0.00029
I	-0.42442	-0.37192	0.00053	0.00066	0.00001	0.00026
J	-0.39057	-0.54332	0.00053	0.00089	0.00001	0.00049
K	-0.42525	0.39949	0.00055	0.00050	0.00005	0.00034
L	-0.19045	0.11175	0.00053	0.00060	0.00001	0.00036
M	-0.22337	-0.12222	0.00053	0.00065	0.00001	0.00033
N	0.20844	0.16994	0.00052	0.00056	0.00001	0.00031
O	-0.18186	0.13673	0.00054	0.00057	0.00007	0.00031

Taylor diagrams associated with the comparisons are shown in Figure 10-9. Figure 10-9a shows statistical terms of comparisons when spatial linear trend was computed from whole time period of simulations. Figure 10-9b shows statistical terms of comparisons when spatial linear trend was computed from reduced time period of simulations.

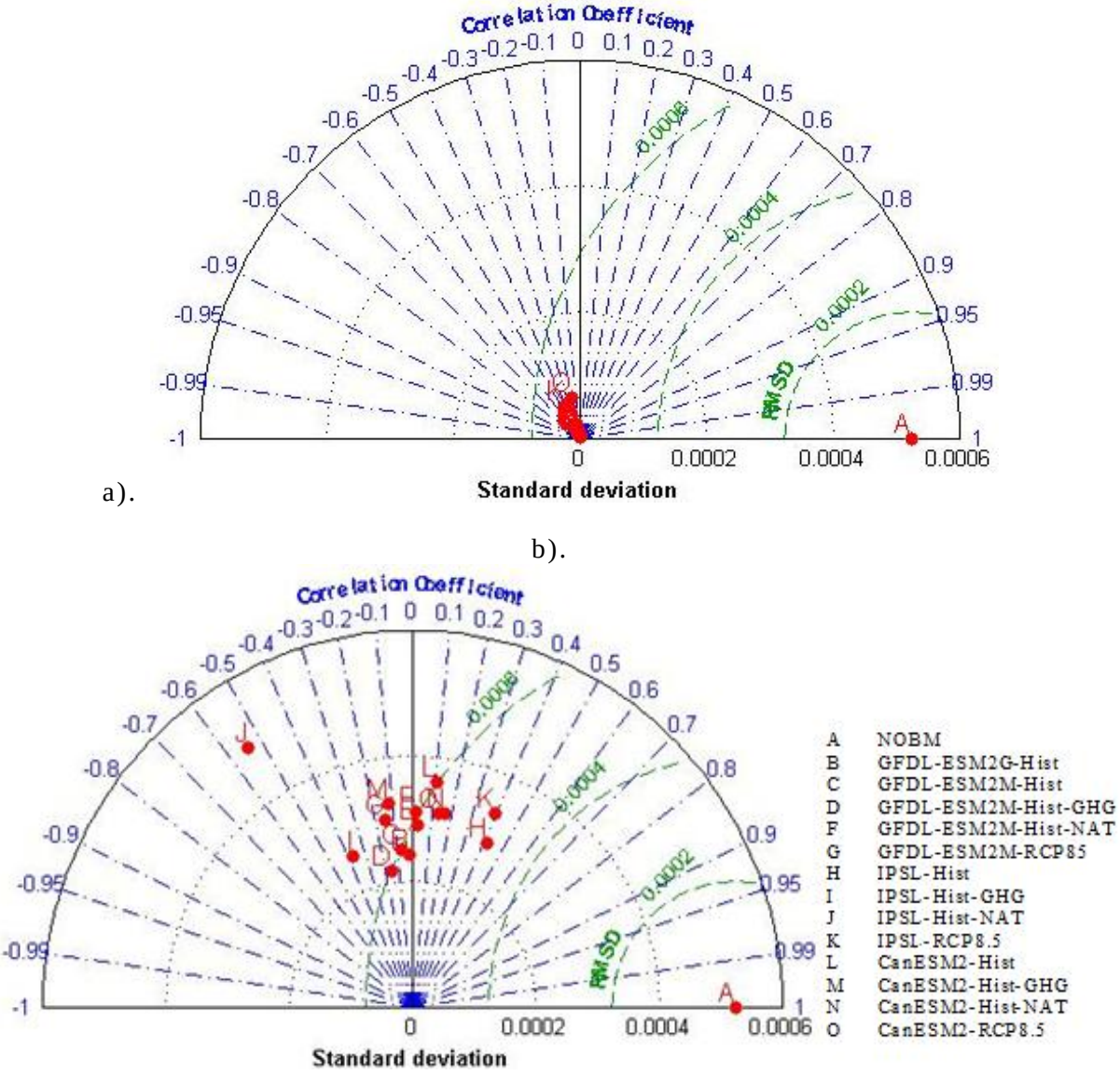

Figure 10-9. Taylor diagrams associated with the comparisons of spatial linear trend for IO region computed from a). whole time period of simulations b). reduced time period of simulations with spatial linear trend for IO region computed from NOBM.

From Figure 10-9, it can be seen that the correlation coefficient for all the model simulations is low (-0.5433 to 0.4206 in this study). Low correlation coefficient indicates that the spatial linear trend from model simulations is not correctly phased with NOBM. For most of the simulations correlation coefficient changes sign and magnitude for the two time periods for which linear trend is computed. This indicates that signal from whole time period of data is not the same as the reduced time period of data and they should be treated as two different metrics of signal computation. It should also be noted from Figure 10-9 that there is consistency in the sign of

correlation coefficient obtained from same forcing simulation from different models. For example, correlation coefficient obtained for whole time period of historical greenhouse gas simulation from all the three models is negative (ESM2M, IPSL and CanESM2).

From Figure 10-9, it can also be seen that the standard deviation of all the model simulations for both the time periods is lower than NOBM. The difference between the standard deviations of NOBM and model simulations for the whole time period (10^{-4}) is higher compared to the difference between the standard deviations of NOBM and the model simulations for the reduced time period (10^{-5}). From this it can be concluded that the amplitude of the spatial linear trend from the 'whole time period' of model simulations underestimates the amplitude of the spatial linear trend of chl and the 'reduced time period' of model simulations gives a much closer estimate to the amplitude of the spatial linear trend from NOBM.

10.3. Level of truncation

Table 10-6. Level of truncation chosen for the noise covariance matrix

Model Simulation Alphabet	NA		SA		NP		SP		IO	
	W	R	W	R	W	R	W	R	W	R
B	22.56	22.56	18.80	18.80	18.80	11.28	26.32	22.56	22.56	22.56
C	14.71	22.06	14.71	18.38	22.06	14.71	22.06	14.71	11.03	18.38
D	18.38	22.06	7.35	22.06	18.38	18.38	14.71	22.06	14.71	14.71
F	22.06	25.74	14.71	11.03	18.38	7.35	25.74	25.74	14.71	14.71
G	18.38	14.71	14.71	22.06	18.38	18.38	25.74	25.74	18.38	22.06
H	10.20	10.20	13.61	10.20	10.20	6.80	13.61	13.61	17.01	17.01
I	13.61	13.61	10.20	13.61	13.61	10.20	13.61	10.20	17.01	17.01
J	10.20	10.20	13.61	13.61	10.20	10.20	13.61	13.61	17.01	17.01
K	13.61	10.20	13.61	10.20	6.80	10.20	17.01	17.01	17.01	17.01
L	6.85	10.27	13.70	20.55	13.70	17.12	13.70	10.27	20.55	20.55
M	23.97	30.82	17.12	17.12	13.70	10.27	17.12	23.97	17.12	17.12
N	17.12	17.12	17.12	17.12	13.70	13.70	17.12	23.97	17.12	17.12
O	23.97	10.27	20.55	23.97	10.27	20.55	17.12	17.12	17.12	17.12

10.4. Detection Results

Beta values obtained after the implementation of the OF method indicate whether the signal has been detected in the observations or not.

Table 10-7. Beta values for NA region

Model Simulation	BETA	
	WHOLE	REDUCED
B	35.824	-5.148
C	-234.160	-1.781
D	64.732	1.251
E	659.350	-4.840
F	-597.030	-11.396
G	6.398	-4.391
H	201.484	0.842
I	24.516	0.683
J	-42.256	0.637
K	1.954	0.835
L	-2184.865	0.636
M	43.069	-1.097
N	-296.623	-0.6774
O	5.253	-1.894

10.4.1. Results for South Atlantic Region

Scaling factors obtained as a result of the implementation of the OF method in spatial linear trend of chl in SA region of the ocean (using spatial linear trend from model forced simulations as the signal) is shown in Figure 10-10 and given in Table 10-8.

a).

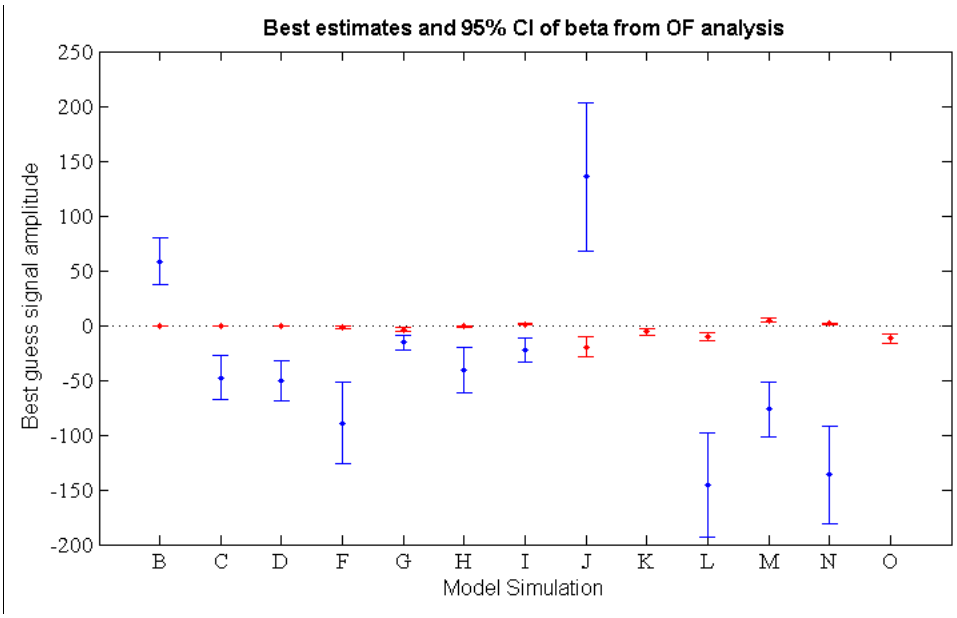

B	GFDL-ESM2G-Hist
C	GFDL-ESM2M-Hist
D	GFDL-ESM2M-Hist-GHG
F	GFDL-ESM2M-Hist-NAT
G	GFDL-ESM2M-RCP85
H	IPSL-Hist
I	IPSL-Hist-GHG
J	IPSL-Hist-NAT
K	IPSL-RCP8.5
L	CanESM2-Hist
M	CanESM2-Hist-GHG
N	CanESM2-Hist-NAT
O	CanESM2-RCP8.5

b).

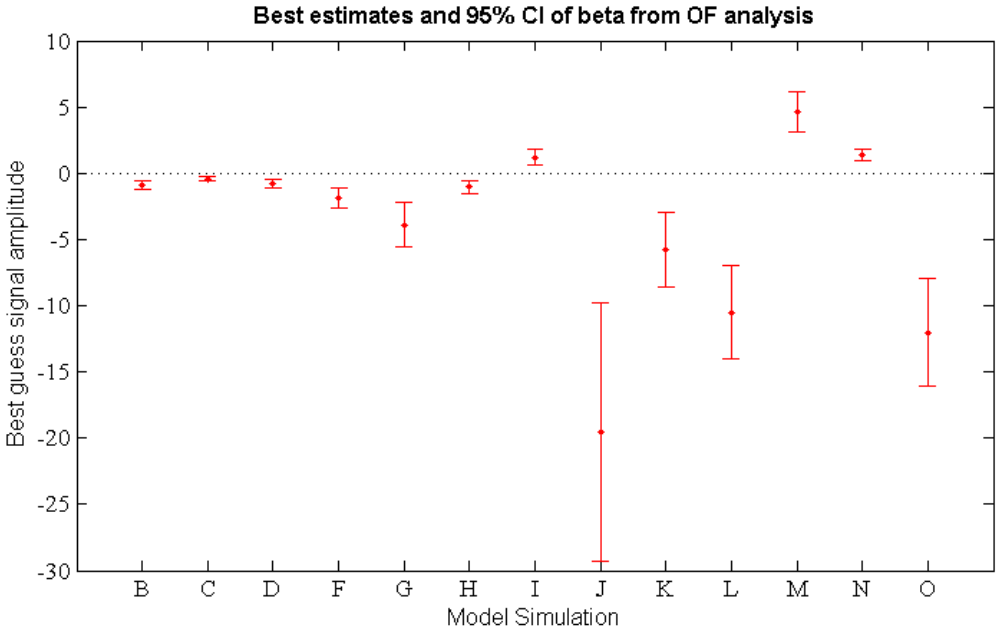

Figure 10-10. Graph of signal amplitude along with the Confidence Interval (CI), obtained for OF implementation in SA region using signals from whole and reduced time period of model simulations. a). result for both whole (blue) and reduced (red) time period of model simulations used to compute the signal. b). result for only reduced time period of model simulations.

Figure 10-10 above shows the beta values obtained in SA region for signals obtained from model forced simulations along with the confidence interval (CI) associated with each beta value. Figure 10-10 part (a) shows beta values for both whole (blue) and reduced (red) time period of model simulations and part (b) shows beta values for only reduced time period of model simulations used to compute the signal.

Table 10-8. Beta values for SA region

Model Simulation	**BETA**	
	WHOLE	**REDUCED**
B	58.535	-0.863
C	-47.563	-0.411
D	-50.226	-0.776
E	-160.166	3.682
F	-89.072	-1.841
G	-15.487	-3.893
H	-41.162	-1.014
I	-22.794	1.218
J	135.679	-19.521
K	-5.785	-5.746
L	-145.430	-10.492
M	-76.654	4.6118
N	-136.442	1.388
O	-12.135	-12.031

For the whole time period of model simulations, it can be seen from the Figure (blue dots and CI lines) that positive beta values are obtained for signals from whole time period of GFDL-ESM2G historical and IPSL historical natural simulations. This indicates that signals from these model simulations are detected in the observations. For the reduced time period of model simulations, it can be seen from the Figure (red dots and CI lines) that positive beta values are obtained for signals from reduced time period of IPSL historical GHG, CanESM2 historical GHG and CanESM2 Historical Natural simulations.

The graph below shows results for the OF implementation using the signals from the model simulations where the consistency test passed (Table 3.3). Simulations from whole and reduced time period of model simulations is represented with a 'W' and 'R' respectively.

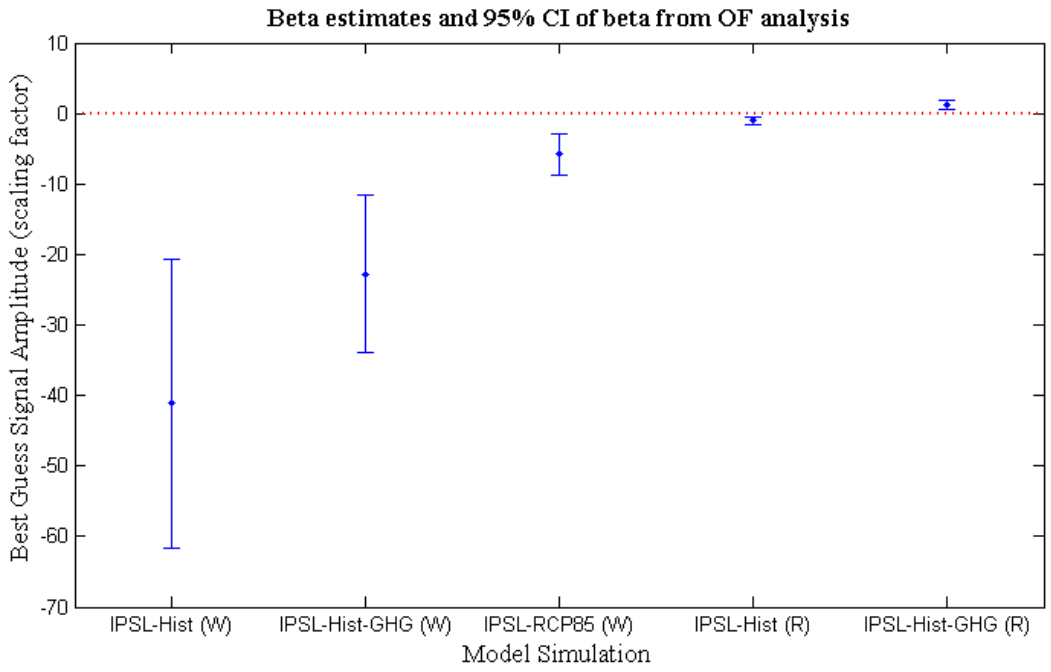

Figure 10-11. Scaling factor and their 5-95% CI for signals from model forced simulations for which consistency test passes in SA region

As it can be seen from the Figure above, scaling factors for reduced time period of greenhouse gas simulation from IPSL model is 1.218 which is significantly different from 0 with 95% confidence interval. This indicates that the effect of greenhouse gas forcing is detectable in the observations. As the beta value is ~1, it can be inferred that model simulated response of chl to external forcing is consistent with observations.

10.4.2. Results for North Pacific Region

Scaling factors obtained as a result of the implementation of the OF method in spatial linear trend of chl in NP region of the ocean (using spatial linear trend from model forced simulations as the signal) is shown in Figure 10-12 and Table 10.9.

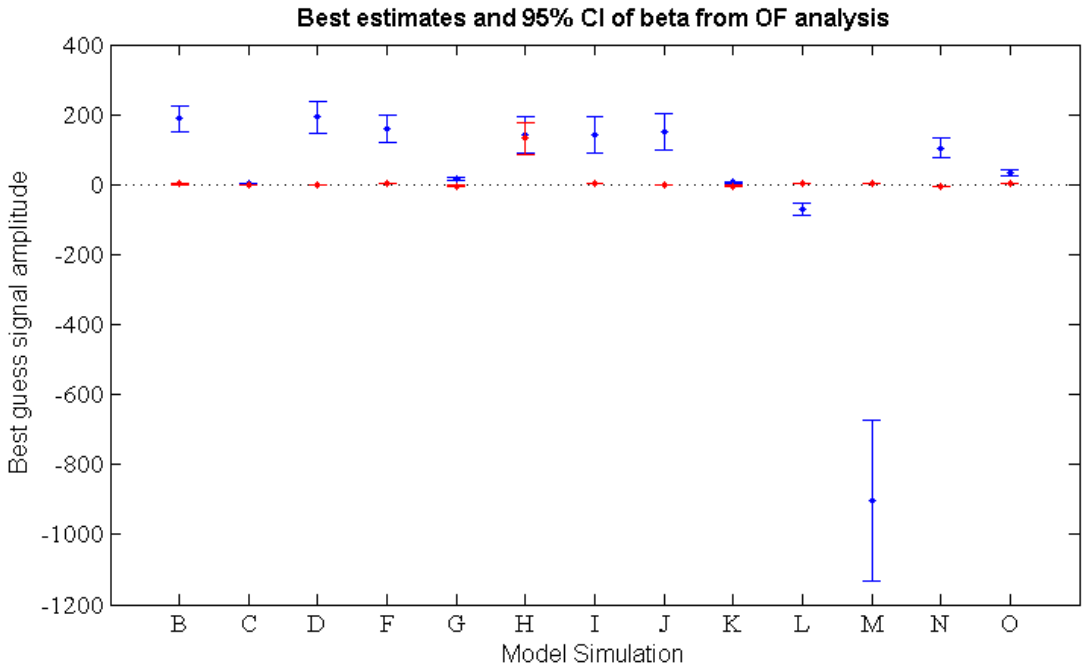

a).

B GFDL-ESM2G-Hist
C GFDL-ESM2M-Hist
D GFDL-ESM2M-Hist-GHG
F GFDL-ESM2M-Hist-NAT
G GFDL-ESM2M-RCP85
H IPSL-Hist
I IPSL-Hist-GHG
J IPSL-Hist-NAT
K IPSL-RCP8.5
L CanESM2-Hist
M CanESM2-Hist-GHG
N CanESM2-Hist-NAT
O CanESM2-RCP8.5

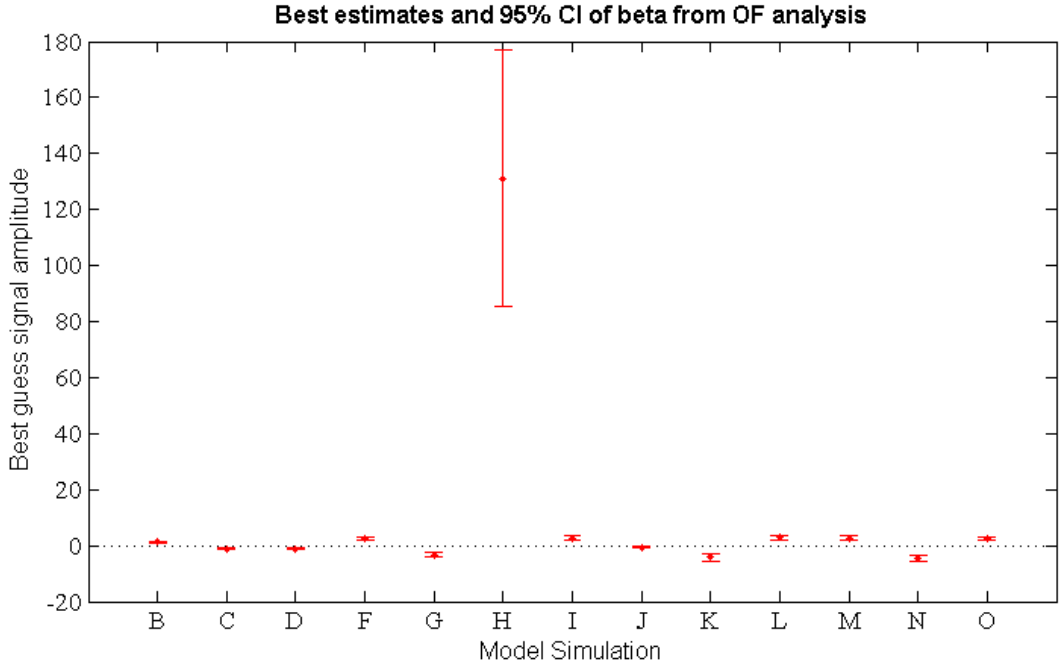

b).

Figure 10-12. Graph of signal amplitude along with the CI, obtained for OF implementation in NP region using signals from whole and reduced time period of

model simulations. a). result for both whole (blue) and reduced (red) time period of model simulations used to compute the signal.

Figure 10-12 above shows the beta values obtained in NP region for signals obtained from model forced simulations along with the confidence interval (CI) associated with each beta value. Figure 10-12 part (a) shows beta values for both whole (blue) and reduced (red) time period of model simulations and part (b) shows beta values for only reduced time period of model simulations used to compute the signal.

Table 10-9. Beta values for NP region

Model Simulation	**BETA**	
	WHOLE	**REDUCED**
B	188.954	1.1894
C	1.217	-1.123
D	192.195	-1.263
E	56.693	-1302.689
F	159.299	2.292
G	17.173	-3.309
H	142.353	131.174
I	141.673	2.659
J	150.578	-0.5
K	6.924	-4.168
L	-69.901	2.848
M	-903.862	2.662
N	104.888	-4.472
O	32.954	2.477

For the whole time period of model simulations, it can be seen from the Figure (blue dots and CI lines) that positive beta values are obtained for most of the signals except for CanESM2 Historical and Historical GHG simulations. For the reduced time period of model simulations, it can be seen from the Figure (red dots and CI lines) that positive beta values are obtained for signals from reduced time period of GFDL-ESM2G Historical, GFDL-

ESM2M historical Natural, IPSL historical, IPSL historical GHG, CanESM2 historical and CanESM2 Historical GHG simulations.

Consistency test for the internal variability passes for the signal from whole time period of RCP8.5 simulation from IPSL model. Scaling factor determined is 6.924 which is significantly different from 0 with 95% confidence interval. This indicates that the effect of future emissions is large enough to be detectable. Since, the beta value is greater than unity, it can be inferred that the model simulated response of chl to external forcings is significantly underestimated and it needs to be amplified (by a factor of ~6) to be consistent with observations.

10.4.3. Results for South Pacific Region

Scaling factors obtained as a result of the implementation of the OF method in spatial linear trend of chl in SP region of the ocean (using spatial linear trend from model forced simulations as the signal) is shown in Figure 10-13 and Table 10-10.

a).

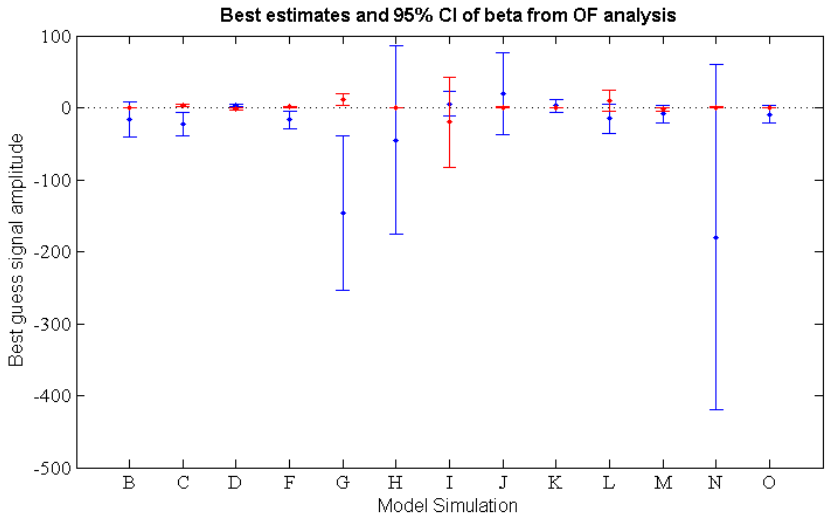

B GFDL-ESM2G-Hist
C GFDL-ESM2M-Hist
D GFDL-ESM2M-Hist-GHG
F GFDL-ESM2M-Hist-NAT
G GFDL-ESM2M-RCP85
H IPSL-Hist
I IPSL-Hist-GHG
J IPSL-Hist-NAT
K IPSL-RCP8.5
L CanESM2-Hist
M CanESM2-Hist-GHG
N CanESM2-Hist-NAT
O CanESM2-RCP8.5

b).

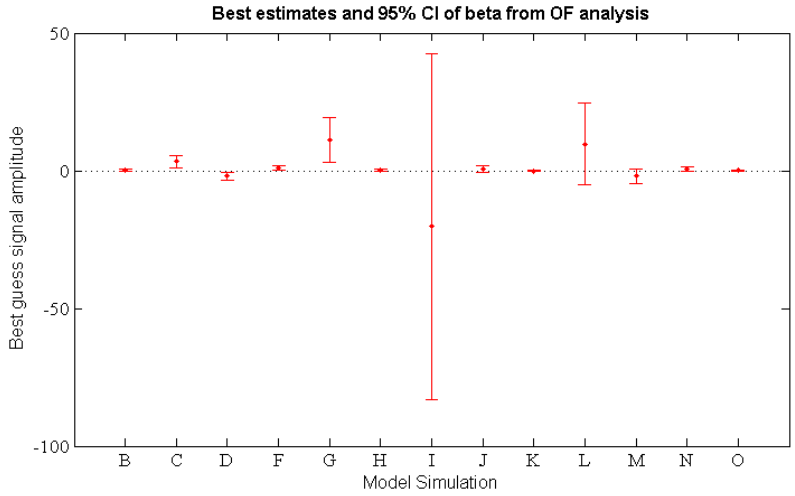

Figure 10-13. Graph of signal amplitude along with the CI, obtained for OF implementation in SP region using signals from whole and reduced time period of model simulations. a). result for both whole (blue) and reduced (red) time period of model simulations used to compute the signal.

Figure 10-13 above shows the beta values obtained in SP region for signals obtained from model forced simulations along with the confidence interval (CI) associated with each beta value. Figure 10-13 part (a) shows beta values for both whole (blue) and reduced (red) time period of model simulations and part (b) shows beta values for only reduced time period of model simulations used to compute the signal.

Table 10-10. Beta values for SP region

Model Simulation	BETA	
	WHOLE	REDUCED
B	-15.597	0.275
C	-23.119	3.294
D	3.294	-1.971
E	243.150	0.997
F	-17.000	1.082
G	-146.16	11.203
H	-45.297	0.195
I	5.679	-20.301
J	19.524	0.424
K	3.129	-0.097
L	-14.941	9.74
M	-8.773	-2.014
N	-180.202	0.565
O	-9.088	0.121

For the whole time period of model simulations, it can be seen from the Figure (blue dots and CI lines) that positive beta values are obtained for signals from whole time period of GFDL-ESM2M Historical GHG and Historical Miscellaneous, IPSL Historical GHG, Historical Natural and RCP8.5 simulations. For the reduced time period of model simulations, it can be seen from the Figure (red dots and CI lines) that positive beta values are obtained for signals from reduced time period of GFDL-ESM2G Historical, GFDL-ESM2M historical, historical Miscellaneous, historical Natural and RCP8.5, IPSL historical and historical Natural, CanESM2 historical, historical Natural and RCP8.5 simulations.

Significance of the scaling factors for the simulations for which the consistency test failed (Table 3.3) is questionable and therefore, only those results would be considered significant where the consistency test passed. Thus, the graph below shows results for the OF implementation using the signals from the model simulations where the consistency test passed. Simulations from whole and reduced time period of model simulations is represented with a 'W' and 'R' respectively.

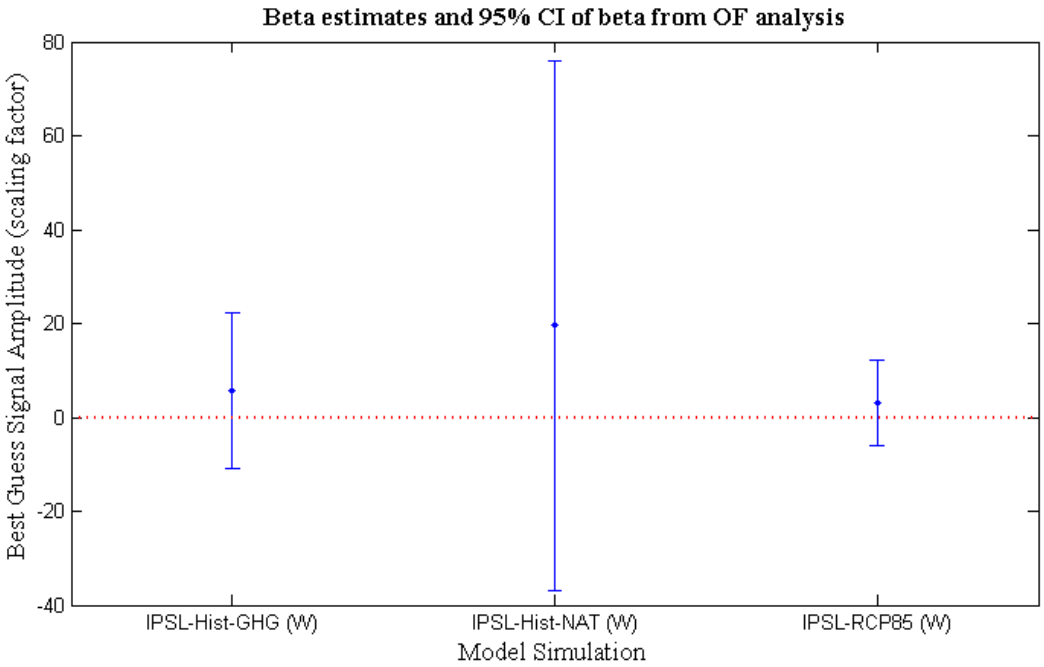

Figure 10-14. Scaling factor and their 5-95% CI for signals from model forced simulations for which consistency test passes in SP region.

As it can be seen from the Figure 10-14 above, scaling factors for whole time period of greenhouse gas, natural and RCP8.5 simulation from IPSL is 5.679, 19.524 and 3.129 respectively. As can be seen that the confidence intervals of the scaling factors is not different from 0 therefore, these scaling factors are not significant. Thus, effect of external forcings is not being detected in the observations.

10.4.4. Results for Indian Ocean Region

Scaling factors obtained as a result of the implementation of the OF method in spatial linear trend of chl in IO region of the ocean (using spatial linear trend from model forced simulations as the signal) is shown in Figure 10-15 and Table 10-11.

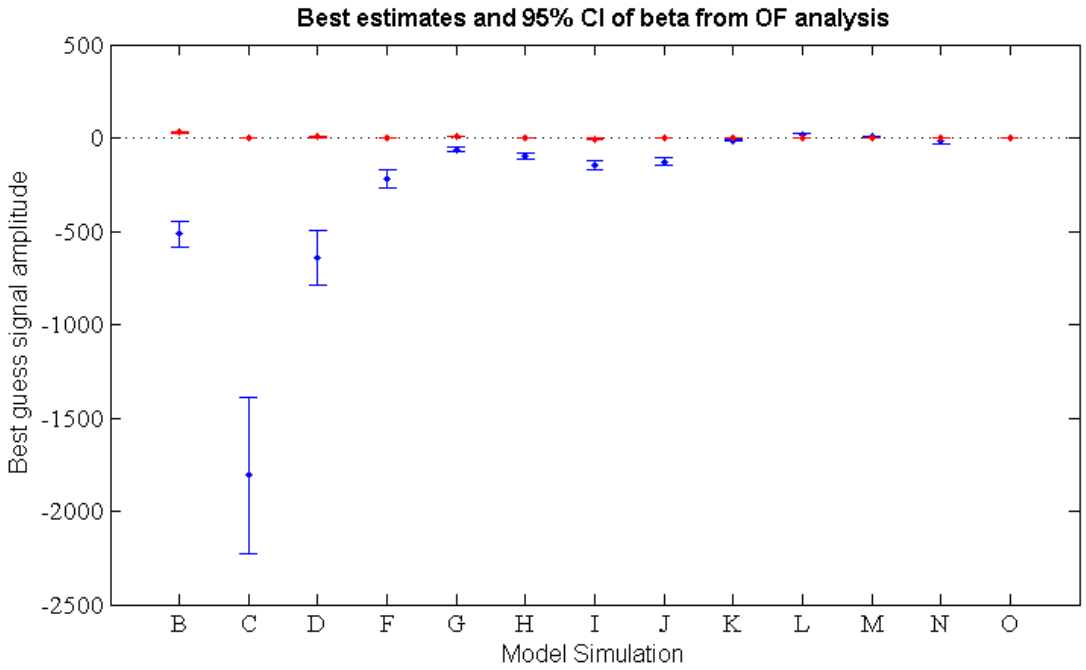

a).

B GFDL-ESM2G-Hist
C GFDL-ESM2M-Hist
D GFDL-ESM2M-Hist-GHG
F GFDL-ESM2M-Hist-NAT
G GFDL-ESM2M-RCP85
H IPSL-Hist
I IPSL-Hist-GHG
J IPSL-Hist-NAT
K IPSL-RCP8.5
L CanESM2-Hist
M CanESM2-Hist-GHG
N CanESM2-Hist-NAT
O CanESM2-RCP8.5

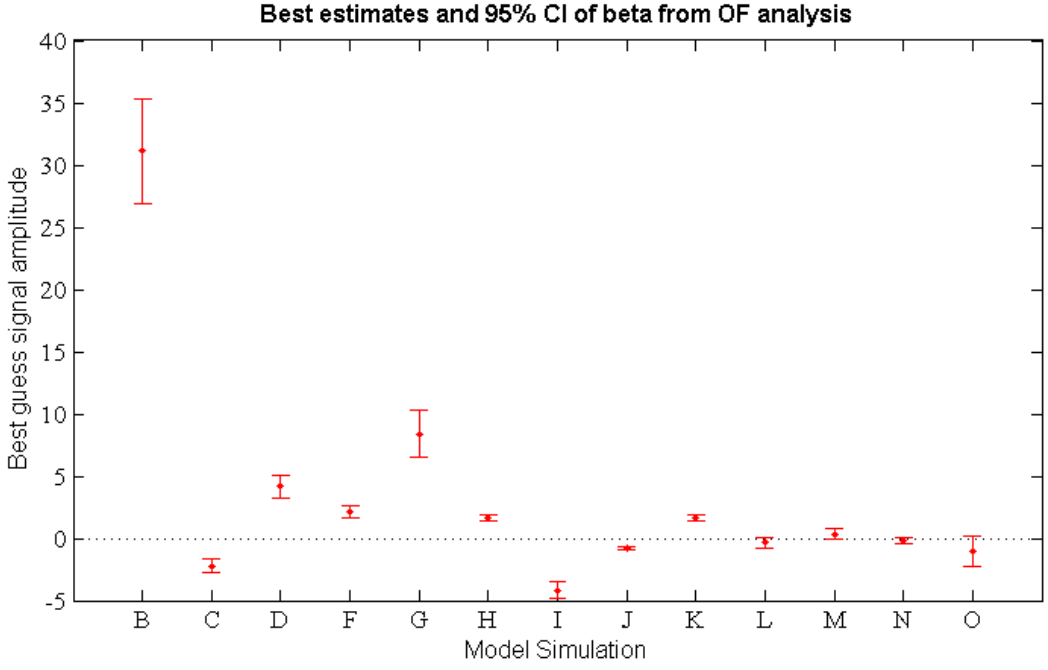

b).

Figure 10-15. Graph of signal amplitude along with the CI, obtained for OF implementation in IO region using signals from whole and reduced time period of model simulations. a). result for both whole (blue) and reduced (red) time period of model simulations used to compute the signal.

Figure 10-15 above shows the beta values obtained in IO region for signals obtained from model forced simulations along with the confidence interval (CI) associated with each beta value. Figure 10-15 part (a) shows beta values for both whole (blue) and reduced (red) time period of model simulations and part (b) shows beta values for only reduced time period of model simulations used to compute the signal.

Table 10-11. Beta values for IO region

Model Simulation	**BETA**	
	W	**R**
B	-514.088	31.113
C	-1806.551	-2.200
D	-639.988	4.160
E	499.253	16.142
F	-216.431	2.1474
G	-62.031	8.399
H	-96.462	1.626
I	-144.190	-4.18
J	-128.272	-0.792
K	-13.110	1.657
L	12.333	-0.351
M	5.534	0.352
N	-15.843	-0.196
O	1.524	-1.022

For the whole time period of model simulations, it can be seen from the Figure (blue dots and CI lines) that positive beta values are obtained for signals from whole time period of GFDL-ESM2M Historical Miscellaneous, CanESM2 Historical, Historical GHG and RCP8.5 simulations. For the reduced time period of model simulations, it can be seen from the Figure (red dots and CI lines) that positive beta values are obtained for signals from reduced time period of GFDL-ESM2G Historical, GFDL-ESM2M historical GHG, historical Miscellaneous, historical Natural and RCP8.5, IPSL historical and RCP8.5, CanESM2 historical GHG simulations.

Significance of the scaling factors for the simulations for which the consistency test failed (Table 3.3) is questionable and therefore, only those results would be considered significant where the consistency test passed.

Thus, the graph below shows results for the OF implementation using the signals from the model simulations where the consistency test passed. Simulations from whole and reduced time period of model simulations is represented with a 'W' and 'R' respectively.

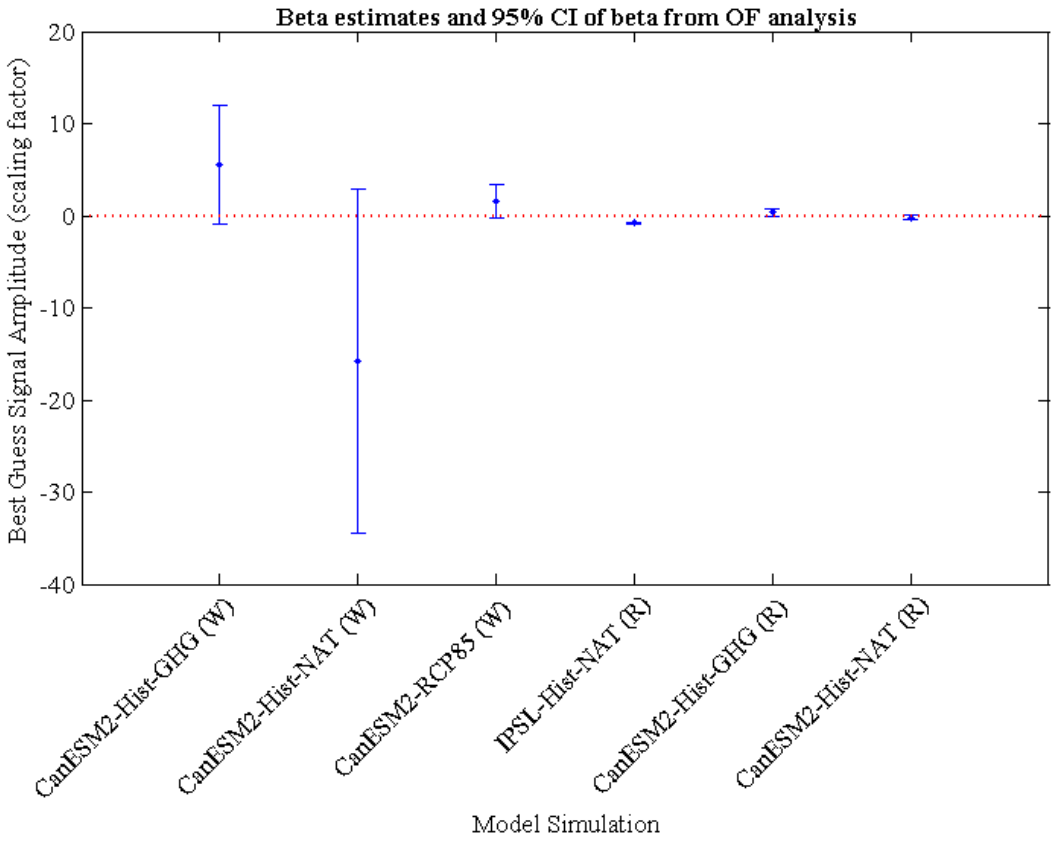

Figure 10-16. Scaling factor and their 5-95% CI for signals from model forced simulations for which consistency test passes in IO region.

As it can be seen from the Figure 10-16 above, scaling factors for whole time period of greenhouse gas and RCP8.5 simulation from CanESM2 model and reduced time period of greenhouse gas from CanESM2 model is 5.534, 1.524 and 0.352. As can be seen that the confidence intervals of the scaling factors is not different from 0 therefore, these scaling factors are not significant. Thus, effect of external forcings is not being detected in the observations.

11. Appendix V-Results for Chapter 4

11.1. Results of comparison of linear trend from model simulations with NOBM data

11.1.1. Results for North Atlantic Region

Table 11-1 below shows the value of the statistical terms of comparison i.e. the correlation coefficient, root mean square difference and standard deviation when linear trend of zonal average for NA region of the ocean computed from different model simulations for two time periods (whole and reduced) was compared with linear trend of zonal average from NOBM.

Table 11-1. Statistical terms of comparison for North Atlantic region.

Model Simulation	Correlation Coefficient		RMS difference		Standard Deviation	
	W	R	W	R	W	R
B	0.72513	-0.31136	0.00374	0.00458	0.00005	0.00167
C	0.15607	-0.09853	0.00377	0.00479	0.00006	0.00259
D	0.20251	-0.10208	0.00376	0.00480	0.00008	0.00261
F	-0.08046	0.35366	0.00378	0.00374	0.00003	0.00256
G	0.01358	-0.20330	0.00378	0.00501	0.00023	0.00264
H	0.10502	0.43895	0.00376	0.00499	0.00014	0.00531
I	0.34122	0.42234	0.00370	0.00688	0.00023	0.00757
J	-0.74059	-0.12672	0.00386	0.00654	0.00011	0.00488
K	0.53857	0.45742	0.00332	0.00403	0.00107	0.00396
L	0.31289	0.28604	0.00376	0.00457	0.00006	0.00387
M	0.56541	-0.43436	0.00373	0.00720	0.00008	0.00471
N	0.25408	-0.69149	0.00376	0.00899	0.00006	0.00596
O	0.45543	-0.48180	0.00351	0.00680	0.00072	0.00412

11.1.2. Results for South Atlantic Region

Linear Trend of zonal average for SA region from NOBM and greenhouse gas simulations of the whole and reduced time period of model simulations is shown in Figure 11.1. Linear trend of zonal average from greenhouse gas simulations is chosen as an example for visual comparison because this is the signal that is of interest in this detection study. Trends from NOBM were 10 times higher than the trends from whole time period of simulations, therefore for clarity in presentation; trends from NOBM were plotted after dividing them by 10. From Figure 11.1 it can be seen that in observations (blue line in graph) that there is a declining trend of zonal chl in sub-tropical and mid-latitudes (-25^o to -50^{o}N) and there is an increasing trend from (-50^o to -70^{o}N) in SA region. This pattern in trend of zonal average is also observed in all the model forced simulations from whole time period (Figure 11.1a) but with a shift towards the positive trend and the pattern in trend is also observed in model forced simulations from reduced time period (Figure 11.1b) but with a slight shift toward the south compared to the observations. For example, the declining trend from whole and reduced time period of greenhouse gas simulation from IPSL is from -35^o to -60^o N which is shifted southward compared to the declining trend in NOBM (-25^o to -50^{o}N). From the Figure 11.1 it can also be seen that the pattern of trends from reduced time period of ESM2M-Hist-GHG, IPSL-Hist-GHG and CanESM2-Hist-GHG follow each other closely in all the latitudinal zones but the amplitude of trend is different in IPSL-Hist-GHG than ESM2M-Hist-GHG and CanESM2-Hist-GHG. Thus, visual comparison of the trends from model simulations indicates consistency between signals obtained from the same model forcing simulation from different models. Also, pattern of trends from model simulations are similar to patterns from NOBM. Statistical terms of comparison such as correlation coefficient is also computed and presented in the form of Taylor diagram (Figure 11.2).

a). b).

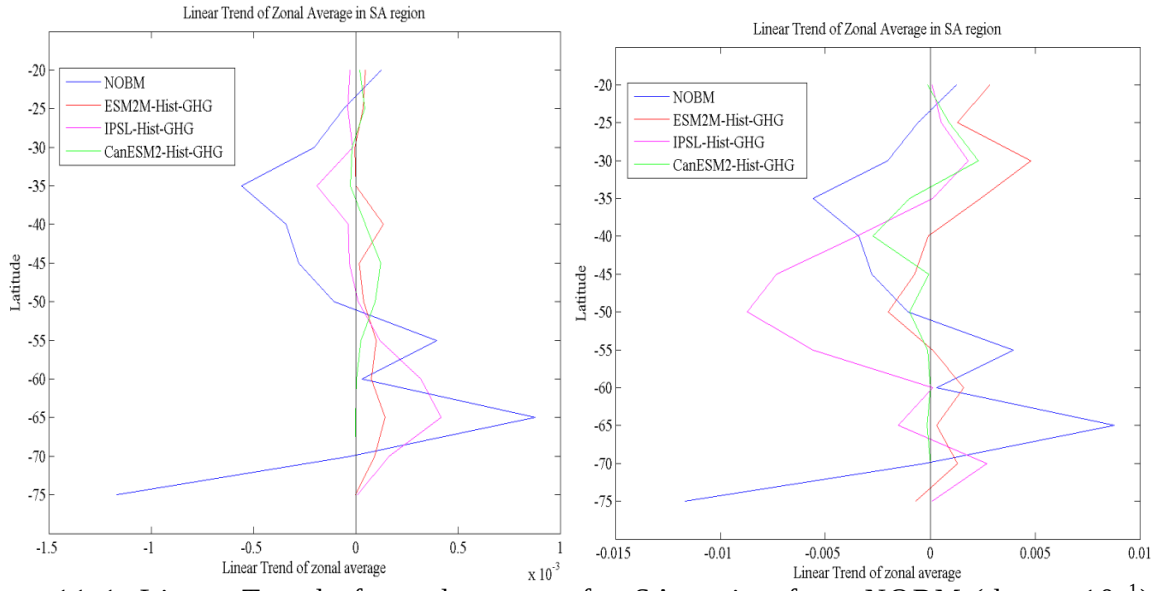

Figure 11-1. Linear Trend of zonal average for SA region from NOBM (data x 10^{-1}) and greenhouse gas simulations from models. a). Linear trend computed for whole time period and b). Linear trend computed for reduced time period.

Statistical terms of comparison between linear trend of zonal average from model simulations and NOBM that were computed are correlation coefficient, centered root mean square difference and amplitude of the variation i.e. standard deviation. Linear trend of zonal average for model simulations was computed for two time periods i.e. whole and reduced. The results are presented in the form of a Taylor Diagram (Taylor, 2001) (Figure 11.2). Table of values associated with the Figure are presented in Table 11-2. Figure 11.2a shows statistical terms of comparison when linear trend of zonal average was computed from whole time period of simulations. Figure 11.2c shows statistical terms of comparison when linear trend of zonal average was computed from reduced time period of simulations.

Table 11-2 below shows the value of the statistical terms of comparison i.e. the correlation coefficient, root mean square difference and standard deviation when linear trend of zonal average for SA region of the ocean computed from different model simulations for two time periods (whole and reduced) was compared with linear trend of zonal average from NOBM.

Table 11-2. Statistical terms of comparison for South Atlantic region.

Model Simulation	Correlation Coefficient		RMS difference		Standard Deviation	
	W	R	W	R	W	R
B	0.34672	0.09993	0.00475	0.00664	0.00005	0.00512
C	0.41049	0.01705	0.00475	0.00567	0.00005	0.00315
D	0.67061	0.07529	0.00474	0.00496	0.00005	0.00177
F	0.45787	-0.02291	0.00475	0.00521	0.00004	0.00199
G	0.48405	0.56070	0.00471	0.00398	0.00013	0.00221
H	0.73420	-0.44657	0.00470	0.00679	0.00009	0.00316
I	0.65765	-0.11582	0.00466	0.00625	0.00016	0.00352
J	0.15434	0.83703	0.00476	0.00263	0.00004	0.00431
K	0.46250	-0.67216	0.00447	0.00874	0.00076	0.00479
L	0.06804	0.00422	0.00477	0.00497	0.00005	0.00142
M	0.00712	0.10384	0.00477	0.00479	0.00004	0.00113
N	0.02187	-0.30770	0.00477	0.00501	0.00002	0.00065
O	0.15997	-0.31971	0.00472	0.00654	0.00044	0.00321

a).

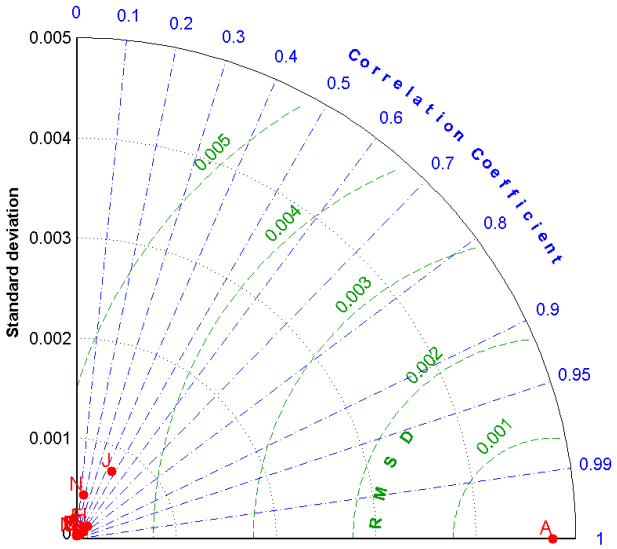

b).

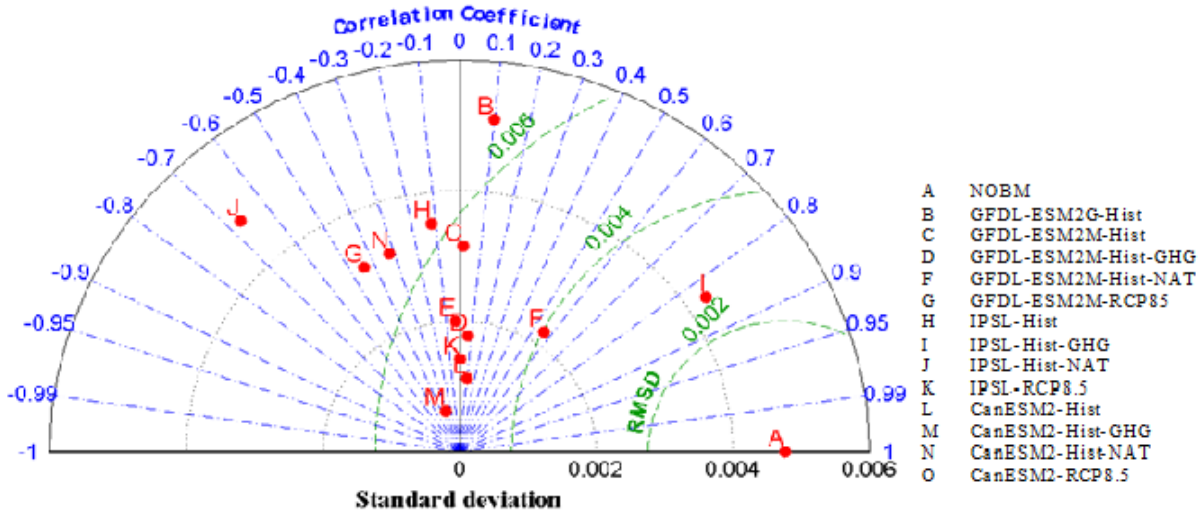

Figure 11-2. Taylor diagrams associated with the comparisons of linear trend of zonal average for SA region computed from a). whole time period of simulations b). reduced time period of simulations with linear trend of zonal average for SA region computed from NOBM.

From Figure 11.2, it can be seen that the correlation coefficient for all the model simulations is moderate (-0.6722 to 0.8370 in this study). This indicates that linear trend of zonal average from model simulations is partially phased with NOBM. For most of the simulations correlation coefficient changes sign and magnitude for the two time periods for which linear trend is computed. This indicates that signal from whole time period of data is not the same as the reduced time period of data and they should be

treated as two different metrics of signal computation. It should also be noted from Figure 11.2 that the sign of the correlation coefficient from the same forcing simulation for different models is consistent for whole time period of simulations. For example, correlation coefficient obtained for whole time period of historical greenhouse gas simulation from ESM2M, IPSL and CanESM2 is positive but for reduced time period correlation coefficient is negative for greenhouse gas simulation from IPSL and is positive for greenhouse gas simulation from ESM2M and CanESM2.

From Figure 11.2, it can also be seen that the standard deviation of all the model simulations is lower than NOBM for the 'whole time period'. On the other hand, for the reduced time period, standard deviation for some model simulations is larger than NOBM. The difference between the standard deviations of NOBM and model simulations for the whole time period (10^{-3}) is higher compared to the difference between the standard deviations of NOBM and the model simulations for the reduced time period (10^{-5}-10^{-3}). From this it can be concluded that the amplitude of the linear trend of zonal average from the 'whole time period' of model simulations underestimates the amplitude of the linear trend of zonal average of chl from NOBM and the 'reduced time period' of model simulations gives a much closer estimate to the amplitude of the linear trend of zonal average from NOBM.

11.1.3. Results for North Pacific Region

Linear Trend of zonal average for NP region from NOBM and greenhouse gas simulations of the whole and reduced time period of model simulations is shown in Figure 11.3. Linear trend of zonal average from greenhouse gas simulations is chosen as an example for visual comparison because this is the signal that is of interest in this detection study. Trends from NOBM were 10 times higher than the trends from whole time period of simulations, therefore for clarity in presentation, trends from NOBM were plotted after dividing them by 10. From Figure 11.3 it can be seen that in observations (blue line in graph), the linear trend of zonal chl decreases in sub-polar and mid-latitudes (35^{o} to 60^{o} N) in NP region. This decrease in

trend is observed partially in forced simulations from whole and reduced time period of CanESM2 model (Figure 11.3a & b). From the Figure 11.3 it can also be seen that pattern of trends from ESM2M-Hist-GHG and IPSL-Hist-GHG follow each other closely in all the latitudinal zones. Pattern of trend from CanESM2-Hist-GHG is slight different than the other two models in whole time period (Figure 11.3a). Thus, visual comparison of the trends from model simulations indicate consistency between signals obtained from the same model forcing simulation from different models. Also, pattern of trends from CanESM2 model simulation are similar to patterns from NOBM.

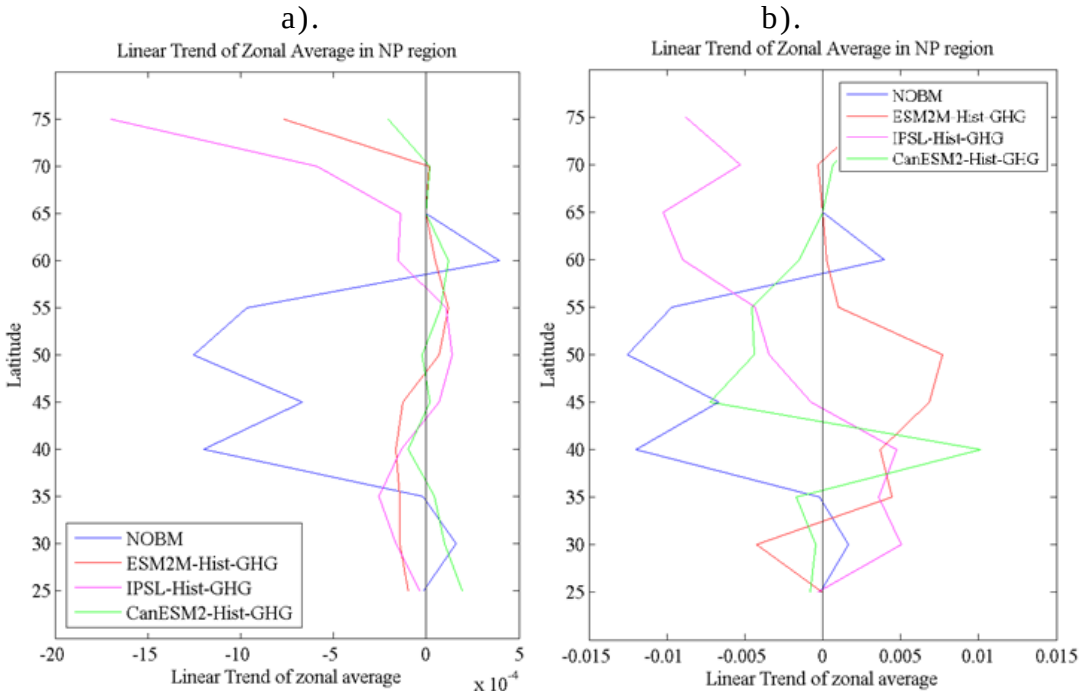

Figure 11-3. Linear Trend of zonal average for NP region from NOBM (data x 10^{-1}) and greenhouse gas simulations from models. a). Linear trend computed for whole time period and b). Linear trend computed for reduced time period.

Statistical terms of comparison between linear trend of zonal average from model simulations and NOBM that were computed are correlation coefficient, centered root mean square difference and amplitude of the variation i.e. standard deviation. Linear trend of zonal average for model simulations was computed for two time periods i.e. whole and reduced. The results are presented in the form of a Taylor Diagram (Figure 11.4). Table of values associated with the Figure are presented in Table 11-3. Figure 11.4a

shows statistical terms of comparisons when linear trend of zonal average was computed from whole time period of simulations. Figure 11.4b shows statistical terms of comparisons when linear trend of zonal average was computed from reduced time period of simulations.

Table 11-3 below shows the value of the statistical terms of comparison i.e. the correlation coefficient, root mean square difference and standard deviation when linear trend of zonal average for NP region of the ocean computed from different model simulations for two time periods (whole and reduced) was compared with linear trend of zonal average from NOBM.

Table 11-3~~11-3~~. Statistical terms of comparison for North Pacific region.

Model Simulation	**Correlation Coefficient**		**RMS difference**		**Standard Deviation**	
	W	**R**	**W**	**R**	**W**	**R**
B	-0.16168	0.40567	0.00558	0.00521	0.00008	0.00336
C	-0.03607	-0.46232	0.00558	0.00797	0.00021	0.00368
D	-0.21701	-0.63700	0.00562	0.00811	0.00023	0.00334
F	-0.21702	0.26834	0.00562	0.00598	0.00023	0.00414
G	-0.24138	-0.07395	0.00571	0.00671	0.00050	0.00336
H	-0.51606	0.29843	0.00563	0.00546	0.00011	0.00292
I	-0.38509	-0.269826	0.00578	0.00866	0.00049	0.00529
J	-0.13719	-0.79578	0.00560	0.01351	0.00022	0.00865
K	-0.11402	-0.45989	0.00579	0.00864	0.00107	0.00452
L	0.07027	0.49767	0.00556	0.00492	0.00012	0.00368
M	0.30661	0.00163	0.00554	0.00708	0.00010	0.00438
N	0.29137	0.25019	0.00556	0.00581	0.00004	0.00357
O	0.52198	0.28525	0.00534	0.00687	0.00047	0.00599

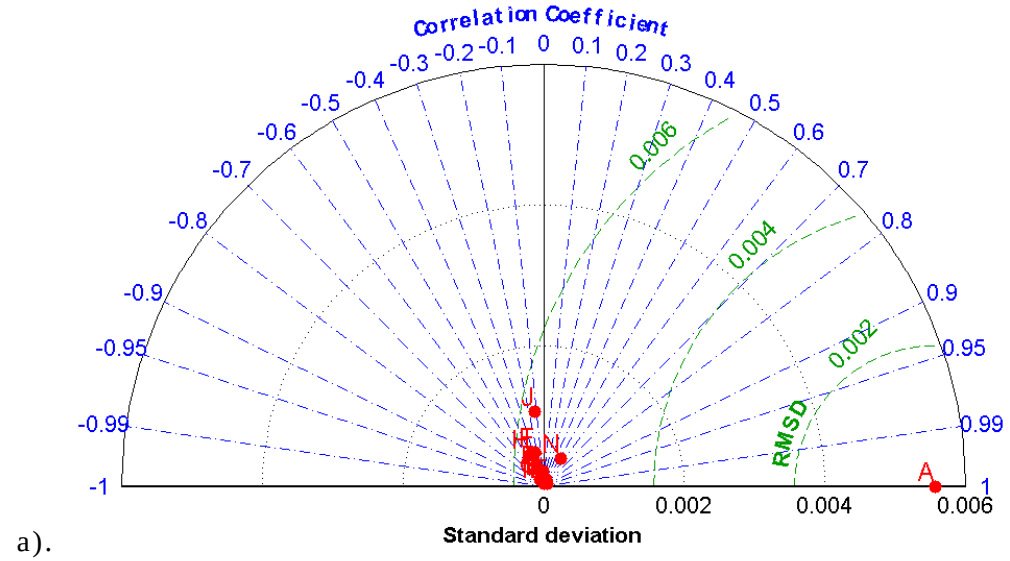

a).

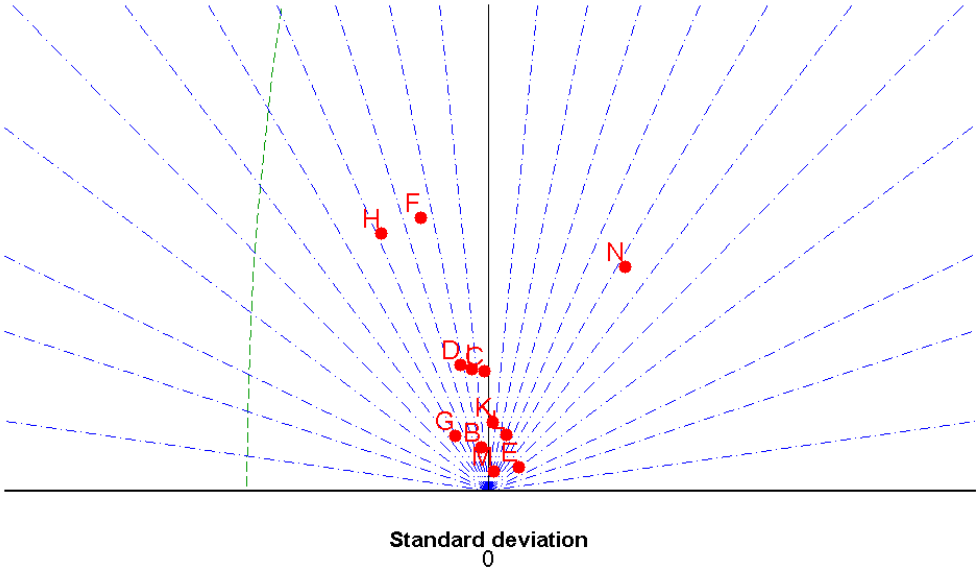

b).

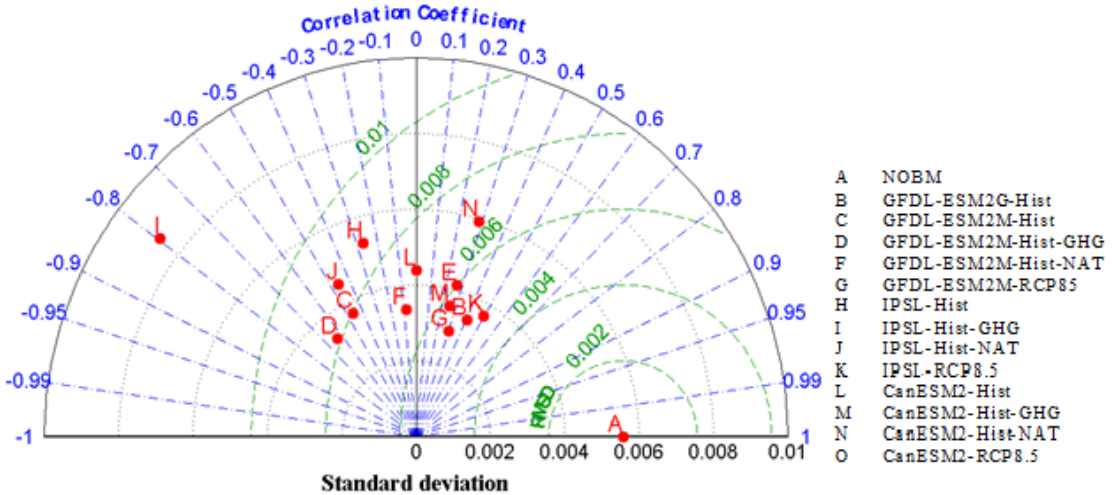

c).

Figure 11-4. Taylor diagrams associated with the comparisons of linear trend of zonal average for NP region computed from a). whole time period of simulations and b). reduced time period of simulations, with linear trend of zonal average for NA region computed from NOBM.

From Figure 11.4, it can be seen that the correlation coefficient for all the model simulations is moderate i.e. not very low or very high (-0.7958 to 0.5220 in this study). This indicates that linear trend of zonal average from model simulations is partially phased with NOBM. For most of the simulations correlation coefficient does not change sign but the magnitude for the two time periods for which linear trend is computed is different. This indicates that the phase of signal from whole time period of data is the same as the reduced time period of data but the amplitudes are different and the signals from these two time periods should be treated as two different metrics of signal computation. It should also be noted from Figure that sign of the correlation coefficient from same forcing simulation from different models is not consistent for both whole and reduced time period. For example, correlation coefficient obtained for whole and reduced time period of historical greenhouse gas simulation from ESM2M and IPSL is negative but it is positive for CanESM2.

From Figure 11.4, it can also be seen that the standard deviation of all the model simulations is lower than NOBM for the 'whole time period'. On the other hand, for the reduced time period, standard deviation for some model simulations is larger than NOBM. The difference between the standard deviations of NOBM and model simulations for the whole time period (10^{-3}) is higher compared to the difference between the standard deviations of NOBM and the model simulations for the reduced time period (10^{-4}-10^{-3}). From this it can be concluded that the amplitude of the linear trend of zonal average from the 'whole time period' of model simulations underestimates the amplitude of the linear trend of zonal average of chl from NOBM and the 'reduced time period' of model simulations gives a much closer estimate to the amplitude of the linear trend of zonal average from NOBM.

11.1.4. Results for South Pacific Region

Linear Trend of zonal average for SP region from NOBM and greenhouse gas simulations of the whole and reduced time period of model simulations is shown in Figure 11.5. Linear trend of zonal average from

greenhouse gas simulations is chosen as an example for visual comparison because this is the signal that is of interest in this detection study. Trends from NOBM were 10 times higher than the trends from whole time period of simulations, therefore for clarity in presentation, trends from NOBM were plotted after dividing them by 10. From Figure 11.5 it can be seen that in observations (blue line in graph), the linear trend of zonal chl increases in subtropical latitudes (-25 to -30oS) and decreases in subpolar and mid-latitudes (-50 to -70oS) in SP region. This pattern of trend is not observed in greenhouse gas simulations from the models (Figure 11.5). However, pattern of trends are consistent between the models. Thus, visual comparison of the trends from model simulations indicate consistency between signals obtained from the same model forcing simulation from different models but the trends from signals are not similar to those from NOBM.

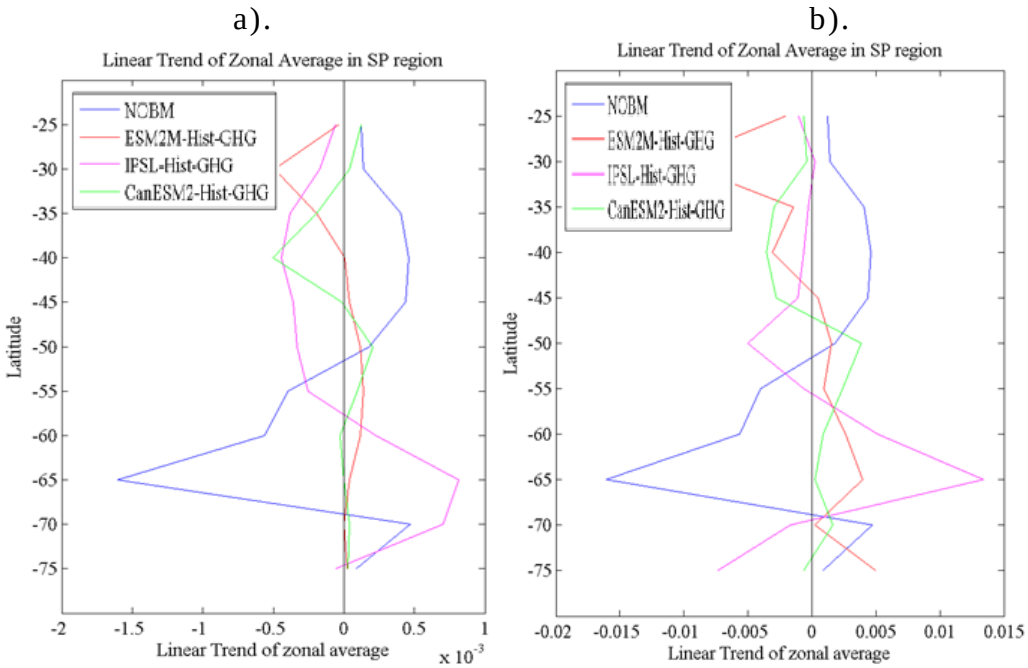

Figure 11-5. Linear Trend of zonal average for SP region from NOBM (data x 10^{-1}) and greenhouse gas simulations from models. a). Linear trend computed for whole time period and b). Linear trend computed for reduced time period.

Statistical terms of comparison between linear trend of zonal average from model simulations and NOBM that were computed are correlation coefficient, centered root mean square difference and amplitude of the variation i.e. standard deviation. Linear trend of zonal average for model

simulations was computed for two time periods i.e. whole and reduced. The results are presented in the form of a Taylor Diagram (Figure 11.6). Table of values associated with the Figure are presented in Table 11-4. Figure 11.6a shows statistical terms of comparisons when linear trend of zonal average was computed from whole time period of simulations. Figure 11.6b shows statistical terms of comparisons when linear trend of zonal average was computed from reduced time period of simulations.

Table 11-4 below shows the value of the statistical terms of comparison i.e. the correlation coefficient, root mean square difference and standard deviation when linear trend of zonal average for SP region of the ocean computed from different model simulations for two time periods (whole and reduced) was compared with linear trend of zonal average from NOBM.

Table 11-4. Statistical terms of comparison for South Pacific region.

Model Simulation	Correlation Coefficient		RMS difference		Standard Deviation	
	W	R	W	R	W	R
B	-0.24991	0.22732	0.00598	0.00583	0.00005	0.00187
C	-0.40679	-0.33082	0.00601	0.00681	0.00011	0.00185
D	-0.26068	-0.41574	0.00601	0.00847	0.00017	0.00402
F	-0.11905	0.30333	0.00597	0.00638	0.00005	0.00471
G	-0.38337	-0.13854	0.00616	0.00667	0.00047	0.00227
H	-0.37731	0.26491	0.00602	0.00699	0.00015	0.00555
I	-0.59607	-0.81401	0.00622	0.01058	0.00041	0.00514
J	-0.67895	0.08427	0.00602	0.00917	0.00008	0.00749
K	-0.70064	0.53496	0.00653	0.00737	0.00077	0.00857
L	-0.19224	0.10861	0.00599	0.00606	0.00014	0.00191
M	-0.22480	-0.32037	0.00601	0.00699	0.00018	0.00221
N	-0.08822	-0.14957	0.00597	0.00710	0.00003	0.00306
O	-0.18344	0.20864	0.00615	0.00737	0.00077	0.00575

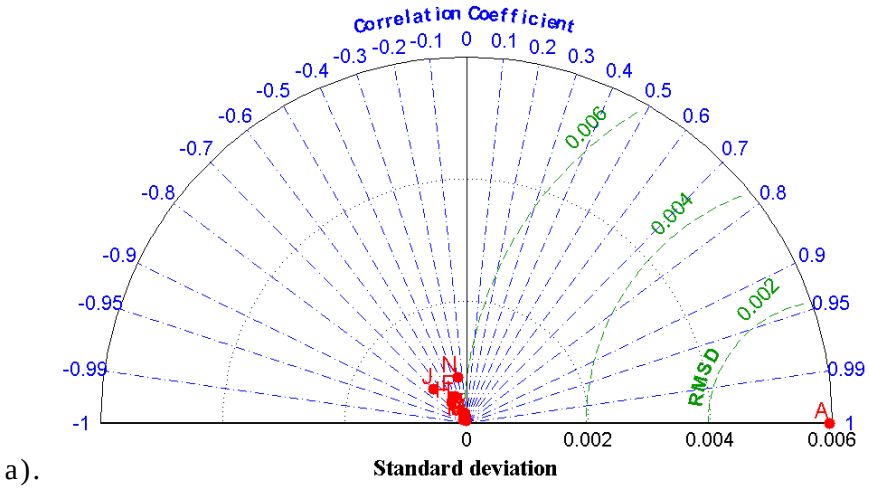

a).

b).

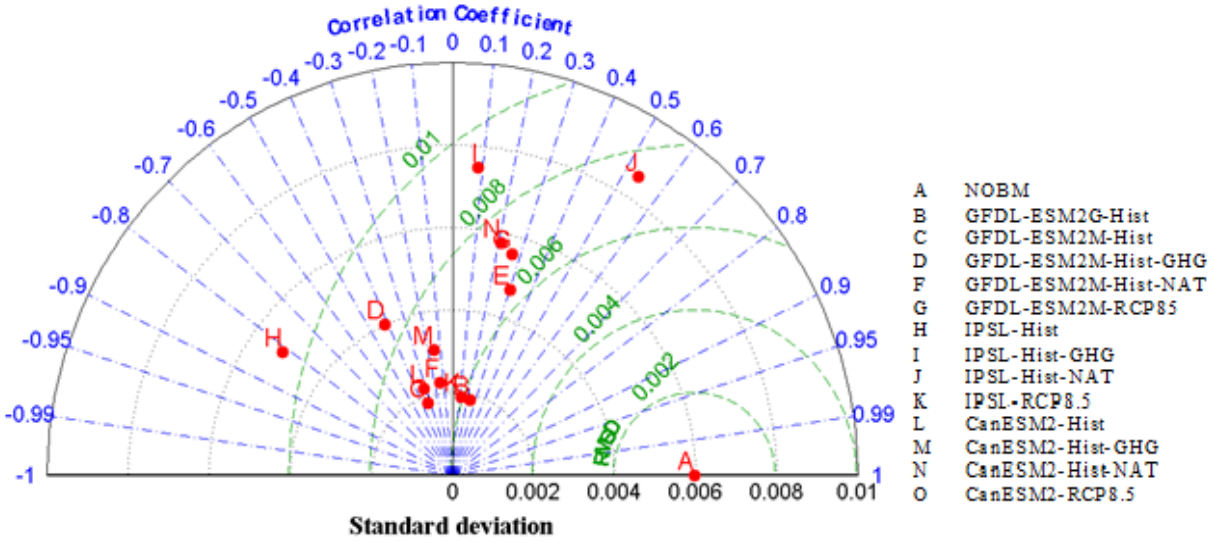

Figure 11-6. Taylor diagrams associated with the comparisons of linear trend of zonal average for SP region computed from a). whole time period of simulations and b). reduced time period of simulations, with linear trend of zonal average for SP region computed from NOBM.

From Figure 11.6, it can be seen that the correlation coefficient for all the model simulations is moderate i.e. not very low or very high (-0.8140 to 0.5350 in this study). This indicates that linear trend of zonal average from model simulations is partially phased with NOBM. For most of the simulations correlation coefficient changes sign and magnitude for the two time periods for which linear trend is computed. This indicates that signal from whole time period of data is not the same as the reduced time period of data and they should be treated as two different metrics of signal computation. It should also be noted from Figure that sign of the correlation

coefficient from same forcing simulation from different models is consistent for whole time period than for reduced time period. For example, correlation coefficient obtained for whole time period of historical simulation from ESM2M, IPSL and CanESM2 is negative but for reduced time period correlation coefficient is negative for historical simulation from ESM2M but is positive for historical simulation from IPSL and CanESM2.

From Figure 11.6, it can also be seen that the standard deviation of all the model simulations is lower than NOBM for the 'whole time period'. On the other hand, for the reduced time period, standard deviation for some model simulations is larger than NOBM. The difference between the standard deviations of NOBM and model simulations for the whole time period (10^{-3}) is higher compared to the difference between the standard deviations of NOBM and the model simulations for the reduced time period (10^{-4}-10^{-3}). From this it can be concluded that the amplitude of the linear trend of zonal average from the 'whole time period' of model simulations underestimates the amplitude of the linear trend of zonal average of chl from NOBM and the 'reduced time period' of model simulations gives a much closer estimate to the amplitude of the linear trend of zonal average from NOBM.

11.1.5. Results for Indian Ocean Region

Linear Trend of zonal average for IO region from NOBM and greenhouse gas simulations of the whole and reduced time period of model simulations is shown in Figure 11.7. Linear trend of zonal average from greenhouse gas simulations is chosen as an example for visual comparison because this is the signal that is of interest in this detection study. Trends from NOBM were 10 times higher than the trends from whole time period of simulations, therefore for clarity in presentation, trends from NOBM were plotted after dividing them by 10. From Figure 11.7 it can be seen that in observations (blue line in graph), the linear trend of zonal chl is increasing in mid-latitudes (-37^{o} to -42^{o}N) and it is decreasing in sub-polar and mid-latitude (-70^{o} to -42^{o} N) in IO region. This pattern in trend of zonal average is not observed in model simulations (Figure 11.7). From the Figure 11.7 it

can also be seen that pattern of trends from ESM2M-Hist-GHG, IPSL-Hist-GHG and CanESM2-Hist-GHG follow each other closely in all the latitudinal zones. Thus, visual comparison of the trends from model simulations indicate consistency between signals obtained from the same model forcing simulation from different models. Also, pattern of trends from model simulations are not similar to patterns from NOBM.

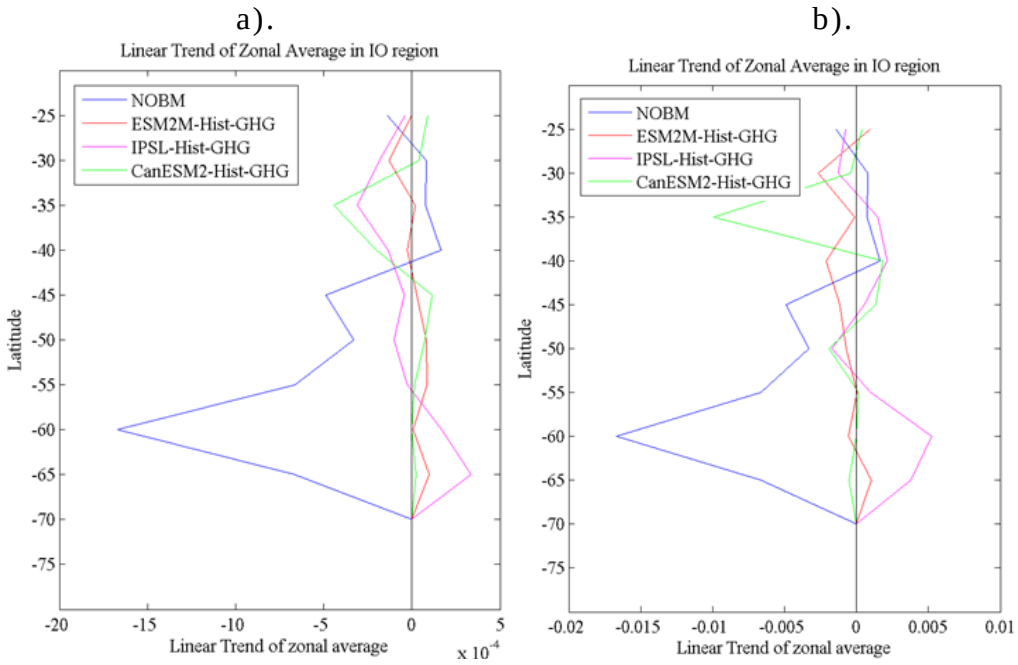

Figure 11-7. Linear Trend of zonal average for IO region from NOBM (data x 10^{-1}) and greenhouse gas simulations from models. a). Linear trend computed for whole time period and b). Linear trend computed for reduced time period.

Statistical terms of comparison between linear trend of zonal average from model simulations and NOBM that were computed are correlation coefficient, centered root mean square difference and amplitude of the variation i.e. standard deviation. Linear trend of zonal average for model simulations was computed for two time periods i.e. whole and reduced. The results are presented in the form of a Taylor Diagram (Figure 11.8). Table of values associated with the Figure are presented in Table 11-5. Figure 11.8a shows statistical terms of comparisons when linear trend of zonal average was computed from whole time period of simulations. Figure 11.8b shows statistical terms of comparisons when linear trend of zonal average was computed from reduced time period of simulations.

Table 11-5 below shows the value of the statistical terms of comparison i.e. the correlation coefficient, root mean square difference and standard deviation when linear trend of zonal average for IO region of the ocean computed from different model simulations for two time periods (whole and reduced) was compared with linear trend of zonal average from NOBM.

Table 11-5. Statistical terms of comparison for Indian Ocean region.

Model Simulation	**Correlation Coefficient**		**RMS difference**		**Standard Deviation**	
	W	**R**	**W**	**R**	**W**	**R**
B	-0.69455	0.28697	0.00515	0.00493	0.00005	0.00092
C	-0.82346	-0.00392	0.00517	0.00543	0.00008	0.00181
D	-0.38960	-0.23733	0.00514	0.00547	0.00006	0.00109
F	-0.05952	0.04720	0.00511	0.00550	0.00002	0.00228
G	-0.63861	-0.41424	0.00525	0.00658	0.00021	0.00253
H	-0.78795	0.87466	0.00520	0.00294	0.00012	0.00290
I	-0.65153	-0.67394	0.00522	0.00664	0.00016	0.00202
J	-0.85902	-0.93568	0.00515	0.01141	0.00005	0.00648
K	-0.73322	0.84735	0.00573	0.00283	0.00081	0.00353
L	-0.29123	0.31035	0.00514	0.00498	0.00010	0.00270
M	-0.32110	-0.19276	0.00516	0.00642	0.00015	0.00302
N	0.32063	0.41072	0.00510	0.00468	0.00004	0.00258
O	-0.27832	0.28411	0.00541	0.00508	0.00086	0.00277

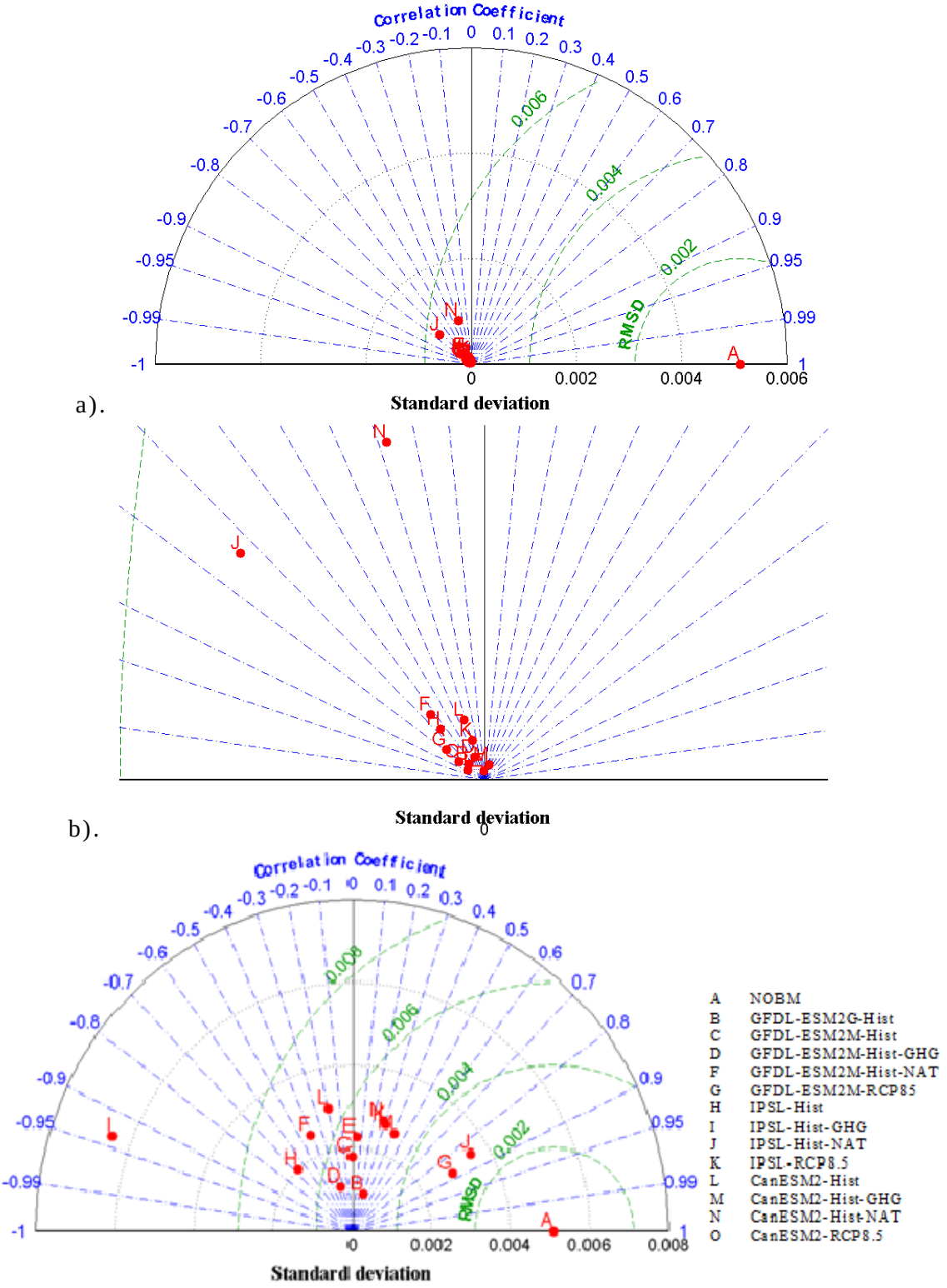

Figure 11-8. Taylor diagrams associated with the comparisons of linear trend of zonal average for IO region computed from a). whole time period of simulations and b). reduced time period of simulations, with linear trend of zonal average for IO region computed from NOBM.

From Figure 11.8, it can be seen that the correlation coefficient for all the model simulations is moderate i.e. not very low or very high (-0.9357 to 0.8747 in this study). This indicates that linear trend of zonal average from model simulations is highly phased with NOBM. For most of the simulations correlation coefficient changes sign and magnitude for the two time periods for which linear trend is computed. This indicates that signal from whole time period of data is not the same as the reduced time period of data and they should be treated as two different metrics of signal computation. It should also be noted from Figure that sign of the correlation coefficient from same forcing simulation from different models is consistent for whole time period than for reduced time period. For example, correlation coefficient obtained for whole time period of historical simulation from ESM2M, IPSL and CanESM2 is negative but for reduced time period correlation coefficient is negative for historical simulation from ESM2M and is positive for greenhouse gas simulation from IPSL and CanESM2.

From Figure 11.8, it can also be seen that the standard deviation of all the model simulations is lower than NOBM for the 'whole time period'. On the other hand, for the reduced time period, standard deviation for some model simulations is larger than NOBM. The difference between the standard deviations of NOBM and model simulations for the whole time period and reduced time period is not very small (10^{-3}) and therefore it can be concluded that the amplitude of the linear trend of zonal average from the whole and reduced time period of model simulations underestimates the amplitude of the linear trend of zonal average of chl from NOBM.

11.2. Level of truncation

Table 11-6. Percent of eigenvectors chosen for the noise covariance matrix

Model Simulation Alphabet	NA		SA		NP		SP		IO	
	W	R	W	R	W	R	W	R	W	R
B	36.36	63.64	58.33	50.00	54.55	45.45	45.45	45.45	63.64	45.45
C	54.55	54.55	50.00	50.00	72.73	45.45	63.64	45.45	63.64	54.55
D	54.55	54.55	50.00	58.33	63.64	54.55	63.64	45.45	63.64	72.73
F	54.55	45.45	41.67	50.00	63.64	54.55	63.64	72.73	54.55	45.45
G	45.45	54.55	50.00	41.67	63.64	54.55	63.64	45.45	54.55	45.45
H	63.64	54.55	50.00	58.33	63.64	54.55	63.64	54.55	54.55	63.64
I	54.55	63.64	50.00	58.33	45.45	63.64	81.82	54.55	54.55	45.45
J	45.45	54.55	41.67	50.00	54.55	45.45	81.82	63.64	54.55	54.55
K	45.45	54.55	58.33	50.00	54.55	63.64	81.82	63.64	54.55	54.55
L	63.64	54.55	50.00	50.00	36.36	63.64	54.55	54.55	45.45	54.55
M	54.55	72.73	33.33	33.33	45.45	45.45	45.45	54.55	54.55	54.55
N	63.64	54.55	41.67	41.67	54.55	63.64	72.73	63.64	54.55	54.55
O	54.55	54.55	50.00	41.67	54.55	54.55	54.55	54.55	45.45	72.73

11.3. Detection Results

Beta values obtained after the implementation of the OF method indicate whether the signal has been detected in the observations or not.

Table 11-7. Beta values for NA region

Model Simulation	BETA	
	WHOLE	REDUCED
B	30.15	-8.63
C	-136.99	-1.93
D	55.47	0.92
F	-625.51	-2.6
G	3.44	12.77
H	79.47	0.77
I	10.75	0.39
J	-42.46	0.91
K	1.66	1.08
L	-87.71	0.67
M	55.18	-1.94
N	-260.9	-0.53
O	5.364	-4.72

11.3.1. Results for South Atlantic Region

Scaling factors obtained as a result of the implementation of the OF method in linear trend of zonal average of chl in SA region of the ocean using linear trend of zonal average from model forced simulations as the signal is shown in Figure 11.9 and given in Table 11-8.

a).

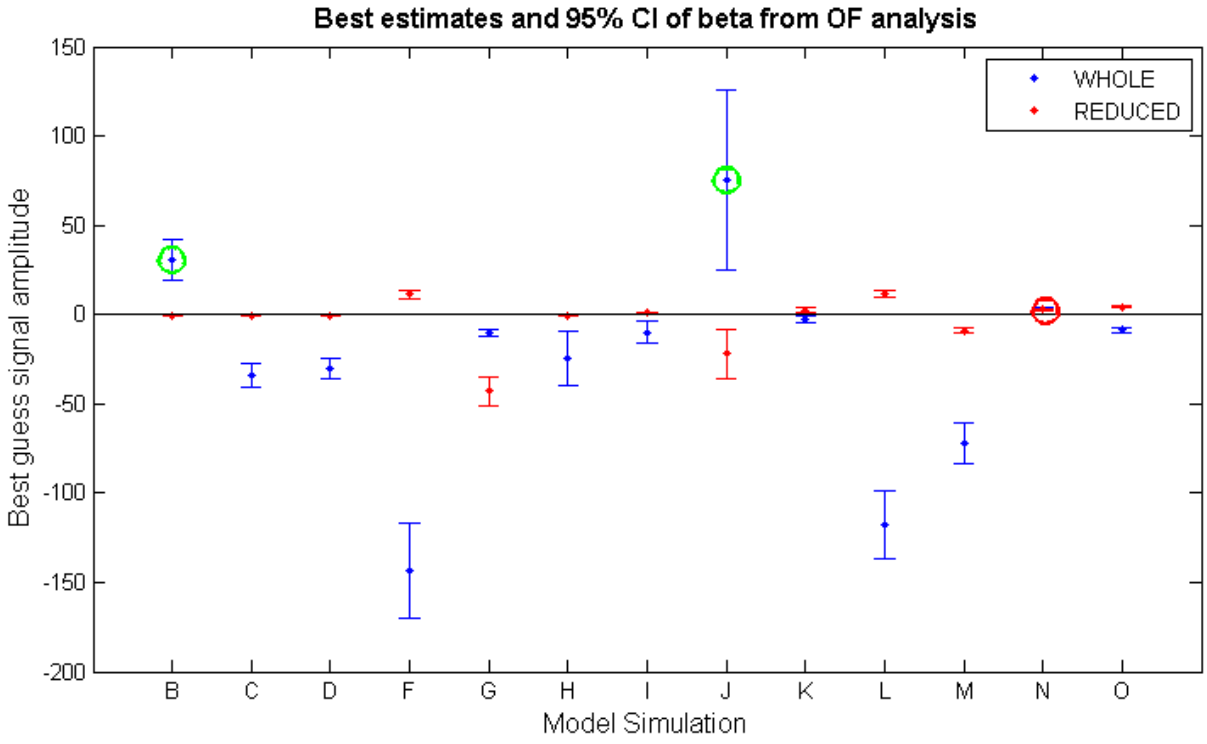

B	GFDL-ESM2G-Hist
C	GFDL-ESM2M-Hist
D	GFDL-ESM2M-Hist-GHG
F	GFDL-ESM2M-Hist-NAT
G	GFDL-ESM2M-RCP85
H	IPSL-Hist
I	IPSL-Hist-GHG
J	IPSL-Hist-NAT
K	IPSL-RCP8.5
L	CanESM2-Hist
M	CanESM2-Hist-GHG
N	CanESM2-Hist-NAT
O	CanESM2-RCP8.5

b).

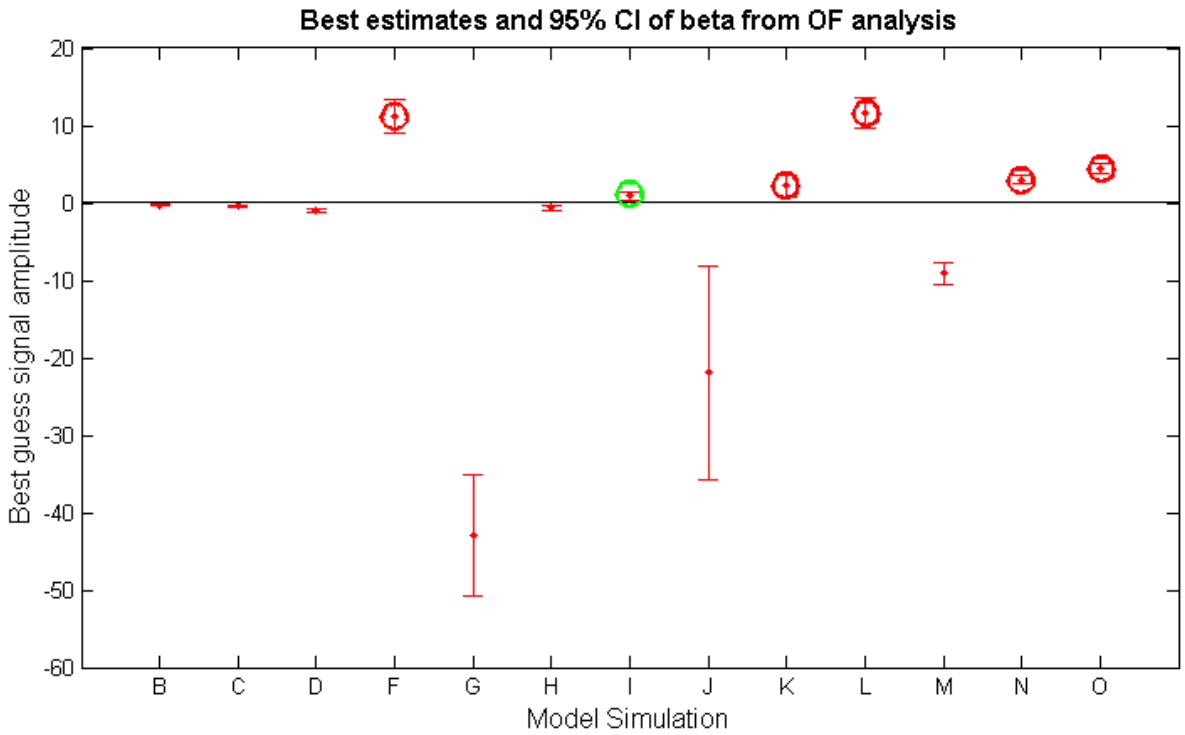

Figure 11-9. Graph of signal amplitude along with the CI, obtained for OF implementation in SA region using signals from whole and reduced time period of model simulations. a). result for both whole (blue) and reduced (red) time period of model simulations used to compute the signal. b). result for only reduced time period of model simulations. Green circles indicate scaling factors which are positive and are obtained for the simulations for which consistency test passed. Red circles indicate scaling factors which are positive and are obtained for the simulations for which consistency test failed. Circles in a) are drawn only for whole time period of simulations.

Figure 11.9 above shows the beta values obtained in SA region for signals obtained from model forced simulations along with the confidence interval (CI) associated with each beta value. Figure 11.9 part (a) shows beta values for both whole (blue) and reduced (red) time period of model simulations and part (b) shows beta values for only reduced time period of model simulations used to compute the signal.

Table 11-8. Beta values for SA region

Model Simulation	BETA	
	WHOLE	REDUCED
B	30.65	-0.31
C	-33.98	-0.42
D	-30.13	-0.94
F	-143.62	11.24
G	-10.03	-42.92
H	-24.28	-0.64
I	-9.92	0.89
J	75.49	-21.94
K	-2.63	2.21
L	-117.86	11.60
M	-72.11	-9.13
N	3.15	2.98
O	-8.80	4.39

For the whole time period of model simulations, it can be seen from the Figure 11.9a (blue dots and CI lines) that positive beta values are obtained for signals from whole time period of GFDL-ESM2G historical, GFDL-ESM2M historical natural and CanESM2 historical natural. This indicates that signals from these model simulations are detected in the observations. For the reduced time period of model simulations, it can be seen from the Figure 11.9b (red dots and CI lines) that positive beta values are obtained for signals from reduced time period of GFDL-ESM2M historical natural, IPSL historical GHG and RCP8.5 and CanESM2 historical, historical natural and RCP8.5 simulations. As there is no consistency in the estimation of scaling factor values from the four models, it is difficult to judge the result of the detection of a signal from particular model simulation in the observations. For example, for the signals from the whole time period of model simulations, positive scaling factor is obtained for historical simulation from GFDL-ESM2G model. For the other three models (ESM2M, IPSL and CanESM2) scaling factors are negative. Thus, it is difficult to conclude the

detection result of the signal from historical forcing simulation in the observations.

Significance of the scaling factors for the simulations for which the consistency test failed (Table 4.3) is questionable and therefore, only those results would be considered significant where the consistency test passed. Green circles in Figure 11.9 indicate scaling factors which are positive and are obtained for the simulations for which consistency test passed. Red circles in Figure 11.9 indicate scaling factors which are positive and are obtained for the simulations for which consistency test failed. As it can be seen from the Figure 11.9 above, scaling factors for whole time period of historical simulation from GFDL-ESM2G model and historical natural simulation from IPSL model is 30.65 and 75.49 respectively, which are significantly different from 0 with 5-95% confidence interval. Also, scaling factors for reduced time period of historical greenhouse gas simulation from IPSL model is 0.89, which is significantly different from 0 with 5-95% confidence interval. As the signals from different model simulations are detected in the observations, it implies that signal detection is not consistent between the models for any forcing simulation and is also not consistent between whole and reduced time period of simulations from the models. Beta values are greater than unity for whole time period of model simulations, it can be inferred that the model simulated response of chl to external forcings is significantly underestimated and it needs to be amplified (by a factor of ~30 and ~75) to be consistent with observations. Beta value is less than unity for reduced time period of model simulation, it can be inferred that the model simulated response of chl to external forcings is being overestimated and it needs to be decreased to be consistent with observations.

11.3.2. Results for North Pacific Region

Scaling factors obtained as a result of the implementation of the OF method in spatial linear trend of chl in NP region of the ocean using linear trend of zonal average from model forced simulations as the signal is shown in Figure 11.10 and given in Table 11-9.

a).

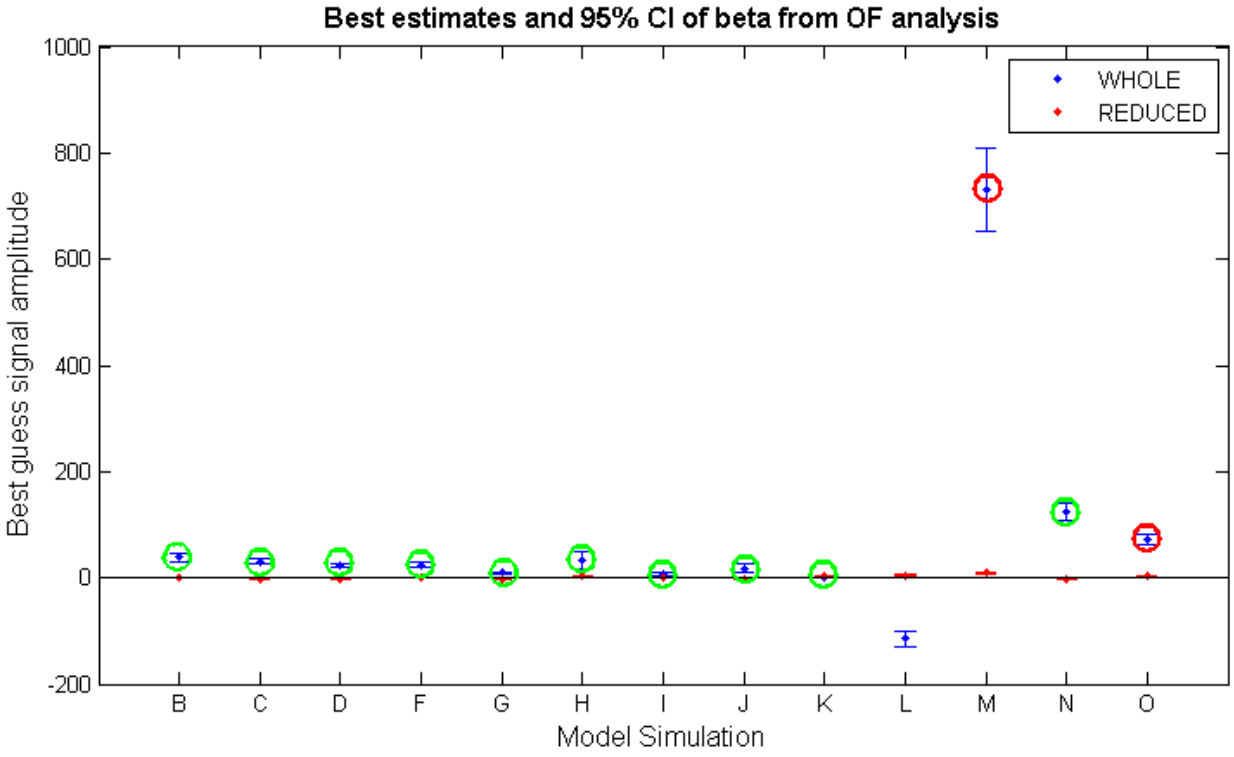

B	GFDL-ESM2G-Hist
C	GFDL-ESM2M-Hist
D	GFDL-ESM2M-Hist-GHG
F	GFDL-ESM2M-Hist-NAT
G	GFDL-ESM2M-RCP85
H	IPSL-Hist
I	IPSL-Hist-GHG
J	IPSL-Hist-NAT
K	IPSL-RCP8.5
L	CanESM2-Hist
M	CanESM2-Hist-GHG
N	CanESM2-Hist-NAT
O	CanESM2-RCP8.5

b).

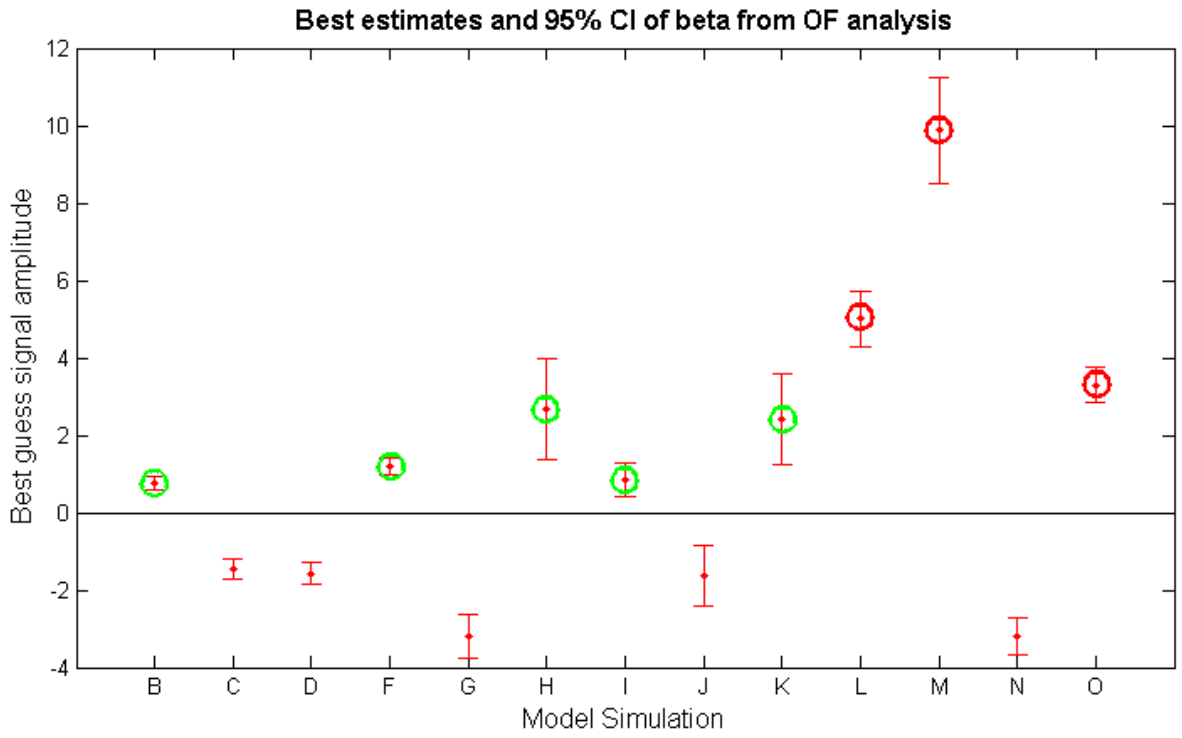

Figure 11-10. Graph of signal amplitude along with the CI, obtained for OF implementation in NP region using signals from whole and reduced time period of model simulations. a). result for both whole (blue) and reduced (red) time period of model simulations used to compute the signal. b). result for only reduced time period of model simulations. Green circles indicate scaling factors which are positive and are obtained for the simulations for which consistency test passed. Red circles indicate scaling factors which are positive and are obtained for the simulations for which consistency test failed. Circles in a) are drawn only for whole time period of simulations.

Figure 11.10 above shows the beta values obtained in NP region for signals obtained from model forced simulations along with the confidence interval (CI) associated with each beta value. Figure 11.10 part (a) shows beta values for both whole (blue) and reduced (red) time period of model simulations and part (b) shows beta values for only reduced time period of model simulations used to compute the signal.

Table 11-9. Beta values for NP region

Model Simulation	BETA	
	WHOLE	REDUCED
B	38.587	0.766
C	30.753	-1.471
D	23.665	-1.571
F	24.072	1.195
G	9.375	-3.194
H	33.776	2.689
I	7.722	0.854
J	17.621	-1.617
K	1.827	2.411
L	-114.351	5.002
M	730.222	9.873
N	124.312	-3.194
O	71.916	3.303

For the whole time period of model simulations, it can be seen from the Figure 11.10a (blue dots and CI lines) that positive beta values are obtained for signals from all the model simulations except for historical simulation from CanESM2 model. This indicates that signals from these model simulations are detected in the observations. For the reduced time period of model simulations, it can be seen from the Figure 11.10b (red dots and CI lines) that positive beta values are obtained for signals from GFDL-ESM2G historical, GFDL-ESM2M historical natural, IPSL historical, historical GHG and RCP8.5 and CanESM2 historical, historical GHG and RCP8.5 simulations. Thus, it can be seen that there is consistency in the detection results from whole time period of model simulations but detection results from reduced time period of simulations is not consistent. For example, positive scaling factor is obtained from whole time period of greenhouse gas simulation from ESM2M, IPSL and CanESM2 model. However, for reduced time period of simulations, positive scaling factor is obtained for greenhouse gas simulation from IPSL and CanESM2 model and negative scaling factor is

obtained for greenhouse gas simulation from ESM2M model. This inconsistency makes it difficult to judge the result of the detection of a signal from particular reduced time period of model simulations in the observations.

Significance of the scaling factors for the simulations for which the consistency test failed (Table 4.3) is questionable and therefore, only those results would be considered significant where the consistency test passed. Green circles in Figure 11.10 indicate scaling factors which are positive and are obtained for the simulations for which consistency test passed. Red circles in Figure 11.10 indicate scaling factors which are positive and are obtained for the simulations for which consistency test failed. As it can be seen from the Figure 11.10 above, scaling factors for whole time period of all the forcing simulations from ESM2G, ESM2M and IPSL model and only historical natural simulation from CanESM2 model are significantly different than 0 with 5-95% confidence interval. Values of the scaling factors ranges for signals from whole time period of simulation ranges from 1.8 to 124.3. This indicates that model simulated response of chl to external forcings is significantly underestimated and it needs to be amplified (by a factor of ~2 to ~124) to be consistent with observations Scaling factors for reduced time period of ESM2G historical, ESM2M historical natural, IPSL historical, historical GHG and RCP8.5 simulations are 0.77, 1.2, 2.69, 0.85 and 2.41 respectively, which are significantly different from 0 with 5-95% confidence interval. As the value of the scaling factors are not very different from unity it indicates that though the model simulated response of chl to external forcings from reduced time period of simulations is being underestimated or overestimated, it is a much closer estimate to observations than the response from whole time period of model simulations.

11.3.3. Results for South Pacific Region

Scaling factors (β)/beta obtained as a result of the implementation of the OF method in spatial linear trend of chl in SP region of the ocean using linear trend of zonal average from model forced simulations as the signal is shown in Figure 11.10 and given in Table 11-10.

a).

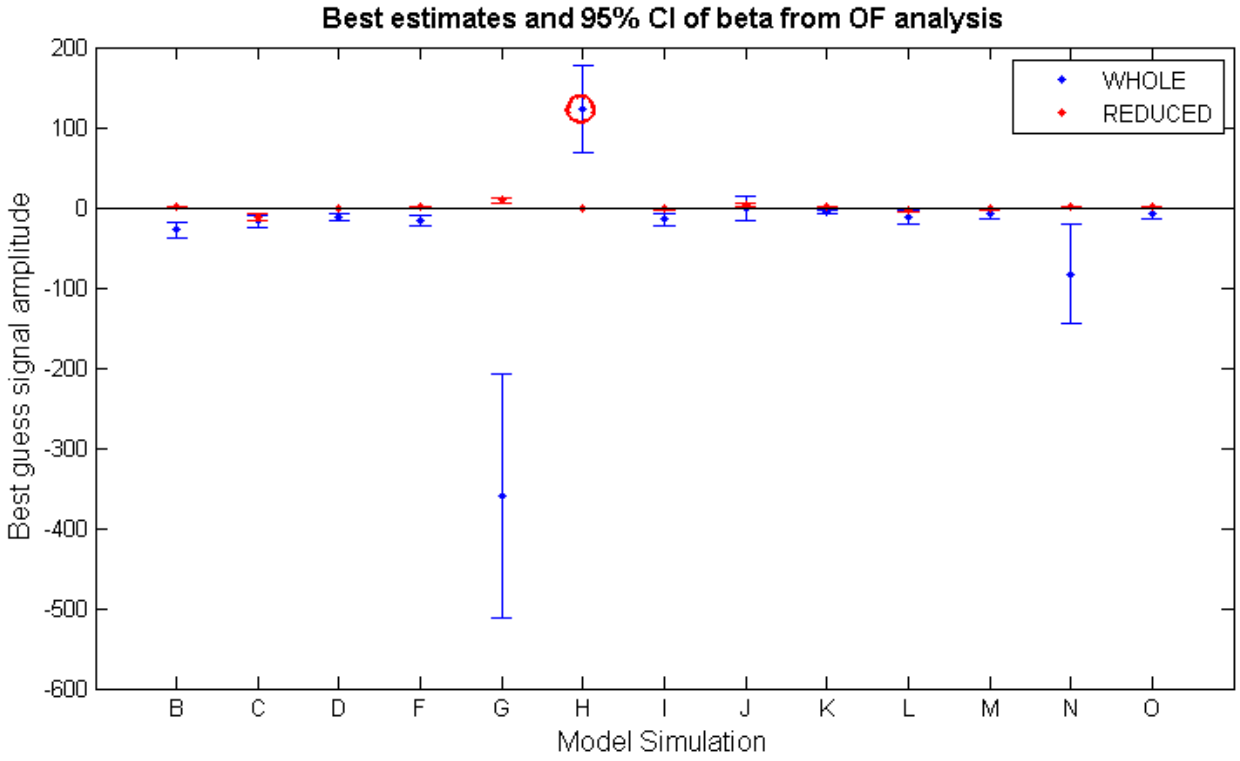

B	GFDL-ESM2G-Hist
C	GFDL-ESM2M-Hist
D	GFDL-ESM2M-Hist-GHG
F	GFDL-ESM2M-Hist-NAT
G	GFDL-ESM2M-RCP85
H	IPSL-Hist
I	IPSL-Hist-GHG
J	IPSL-Hist-NAT
K	IPSL-RCP8.5
L	CanESM2-Hist
M	CanESM2-Hist-GHG
N	CanESM2-Hist-NAT
O	CanESM2-RCP8.5

b).

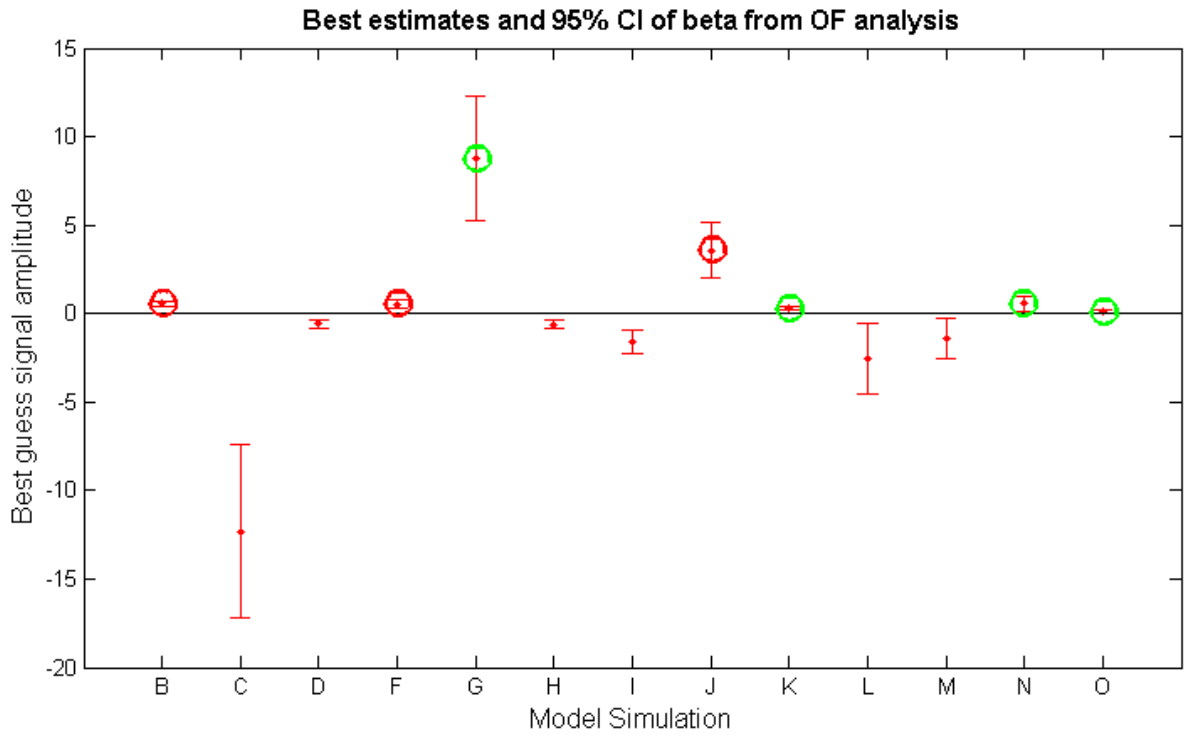

Figure 11-11. Graph of signal amplitude along with the CI, obtained for OF implementation in SP region using signals from whole and reduced time period of model simulations. a). result for both whole (blue) and reduced (red) time period of model simulations used to compute the signal. b). result for only reduced time period of model simulations. Green circles indicate scaling factors which are positive and are obtained for the simulations for which consistency test passed. Red circles indicate scaling factors which are positive and are obtained for the simulations for which consistency test failed. Circles in a) are drawn only for whole time period of simulations.

Figure 11.11 above shows the beta values obtained in SP region for signals obtained from model forced simulations along with the confidence interval (CI) associated with each beta value. Figure 11.11 part (a) shows beta values for both whole (blue) and reduced (red) time period of model simulations and part (b) shows beta values for only reduced time period of model simulations used to compute the signal.

Table 11-10. Beta values for SP region

Model Simulation	BETA	
	WHOLE	REDUCED
B	-28.149	0.546
C	-17.18	-12.331
D	-12.083	-0.582
F	-15.541	0.528
G	-359.715	8.782
H	123.25	-0.605
I	-15.151	-1.572
J	-1.578	3.574
K	-5.091	0.295
L	-11.572	-2.565
M	-8.153	-1.429
N	-82.714	0.549
O	-8.295	0.131

For the whole time period of model simulations, it can be seen from the Figure 11.11a (blue dots and CI lines) that positive beta values are obtained for signals from historical simulation from IPSL model. For the reduced time period of model simulations, it can be seen from the Figure 11.11b (red dots and CI lines) that positive beta values are obtained for signals from GFDL-ESM2G historical, GFDL-ESM2M historical natural and RCP8.5, IPSL historical natural and RCP8.5 and CanESM2 historical natural and RCP8.5 simulations. This indicates that signals from these model simulations are detected in the observations. Thus, it can be seen that there is consistency in the detection results from whole and reduced time period of model simulations. For example, positive scaling factor is obtained from reduced time period of historical natural simulation from ESM2M, IPSL and CanESM2 model. This consistency in signal detection makes it easy to judge the result of the detection of a signal from model simulations in the observations.

Significance of the scaling factors for the simulations for which the consistency test failed (Table 4.3) is questionable and therefore, only those results would be considered significant where the consistency test passed. Green circles in Figure 11.11 indicate scaling factors which are positive and are obtained for the simulations for which consistency test passed. Red circles in Figure 11.11 indicate scaling factors which are positive and are obtained for the simulations for which consistency test failed. As it can be seen from the Figure 11.11 above, scaling factors for whole time period of all the forcing simulations from the four models is negative. This indicates that no signal is significantly detected for whole time period of model simulations. Scaling factors for reduced time period of IPSL RCP8.5 and CanESM2 historical natural and RCP8.5 simulations are 0.295, 0.55 and 0.131 respectively, which are significantly different from 0 with 5-95% confidence interval. As the value of the scaling factors are less than unity it indicates that the model simulated response of chl to external forcings from reduced time period of simulations is being overestimated and hence, the response needs to be subdued in order to be consistent with observations.

11.3.4. Results for Indian Ocean Region

Scaling factors (β)/beta obtained as a result of the implementation of the OF method in spatial linear trend of chl in IO region of the ocean using linear trend of zonal average from model forced simulations as the signal is shown in Figure 11.12 and given in Table 11-11.

a).

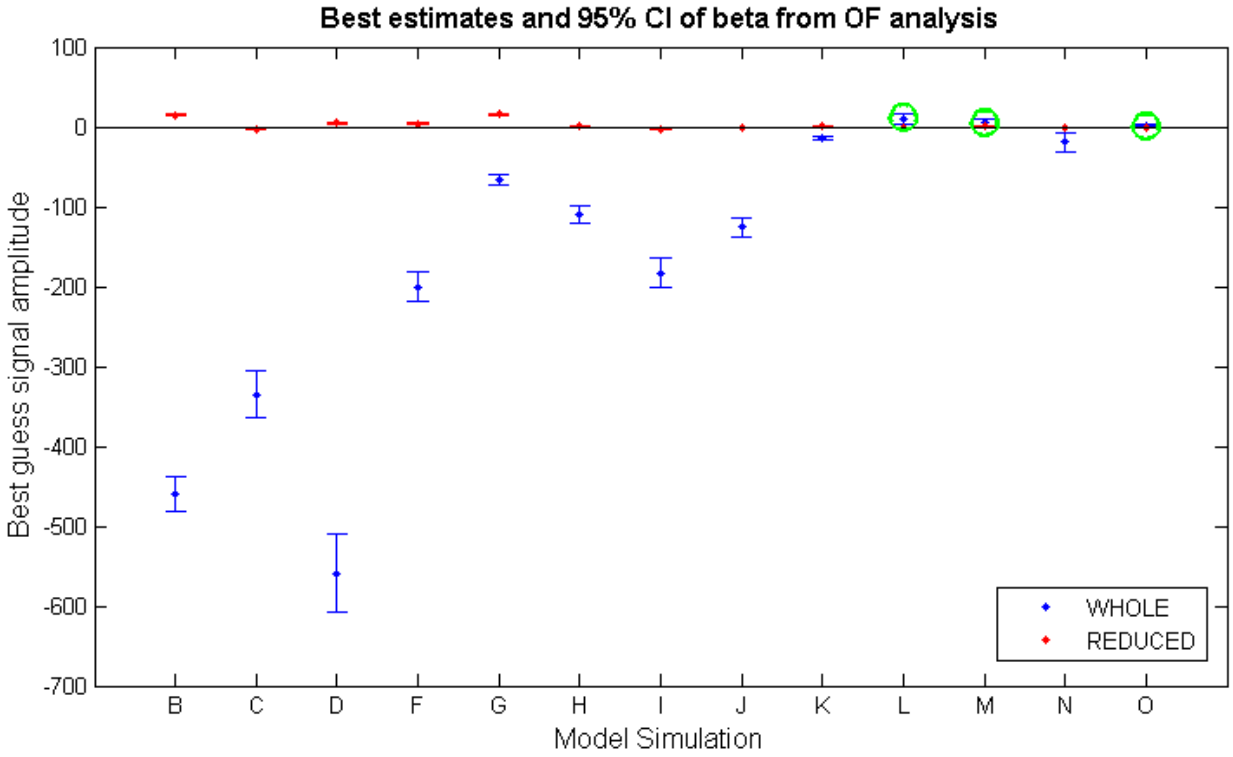

B	GFDL-ESM2G-Hist
C	GFDL-ESM2M-Hist
D	GFDL-ESM2M-Hist-GHG
F	GFDL-ESM2M-Hist-NAT
G	GFDL-ESM2M-RCP85
H	IPSL-Hist
I	IPSL-Hist-GHG
J	IPSL-Hist-NAT
K	IPSL-RCP8.5
L	CanESM2-Hist
M	CanESM2-Hist-GHG
N	CanESM2-Hist-NAT
O	CanESM2-RCP8.5

b).

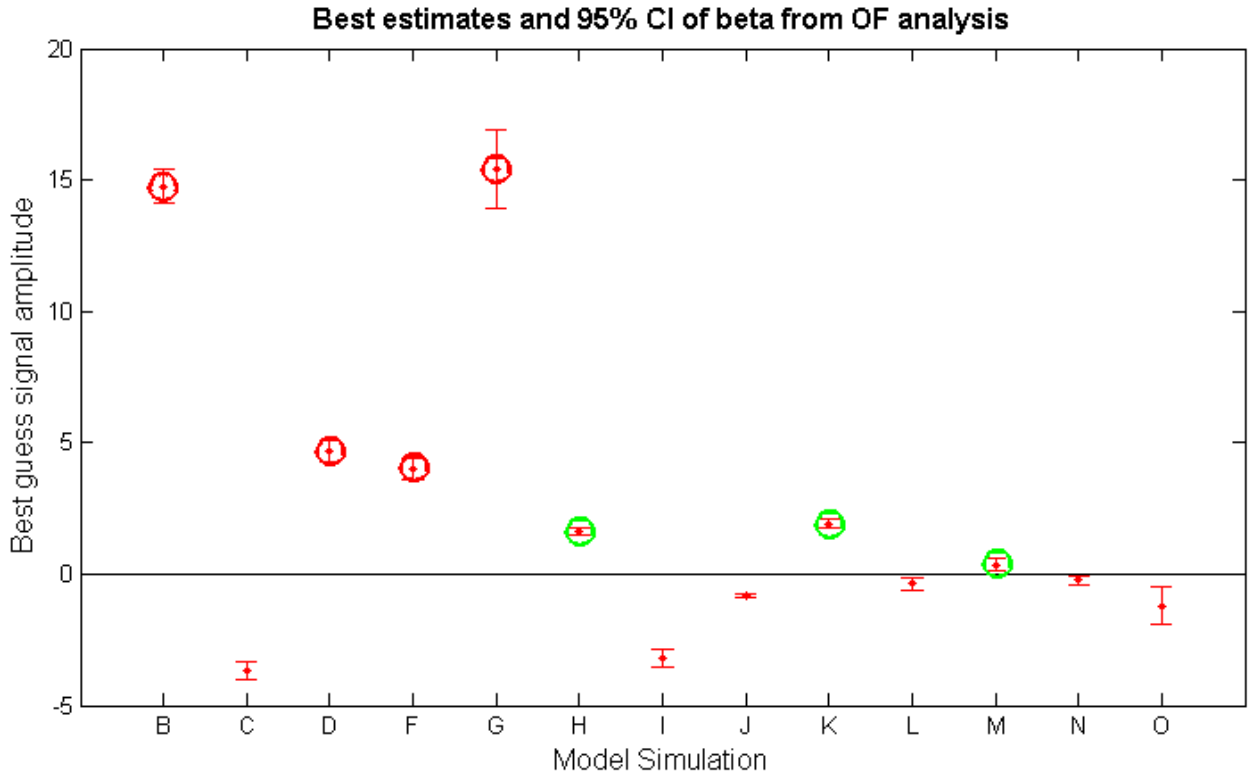

Figure 11-12. Graph of signal amplitude along with the CI, obtained for OF implementation in IO region using signals from whole and reduced time period of model simulations. a). result for both whole (blue) and reduced (red) time period of model simulations used to compute the signal. b). result for only reduced time period of model simulations. Green circles indicate scaling factors which are positive and are obtained for the simulations for which consistency test passed. Red circles indicate scaling factors which are positive and are obtained for the simulations for which consistency test failed. Circles in a) are drawn only for whole time period of simulations.

Figure 11.12 above shows the beta values obtained in IO region for signals obtained from model forced simulations along with the confidence interval (CI) associated with each beta value. Figure 11.12 part (a) shows beta values for both whole (blue) and reduced (red) time period of model simulations and part (b) shows beta values for only reduced time period of model simulations used to compute the signal.

Table 11-11. Beta values for IO region

Model Simulation	BETA	
	WHOLE	REDUCED
B	-460.182	14.751
C	-334.810	-3.704
D	-559.539	4.658
F	-200.013	4.0111
G	-66.131	15.396
H	-109.081	1.628
I	-183.333	-3.197
J	-126.025	-0.839
K	-14.334	1.917
L	10.7	-0.367
M	5.73	0.351
N	-19.295	-0.239
O	1.39	-1.214

For the whole time period of model simulations, it can be seen from the Figure 11.12a (blue dots and CI lines) that positive beta values are obtained for signals from historical, historical GHG and RCP8.5 simulations from CanESM2 model. For the reduced time period of model simulations, it can be seen from the Figure 11.12b (red dots and CI lines) that positive beta values are obtained for signals from GFDL-ESM2G historical, GFDL-ESM2M historical GHG, historical natural and RCP8.5, IPSL historical and RCP8.5 and CanESM2 historical GHG simulations. This indicates that signals from these model simulations are detected in the observations. Thus, it can be seen that there is no consistency in the detection results from whole and reduced time period of model simulations. For example, positive scaling factor is obtained from reduced time period of greenhouse gas simulation from ESM2M and CanESM2 models but scaling factor is negative for IPSL model. This inconsistency makes it difficult to judge the result of the detection of a signal from model simulations in the observations.

Significance of the scaling factors for the simulations for which the consistency test failed (Table 4.3) is questionable and therefore, only those results would be considered significant where the consistency test passed. Green circles in Figure 11.12 indicate scaling factors which are positive and are obtained for the simulations for which consistency test passed. Red circles in Figure 11.12 indicate scaling factors which are positive and are obtained for the simulations for which consistency test failed. As it can be seen from the Figure 11.12 above, scaling factors for whole time period of CanESM2 historical, historical GHG and RCP8.5 simulations are 10.7, 5.73 and 1.39 respectively, which are significantly different than 0 with 5-95% confidence interval. This indicates that model simulated response of chl to external forcings is significantly underestimated and it needs to be amplified (by a factor of ~10, ~5 and ~1.4) to be consistent with observations Scaling factors for reduced time period of IPSL historical and RCP8.5 and CanESM2 historical GHG simulations are 1.63, 1.92 and 0.35 respectively, which are significantly different from 0 with 5-95% confidence interval. As the value of the scaling factors are not very different from unity except for CanESM2 GHG simulation, it indicates that though the model simulated response of chl to external forcings from reduced time period of simulations is being underestimated or overestimated, it is a much closer estimate to observations than the response from whole time period of model simulations.

12. Appendix VI-Results for Chapter 5

12.1. Results of comparison of size of the gyres from model simulations with NOBM data

12.1.1. Results for North Atlantic Gyre

Table 12-1. Linear Trend (km^2 per month) in size of the NA gyre (1999-2005) and the column indicating whether the trend is significant or not by a 'Y' and a 'N' respectively.

Model Simulation	Linear Trend	Significant Trend
A	6576.80	Y
B	1140.00	N
C	829.71	N
D	6772.59	Y
F	12849.85	Y
G	5383.93	Y
H	-7763.03	Y
I	5663.54	Y
J	-1317.40	N
K	8542.20	Y
L	-997.10	N
M	-10852.44	Y
N	353.82	N
O	-3104.93	Y

Table 12-2. Statistical terms of comparison for time series of North Atlantic gyre area.

Model Simulation	Correlation Coefficient	RMS difference	Standard Deviation
B	-0.1609	1241014.3	730191.5
C	-0.0812	1111353.2	593258.9
D	-0.1904	1159655.0	589284.9
F	-0.0691	1085954.2	559540.5
G	-0.0204	1054946.2	544004.9
H	-0.2264	1450567.0	958832.8
I	0.0729	1271832.2	973172.4
J	0.0127	1191504.5	800410.1
K	0.2150	1816682.9	1785714.6
L	0.2181	976590.3	635737.3
M	-0.0662	1293544.4	878784.3
N	0.1342	1448916.8	1267223.6
O	-0.0153	1318640.5	956787.2

12.1.2. Results for South Atlantic Gyre

Time series of the SA Gyre area from NOBM and greenhouse gas simulations of the models is shown in Figure 12.1. Size of the gyres from greenhouse gas simulations is chosen as an example for visual comparison because this is the signal that is of interest in this detection study. From Figure 12.1 it can be seen in observations (NOBM) that there is a peak in the size of the gyres in mid 1999. After this the size of the gyres is decreasing till end of 2000 and then it is increasing each year in all the seasons except in winter where the size is decreasing. This pattern continues till end of 2004 after which the size of the gyre decreases in 2005. This pattern of increase and decrease in size of the gyre is followed partially by greenhouse gas simulations of the model. Observing the linear trend in the gyre size, it can be seen that there is an increasing trend (1408.74 km^2 per month) from NOBM, which is not observed in greenhouse gas simulations from the

models. Decreasing trend is observed in the size of the gyres from ESM2M (-7353.15 km^2 per month), IPSL (-5999.58 km^2 per month) and CanESM2 -3618.71 km^2 per month) model. However, trend in gyre size from NOBM and greenhouse gas simulation from CanESM2 are not significant. Also, there are several other simulations for which the trend in gyre size is not significant (Table 12-3). This shows that models are consistent with the outputs from the same forcing simulations and also, model outputs are not consistent with observations in pattern and trend. Trend in the size of the gyre from other simulations is given in Table 12-3.

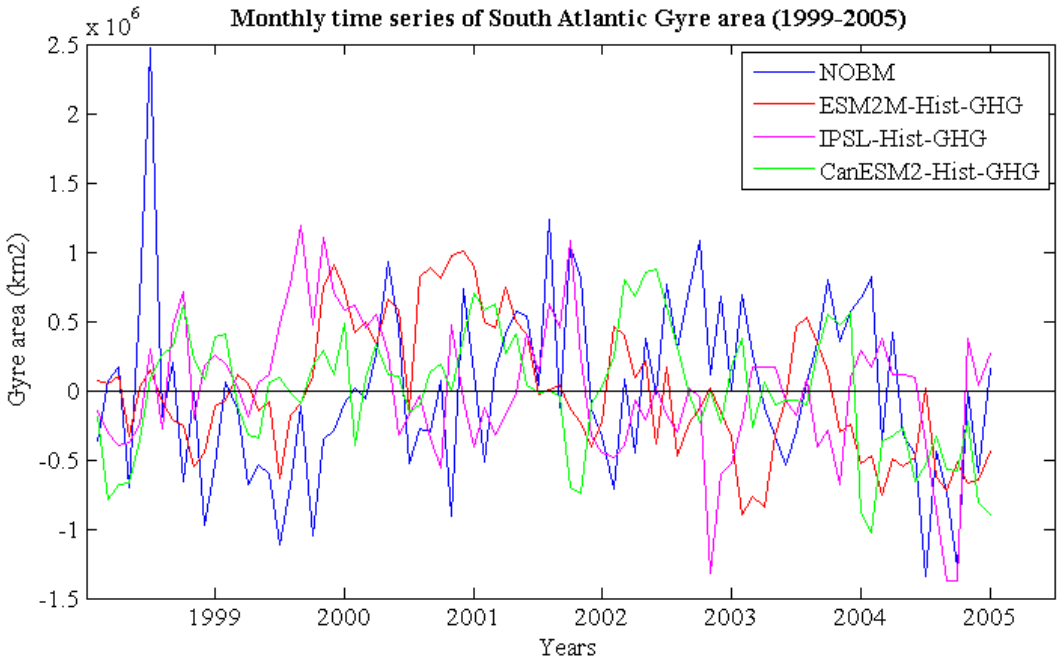

Figure 12-1. Monthly time series of the size of the NA gyre i.e. gyre area in km^2.

Table 12-3. Linear Trend (km^2 per month) in size of the SA gyre (1999-2005) and the column indicating whether the trend is significant or not by a 'Y' and a 'N' respectively.

Model Simulation	Linear Trend	Significant Trend
A	1408.74	N
B	8738.77	Y
C	-11209.48	Y
D	-7353.15	Y
F	-2372.82	N
G	1215.93	N
H	5853.88	Y
I	-5999.58	Y
J	-2229.49	N
K	-3226.59	N
L	3998.31	N
M	-3618.71	N
N	3149.19	N
O	-7242.87	Y

Statistical terms of comparison between size of the gyres from model simulations and NOBM that were computed are correlation coefficient, centered root mean square difference and amplitude of the variation i.e. standard deviation. The results are presented in the form of a Taylor Diagram (Taylor, 2001) (Figure 12-2) and Table of values associated with the Figure are presented in Table 12-4 below.

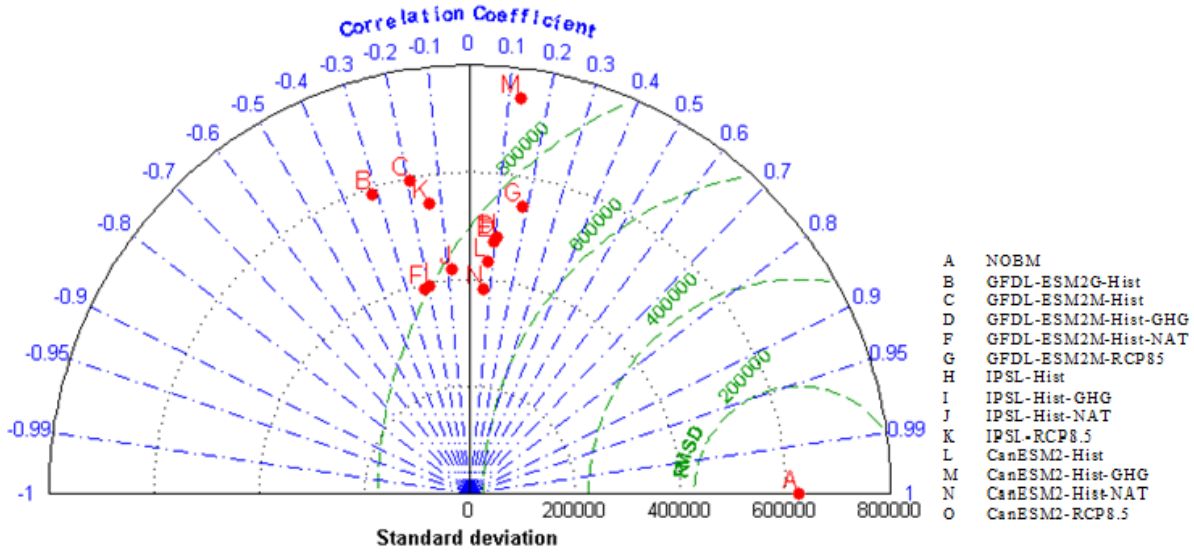

Figure 12-2. Taylor diagram associated with the comparisons of time series of gyre area for SA gyre computed from model simulations with time series of gyre area from NOBM.

Table 12-4. Statistical terms of comparison for time series of South Atlantic gyre area.

Model Simulation	Correlation Coefficient	RMS difference	Standard Deviation
B	-0.3168	984816.7	587582.4
C	-0.1918	943119.0	595663.8
D	0.0999	748793.0	478393.0
F	0.0980	745852.0	471742.4
G	-0.2180	807626.2	391984.6
H	0.1844	750444.8	545297.7
I	0.1081	747486.8	481951.5
J	-0.1912	801659.3	395443.1
K	-0.0818	781673.8	419996.5
L	-0.1382	886815.7	547793.1
M	0.0777	733464.2	434257.5
N	0.1296	907667.8	743546.5
O	0.0654	711995.2	382930.8

From Figure 12-2, it can be seen that the correlation coefficient for all the model simulations is low (-0.3168 to 0.1844 in this study). This indicates

that time series of the size of the gyres from model simulations is not correctly phased with NOBM. It should be noted from Figure 12-2 that sign of the correlation coefficient from same forcing simulation from different models is consistent. For example, correlation coefficient obtained for historical greenhouse gas simulation from ESM2M, IPSL and CanESM2 is positive.

From Figure 12-2, it can also be seen that the standard deviation of model simulations is lower than NOBM except for RCP8.5 simulation from CanESM2 model. This shows that model simulations underestimate the gyre area compared to the gyre area from observations.

12.1.3. Results for North Pacific Gyre

Time series of the NP Gyre area from NOBM and greenhouse gas simulations of the models is shown in Figure 12-3. Size of the gyres from greenhouse gas simulations is chosen as an example for visual comparison because this is the signal that is of interest in this detection study. From Figure 12-3 it can be seen in observations that there is a peak in the gyre size in mid 1999 after which the pattern of variability in the gyre size is not distinct and it is difficult to see a distinct pattern in the time series. Similar pattern is observed in greenhouse gas simulation from CanESM2. Greenhouse gas simulation from ESM2M show a decrease in size of the gyre from 1999 to mid 2002 beyond which the pattern of trend is increasing till 2005. Greenhouse gas simulation from CanESM2 model show an increase in the size of the gyres from 1999 to mid 2001 followed by a indistict pattern of variability in the size of the gyre. Observing the linear trend in the gyre size, it can be seen that there is an increasing trend (29324.35 km^2 per month) from NOBM, which is also observed in greenhouse gas simulations from ESM2M (44929.55 km^2 per month) and CanESM2 (3620.98 km^2 per month). However, greenhouse gas simulation from IPSL model shows a declining trend (-11805.40 km^2 per month) in the size of the gyres. Trend in gyre size from greenhouse gas simulation from CanESM2 model is not significant. Also, there are several other simulations for which the trend in gyre size is

not significant (Table 12-5). This shows that models are not always consistent with the outputs from the same forcing simulations and also, model outputs are not always consistent with observations in pattern and trend. Trend in the size of the gyre from other simulations is given in Table 1 of Appendix VI. Trend in the size of the gyre from other simulations is given in Table 12-5.

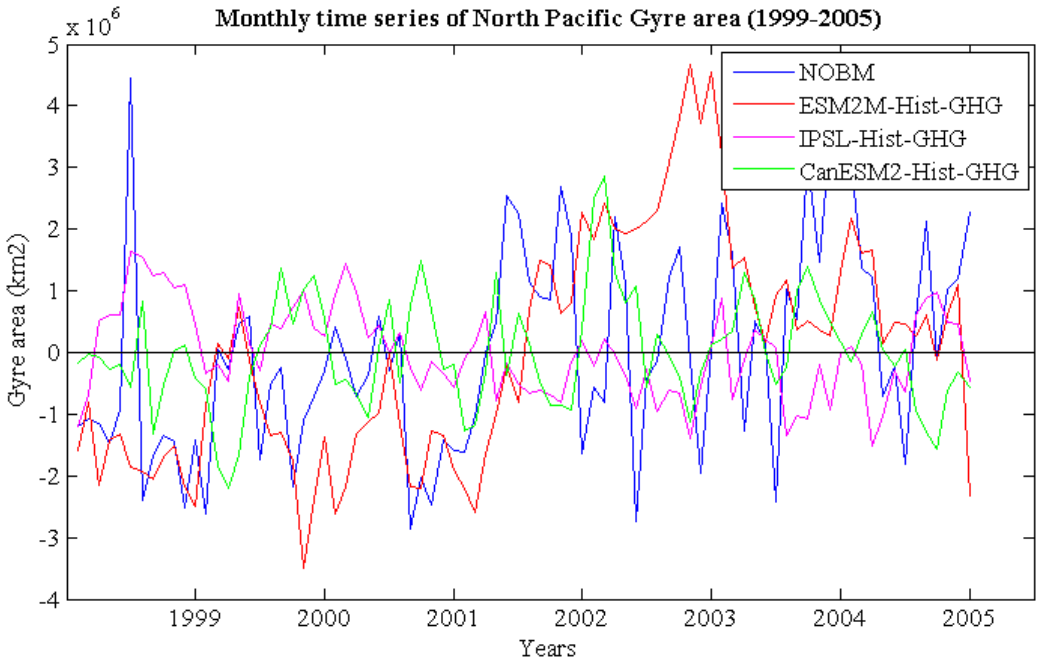

Figure 12-3. Monthly time series of the size of the NP gyre i.e. gyre area in km^2.

Table 12-5. Linear Trend (km^2 per month) in size of the NP gyre (1999-2005) and the column indicating whether the trend is significant or not by a 'Y' and a 'N' respectively.

Model Simulation	Linear Trend	Significant Trend
A	29324.35	Y
B	4564.58	N
C	-23602.25	Y
D	44929.55	Y
F	-5676.96	N
G	392.30	N
H	4058.78	N
I	-11805.40	Y
J	-14.72	N
K	9255.72	Y
L	-5938.07	Y
M	3620.98	N
N	18336.70	Y
O	-16806.02	Y

Statistical terms of comparison between size of the gyres from model simulations and NOBM that were computed are correlation coefficient, centered root mean square difference and amplitude of the variation i.e. standard deviation. The results are presented in the form of a Taylor Diagram (Taylor, 2001) (Figure 12-4) and Table of values associated with the Figure are presented in Table 12-6 below.

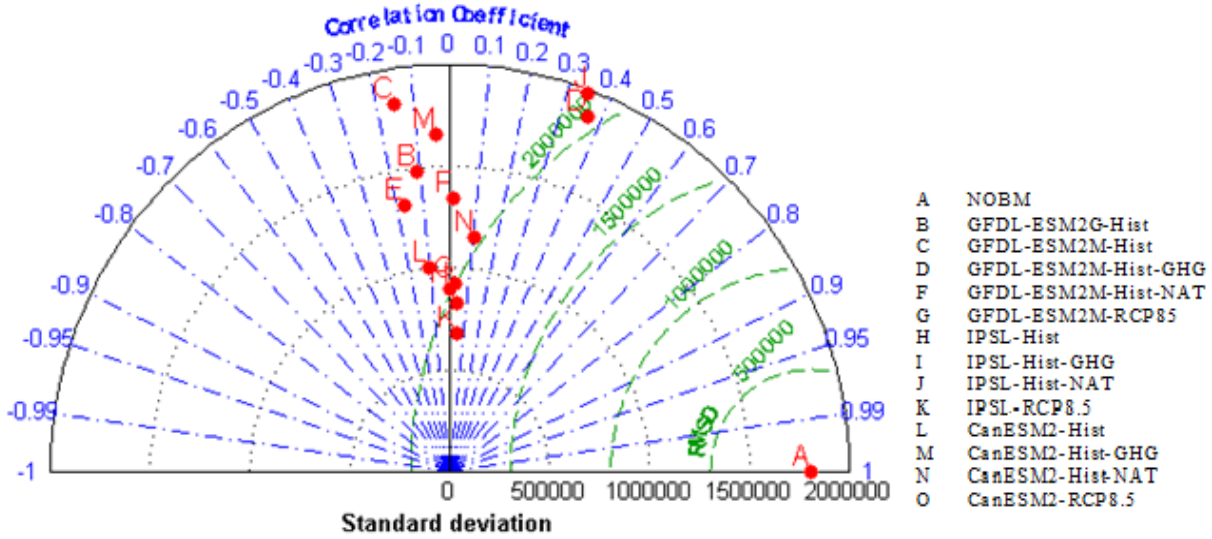

Figure 12-4. Taylor diagram associated with the comparisons of time series of gyre area for NP gyre computed from model simulations with time series of gyre area from NOBM.

Table 12-6. Statistical terms of comparison for time series of North Pacific gyre area.

Model Simulation	Correlation Coefficient	RMS difference	Standard Deviation
B	-0.1128	2463226.4	1485318.7
C	-0.1525	2757642.2	1828160.5
D	0.3667	2071676.8	1875553.4
F	-0.1705	2416189.5	1328240.8
G	0.0105	2235943.6	1339364.9
H	0.0290	2001812.8	920409.7
I	0.0022	2014409.8	899227.3
J	0.0451	1949673.9	823824.1
K	0.3467	2166998.7	1978644.3
L	0.0513	1895884.3	681233.3
M	-0.1085	2158484.1	1004625.0
N	-0.0426	2503629.3	1660241.9
O	0.1020	2043006.3	1159317.3

From Figure 12-4, it can be seen that the correlation coefficient for all the model simulations is low (-0.1705 to 0.3667 in this study). This indicates that time series of the size of the gyres from model simulations is not correctly phased with NOBM. It should be noted from Figure 12-4 that sign of the correlation coefficient from same forcing simulation from different models is not consistent. For example, correlation coefficient obtained for historical greenhouse gas simulation from ESM2M and IPSL is positive but is negative for greenhouse gas simulation from CanESM2.

From Figure 12-4, it can also be seen that the standard deviation of model simulations is lower than NOBM except historical and historical greenhouse gas simulation from ESM2M model and RCP8.5 simulation from

IPSL model. This shows that model simulations underestimate the gyre area compared to the gyre area from observations.

12.1.4. Results for South Pacific Gyre

Time series of the SP Gyre area from NOBM and greenhouse gas simulations of the models is shown in Figure 12-5. Size of the gyres from greenhouse gas simulations is chosen as an example for visual comparison because this is the signal that is of interest in this detection study. From Figure 12-5 it can be seen in observations that there is a peak in the gyre size in mid 1999 followed by a decrease in the gyre size till mid 2000. There is an increasing trend in the gyre size till mid 2002 after which the size decreases till mid 2003 and then there is a increase in the gyre size till 2005 with a sporadic decrease at the end of 2004. This pattern in the size of the gyres is partially followed in the gyre size from greenhouse gas simulations from models. Observing the linear trend in the gyre size, it can be seen that there is an increasing trend (20211.17 km^2 per month) from NOBM, which is also observed in greenhouse gas simulations from ESM2M (3842.16 km^2 per month) and IPSL (5716.43 km^2 per month). However, greenhouse gas simulation from CanESM2 model shows a declining trend (-18447.51 km^2 per month) in the size of the gyres. Trend in gyre size from greenhouse gas simulation of ESM2M and IPSL model is not significant. Also, there are several other simulations for which the trend in gyre size is not significant (Table 12-7). This shows that models are not always consistent with the outputs from the same forcing simulations and also, model outputs are not always consistent with observations in pattern and trend. Trend in the size of the gyre from other simulations is given in Table 12-7.

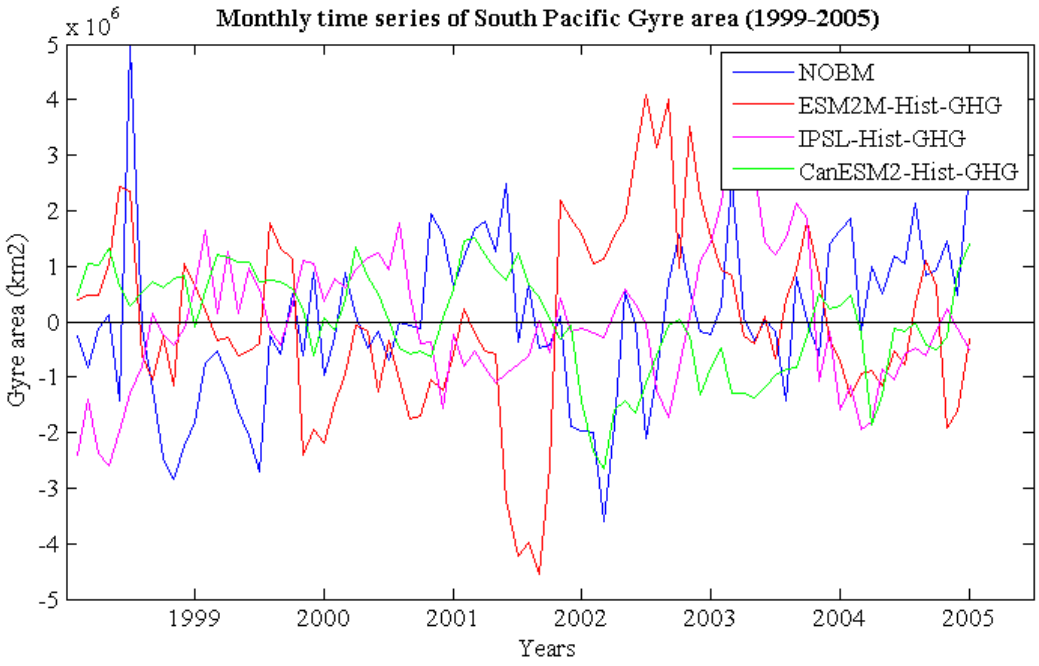

Figure 12-5. Monthly time series of the size of the SP gyre i.e. gyre area in km^2.

Table 12-7. Linear Trend (km^2 per month) in size of the SP gyre (1999-2005) and the column indicating whether the trend is significant or not by a 'Y' and a 'N' respectively.

Model Simulation	Linear Trend	Significant Trend
A	20211.17	Y
B	-14774.08	Y
C	12749.96	N
D	3842.16	N
F	-34326.57	Y
G	-2531.00	N
H	-13128.27	Y
I	5716.43	N
J	-2955.22	N
K	31395.75	Y
L	9584.07	Y
M	-18447.51	Y
N	1612.75	N
O	-16069.82	Y

Statistical terms of comparison between size of the gyres from model simulations and NOBM that were computed are correlation coefficient, centered root mean square difference and amplitude of the variation i.e. standard deviation. The results are presented in the form of a Taylor Diagram (Taylor, 2001) (Figure 12-6) and Table of values associated with the Figure are presented in Table 12-8.

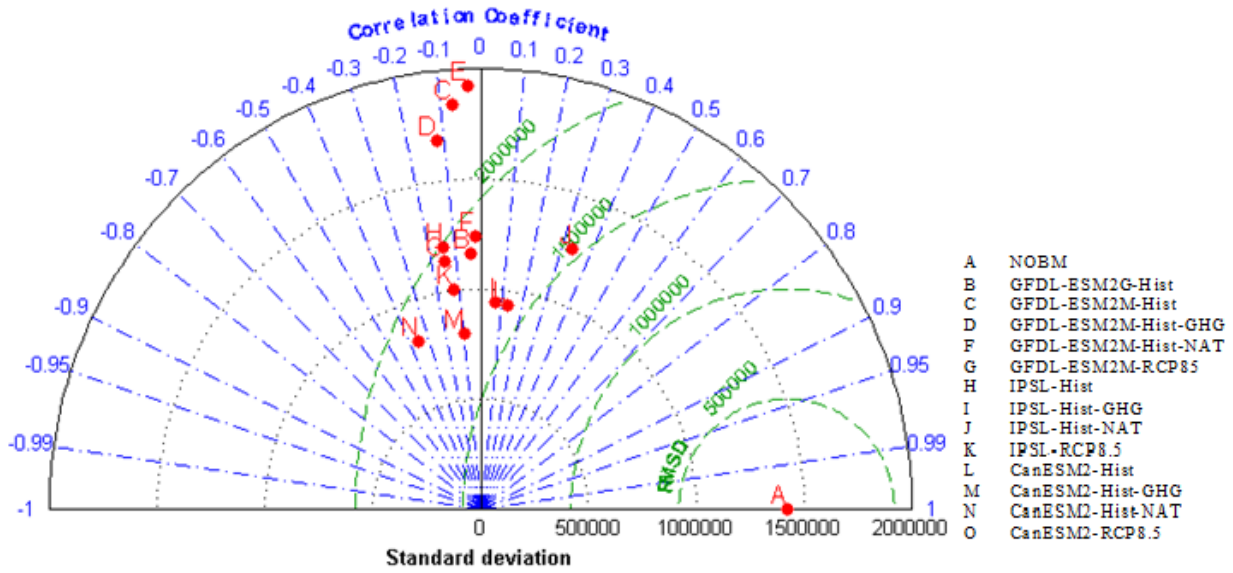

Figure 12-6. Taylor diagram associated with the comparisons of time series of gyre area for SP gyre computed from model simulations with time series of gyre area from NOBM.

Table 12-8. Statistical terms of comparison for time series of South Pacific gyre area.

Model Simulation	Correlation Coefficient	RMS difference	Standard Deviation
B	-0.0417	1868790.6	1160661.4
C	-0.0725	2404949.0	1843132.4
D	-0.1219	2331855.2	1687175.7
F	-0.0301	2420456.2	1920028.1
G	-0.0183	1897306.2	1235989.5
H	-0.1478	1942699.7	1135900.6
I	-0.1473	1986487.5	1198934.5
J	0.0751	1641869.6	942475.6
K	0.3374	1544222.8	1255953.8
L	-0.1247	1838047.2	1007138.2
M	0.1315	1590978.3	933168.6
N	-0.0964	1694891.2	803163.1
O	-0.3550	1868165.1	814124.1

From Figure 12-6, it can be seen that the correlation coefficient for all the model simulations is low (-0.355 to 0.3374 in this study). This indicates that time series of the size of the gyres from model simulations is not correctly phased with NOBM. It should be noted from Figure 12-6 that sign of the correlation coefficient from same forcing simulation from different models is not consistent. For example, correlation coefficient obtained for historical greenhouse gas simulation from ESM2M and IPSL is negative but is positive for greenhouse gas simulation from CanESM2.

From Figure 12-6, it can also be seen that the standard deviation of model simulations is lower than NOBM except for historical, historical greenhouse gas and historical natural simulation from ESM2M model. This shows that model simulations underestimate the gyre area compared to the gyre area from observations.

12.1.5. Results for Indian Ocean Gyre

Time series of the IO Gyre area from NOBM and greenhouse gas simulations of the models is shown in Figure **12-7**. Size of the gyres from greenhouse gas simulations is chosen as an example for visual comparison because this is the signal that is of interest in this detection study. From Figure 12-7 it can be seen in observations that the pattern of increase or decrease in gyre area is indistict which is also the case for gyre area from greenhouse gas simulations. Observing the linear trend in the gyre size, it can be seen that there is an increasing trend (11464.79 km^2 per month) from NOBM, which is also observed in greenhouse gas simulations from ESM2M (7271.09 km^2 per month), IPSL (4391.00 km^2 per month) and CanESM2 (3653.88 km^2 per month) model. Trend in gyre size from greenhouse gas simulation from ESM2M and CanESM2M model is not significant. Also, there are several other simulations for which the trend in gyre size is not significant (Table 12-10)This shows that models are consistent with the outputs from the same forcing simulations and also, model outputs are consistent with observations. Trend in the size of the gyre from other simulations is given in Table 12-10.

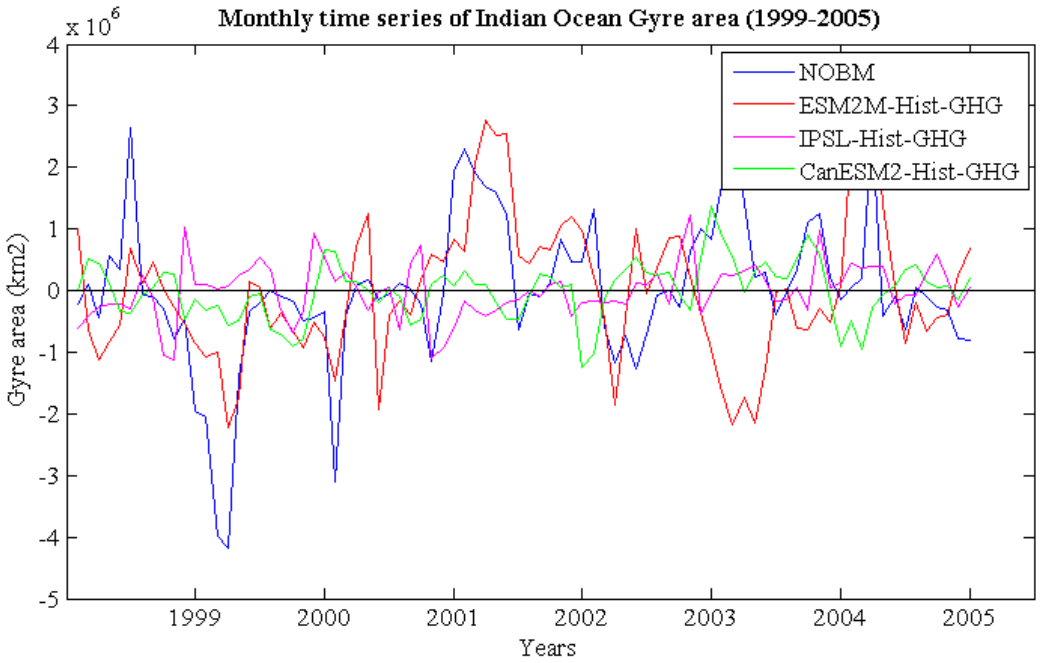

Figure 12-7. Monthly time series of the size of the IO gyre i.e. gyre area in km^2.

Table 12-9. Linear Trend (km^2 per month) in size of the IO gyre (1999-2005) and the column indicating whether the trend is significant or not by a 'Y' and a 'N' respectively.

Model Simulation	Linear Trend	Significant Trend
A	11464.79	Y
B	-8450.86	N
C	-5371.60	N
D	7271.09	N
F	43716.44	Y
G	1157.57	N
H	10909.77	Y
I	4391.00	Y
J	9931.58	Y
K	-436.01	N
L	-6438.85	Y
M	3653.88	N
N	6563.55	Y
O	-3085.45	Y

Statistical terms of comparison between size of the gyres from model simulations and NOBM that were computed are correlation coefficient, centered root mean square difference and amplitude of the variation i.e. standard deviation. The results are presented in the form of a Taylor Diagram (Taylor, 2001) (Figure 12-8) and Table of values associated with the Figure are presented in Table 12-10 below.

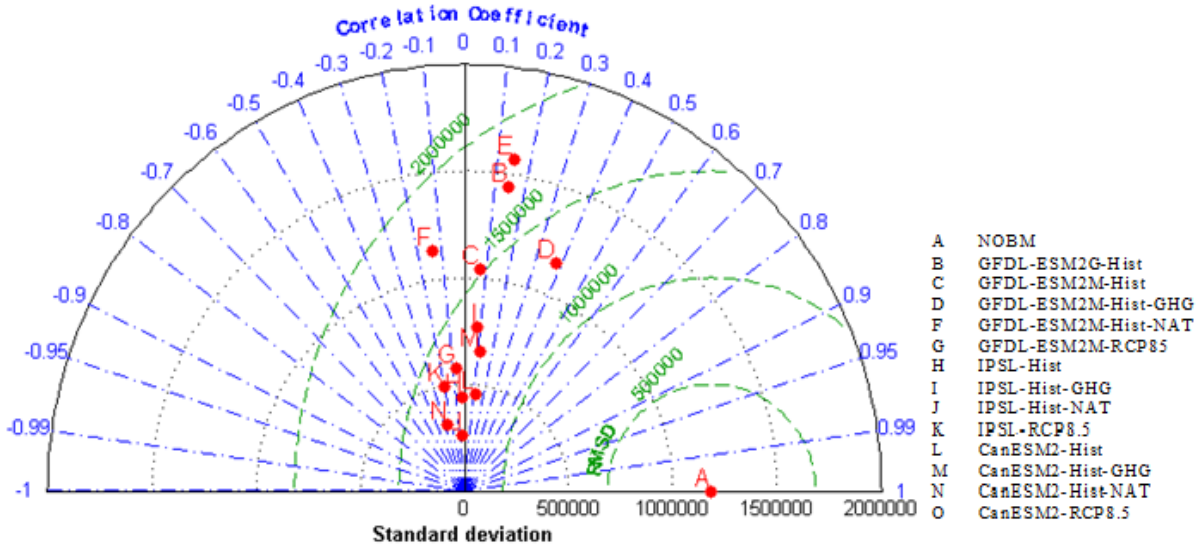

Figure 12-8. Taylor diagram associated with the comparisons of time series of gyre area for IO gyre computed from model simulations with time series of gyre area from NOBM.

Table 12-10. Statistical terms of comparison for time series of Indian Ocean gyre area.

Model Simulation	Correlation Coefficient	RMS difference	Standard Deviation
B	0.14601	1728350	1442927
C	0.072249	1522277	1044861
D	0.377829	1304666	1153559
F	0.153046	1819419	1573737
G	-0.13282	1746841	1135539
H	-0.07222	1353828	574452.7
I	-0.02333	1274212	441236.3
J	0.082845	1360417	773348.3
K	-0.03334	1222189	261789.8
L	-0.19585	1373060	499088.7
M	0.112075	1220880	454795.3
N	0.118043	1285238	656503.3
O	-0.26015	1306085	321284.6

From Figure 12-8, it can be seen that the correlation coefficient for all the model simulations is low (-0.2602 to 0.3778 in this study). This indicates that time series of the size of the gyres from model simulations is not correctly phased with NOBM. It should be noted from Figure 12-8 that sign of the correlation coefficient from same forcing simulation from different models is not always consistent. For example, correlation coefficient obtained for historical greenhouse gas simulation from ESM2M and CanESM2 is positive but correlation coefficient for historical greenhouse gas simulation from IPSL is negative.

From Figure 12-8, it can also be seen that the standard deviation of model simulations is lower than NOBM except for historical simulation from ESM2G and historical natural simulation from ESM2M model. This shows that model simulations underestimate the gyre area compared to the gyre area from observations.

12.2. Level of truncation

Table 12-11. Percent of eigenvectors chosen for the noise covariance matrix

Model Simulation Alphabet	NA	SA	NP	SP	IO
B	99.97	99.98	98.8	99.85	99.62
C	99.99	99.89	99.98	99.95	99.96
D	99.98	99.98	99.99	99.98	99.99
F	100	99.99	99.99	99.95	99.99
G	100	100	99.97	99.95	99.96
H	99.65	100	99.98	99.99	99.96
I	99.91	99.97	99.98	99.93	99.96
J	99.91	99.42	99.98	99.77	99.96
K	99.65	99.97	99.76	99.99	99.96
L	98.02	99.85	100	99.74	99.9
M	98.02	99.68	100	99.45	99.9
N	99.91	98.38	100	99.74	99.77
O	99.91	99.97	100	99.81	99.19

12.3. Detection Results

Beta values obtained after the implementation of the OF method indicate whether the signal has been detected in the observations or not.

Table 12-12. Beta values for NA gyre

Model Simulation	Beta	CI
B	-3.6987	-31.6561
C	-13.2169	-65.6266
D	5.4285	-26.8686
F	2.0217	-10.4447
G	33.0348	-170.6697
H	-0.0187	-4.1290
I	0.0746	-18.1807
J	0.0665	-16.2047
K	0.1868	-41.2596
L	0.5839	-4.1698
M	-3.7127	-26.5139
N	0.6365	-6.8658
O	-35.2181	-379.8650

12.3.1. Results for South Atlantic Gyre

Scaling factors obtained as a result of the implementation of the OF method on time series of the gyre area in SA region of the ocean using time series of the gyre area from model forced simulations as the signal is shown in Figure 3-8 and given in Table 12-13.

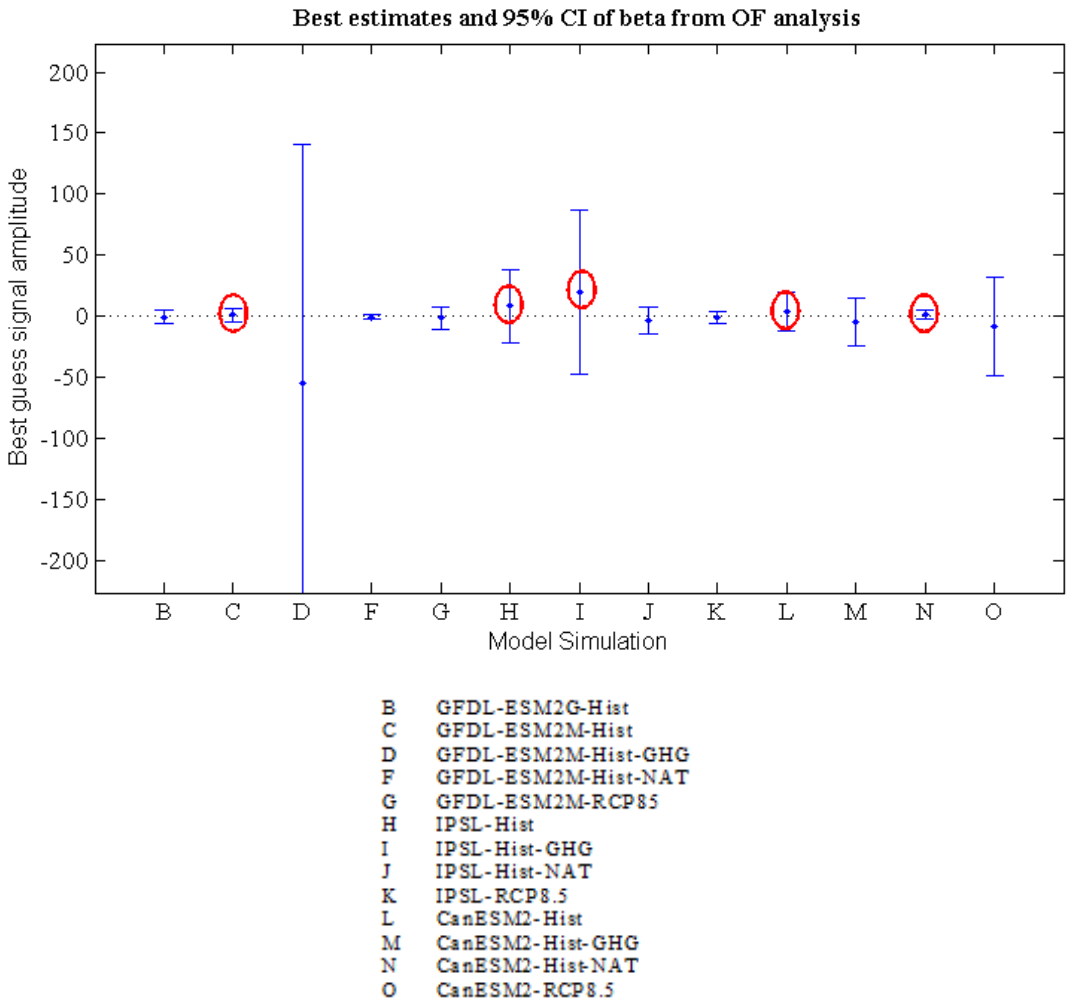

Figure 12-9. Graph of signal amplitude along with the CI, obtained for OF implementation in SA gyre using signals from model forced simulations. Red circles indicate scaling factors which are positive and are obtained for the simulations for which consistency test failed.

Table 12-13. Beta values for SA gyre

Model Simulation	Beta	CI
B	-0.7097	-5.3706
C	1.0792	-5.2788
D	-54.6373	-195.6932
F	-0.4526	-2.3756
G	-1.6285	-8.6669
H	8.2008	-30.0647
I	19.9813	-67.4106
J	-3.4713	-10.6860
K	-1.4507	-4.8943
L	3.5399	-15.9978
M	-4.7174	-19.9708
N	0.9369	-3.7711
O	-8.1369	-40.5686

Figure 12-9 above shows the beta values obtained in SA gyre for signals obtained from model forced simulations along with the confidence interval (CI) associated with each beta value. From the Figure 12-9a it can be seen that even though there are some model simulations for which scaling factors are positive but none of the scaling factors are significantly different from 0 and with 95% confidence interval. This indicates that the effect of external forcings is not being detected in the SA gyre and the null hypothesis that changes in size of the gyres is caused by internal variability cannot be rejected.

12.3.2. Results for North Pacific Gyre

Scaling factors obtained as a result of the implementation of the OF method on time series of the gyre area in NP region of the ocean using time series of the gyre area from model forced simulations as the signal is shown in Figure 12-10 and given in Table 12-14.

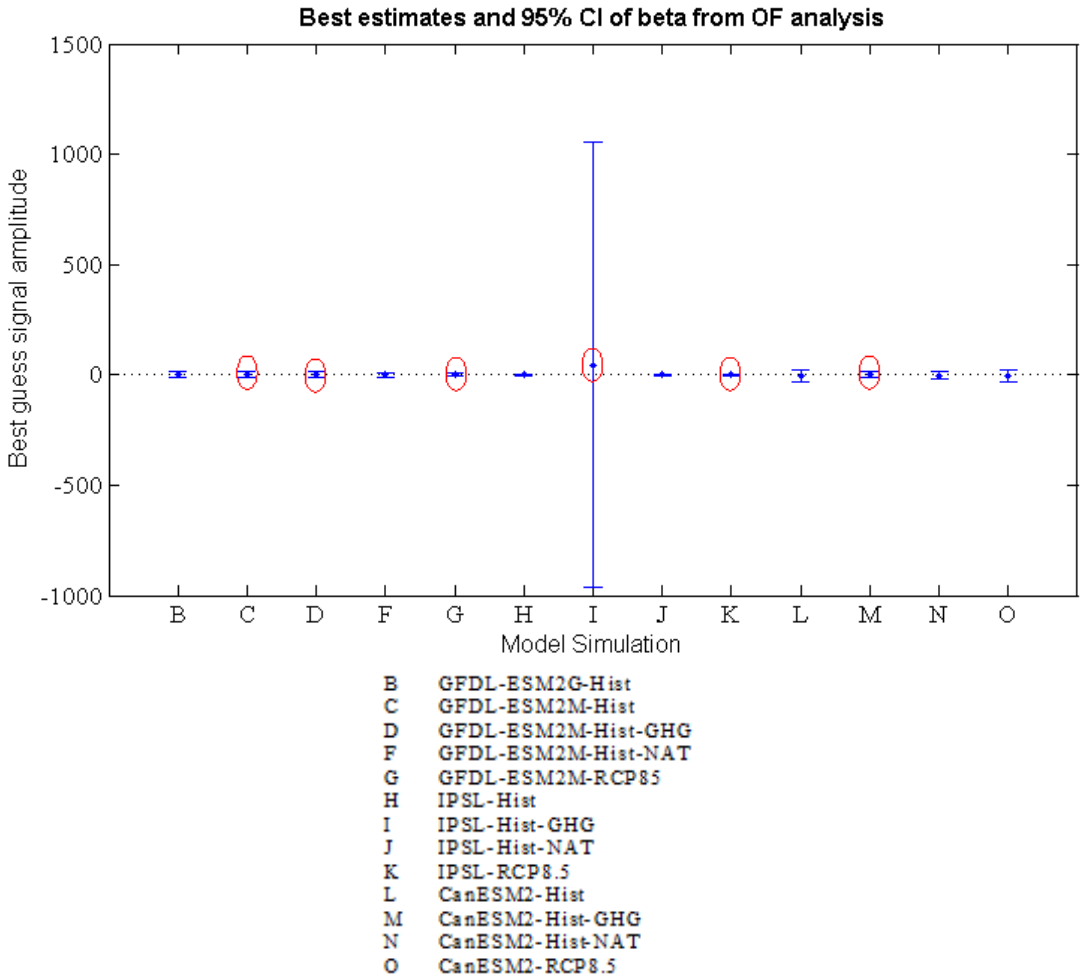

Figure 12-10. Graph of signal amplitude along with the CI, obtained for OF implementation in NP gyre using signals from model forced simulations. Red circles indicate scaling factors which are positive and are obtained for the simulations for which consistency test failed.

Table 12-14. Beta values for NP gyre

Model Simulation	Beta	CI
B	-0.4118	-13.8347
C	1.2551	-12.8816
D	1.4671	-15.5231
F	-0.7516	-7.9520
G	0.5213	-5.1919
H	-0.0966	-2.1211
I	45.9869	-1010.0080
J	-0.0961	-2.1106
K	0.2033	-2.8773
L	-4.4889	-26.4401
M	2.6006	-13.6609
N	-2.8300	-18.3808
O	-4.7296	-24.8835

Figure 12-10 above shows the beta values obtained in NP region for signals obtained from model forced simulations along with the confidence interval (CI) associated with each beta value. From the Figure 12-10a it can be seen that even though there are some model simulations for which scaling factors are positive but none of the scaling factors are significantly different from 0 and with 95% confidence interval. This indicates that the effect of external forcings is not being detected in the NP gyre and the null hypothesis that changes in size of the gyres is caused by internal variability cannot be rejected.

12.3.3. Results for South Pacific Gyre

Scaling factors obtained as a result of the implementation of the OF method on time series of the gyre area in SP region of the ocean using time series of the gyre area from model forced simulations as the signal is shown in Figure 12-11 and given in Table 12-15.

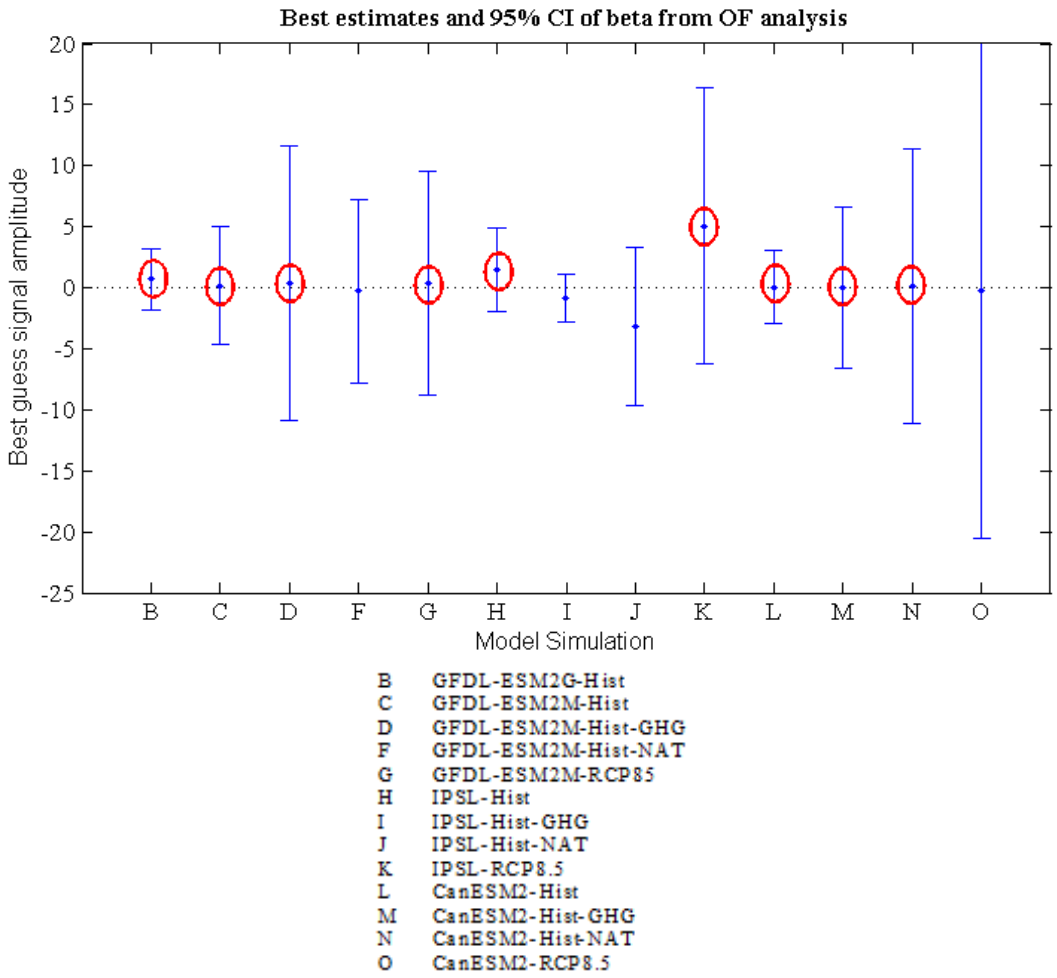

Figure 12-11. Graph of signal amplitude along with the CI, obtained for OF implementation in SP gyre using signals from model forced simulations. Red circles indicate scaling factors which are positive and are obtained for the simulations for which consistency test failed.

Table 12-15. Beta values for SP gyre

Model Simulation	Beta	CI
B	0.6860	-2.5597
C	0.1809	-4.7968
D	0.3795	-11.2892
F	-0.2854	-7.5678
G	0.3470	-9.2011
H	1.5268	-3.4269
I	-0.8967	-1.9604
J	-3.1858	-6.5035
K	5.0468	-11.3272
L	0.0344	-3.0137
M	0.0323	-6.6262
N	0.1287	-11.2724
O	-0.2723	-20.2485

Figure 12-11 above shows the beta values obtained in SP region for signals obtained from model forced simulations along with the confidence interval (CI) associated with each beta value. From the Figure 12-11a it can be seen that even though there are some model simulations for which scaling factors are positive but none of the scaling factors are significantly different from 0 and with 95% confidence interval. This indicates that the effect of external forcings is not being detected in the SP gyre and the null hypothesis that changes in size of the gyres is caused by internal variability cannot be rejected.

12.3.4. Results for Indian Ocean Gyre

Scaling factors obtained as a result of the implementation of the OF method on time series of the gyre area in IO region of the ocean using time series of the gyre area from model forced simulations as the signal is shown in Figure 12-12 and given in Table 12-16.

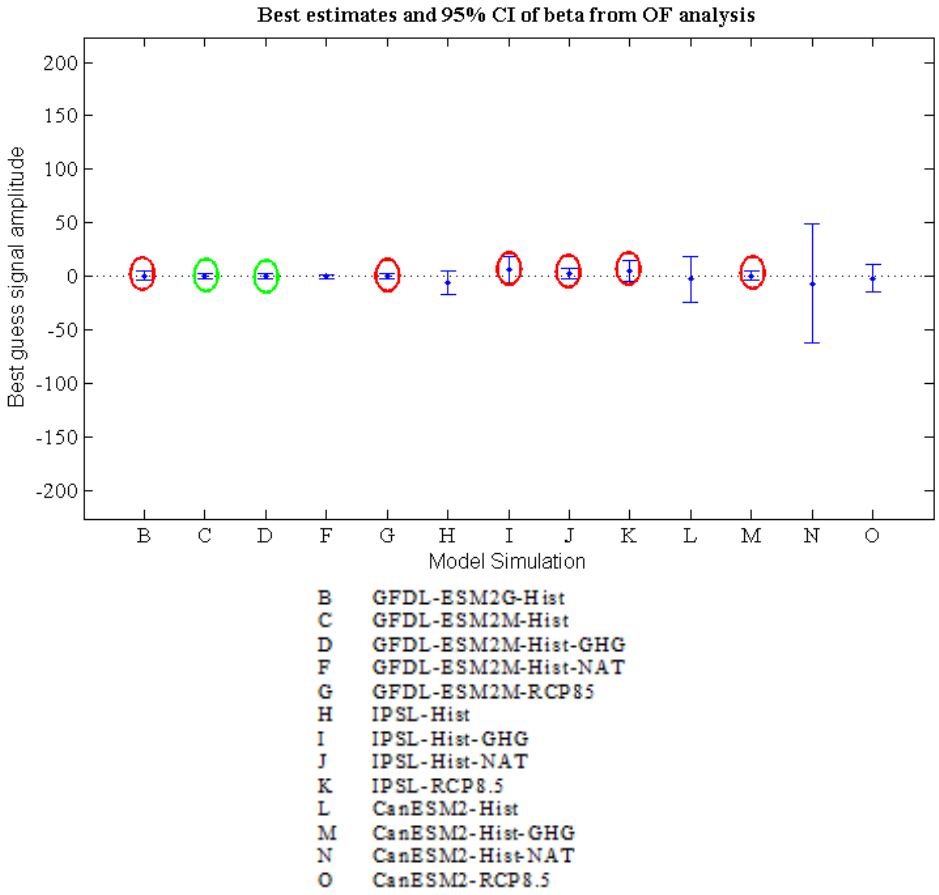

Figure 12-12. Graph of signal amplitude along with the CI, obtained for OF implementation in IO gyre using signals from model forced simulations. Green circles indicate scaling factors which are positive and are obtained for the simulations for which consistency test passed. Red circles indicate scaling factors which are positive and are obtained for the simulations for which consistency test failed.

Table 12-16. Beta values for IO gyre

Model Simulation	Beta	CI
B	0.6974	-3.8378
C	0.4982	-2.5522
D	0.4794	-2.5630
F	-0.3688	-1.9719
G	0.4651	-2.3827
H	-5.6241	-11.1830
I	6.1351	-12.1992
J	2.4285	-4.8289
K	5.0716	-10.0845
L	-2.7867	-21.6671
M	0.5504	-4.2792
N	-6.7562	-55.3402
O	-1.6747	-12.5246

Figure 12-12 above shows the beta values obtained in IO region for signals obtained from model forced simulations along with the confidence interval (CI) associated with each beta value. From the Figure 12-12a it can be seen that even though there are some model simulations for which scaling factors are positive but none of the scaling factors are significantly different from 0 and with 95% confidence interval. This indicates that the effect of external forcings is not being detected in the IO gyre and the null hypothesis that changes in size of the gyres is caused by internal variability cannot be rejected.

13. References

ALLEN, M. R. & TETT, S. F. B. 1999. Checking for model consistency in optimal fingerprinting. *Climate Dynamics,* 15**,** 419-434.

ANDREWS, O. D., BINDOFF, N. L., HALLORAN, P. R., ILYINA, T. & LE QU´ER´E, C. 2012. Detecting an external influence on recent changes in oceanic oxygen using an optimal fingerprinting method. *Biogeosciences,* 9**,** 12469–12504.

ANTOINE, D., MOREL, A., GORDON, H. R., BANZON, V. F. & EVANS, R. H. 2005. Bridging ocean color observations of the 1980s and 2000s in search of long-term trends. *Journal of Geophysical Research: Oceans,* 110**,** C06009.

ARORA, V. K. & BOER, G. J. 2010. Uncertainties in the 20th century carbon budget associated with land use change. *Global Change Biol.,* 16(12)**,** 3327–3348.

ARORA, V. K. & MATTHEWS, H. D. 2009. Characterizing uncertainty in modeling primary terrestrial ecosystem processes. *Global Biogeochem. Cycles,* 23, GB2016.

AUMONT, O. & BOPP, L. 2006. Globalizing results from ocean in situ iron fertilization studies. *Global Biogeochem Cycles,* 0(2):GB2017.

BAEHR, J., KELLER, K. & MAROTZKE, J. 2008. Detecting potential changes in the meridional overturning circulation at 26˚N in the Atlantic. *Climatic Change,* 91**,** 11-27.

BARNETT, T. P., HASSELMANN, K., CHELLIAH, M., DELWORTH, T., HEGERL, G., JONES, P., RASMUSSON, E., ROECKNER, E., ROPELEWSKI, C., SANTER, B. & TETT, S. 1999. Detection and attribution of recent climate change: A status report. *Bulletin of the American Meteorological Society,* 80**,** 2631-2659.

BARNETT, T. P., PIERCE, D. W. & SCHNUR, R. 2001. Detection of anthropogenic climate change in the world's oceans. *Science,* 292**,** 270-4.

BARNETT, T. P. & SCHLESINGER, M. E. 1987. Detecting Changes in Global Climate Induced by Greenhouse Gases. *Journal of Geophysical Research-Atmospheres,* 92**,** 14772-14780.

BARTON, A. D., GREENE, C. H., MONGER, B. C. & PERSHING, A. J. 2003. Continuous plankton recorder survey of phytoplankton measurements and the North Atlantic Oscillation :interannual to multidecadal variability. *Progress in Oceanography,* 58**,** 337-358.

BEAULIEU, C., HENSON, S. A., SARMIENTO, J. L., DUNNE, J. P., DONEY, S. C., RYKACZEWSKI, R. R. & BOPP, L. 2013. Factors challenging our ability to detect long-term trends in ocean chlorophyll. *Biogeosciences,* 10**,** 2711-2724.

BEHRENFELD, M. J. 2010. Abandoning Sverdrup's Critical Depth Hypothesis on phytoplankton blooms. *Ecology,* 91**,** 977-989.

BEHRENFELD, M. J., O'MALLEY, R. T., SIEGEL, D. A., MCCLAIN, C. R., SARMIENTO, J. L., FELDMAN, G. C., MILLIGAN, A. J., FALKOWSKI, P. G., LETELIER, R. M. & BOSS, E. S. 2006. Climate-driven trends in contemporary ocean productivity. *Nature,* 444**,** 752-5.

BEHRENFELD, M. J., SIEGEL, D. A. & O'MALLEY, R. T. 2008a. Global ocean phytoplankton and productivity, in: State of the Climate in 2007. Levinson, D.H., and J.H. Lawrimore eds.,. *Bulletin of the American Meteorological Society, 89, S56-S61.*

BERGER, W. H., SMETACK, V. S. & WEFER, G. E. 1989. Productivity of the Ocean: Present and Past. *Wiley: New York.*

BERLINER, L. M., LEVINE, R. A. & SHEA, D. J. 2000. Bayesian climate change assessment. *Journal of Climate,* 13**,** 3805-3820.

BLANCHARD, J. L., JENNINGS, S., HOLMES, R., HARLE, J., MERINO, G., ALLEN, J. I., HOLT, J., DULVY, N. K. & BARANGE, M. 2012. Potential consequences of climate change for primary production and fish production in large marine ecosystems. *Royal Society Philosophical Transactions Biological Sciences,* 367**,** 2979-2989.

BOER, G. J., FLATO, G., READER, M. C. & RAMSDEN, D. 2000. A transient climate change simulation with greenhouse gas and aerosol forcing: experimental design and comparison with the instrumental record for the twentieth century. *Climate Dynamics,* 16**,** 405-425.

BOPP, L., MONFRAY, P., AUMONT, O., DUFRESNE, J. L., LE TREUT, H., MADEC, G., TERRAY, L. & ORR, J. C. 2001. Potential impact of climate change on marine export production. *Global Biogeochemical Cycles,* 15**,** 81-99.

BOYCE, D. G., LEWIS, M. R. & WORM, B. 2010. Global phytoplankton decline over the past century. *Nature,* 466**,** 591-6.

BRZEZINSKI, M. A., VILLAREAL, T. A. & LIPSCHULTZ, F. 1998. Silica production and the contribution of diatoms to new and primary production in the central North Pacific. *Marine Ecology Progress Series,* 167**,** 89-104.

CAPONE, D. G. & HUTCHINS, D. A. 2013. Microbial biogeochemistry of coastal upwelling regimes in a changing ocean. *Nature Geosci,* 6**,** 711-717.

CAPONE, D. G., ZEHR, J. P., PAERL, H. W., BERGMAN, B. & CARPENTER, E. J. 1997. Trichodesmium, a globally significant marine cyanobacterium. *Science,* 276**,** 1221-1229.

CAPOTONDI, A. 2013. ENSO diversity in the NCAR CCSM4 climate model. *Journal of Geophysical Research: Oceans,* 118**,** 4755-4770.

CARPENTER, E. J. & MCCARTHY, J. J. 1975. NITROGEN-FIXATION AND UPTAKE OF COMBINED NITROGENOUS NUTRIENTS BY OSCILLATORIA (TRICHODESMIUM) THIEBAUTII IN WESTERN SARGASSO SEA. *Limnology and Oceanography,* 20**,** 389-401.

CESS, R. D. & POTTER, G. L. 1988. A methodology for understanding and intercomparing atmospheric climate feedback processes in general circulation models. *J. Geophys, Res.,* 93**,** 8305-8314.

CHAVEZ, F. P., RYAN, J., LLUCH-COTA, S. E. & NIQUEN, M. 2003. From anchovies to sardines and back: Multidecadal change in the Pacific Ocean. *Science,* 299**,** 217-221.

CHAVEZ, F. P., STRUTTON, P. G., FRIEDERICH, G. E., FEELY, R. A., FELDMAN, G. C., FOLEY, D. G. & MCPHADEN, M. L. 1999. Biological and chemical response of the Equatorial Pacific Ocean to the 1997-1998 El Niño. *Science,* 286**,** 2126-2131.

CHEUNG, W. W. L., LAM, V. W. Y., SARMIENTO, J. L., KEARNEY, K., WATSON, R. & PAULY, D. 2009. Projecting global marine biodiversity impacts under climate change scenarios. *Fish and Fisheries,* 10**,** 235-251.

CHEUNG, W. W. L., LAM, V. W. Y., SARMIENTO, J. L., KEARNEY, K., WATSON, R., ZELLER, D. & PAULY, D. 2010. Large-scale redistribution of maximum fisheries catch potential in the global ocean under climate change. *Global Change Biology,* 16**,** 24-35.

CHRISTIAN, J. R., ARORA, V. K., BOER, G. J., CURRY, C. L., ZAHARIEV, K., DENMAN, K. L., FLATO, G. M., LEE, W. G., MERRYFIELD, W. J., ROULET, N. T. & SCINOCCA, J. F. 2010. The global carbon cycle in the Canadian Earth system model (CanESM1): Preindustrial control simulation. *Journal of Geophysical Research: Biogeosciences,* 115**,** G03014.

CICS-NC, N. N. National Oceanic and Atmospheric Administration (NOAA) - National Climatic Data Center (NCDC) / Cooperative Institute for Climate and Satellites (CICS) - NC.

CUBASCH, U. & CESS, R. D. 1990. Processes and modelling. In: Climate Change: The IPCC Scientific Assessment, Intergovernmental Panel on Climate Change (IPCC), Houghton, J.T., Jenkins, G.J. & Ephraums, J.J. (eds.). Cambridge University Press, Cambridge,. 69-91.

CULLEN, J. J. 1982. THE DEEP CHLOROPHYLL MAXIMUM - COMPARING VERTICAL PROFILES OF CHLOROPHYLL-A. *Canadian Journal of Fisheries and Aquatic Sciences,* 39**,** 791-803.

CURRY, R. G. & MCCARTNEY, M. S. 2001. Ocean gyre circulation changes associated with the North Atlantic Oscillation. *Journal of Physical Oceanography,* 31**,** 3374-3400.

CUSHING, D. H. 1975. Marine Ecology and Fisheries. *Cambridge University Press, London***,** 278.

DELWORTH, T. L., BROCCOLI, A. J., ROSATI, A., STOUFFER, R. J., BALAJI, V., BEESLEY, J. A., COOKE, W. F., DIXON, K. W., DUNNE, J., DUNNE, K. A., DURACHTA, J. W., FINDELL, K. L., GINOUX, P., GNANADESIKAN, A., GORDON, C. T., GRIFFIES, S. M., GUDGEL, R., HARRISON, M. J., HELD, I. M., HEMLER, R. S., HOROWITZ, L. W., KLEIN, S. A., KNUTSON, T. R., KUSHNER, P. J., LANGENHORST, A. R., LEE, H.-C., LIN, S.-J., LU, J., MALYSHEV, S. L., MILLY, P. C. D., RAMASWAMY, V., RUSSELL, J., SCHWARZKOPF, M. D., SHEVLIAKOVA, E., SIRUTIS, J. J., SPELMAN, M. J., STERN, W. F., WINTON, M., WITTENBERG, A. T., WYMAN, B., ZENG, F. & ZHANG, R. 2006. GFDL's CM2 Global Coupled Climate Models. Part I: Formulation and Simulation Characteristics. *Journal of Climate,* 19**,** 643-674.

DENMAN, K. & PENA, A. 1999. A coupled 1-D biological/physical model of the northeast subarctic Pacific Ocean with iron limitation. *Deep Sea Research Part II,* 46**,** 2877-2908.

DICKEY, T. 2003. Emerging Ocean Observations for interdisciplinary data assimilation systems. *Journal of Marine Systems,* 40-41:5-48.

DOBRYNIN, M., MURAWSKI, J., BAEHR, J. & ILYINA, T. 2014. Detection and Attribution of Climate Change Signal in Ocean Wind Waves. *Journal of Climate,* 28**,** 1578-1591.

DONEY, S. C. 2006. Oceanography - Plankton in a warmer world. *Nature,* 444**,** 695-696.

DUFRESNE, J. L., FOUJOLS, M. A., DENVIL, S., ., ., ., ., VIOVY, N. & VUICHARD, N. 2013. Climate change projections using the IPSL-CM5 Earth System Model: from CMIP3 to CMIP5. *Clim Dyn,* 40**,** 2123–2165.

DUNNE, J. P., ARMSTRONG, R. A., GNANADESIKAN, A. & SARMIENTO, J. L. 2005. Empirical and mechanistic models of the particle export ratio. *Global Biogeochemical Cycles,* 19:GB4026.

DUNNE, J. P., JOHN, J. G., ADCROFT, A. J., GRIFFIES, S. M., HALLBERG, R. W., SHEVLIAKOVA, E., STOUFFER, R. J., COOKE, W., DUNNE, K. A., HARRISON, M. J., KRASTING, J. P., MALYSHEV, S. L., MILLY, P. C. D., PHILLIPPS, P. J., SENTMAN, L. T., SAMUELS, B. L., SPELMAN, M. J., WINTON, M., WITTENBERG, A. T. & ZADEH, N. 2012a. GFDL's ESM2 Global Coupled Climate–Carbon Earth System Models. Part I: Physical Formulation and Baseline Simulation Characteristics. *Journal of Climate,* 25**,** 6646-6665.

DUNNE, J. P., JOHN, J. G., SHEVLIAKOVA, E., STOUFFER, R. J., KRASTING, J. P., MALYSHEV, S. L., MILLY, P. C. D., SENTMAN, L. T., ADCROFT, A. J., COOKE, W., DUNNE, K. A., GRIFFIES, S. M., HALLBERG, R. W., HARRISON, M. J., LEVY, H., WITTENBERG, A. T., PHILLIPS, P. J. & ZADEH, N. 2012b. GFDL's ESM2 Global Coupled Climate–Carbon Earth System Models. Part II: Carbon System Formulation and Baseline Simulation Characteristics*. *Journal of Climate,* 26**,** 2247-2267.

DUNNE, J. P., SARMIENTO, J. L. & GNANADESIKAN, A. 2007. A synthesis of global particle export from the surface ocean and cycling through the ocean interior and on the seafloor. *Global Biogeochem. Cy.,* 21**,** 1-16.

EPPLEY, R. W. 1972. Temperature and phytoplankton growth in the sea. *Fishery Bulletin,* 70.

FALKOWSKI, P. G., BARBER, R. T. & SMETACEK, V. 1998. Biogeochemical Controls and Feedbacks on Ocean Primary Production. *Science,* 281**,** 200-206.

FALKOWSKI, P. G. & WOODHEAD, A. D. 1992. Primary Productivity and Biogeochemical Cycles in the Sea. *Plenum Press, New York* 550.

FAO 2007. The State of World Fisheries and Aquaculture Rome, Italy.

FAO 2010. The State of World Fisheries and Aquaculture.

FEDOROV, A. V. & PHILANDER, S. G. 2000. Is El Niño changing? . *Science,* 288**,** 1997–2002.

FICHEFET, T. & MAQUEDA, M. M. A. 1997. Sensitivity of a global sea ice model to the treatment of ice thermodynamics and dynamics. *J Geophys Res,* 102(C6)**,** 12609–12646.

FIELD, C. B., BEHRENFELD, M. J., RANDERSON, J. T. & FALKOWSKI, P. 1998. Primary production of the biosphere: Integrating terrestrial and oceanic components. *Science,* 281**,** 237-240.

FOLLOWS, M. & DUTKIEWICZ, S. 2002. Meteorological modulation of the North Atlantic spring bloom. *Deep-Sea Research Part II-Topical Studies in Oceanography,* 49**,** 321-344.

GALLISAI, R., PETERS, F., VOLPE, G., BASART, S. & BALDASANO, J. M. 2014. Saharan Dust Deposition May Affect Phytoplankton Growth in the Mediterranean Sea at Ecological Time Scales. *Plos One,* 9.

GAUBE, P., CHELTON, D. B., STRUTTON, P. G. & BEHRENFELD, M. J. 2013. Satellite observations of chlorophyll, phytoplankton biomass, and Ekman pumping in

nonlinear mesoscale eddies. *Journal of Geophysical Research: Oceans,* 118**,** 6349–6370.

GENT, P. R., ET AL. 1998. he NCAR Climate System Model global ocean component. *J. Clim.,* 11**,** 1287–1306.

GORDON, H. R., BROWN, O. B., EVANS, R. H., BROWN, J. W., SMITH, R. C., BAKER, K. S. & CLARK, D. K. 1988. A semianalytic radiance model of ocean color. *J. Geophys. Res.,* 93**,** 909-10,924.

GREGG, W. W. 2002. A coupled ocean-atmosphere radiative model for global ocean biogeochemical models. *NASA Global Modelling and Assimilation Series*.

GREGG, W. W. 2005. Recent trends in global ocean chlorophyll. *Geophysical Research Letters,* 32.

GREGG, W. W. & CONKRIGHT, M. E. 2002. Decadal changes in global ocean chlorophyll. *Geophysical Research Letters,* 29.

GREGG, W. W., GINOUX, P., SCHOPF, P. S. & CASEY, N. W. 2003b. Phytoplankton and iron: validation of a global three-dimensional ocean biogeochemical model. *Deep-Sea Research Part Ii-Topical Studies in Oceanography,* 50**,** 3143-3169.

GRIFFIES, S. M. 2009. The Gent–McWilliams skew flux. *J. Phys. Oceanogr.,* 28**,** 831–841.

GUPTA, A. S., JOURDAIN, N. C., BROWN, J. N. & MONSELESAN, D. 2013. Climate Drift in the CMIP5 Models*. *Journal of Climate,* 26**,** 8597-8615.

HALLBERG, R. 1995. Some aspects of the circulation in ocean basins with isopycnals intersecting the sloping boundaries. *Ph.D. thesis, University of Washington, 244 pp [Available from University Microfilms, 1490 Eisenhower Place, P.O. Box 975, Ann Arbor, MI 48106]*.

HAMZA, W., ENAN, M. R., AL-HASSINI, H., STUUT, J.-B. & DE-BEER, D. 2011. Dust storms over the Arabian Gulf: a possible indicator of climate changes consequences. *Aquatic Ecosystem Health & Management,* 14**,** 260-268.

HARRISON, R. G., SHINE, K. P., PREDICTION, H. C. F. C. & RESEARCH 1999. *A Review of Recent Studies of the Influence of Solar Changes on the Earth's Climate/R. G. Harrison*, Hadley Centre for Climate Prediction and Research Meteorological Office.

HASSELMANN, K. 1979. On the signal-to-noise problem in atmospheric studies. *Meteorology over the tropical oceans, D.B. Shaw ed., Roy Meteorol. Soc.***,** 251-259.

HASSELMANN, K. 1993. Optimal Fingerprints for the Detection of Time-Dependent Climate-Change. *Journal of Climate,* 6**,** 1957-1971.

HASSELMANN, K. 1997. Multi-pattern fingerprint method for detection and attribution of climate change. *Climate Dynamics,* 13**,** 601-611.

HASTIE, T. & TIBSHIRANI, R. 1990. Generalized Additive Models. Chapman and Hall, London, UK.

HAYS, G. C., RICHARDSON, A. J. & ROBINSON, C. 2005. Climate change and marine plankton. *Trends in Ecology & Evolution,* 20**,** 337-344.

HAYWARD, T. L. 1987a. THE NUTRIENT DISTRIBUTION AND PRIMARY PRODUCTION IN THE CENTRAL NORTH PACIFIC. *Deep-Sea Research Part a-Oceanographic Research Papers,* 34**,** 1593-1627.

HAYWARD, T. L. 1987b. The Nutrient Distribution and Primary Production in the Central North Pacific. *Deep-Sea Research Part a-Oceanographic Research Papers,* 34**,** 1593-1627.

HAYWARD, T. L. 1991. PRIMARY PRODUCTION IN THE NORTH PACIFIC CENTRAL GYRE - A CONTROVERSY WITH IMPORTANT IMPLICATIONS. *Trends in Ecology & Evolution,* 6**,** 281-284.

HEGERL, G. C., HASSELMANN, K., CUBASCH, U., MITCHELL, J. F. B., ROECKNER, E., VOSS, R. & WASZKEWITZ, J. 1997. Multi-fingerprint detection and attribution analysis of greenhouse gas, greenhouse gas-plus-aerosol and solar forced climate change. *Climate Dynamics,* 13**,** 613-634.

HEGERL, G. C. & NORTH, G. R. 1997. Comparison of statistically optimal approaches to detecting anthropogenic climate change. *Journal of Climate,* 10**,** 1125-1133.

HEGERL, G. C., STOTT, P. A., ALLEN, M. R., MITCHELL, J. F. B., TETT, S. F. B. & CUBASCH, U. 2000. Optimal detection and attribution of climate change: sensitivity of results to climate model differences. *Climate Dynamics,* 16**,** 737-754.

HEGERL, G. C., VONSTORCH, H., HASSELMANN, K., SANTER, B. D., CUBASCH, U. & JONES, P. D. 1996. Detecting greenhouse-gas-induced climate change with an optimal fingerprint method. *Journal of Climate,* 9**,** 2281-2306.

HEGSETH, E. N. & SUNDFJORD, A. 2008. Intrusion and blooming of Atlantic phytoplankton species in the high Arctic. *Journal of Marine Systems,* 74**,** 108-119.

HENSON, S. A., DUNNE, J. P. & SARMIENTO, J. L. 2009a. Decadal variability in North Atlantic phytoplankton blooms. *Journal of Geophysical Research: Oceans,* 114**,** C04013.

HENSON, S. A., RAITSOS, D., DUNNE, J. P. & MCQUATTERS-GOLLOP, A. 2009b. Decadal variability in biogeochemical models: Comparison with a 50-year ocean colour dataset. *Geophysical Research Letters,* 36**,** L21601.

HENSON, S. A., ROBINSON, I., ALLEN, J. T. & WANIEK, J. J. 2006. Effect of meteorological conditions on interannual variability in timing and magnitude of the spring bloom in the Irminger Basin, North Atlantic. *Deep-Sea Research Part I-Oceanographic Research Papers,* 53**,** 1601-1615.

HENSON, S. A. & THOMAS, A. C. 2007. Interannual variability in timing of bloom initiation in the California Current System. *Journal of Geophysical Research: Oceans,* 112**,** C08007.

HOURDIN, F., MUSAT, I., BONY, S., BRACONNOT, P., CODRON, F., DUFRESNE, J. L., FAIRHEAD, L., FILIBERTI, M. A., FRIEDLINGSTEIN, P., GRANDPEIX, J. Y., KRINNER, G., LEVAN, P. & LOTT, F. 2006. The LMDZ4 general circulation model: climate performance and sensitivity to parametrized physics with emphasis on tropical convection. *Clim Dyn,* 27(7-8)**,** 787–813.

HUANG, R. X. & RUSSELL, S. 1994. VENTILATION OF THE SUBTROPICAL NORTH PACIFIC. *Journal of Physical Oceanography,* 24**,** 2589-2605.

HURRELL, J. W. 1995. Decadal Trends in the North-Atlantic Oscillation - Regional Temperatures and Precipitation. *Science,* 269**,** 676-679.

IPCC 2007a. Historical Overview of Climate Change. In: Climate Change 2007: The Physical Science Basis. Contribution of Working Group I to the Fourth Assessment Report of the Intergovernmental Panel on Climate Change [Solomon, S., D. Qin, M. Manning, Z. Chen, M. Marquis, K.B. Averyt, M. Tignor and H.L. Miller (eds.)]. Cambridge University Press, Cambridge, United Kingdom and New York, NY, USA.

IPCC 2013. Climate Change 2013: The Physical Science Basis. Contribution of Working Group I to the Fifth Assessment Report of the Intergovernmental Panel on Climate Change [Stocker, T.F., D. Qin, G.-K. Plattner, M. Tignor, S.K. Allen, J. Boschung, A. Nauels, Y. Xia, V. Bex and P.M. Midgley (eds.)]. *Cambridge University Press, Cambridge, United Kingdom and New York, NY, USA***,** 1535.

IPCC, C. C. S. R. 2007b. Contribution of Working Groups I, II and III to the Fourth Assessment Report of the Intergovernmental Panel on Climate Change. *[Core Writing Team, Pachauri, R.K and Reisinger, A. (eds.)]*. . IPCC, Geneva, Switzerland, 104 pp.

IRWIN, A. J. & OLIVER, M. J. 2009. Are ocean deserts getting larger? *Geophysical Research Letters,* 36**,** L18609.

IVERSON, R. L. 1990. CONTROL OF MARINE FISH PRODUCTION. *Limnology and Oceanography,* 35**,** 1593-1604.

JENKINS, W. J. & GOLDMAN, J. C. 1985. SEASONAL OXYGEN CYCLING AND PRIMARY PRODUCTION IN THE SARGASSO SEA. *Journal of Marine Research,* 43**,** 465-491.

JONES, D. R., KARL, D. M. & LAWS, E. A. 1996. Growth rates and production of heterotrophic bacteria and phytoplankton in the North Pacific subtropical gyre. *Deep-Sea Research Part I-Oceanographic Research Papers,* 43**,** 1567-1580.

KAHRU, M., GILLE, S. T., MURTUGUDDE, R., STRUTTON, P. G., MANZANO-SARABIA, M., WANG, H. & MITCHELL, B. G. 2010. Global correlations between winds and ocean chlorophyll. *Journal of Geophysical Research: Oceans,* 115**,** C12040.

KAHRU, M., KUDELA, R., MANZANO-SARABIA, M. & MITCHELL, B. G. 2009. Trends in primary production in the California Current detected with satellite data. *Journal of Geophysical Research: Oceans,* 114**,** C02004.

KARL, D. M., CHRISTIAN, J. R., DORE, J. E., HEBEL, D. V., LETELIER, R. M., TUPAS, L. M. & WINN, C. D. 1996. Seasonal and interannual variability in primary production and particle flux at Station ALOHA. *Deep-Sea Research Part II-Topical Studies in Oceanography,* 43**,** 539-568.

KARL, D. M. & LUKAS, R. 1996. The Hawaii Ocean Time-series (HOT) program: Background, rationale and field implementation. *Deep-Sea Research Part Ii-Topical Studies in Oceanography,* 43**,** 129-156.

KIM, H.-M., WEBSTER, P. J. & CURRY, J. A. 2012. Evaluation of short-term climate change prediction in multi-model CMIP5 decadal hindcasts. *Geophysical Research Letters,* 39**,** L10701.

KNUTSON, T. R. 2000. Model assessment of regional surface temperature trends. *Journal of Geophysical Research,* 104**,** 30981-30996.

KRINNER, G., VIOVY, N., DE NOBLET-DUCOUDRE´ N, O. E. J., POLCHER, J., FRIEDLINGSTEIN, P., CIAIS, P., SITCH, S. & PRENTICE, I. C. 2005. A dynamic global vegetation model for studies of the coupled atmospherebiosphere system. *Global Biogeochem Cycles,* 19(1):GB1015.

KRISTIANSEN, T., F., D., LOUGH, R. G. & SUNDBY, S. 2011. Recruitment Variability in North Atlantic Cod and Match-Mismatch Dynamics. *PLoS One,* 6, e17456. doi:10.1371/journal.pone.0017456.

LANDSEA, C. W. & KNAFF, J. A. 2000. How much skill was there in forecasting the very strong 1997–98 El Niño. *Bulletin of the American Meteorological Society,* 81**,** 2107–2119.

LEFEVRE, F., BRASSEUR, G. P., FOLKINS, I., SMITH, A. K. & SIMON, P. 1994. Chemistry of the 1991-1992 stratospheric winter: three-dimensional model simulations. *J Geophys Res Atm,* 99(D4)**,** 8183–8195.

LEFEVRE, F., FIGAROL, F., CARSLAW, K. S. & PETER, T. 1998. The 1997 Arctic ozone depletion quantified from three-dimensional model simulations. *Geophys Res Lett,* 25(13)**,** 2425–2428.

LEVITUS, S., ANTONOV, J. I., WANG, J., DELWORTH, T. L., DIXON, K. W. & BROCCOLI, A. J. 2001. Anthropogenic warming of Earth's climate system. *Science,* 292**,** 267-270.

LIENERT, F., FYFE, J. C. & MERRYFIELD, W. J. 2011. Do climate models capture the tropical influences on North Pacific sea surface temperature variability. *Journal of Climate,* 24**,** 6203–6209.

LIN, S. J. 2004. A‘‘vertically Lagrangian’’ finite-volume dynamical core for global models. *Mon. Wea. Rev,* 132**,** 2293–2307.

LONGHURST, A. 1995. Seasonal cycles of pelagic production and consumption. *Progress in Oceanography,* 36**,** 77-167.

MACKAS, D. L. 2011. Does blending of chlorophyll data bias temporal trend? *Nature,* 472**,** E4-E5.

MADEC, G. 2008. NEMO ocean engine. Technical note, IPSL, available at http://www.nemo-ocean.eu/content/download/11245/56055/file/NEMO_book_v3_2.pdf.

MANABE, S. & STOUFFER, R. J. 1980. Sensitivity of a Global Climate Model to an Increase of Co2 Concentration in the Atmosphere. *Journal of Geophysical Research-Oceans and Atmospheres,* 85**,** 5529-5554.

MANTUA, N. J. & HARE, S. R. 2002. The Pacific decadal oscillation. *Journal of Oceanography,* 58**,** 35-44.

MARTINEZ, E., ANTOINE, D., D'ORTENZIO, F. & GENTILI, B. 2009. Climate-Driven Basin-Scale Decadal Oscillations of Oceanic Phytoplankton. *Science,* 326**,** 1253-1256.

MCCLAIN, C. R. 2009. A decade of satellite ocean color observations. *Annu. Rev. Mar. Sci.,* 1**,** 19-42.

MCCLAIN, C. R., CHRISTIAN, J. R., SIGNORINI, S. R., LEWIS, M. R., ASANUMA, I., TURK, D. & DUPOUY-DOUCHEMENT, C. 2002. Satellite ocean-color

observations of the tropical Pacific Ocean. *Deep-Sea Research Part Ii-Topical Studies in Oceanography,* 49**,** 2533-2560.

MCCLAIN, C. R., O'REILLY, J.E., MARITORENA, S., SIEGEL, D. A., O'BRIEN, M. C., TOOLE, D., CHAVEZ, F. P., STRUTTON, P., COTA, G. F., HOOKER, S. B., CARDER, K. L., MULLER-KARGER, F., HARDING, L., MAGNUSON, A., PHINNEY, D., MOORE, G. F., AIKEN, J., ARRIGO, K. R., LETELIER, R. & CULVER, M. 2000. Ocean Chlorophyll a Algorithms for SeaWiFS, OC2, and OC4: Version 4. In O'Reilly, J.E., and 24 Coauthors, SeaWiFS Postlaunch Calibration and Validation Analyses, Part 3. NASA Tech. Memo. 2000-206892,. 11**,** 9-19.

MCCLAIN, C. R., SIGNORINI, S. R. & CHRISTIAN, J. R. 2004. Subtropical gyre variability observed by ocean-color satellites. *Deep Sea Research Part II: Topical Studies in Oceanography,* 51**,** 281-301.

MCQUATTERS-GOLLOP, A., REID, P. C., MARTIN EDWARDS, PETER H. BURKILL, CLAUDIA CASTELLANI, SONIA BATTEN, WINFRIED GIESKES, DOUG BEARE, ROBERT R. BIDIGARE, ERICA HEAD, ROD JOHNSON, MATI KAHRU, KOSLOW, J. A. & PENA, A. 2011. Is there a decline in marine phytoplankton? *Nature,* 472, E6-E7, doi:10.1038/nature09950.

MICHAELS, A. F. & SILVER, M. W. 1988. PRIMARY PRODUCTION, SINKING FLUXES AND THE MICROBIAL FOOD WEB. *Deep-Sea Research Part a-Oceanographic Research Papers,* 35**,** 473-490.

MITCHELL, J. F. B., KAROLY, D. J., HEGERL, G. C., ZWIERS, F. W., ALLEN, M. R. & MARENGO, J. 2001. Detection of Climate Change and Attribution of Causes In : Climate Change 2001: The Scientific Basis. Contribution of Working Group I to the Third Assessment Report of the Intergovernmental Panel on climate Change [Houghton, J.T., Y. Ding, D.J. Griggs, M. Noguer, P.J. van der Linden, X. Dai, K. Maskell, and C.A. Johnson (eds.)]. Cambridge University Press, Cambridge, United Kingdom and New York, NY, USA]. 697-735.

MURRAY, R. J. 1996. Explicit generation of orthogonal grids for ocean models. *J. Comput. Phys,* 126**,** 251–273.

NERGER, L. & GREGG, W. W. 2007. Assimilation of SeaWiFS data into a global ocean-biogeochemical model using a local SEIK filter. *Journal of Marine Systems,* 68**,** 237-254.

NORTH, G. R. & STEVENS, M. J. 1998. Detecting climate signals in the surface temperature record. *Journal of Climate,* 11**,** 563-577.

NORTH, G. R. & WU, Q. G. 2001. Detecting climate signals using space-time EOFs. *Journal of Climate,* 14**,** 1839-1863.

PAETH, H. & HENSE, A. 2001. Signal analysis of the atmospheric mean 500/1000 hPa temperature north of 55 degrees N between 1949 and 1994. *Climate Dynamics,* 18**,** 345-358.

PASSOW, U. & CARLSON, C. 2012. The biological pump in a high CO2 world. *Marine Ecology Progress Series,* 470**,** 249-271.

PINCUS, R., BATSTONE, C. P., HOFMANN, R. J. P., TAYLOR, K. E. & GLECKER, P. J. 2008. Evaluating the present-day simulation of clouds, precipitation, and radiation in climate models. . *J. Geophys. Res. Atmos.,* 113, D14209.

PLATT, T., SATHYENDRANATH, S., WHITE, G. N., III, FUENTES-YACO, C., ZHAI, L., DEVRED, E. & TANG, C. 2010. Diagnostic Properties of Phytoplankton Time Series from Remote Sensing. *Estuaries and Coasts,* 33. doi:10.1007/s12237-009-9161-0.

POLOVINA, J. J., HOWELL, E. A. & ABECASSIS, M. 2008. Ocean's least productive waters are expanding. *Geophysical Research Letters,* 35**,** L03618.

REICHLER, T. & KIM, J. 2008. How well do coupled models simulate today's climate? *Bull. Am. Meteorol. Soc.,* 89**,** 303–311.

RESING, J. A. & BARRETT, P. M. 2014. OCEAN CHEMISTRY Fingerprints of a trace nutrient. *Nature,* 511**,** 164-165.

RILEY, G. A. 1947. Factors controlling phytoplankton populations on Georges Bank. *Journal of Marine Research,* 6**,** 54-73.

RYKACZEWSKI, R. R. & DUNNE, J. P. 2011. A measured look at ocean chlorophyll trends. *Nature,* 472, E5-E6, doi:10.1038/nature09952.

RYTHER, J. H. & YENTSCH, C. S. 1957. The estimation of phytoplankton production in the ocean from chlorophyll and light data. *Limnol. Oceanogr.,* 2**,** 281-286.

SABA, V. S., FRIEDRICHS, M. A. M., ANTOINE, D., ARMSTRONG, R. A., ASANUMA, I., BEHRENFELD, M. J., CIOTTI, A. M., DOWELL, M., HOEPFFNER, N., HYDE, K. J. W., ISHIZAKA, J., KAMEDA, T., MARRA, J., MELIN, F., MOREL, A., O'REILLY, J., SCARDI, M., SMITH, W. O., SMYTH, T. J., TANG, S., UITZ, J., WATERS, K. & WESTBERRY, T. K. 2011. An evaluation of ocean color model estimates of marine primary productivity in coastal and pelagic regions across the globe. *Biogeosciences,* 8**,** 489-503.

SABA, V. S., FRIEDRICHS, M. A. M., CARR, M.-E., ANTOINE, D., ARMSTRONG, R. A., ASANUMA, I., AUMONT, O., BATES, N. R., BEHRENFELD, M. J., BENNINGTON, V., BOPP, L., BRUGGEMAN, J., BUITENHUIS, E. T., CHURCH, M. J., CIOTTI, A. M., DONEY, S. C., DOWELL, M., DUNNE, J., DUTKIEWICZ, S., GREGG, W., HOEPFFNER, N., HYDE, K. J. W., ISHIZAKA, J., KAMEDA, T.,

KARL, D. M., LIMA, I., LOMAS, M. W., MARRA, J., MCKINLEY, G. A., MÉLIN, F., MOORE, J. K., MOREL, A., O'REILLY, J., SALIHOGLU, B., SCARDI, M., SMYTH, T. J., TANG, S., TJIPUTRA, J., UITZ, J., VICHI, M., WATERS, K., WESTBERRY, T. K. & YOOL, A. 2010a. Challenges of modeling depth-integrated marine primary productivity over multiple decades: A case study at BATS and HOT. *Global Biogeochemical Cycles,* 24**,** GB3020.

SABA, V. S., FRIEDRICHS, M. A. M., CARR, M. & YOOL, A. 2010b. Challenges of modeling depth-integrated marine primary productivity over multiple decades: A case study at BATS and HOT. *Global Biogeochemical Cycles,* 24.

SCHOPF, P. S. & LOUGHE, A. 1995. A reduced gravity isopycnal ocean model: hindcasts of El Nino. *Monthly Weather Review,* 123**,** 2839–2863.

SCHULZ, M. 2007. Constraining model estimates of the aerosol radiative forcing. *The`se d'Habilitation a` Diriger des Recherches, Universite´ Pierre et Marie Curie, Paris, France*.

SCINOCCA, J. F., MCFARLANE, N. A., LAZARE, M., LI, J. & PLUMMER, D. 2008. Technical Note: The CCCma third generation AGCM and its extension into the middle atmosphere. *Atmos. Chem. Phys.,* 8**,** 7055–7074.

SEFERIAN, R., BOPP, L., GEHLEN, M., ORR, J. C., ETHE, C., CADULE, P., AUMONT, O., SALAS Y MELIA, D., VOLDOIRE, A. & MADEC, G. 2013. Skill assessment of three earth system models with common marine biogeochemistry. *Climate Dynamics,* 40**,** 2549-2573.

SHEVLIAKOVA, E., PACALA, S. W., MALYSHEV, S., HURTT, G. C., MILLY, P. C. D., CASPERSEN, J. P., SENTMAN, L. T., FISK, J. P., WIRTH, C. & CREVOISIER, C. 2009. Carbon cycling under 300 years of land use change: Importance of the secondary vegetation sink. *Global Biogeochemical Cycles,* 23**,** GB2022.

SHINE, K., DERWENT, R. G., WUEBBLES, D. J. & MORCETTE, J. J. 1990. Radiative forcing of climate. In: Climate Change: The IPCC Scientific Assessment, Intergovernmental Panel on Climate Change (IPCC), Houghton, J.T., Jenkins, G.J. & Ephraums, J.J. (eds.). Cambridge University Press, Cambridge.

SIEGEL, D. A., BEHRENFELD, M. J., MARITORENA, S., MCCLAIN, C. R., ANTOINE, D., BAILEY, S. W., BONTEMPI, P. S., BOSS, E. S., DIERSSEN, H. M., DONEY, S. C., EPLEE JR., R. E., EVANS, R. H., FELDMAN, G. C., FIELDS, E., FRANZ, B. A., KURING, N. A., MENGELT, C., NELSON, N. B., PATT, F. S., ROBINSON, W. D., SARMIENTO, J. L., SWAN, C. M., WERDELL, P. J., WESTBERRY, T. K., WILDING, J. G. & YODER, J. A. 2013. Regional to Global Assessments of Phytoplankton Dynamics from the SeaWiFS Mission. *Remote Sensing of the Environment,* 135**,** 77-91.

SIGNORINI, S. R. & MCCLAIN, C. R. 2012. Subtropical gyre variability as seen from satellites. *Remote Sensing Letters,* 3**,** 471-479.

SOMMER, U. & LENGFELLNER, K. 2008. Climate change and the timing, magnitude, and composition of the phytoplankton spring bloom. *Global Change Biology,* 14**,** 1199-1208.

STEELE, J. H. 1978. Spatial Patterns in Plankton Communities. *Plenum, New York.*

STRAHLER, A. N. 1960. *Physical geography,* Wiley.

STUART, A. C., JOCHEM, M., STEVEN, A., JOHANN, H. J., JOHANNA, B. & HELMUTH, H. 2007. Timely Detection of Changes in the Meridional Overturning Circulation at 26°N in the Atlantic. *Journal of Climate,* 20**,** 5827.

SUBRAMANIAM, A., YAGER, P. L., CARPENTER, E. J., MAHAFFEY, C., BJORKMAN, K., COOLEY, S., KUSTKA, A. B., MONTOYA, J. P., SANUDO-WILHELMY, S. A., SHIPE, R. & CAPONE, D. G. 2008. Amazon River enhances diazotrophy and carbon sequestration in the tropical North Atlantic Ocean. *Proceedings of the National Academy of Sciences of the United States of America,* 105**,** 10460-10465.

SVERDRUP, H. U. 1953. On conditions for the vernal blooming of phytoplankton. *J Cons. Cons. Int. Explor. Mer,* 18**,** 287-295.

SWART, N. C. & FYFE, J. C. 2012. Observed and simulated changes in the Southern Hemisphere surface westerly wind-stress. *Geophysical Research Letters,* 39**,** L16711.

SZOPA, S., BALKANSKI, Y., SCHULZ, M., BEKKI, S., CUGNET, D., FORTEMS-CHEINEY, A., TURQUETY, S., COZIC, A., DÉANDREIS, C., HAUGLUSTAINE, D., IDELKADI, A., LATHIÈRE, J., LEFEVRE, F., MARCHAND, M., VUOLO, R., YAN, N. & DUFRESNE, J. L. 2013. Aerosol and ozone changes as forcing for climate evolution between 1850 and 2100. *Climate Dynamics,* 40**,** 2223-2250.

TAYLOR, K. E. 2001. Summarizing multiple aspects of model performance in a single diagram. *Journal of Geophysical Research,* 106**,** 7183-7192.

TAYLOR, K. E., STOUFFER, R. J. & MEEHL, G. A. 2012. An overview of CMIP5 and the experiment design. *Bull. Amer. Meteor. Soc.,* 93**,** 485–498.

TERRAY, L., CORRE, L., CRAVATTE, S., DELCROIX, T., REVERDIN, G. & RIBES, A. 2012. Near-Surface Salinity as Nature's Rain Gauge to Detect Human Influence on the Tropical Water Cycle. *Journal of Climate,* 25**,** 958-977.

TETT, S. F. B., MITCHELL, J. F. B., PARKER, D. E. & ALLEN, M. R. 1996. Human influence on the atmospheric vertical temperature structure: Detection and observations. *Science,* 247**,** 1170-1173.

TETT, S. F. B., STOTT, P. A., ALLEN, M. A., INGRAM, W. J. & MITCHELL, J. F. B. 1999. Causes of twentieth century temperature change. *Nature,* 399**,** 569-572.

THOMAS, A. C., CARR, M. E. & STRUB, P. T. 2001. Chlorophyll variability in eastern boundary currents. *Geophys. Res. Lett.,* 28**,** 3421-3424.

TOL, R. S. J. & DE VOS, A. F. 1998. A Bayesian statistical analysis of the enhanced greenhouse effect. *Climatic Change,* 38**,** 87-112.

TRENBERTH, K. E. 2001. El Niño Southern Oscillation (ENSO). In: EDITORS-IN-CHIEF: JOHN, H. S., KARL, K. T. & STEVE, A. T. (eds.). *Encyclopedia of Ocean Sciences (Second Edition). Oxford: Academic Press*.

TURK, K. A., REES, A. P., ZEHR, J. P., PEREIRA, N., SWIFT, P., SHELLEY, R., LOHAN, M., WOODWARD, E. M. S. & GILBERT, J. 2011. Nitrogen fixation and nitrogenase (nifH) expression in tropical waters of the eastern North Atlantic. *Isme Journal,* 5**,** 1201-1212.

VANCOPPENOLLE, M., MEINERS, K. M., MICHEL, C., BOPP, L., BRABANT, F., CARNAT, G., DELILLE, B., LANNUZEL, D., MADEC, G., MOREAU, S., TISON, J.-L. & VAN DER MERWE, P. 2013. Role of sea ice in global biogeochemical cycles: emerging views and challenges. *Quaternary Science Reviews,* 79**,** 207-230.

VANTREPOTTE, V. & MÉLIN, F. 2011. Inter-annual variations in the SeaWiFS global chlorophyll a concentration (1997–2007). *Deep Sea Research Part I: Oceanographic Research Papers,* 58**,** 429-441.

VENEGAS, S. A. & BJORNSSON, H. 1997. A Manual for EOF and SVD Analysis of Climate Data. *Department of Atmpspheric and Oceanic Sciences and Centre for Climate and Global Change Research, McGill University*.

WALSH, K. & PITTOCK, A. B. 1998. Potential changes in tropical storms, hurricanes, and extreme rainfall events as a result of climate change. . *Climatic Change,* 39**,** 199–213.

WARE, D. M. & THOMSON, R. E. 2005. Bottom-up ecosystem trophic dynamics determine fish production in the northeast Pacific. *Science,* 308**,** 1280-1284.

WERNAND, M. R., VAN DER WOERD, H. J. & GIESKES, W. W. C. 2013. Trends in Ocean Colour and Chlorophyll Concentration from 1889 to 2000, Worldwide. *Plos One,* 8.

WIGLEY, T. M. L., SMITH, R. L. & SANTER, B. D. 1998. Anthropogenic influence on the autocorrelation structure of hemispheric-mean temperatures. *Science,* 282**,** 1676-1679.

WILSON, C. & ADAMEC, D. 2001. Correlations between surface chlorophyll and sea surface height in the tropical Pacific during the 1997-1999 El Nino-Southern Oscillation event. *Journal of Geophysical Research,* 106**,** 31,175-31,188.

WINTON, M. 2000. A reformulated three-layer sea ice model. *J. Atmos. Oceanic Technol,* 17**,** 525–531.

YE, Y., WAGENER, T., VOELKER, C., GUIEU, C. & WOLF-GLADROW, D. A. 2011. Dust deposition: iron source or sink? A case study. *Biogeosciences,* 8**,** 2107-2124.

YODER, J. A. 2003. Seasonal and ENSO variability in global ocean phytoplankton chlorophyll derived from 4 years of SeaWiFS measurements. *Global Biogeochemical Cycles,* 17.

YODER, J. A., MCCLAIN, C. R., FELDMAN, G. C. & ESAIAS, W. E. 1993. Annual Cycles of Phytoplankton Chlorophyll Concentrations in the Global Ocean - a Satellite View. *Global Biogeochemical Cycles,* 7**,** 181-193.

ZHANG, M. H., LIN, W. Y., KLEIN, S. A., BACMEISTER, J. T., BONY, S., CEDERWALL, R. T., DEL GENIO, A. D., HACK, J. J., LOEB, N. G., LOHMANN, U., MINNIS, P., MUSAT, I., PINCUS, R., STIER, P., SUAREZ, M. J., WEBB, M. J., WU, J. B., XIE, S. C., YAO, M.-S. & YANG, J. H. 2005. Comparing clouds and their seasonal variations in 10 atmospheric general circulation models with satellite measurements. *Journal of Geophysical Research Letters,* 110: D15S02.

ZHANG, X., ZWIERS, F. W., HEGERL, G. C., LAMBERT, F. H., GILLETT, N. P., SOLOMON, S., STOTT, P. A. & NOZAWA, T. 2007. Detection of human influence on twentieth-century precipitation trends. *Nature,* 448**,** 461-5.

ZHOU, Y. P., TAO, W. K., HOU, A. Y., OLSON, W. S., SHIE, C. L., LAU, K. M., CHOU, M. D., LIN, X. & GRECU, M. 2007. Use of high-resolution satellite observations to evaluate cloud and precipitation statistics from cloud-resolving model simulations. Part I: South China Sea monsoon experiment. *Journal of the Atmospheric Sciences,* 64**,** 4309–4329.